University of California

Los Angeles

Terahertz Time-Domain Spectroscopy of High-T_c Superconductors

A dissertation submitted in partial satisfaction

of the requirements for the degree

Doctor of Philosophy in Physics

by

Verner Kristian Thorsmølle

2001

The dissertation of Verner Kristian Thorsmølle is approved.

Gary A. Williams

W. Gilbert Clark

Oscar M. Stafsudd

Martin P. Maley

Stuart E. Brown, Committee Chair

University of California, Los Angeles

2001

Til min kære moder og fader

Minnie og Henning

Table of Contents

1 General Introduction and Outline 1

2 Terahertz Time-Domain Spectroscopy 9

2.1 Terahertz Time-Domain Spectrometers 10

2.1.1 Photoconductive generation and detection of THz Pulses . 12

2.1.2 Collimating and Focusing Optics 16

2.1.3 Electro-optic generation and detection of THz Pulses . . . 18

2.2 Time-Domain Analysis 23

2.2.1 Time-Windowing of Data 23

2.2.2 Complex Transmission Coefficients 26

2.2.3 Extraction of Material Parameters 32

2.3 Time-Resolved Optical-Pump Terahertz-Probe Spectroscopy . . . 36

3 Introduction to Vortex Physics in High-T_c Superconductors . 45

3.1 Properties of the Superconducting State 45

3.1.1 Magnetic Properties 47

3.2 Flux Flow, Flux Creep, and Pinning 53

3.3 Magnetic Phase Diagram of High-T_c Superconductors 59

3.4 Zero Field Cooling and Field Cooling 68

3.5 Magnetization Hysteresis 71

3.6 Structure of Vortex Liquid Phase in Irradiated $Bi_2Sr_2CaCu_2O_{8-\delta}$ Crystals 76

4 Josephson Plasma Resonance in High-T_c Superconductors . . 87

4.1 Theory of the Josephson Plasma Resonance 88

4.1.1 Temperature and C-axis Magnetic Field dependence of the Josephson Plasma Resonance 93

(A) The Josephson Plasma Resonance as a Probe to study the Symmetry of the Superconducting Order Parameter 93

(B) Dissipation and Dispersion Effects of the Josephson Plasma Resonance 96

(C) The Josephson Plasma Resonance as a Probe to study the Vortex Structure 97

4.2 C-axis Josephson Plasma Resonance Observed in Transmission in $Tl_2Ba_2CaCu_2O_8$ by use of Terahertz Time-Domain Spectroscopy . 101

4.2.1 Symmetry of the Superconducting Order Parameter 107

4.2.2 C-axis Quasiparticle Damping of the Josephson Plasma Resonance 109

4.3 Angular Dependence of the Josephson Plasma Resonance in $Tl_2Ba_2CaCu_2O_8$ 111

4.4 Direct Evidence for Linelike Vortex Liquid Phase in $Tl_2Ba_2CaCu_2O_8$ Probed by the Josephson Plasma Resonance 121

4.5 Current-driven Vortex State in $Tl_2Ba_2CaCu_2O_8$ Probed by the Josephson Plasma Resonance 137

5 Ultrafast Conductivity Dynamics of Hole Doped Transition Metal Oxides 141

5.1 Nonequilibrium Superconductivity in $Y_{1-x}Pr_xBa_2Cu_3O_7$ Thin Films 142
5.2 Colossal Magnetoresistance Manganites 147
5.2.1 Basic Theory of Colossal Magnetoresistance Manganites . 147
5.2.2 Ultrafast Conductivity Dynamics in Colossal Magnetoresistance Manganites 151

6 Conclusions 163

A Derivation of Transmission Coefficients 165
A.1 Thin Film on Thick Substrate 165
A.1.1 Induced Conductivity as a function of Induced Field . . . 166
A.2 Optical Properties of Uniaxial Anisotropic Media 166
A.2.1 Reflection and Transmission Coefficients at an Interface . . 169

References 173

List of Figures

1.1 Crystal structure of $YBa_2Cu_3O_7$ superconducting compound. . . . 2

1.2 Schematic phase diagram of high-T_c superconductors. 4

1.3 Illustration of the mixed-state magnetic phase diagram. 5

2.1 Schematic diagram of a THz-TDS spectrometer. 11

2.2 The Austin switch configured as a THz emitter. 13

2.3 Refraction of rays from three different substrate lens designs. . . . 14

2.4 The Austin switch configured as a THz detector. 15

2.5 Typical designs for THz optical systems. 17

2.6 Typical optical set-up of a THz-TDS spectrometer using electro-optic techniques. 21

2.7 Measured THz waveforms. 24

2.8 Propagation of a plane wave in a slab of material. 26

2.9 Propagation of a plane wave in a thin film on a thick substrate. . 30

2.10 Measured THz waveforms of an optimally doped 50 nm YBCO thin film on a 0.5 mm MgO substrate. 34

2.11 FFT amplitude of measured THz waveforms. 34

2.12 Complex transmission coefficient of YBCO film. 35

2.13 Complex conductivity of YBCO film. 36

2.14 Ultrafast electron dynamics in metals. 39

2.15 Illustration of the behavior of $\Delta T/T$ as a function of time in a metallic system. 40

2.16 Typical optical set-up of an optical pump THz probe experiment. 42

2.17 Illustration of the conductivity dynamics in a metallic system where $\sigma_{imag} \ll 1$. 44

3.1 Schematic representation of the symmetry of the superconducting order parameter in k-space. 47

3.2 Magnetization versus applied magnetic field for a type I and a type II superconductor. 49

3.3 Schematic representation of the structure of an isolated Abrikosov vortex in a high-T_c superconductor. 50

3.4 Schematic magnetic phase diagram of a high-T_c superconductor. . 51

3.5 Schematic diagram of an Abrikosov vortex lattice. 52

3.6 A schematic view of the flux-flow state with a transport current in a magnetic field. 53

3.7 A single vortex line segment pinned by point defects and acted upon by the Lorentz force. 55

3.8 A vortex density gradient and a current density are always intrinsically related. 56

3.9 Illustration of the "tilted-washboard" potential model. 57

3.10 Crystal structure of $Bi_2Sr_2CaCu_2O_8$ superconducting compound. . 61

3.11 Illustration of a single flux line structure in a strongly layered high-T_c superconductor. 62

3.12 Mixed-state phase diagram of a pristine $Bi_2Sr_2CaCu_2O_8$ crystal. . 64

3.13 Illustration of the sudden disorder of pancake vortices at the second peak. 65

3.14 Mixed-state phase diagram of an irradiated $Bi_2Sr_2CaCu_2O_8$ crystal. 66

3.15 The flux density profiles are straight lines in the Bean model. . . . 69

3.16 Zero field and field cooling on $Bi_2Sr_2CaCu_2O_8$ single crystal ($B||c$). 70

3.17 Magnetic hysteresis measurement on a $Bi_2Sr_2CaCu_2O_8$ single crystal ($B||c$). 72

3.18 Magnetic hysteresis measurements on a $Bi_2Sr_2CaCu_2O_8$ single crystal ($B||c$). 74

3.19 Hysteretic loops of the local magnetization on a $Bi_2Sr_2CaCu_2O_{8+x}$ single crystal. 75

3.20 Dependence of resistivity ρ_c versus $B_\parallel^2$ for perpendicular components $B_\perp$. 81

3.21 Dependence $g(B_\parallel) = \sigma_c[B_\parallel/(B_s B_\perp)^{1/2}]/\sigma_c(0)$ in irradiated and pristine crystals. 82

3.22 The functions $G(r/a)$ (a), and $G(r/R)$ (b) as extracted from $g(B_\parallel)$. 84

3.23 Dependence of the correlation length R as a function of filling factor. 85

4.1 Structure of highly anisotropic High-T_c superconductor with Josephson coupled CuO_2 layers and interstitial insulating layers. 89

4.2 Phase difference induced by pancake vortices in neighboring layers. 91

4.3 Normalized London penetration depth $\lambda_L^2(0)/\lambda_L^2(T)$ versus reduced temperature T/T_c. 94

4.4 Magnetic and Josephson interactions between pancake vortices in adjacent layers. 98

4.5 (a) JPR versus temperature in zero field. (b) JPR versus c-axis applied field at constant temperature in the liquid phase. 98

4.6 JPR measurements in a microwave cavity. 100

4.7 Experimental set-up of THz-TDS spectrometer. 102

4.8 Configuration of the thin film plus substrate with respect to the terahertz beam. 103

4.9 Electric field of the THz pulse in the time-domain transmitted through Tl-2212 film. 104

4.10 Transmission amplitude versus frequency for Tl-2212 film. 106

4.11 JPR frequency versus temperature for Tl-2212 film. 107

4.12 Superfluid fraction versus reduced temperature for Tl-2212 film. . 108

4.13 JPR linewidth versus temperature for Tl-2212 film. 109

4.14 C-axis quasiparticle conductivity versus temperature for Tl-2212 film. 110

4.15 Configuration of the Tl-2212 film with respect to the THz beam for (a) p-polarization, and (b) s-polarization. 112

4.16 JPR at 0, 15, 30, and 45 degrees angles for p-polarization in Tl-2212.113

4.17 JPR versus angle for both p- and s-polarizations in Tl-2212. . . . 113

4.18 Schematic diagram of a layered high-T_c superconductor with B-field component $B_{osc}\|y$. 115

4.19 Atomic force microscopy surface picture of 700 nm thick Tl-2212 thin film showing height profiles along line A and B. 117

4.20 JPR at 0, 15, 30, and 45 degrees angles in Tl-2212. The polarizations of emitter and receiver are crossed. 118

4.21 JPR versus angle for crossed polarizations in Tl-2212. 118

4.22 JPR at 30, 60, 100, 140 and 175 mW optical power at the ZnTe emitter for p-polarization at 0 degrees incidence in Tl-2212. 119

4.23 JPR versus optical power for both p- and s-polarizations at 45 degrees, and at 0 degrees incidence at the Tl-2212 film. 119

4.24 Illustration of the mixed-state phase diagram of (a) Bi-2212, (b) Tl-2212, and (c) Y-123. The focus of these phase diagrams is to see the effect of the anisotropy on the structure of the vortex liquid phase. 122

4.25 Jump in the interlayer phase coherence factor in Bi-2212 single crystal at the melting transition as a function of magnetic field. . 125

4.26 Electric field of THz pulse in the time-domain transmitted through Tl-2212 thin film on MgO substrate at (a) 70 K and 80 K, and at (b) 70 K with and without a 2.5 kG c-axis applied field. 127

4.27 Transmission amplitude versus frequency for Tl-2212 thin film. (a) JPR in zero field from 70 K to 100 K. (b) JPR in 2.5 kG field applied along the c-axis from 70 K to 90 K. 129

4.28 (a) JPR frequency versus temperature in Tl-2212 with and without c-axis applied field of 2.5 kG. (b) Drop in JPR frequency due to c-axis field of 2.5 kG versus temperature. The inset shows the interlayer phase coherence factor $<\cos\varphi_{n,n+1}>$ versus temperature. 130

4.29 Interlayer phase coherence factor $<\cos\varphi_{n,n+1}>$ versus temperature in Tl-2212 with four different magnetic fields applied along the c-axis. 132

4.30 Interlayer phase coherence factor 1-$<\cos\phi_{n,n+1}>$ in Tl-2212 versus c-axis magnetic field at various temperatures. 132

4.31 Comparison between experimental data for the interlayer phase coherence factor $<\cos\phi_{n,n+1}>$ in Tl-2212 at 70, 75, and 85 K, and numerical calculations based on Reference 134 across the melting transition. 136

4.32 Interlayer phase coherence factor $<\cos\phi_{n,n+1}>$ versus applied *ab*-plane current in Tl-2212 in 2.5 kG *c*-axis magnetic field at 10, 60, 80, and 90 K. 139

5.1 Experimental set-up of optical-pump terahertz-probe spectrometer in transmission. 142

5.2 Conductivity at 60 K and 95 K, respectively. The imaginary conductivity is shown with the real conductivity in the insets. 144

5.3 Normalized induced change in the imaginary conductivity (60 K) as a function of time at various frequencies. The curves are displaced vertically for clarity. The solid lines are fits to the function y = a×exp(-t/τ_σ) + b. The inset shows the measured lifetime as a function of frequency. 146

5.4 Temperature profile of resistivity of a $La_{1-x}Ca_xMnO_3$ ($x = 0.3$) single crystal at various magnetic fields. A strong negative magnetoresistance is observed close to the Curie temperature. 147

5.5 Magnetic phase diagram of $La_{1-x}Ca_xMnO_3$. 148

5.6 Crystal ligand-field splitting of five-fold degenerate atomic 3*d* levels into lower t_{2g} (triply degenerate) and higher e_g levels (doubly degenerate levels of Mn^{3+}). Jahn-Teller distortion of MnO_6 octahedron further lifts each degeneracy as shown in the figure. 149

5.7 Illustration of the double-exchange mechanism via the transfer integral t_{ij} (hopping matrix). 150

5.8 Schematic crystal structure of $La_{1-x}Ca_xMnO_3$. The tolerance factor f measures the distortion from the perovskite-based cubic structure. 151

5.9 Temperature dependence of the THz transmission and real conductivity. 153

5.10 a) One minus the normalized induced change in electric field ΔE versus time for LCMO film at various temperatures. (b and c) Real conductivity versus time at various temperatures. 155

5.11 (a and b) Temperature dependence of the lifetime τ_{sl} of the slow component due to spin-lattice relaxation for LCMO and LSMO respectively. The inset shows the induced temperature change. . . 158

5.12 Temperature dependence of the THz transmission and real conductivity. (a) Transmitted electric field at various temperatures for a 90 nm thick LCMO film. (b) Real conductivity versus frequency for LCMO at various temperatures. (c and d) The value of the real conductivity at 0.7 THz as a function of temperature for LCMO and LSMO thin films. 160

A.1 Electromagnetic wave propagating in a uniaxial crystal. 167

A.2 (a and b) Illustration of the directions of the wave normal and the field vectors of an electromagnetic wave propagating in a uniaxial crystal. 170

Acknowledgments

I am indebted to Stuart E. Brown for being my advisor at UCLA and overlooking my Ph.D. progress. I am also indebted to Martin P. Maley for being my advisor at Los Alamos National Laboratory (LANL) and for his outstanding mentorship throughout my Ph.D. research work in the Superconductivity Technology Group at LANL. I truly appreciate his teachings and our many discussions on high-T_c superconductors and vortex physics. Special thanks goes to Antoinette Taylor from the Condensed Matter and Thermal Physics Group for collaborating with us and for inviting me to work in her ultrafast laser laboratories. Soon all my experiments were to take place in these laboratories.

In particular, I owe the most grateful thanks to Richard D. Averitt for more than one reason. First of all for having the opportunity to work with him in the laboratory for the last couple of years, and for teaching me about ultrafast experimental techniques. I am thankful for being introduced into the world of ultrafast time-resolved pump-probe measurements on hole-doped transition metal oxides, and I have benefitted greatly from numerous discussions on these subjects.

I would like also to extend my thanks to Lev Bulaevskii from the Condensed Matter Theory Group for collaborations on the Josephson plasma resonance. I have enjoyed many enlightening discussions on the subject.

In the Superconductivity Technology Group I would like to acknowledge all the people I have interacted and worked with. Particularly, Nikolai Morozov, Takasada Shibauchi, J. Yates Coulter, Jeffrey O. Willis, Vladimir Matijasevic, Quanxi Jia, Adriana C. Serquis, Paul C. Dowden, Eric J. Peterson, David B. Jan, and Dean Peterson. I would like also to acknowledge Melanie Asaki, and Jure Demšar from the Condensed Matter and Thermal Physics Group, and Christian

Helm from the Condensed Matter Theory Group.

I am grateful for the hospitality of George Grüner at UCLA for opening up his laboratory in the early attempts to capture the Josephson plasma resonance, and Eric Helgren for assisting with the experiments.

Special thanks are due to Albert Cardona and Superconductivity Technology, Inc. from Santa Barbara in California for providing the thallium samples used in the Josephson plasma resonance experiments.

Finally, I would like to thank Professor Gary A. Williams, Professor W. Gilbert Clark, and Professor Oscar M. Stafsudd for serving on my committee.

Figure 3.19 is reprinted from Physica C [1], with kind permission from Elsevier Science. Figure 4.6 is reprinted from Physical Review Letters [2], with kind permission from The American Physical Society, and Yuji Matsuda from University of Tokyo in Japan. Figure 4.25 is reprinted from Physical Review Letters [3], with kind permission from The American Physical Society, and Takasada Shibauchi from Kyoto University in Japan. Figure 5.4 and 5.5 is reprinted from Colossal Magnetoresistive Oxides [4], Advances in Condensed Matter Science, Volume 2, with kind permission from Gordon and Breach Publishing, a member of the Taylor and Francis Group.

This research was supported by the University of California Campus-Laboratory Collaborations and by the Los Alamos Directed Research and Development Program by the U.S. Department of Energy.

Vita

August 29, 1962	Born, Copenhagen, Denmark
January 1987	B.S. in Electrical Engineering, Engineering College of Denmark, Copenhagen, Denmark
1987–1990	Electrical Engineer, Motorola A/S, Land Mobile Products Sector, Copenhagen, Denmark
December 1992	M.S. in Physics, San Jose State University, San Jose, California
1993–1994	Physicist, Beckman Instruments, Advanced Development and Applied Research, Brea, California
March 1994	M.S. in Engineering, Technical University of Denmark, Lyngby, Denmark
Summer 1994	Research Assistant, Physics Department, UCLA, Los Angeles, California
1994–1997	Teaching Assistant, Physics Department, UCLA, Los Angeles, California
1994–1997	Danish Research Academy Fellow, Physics Department, UCLA, Los Angeles, California
1997–present	Graduate Research Assistant, Los Alamos National Laboratory, Los Alamos, New Mexico

Publications

"Structure of Vortex Liquid Phase in Irradiated $Bi_2Sr_2CaCu_2O_{8-\delta}$ Crystals", N. Morozov, M. P. Maley, L. N. Bulaevskii, V. K. Thorsmølle, A. E. Koshelev, A. Petrea, and W. K. Kwok, *Physical Review Letters* **82**, No. 5, p. 1008 (1999).

"Observation of the Josephson Plasma Resonance in $Tl_2Ba_2CaCu_2O_8$ using THz Spectroscopy", V. K. Thorsmølle, R. D. Averitt, M. P. Maley, L. N. Bulaevskii, and A. J. Taylor, *Ultrafast Phenomena XII, 12th Annual Proceeding*, edited by T. Elsaesser, S. Mukamel, M. M. Murmane, N. F. Scherer, p. 431−433 (Charleston, SC, USA: New York, Springer-Verlag 2001).

"Ultrafast THz Conductivity Dynamics: Spin-lattice Relaxation in Colossal Magnetoresistive Oxides", R. D. Averitt, A. I. Lobad, C. Kwon, S. A. Trugman, V. K. Thorsmølle, and A. J. Taylor, *Ultrafast Phenomena XII, 12th Annual Proceeding*, edited by T. Elsaesser, S. Mukamel, M. M. Murmane, N. F. Scherer, p. 434−437 (Charleston, SC, USA: New York, Springer-Verlag 2001).

"Ultrafast Conductivity Dynamics in Colossal Magneto-Resistance Manganites", R. D. Averitt, A. I. Lobad, C. Kwon, S. A. Trugman, V. K. Thorsmølle, and A. J. Taylor, *Physical Review Letters* **87**, No. 1, 017401 (2001).

"*C*-axis Josephson Plasma Resonance Observed in $Tl_2Ba_2CaCu_2O_8$ Superconducting Thin Films by use of Terahertz Time-Domain Spectroscopy", V. K. Thorsmølle, R. D. Averitt, M. P. Maley, L. N. Bulaevskii, C. Helm, and A. J. Taylor, *Optics Letters* **26**, No. 16, 1292 (2001).

"Josephson Plasma Resonance in $Tl_2Ba_2CaCu_2O_8$ in a Magnetic Field Measured using THz Spectroscopy", V. K. Thorsmølle, R. D. Averitt, M. P. Maley, L. N. Bulaevskii, C. Helm, and A. J. Taylor, *Physica B*, In press.

"Nonequilibrium superconductivity in $Y_{1-x}Pr_xBa_2Cu_3O_7$ thin films", R. D. Averitt, V. K. Thorsmølle, Q. X. Jia, S. A. Trugman, and A. J. Taylor, *Physica B*, In press.

"Ultrafast Conductivity Dynamics of Novel Electronic Materials", R. D. Averitt, V. K. Thorsmølle, A. I. Lobad, S. A. Trugman, and A. J. Taylor, Submitted to *Optics and Photonics News "Optics in 2001"*.

"Ultrafast Optical-Pump Terahertz-Probe Spectroscopy of Strongly Correlated Electron Materials", R. D. Averitt, V. K. Thorsmølle, A. I. Lobad, Q. X. Jia, S. A. Trugman, and A. J. Taylor, Submitted to *the 26th International Conference on Infrared and Millimeter Waves*.

"Evidence for Linelike Vortex Liquid Phase in $Tl_2Ba_2CaCu_2O_8$ Probed by the Josephson Plasma Resonance", V. K. Thorsmølle, R. D. Averitt, M. P. Maley, A. E. Koshelev, L. N. Bulaevskii, and A. J. Taylor, Submitted to *Physical Review Letters*.

Abstract of the Dissertation

Terahertz Time-Domain Spectroscopy of High-T_c Superconductors

by

Verner Kristian Thorsmølle

Doctor of Philosophy in Physics

University of California, Los Angeles, 2001

Professor Stuart E. Brown, Chair

The c-axis Josephson plasma resonance (JPR) in high-T_c cuprate $Tl_2Ba_2CaCu_2O_8$ (Tl-2212) superconducting thin films is unambiguously observed directly in the time-domain employing terahertz time-domain spectroscopy in transmission as a function of temperature with and without an applied c-axis magnetic field. These are the first observations of the JPR in a high-T_c material in transmission. The temperature dependence of the JPR in zero field indicates d-wave symmetry of the superconducting order parameter in the dirty limit. In a c-axis magnetic field, the JPR is sensitive to the ordering of pancake vortices along the c-axis and is an excellent tool to study the vortex structure. Using the JPR to study the interlayer phase coherence, I find direct evidence for a linelike vortex liquid phase in Tl-2212. The ordering of the vortex lattice is studied as a function of applied ab-plane current at different temperatures in a c-axis magnetic field. The ordering decreases with increased current in the vortex solid phase, but then increases when driving it into the flux-flow state near the melting transition.

Using dc transport measurements the c-axis resistivity in irradiated and pris-

tine $Bi_2Sr_2CaCu_2O_{8-\delta}$ is measured as a function of in-plane field component at fixed out-of-plane component $B_\perp$ in the vortex liquid phase. The average length of vortex line segments inside columnar defects as a function of filling factor $f = B_\perp/B_\Phi$ is then determined. The maximum length, $\sim$15 interlayer distances, is reached near $f \approx 0.35$.

Time-resolved optical-pump terahertz-probe spectroscopy is employed to measure ultrafast conductivity dynamics in hole-doped transition metal oxide thin films. Measurements on $La_{0.7}M_{0.3}MnO_3$ (M = Ca, Sr) from 10 K to $\sim 0.9T_c$ reveal a two-component relaxation. A fast, $\sim$2 ps, conductivity decrease arises from optically induced modification of the effective phonon temperature. The slower component, related to spin-lattice relaxation, has a lifetime that increases upon approaching T_c from below in accordance with an increasing spin specific heat. For $T \ll T_c$, $\partial\sigma/\partial T$ is primarily determined by thermally disordered phonons while spin fluctuations dominate near T_c. For YBCO thin films, optical-pump terahertz-probe spectroscopy was used to study the dynamics of superconducting pairs and quasiparticles following photoexcitation. In particular, by following the dynamic changes of the imaginary conductivity, the phase coherent recovery time was directly measured. This recovery occurs on a picosecond timescale.

CHAPTER 1

General Introduction and Outline

The discovery of superconductivity at the surprisingly high temperature of 34 K in 1986 [5] in the Ba-La-Cu-O system by J. G. Bednorz and K. A. Müller launched a major breakthrough in material science. An enormous world wide research effort followed in the quest of a room temperature superconductor, and the high-T_c era had begun. Within the following year, the critical temperature (T_c) was raised to 92 K with the discovery of the yttrium compound [6, 7]. In 1988, the critical temperature was further increased to 120 K and 125 K with the successive discoveries of the bismuth [8] and thallium [9] cuprates. The current record holder is the mercury cuprate, $Hg_2Ba_2Ca_2Cu_3O_{10-\delta}$ with $T_c = 134$ K at atmosperic pressure, and 164 K when subjected to high pressure [10]. It should be mentioned that high-T_c superconductivity has also been found in other types of compounds, such as the cubic perovskite BaKBiO with $T_c \leq 34$ K [11], and sodium doped WO_3 with $T_c = 90$ K [12]. The most recent discovery of superconductivity is in the metallic compound MgB_2 with $T_c = 39$ K [13], which greatly exceeds $T_c = 23.2$ K of Nb_3Ge (1973), the previous highest T_c in a conventional metallic superconductor.

In parallel with the ongoing discoveries of new high-T_c superconducting materials many important and imaginative industrial applications have been suggested, including high-field magnets, loss-free electrical power transmission, high-efficiency motors, computer logic gates, high-sensitivity superconducting quan-

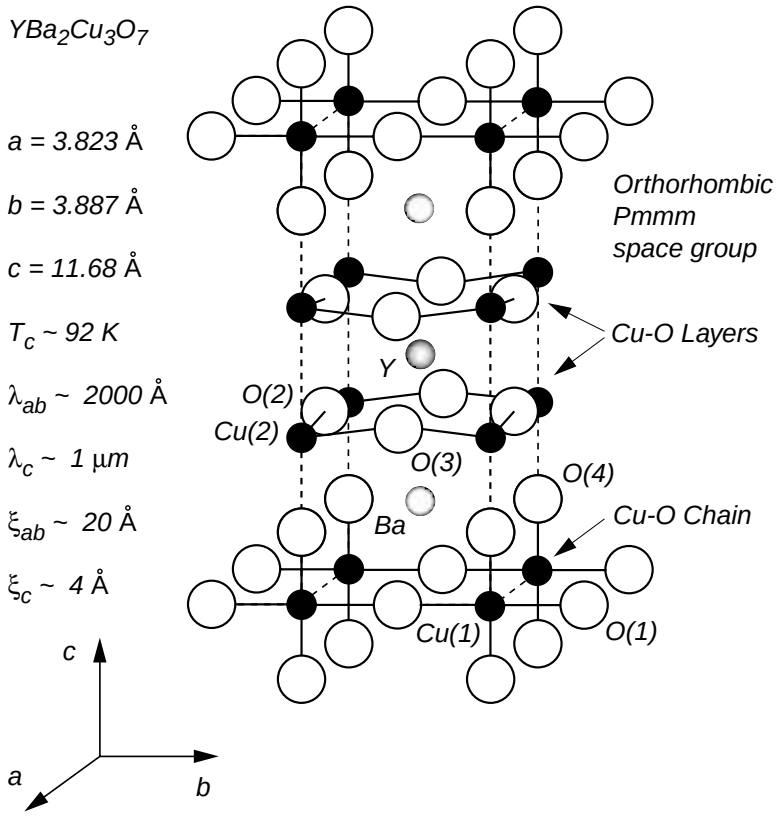

Figure 1.1: Crystal structure of $YBa_2Cu_3O_7$ superconducting compound. The unit cell consists of two CuO_2 planes with a Y ion in between. The third copper oxide plane consists of -Cu-O-Cu-O chains along the b-axis (chains are not pertinent to other superconducting compounds).

tum interference devices, levitated trains, etc. [14]. Critical temperatures now above the boiling temperature of liquid nitrogen has further put the hope for technical applications into reach.

A variety of experimental techniques have been developed to measure the properties of the high-T_c superconducting materials and to gain an understanding of why they superconduct at such high temperatures. The original McMillan formula (1968) for the critical temperature, derived in the BCS theory, with a phonon mediated electron-electron attractive interaction (and taking into account Coulomb repulsion), predicts $T_c \leq 25$ K. It came as a surprise when this

temperature was exceeded with the new ceramic high-T_c superconductors.

High-T_c superconducting cuprates are layered perovskites. They have layered structures with some two-dimensional behavior (see Figure 1.1). The essential structural element is one or more copper oxide planes per unit cell. The interlayer coupling between the CuO_2 planes is very weak and these materials exhibit highly anisotropic properties, and fluctuation effects are prominent.

Charge reservoir layers above and below the CuO_2 planes can accept or donate electrons to the CuO_2 planes via chemical substitution of different-valence ions (e.g. $La_{2-x}Sr_xCuO_4$), changing the oxygen stoichiometry - oxygen doping (e.g. $YBa_2Cu_3O_{7-\delta}$), ion substitution with isovalent ions of different ionic radius, or by a combination. The majority of high-T_c superconductors are hole-doped. A schematic diagram of a hole doped high-T_c superconductor is shown in Figure 1.2.

The undoped parent compound is, below the Néel temperature T_N, an antiferromagnetic insulator. T_N decreases with increasing hole doping p (measured in holes per Cu ion in CuO_2 plane) and the long range antiferromagnetic order vanishes at $p \sim 0.05$. The material exhibits superconductivity at low temperatures in the doping range $0.05 \lesssim p \lesssim 0.25$. The maximum critical temperature is obtained at optimum doping near $p \sim 0.15$ depending slightly on the particular compound. Below and above this doping level the compound is respectively under- and overdoped. The superconductivity vanishes for $p \gtrsim 0.25$ and the material becomes metallic like. Several experiments which probe the density of states (DOS) near the Fermi surface (E_F) suggest an opening of a pseudogap signaled by a suppression in the DOS. The openening of the pseudogap is denoted by the crossover temperature T^* as determined by various experimental techniques [15].

Superconductivity can be destroyed not only by thermal fluctuations when in-

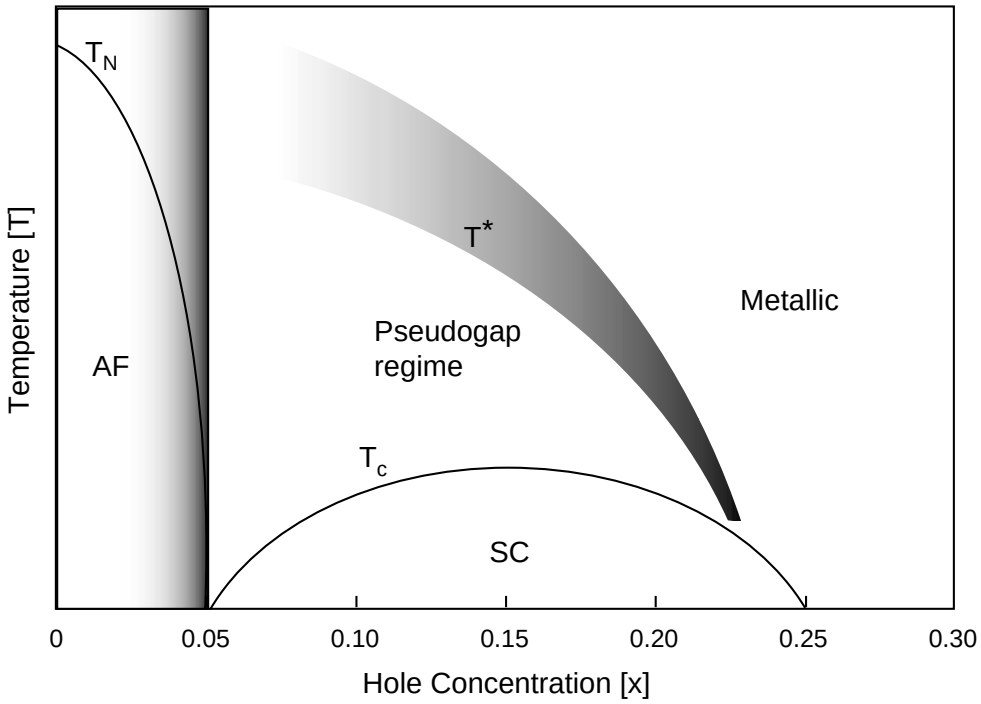

Figure 1.2: Schematic phase diagram of high-T_c superconductors. The abbreviations mean antiferromagnetic insulator (AF), and superconductor (SC). T_N is the Néel temperature, and T^* is the pseudogap crossover temperature.

creasing the temperature through T_c but also by applying a high enough magnetic field or strong electric current. An applied c-axis magnetic field induces a vortex lattice in a high-T_c superconductor in the mixed-state which responds to changes in temperature and to applied currents. The mixed-state phase comprises the superconducting region in which magnetic flux penetrates the high-T_c superconductor in the form of quantized vortices above the Meissner phase. The mixed-state magnetic phase diagram of high-T_c superconductors displays a variety of different phases, including the vortex solid phase, Bose glass phase, pancake liquid phase, etc. as illustrated in the B-T phase diagrams in Figure 1.3. The physical properties of the vortex phase diagram is strongly determined by the anisotropy of the superconductor. In yttrium compounds, which have a low degree of anisotropy, the vortex lines are continuous and the critical current density is substantial in

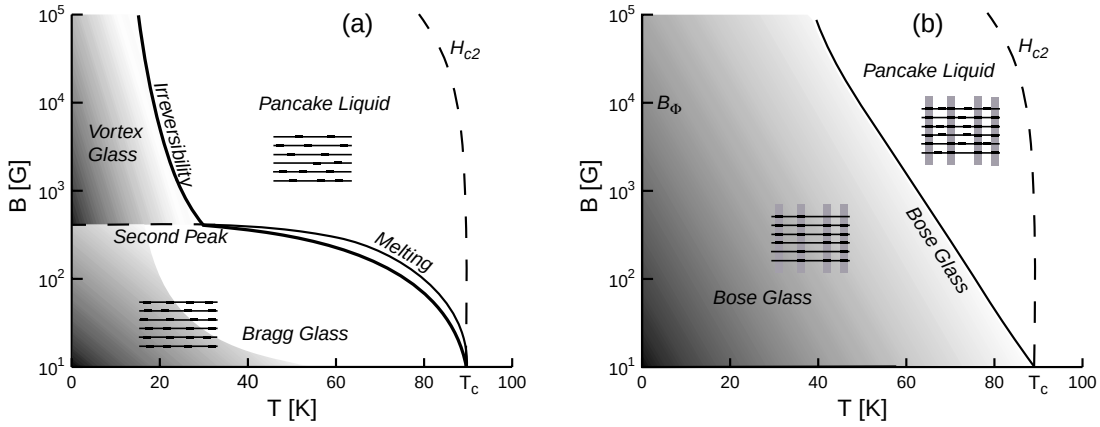

Figure 1.3: Illustration of the mixed-state magnetic phase diagram for (a) a pristine crystal and (b) an irradiated crystal.

a large portion of the phase diagram. In the most anisotropic superconductors such as the bismuth-, thallium-, and mercury-based High-T_c superconductors, the superconductivity is confined to the CuO_2 layers, and the vortex lines are broken into two-dimensional "pancake vortices" in the layers, which are weakly coupled by Josephson interactions and by magnetic interactions. Such a vortex lattice of pancake vortices has close to long-range order at low magnetic fields and temperatures, where the pancake vortices form aligned stacks (vortex lines). However, the interactions are very weak and these vortex lines are easily destroyed due to misalignment of the pancake vortices by either thermal fluctuations at higher temperatures, or by defects in the underlying crystal lattice.

Vortex dynamics are of great importance in determining the transport and magnetic properties of high-T_c superconductors. If one is to utilize high-T_c materials in the form of magnets, power cables or high-frequency filters it is important to understand the pinning properties of vortices and the various phases in the B-T phase diagram. Beneath the melting line or the irreversibility line in the vortex solid phase the vortex lattice is pinned and the critical current density is

nonzero, whereas above in the vortex liquid phase it is unpinned and the critical current density is zero. An applied transport current will exert a Lorentz force on the vortices causing them to move sideways if not properly pinned, which causes resistance and dissipation. Pinning sites are naturally occuring defects in the material in the form of impurities, grain boundaries, oxygen deficiencies, etc. The most efficient pinning sites are created artificially by irradiating the superconductor with very fast heavy ions [16]. The pancake vortices are trapped on these columnar defects which suppresses the thermal vibrations, and moves the melting line up in phase space creating a large region with a substantial critical current density as shown in Figure 1.3(b).

Several techniques such as transport and magnetization measurements are readily utilized in order to study the various phases of the B-T phase diagram [17, 18]. However, measurements of the Josephson plasma resonance (JPR) by either microwave cavity or quasioptical techniques provide unique information of the magnetic properties as well as of the superconducting state, and can be measured in the entire phase diagram. The JPR is a phase collective mode provided by oscillating interlayer Josephson currents. It is sensitive to the correlations of pancake vortices along the c-axis and is therefore an excellent tool to study the vortex structure in high-T_c superconductors with extreme anisotropy such as the bismuth, thallium and mercury compounds. In the absence of a magnetic field the JPR gives information about the interlayer phase coherence [19, 20], and the c-axis penetration depth and hence the symmetry of the order parameter [21].

Microwave cavity techniques, which generally cover a few GHz to $\sim$100 GHz, are well suited to measure the JPR frequency in the most anisotropic crystals such as underdoped $Bi_2Sr_2CaCu_2O_8$ [22]. However, in order to access the frequency range of less anisotropic superconductors such as the thallium and mercury com-

pounds, ∼150 GHz to ∼1 THz, quasioptical techniques are needed [20]. The JPR as well as quasiparticle scattering rates of high-T_c superconductors are contained within the THz regime, which lies between microwave and infrared frequencies, ∼50 GHz - ∼10 THz. The optical properties of high-T_c superconductors in the THz range are easily determined using terahertz time-domain spectroscopy (THz-TDS). The complex conductivity in the superconducting state is determined with almost astonishing simplicity and accuracy without the need for the Kramers-Kronig relations to extract the real and imaginary parts. Combining THz-TDS with optical excitation one can investigate time-dependent phenomena. The sample is optically excited and the frequency-resolved conductivity is obtained as a function of pump-probe delay time with femtosecond resolution. The induced conductivity changes give information about the relaxation dynamics.

The dissertation is organized as follows. Chapter 2 introduces the concepts of THz-TDS including the various elements involved in extracting the desired optical properties of the investigated material. Generation and detection techniques of THz pulses are described, as well as the optical design of THz-TDS in transmission. Chapter 2 also provides a section on time-resolved optical pump THz probe spectroscopy, and its application to metallic systems. Chapter 3 gives an introduction to vortex physics in high-T_c superconductors, necessary to fully appreciate the subsequent JPR experiments. Chapter 3 concludes with a section on the investigation of the structure of the vortex liquid in irradiated $Bi_2Sr_2CaCu_2O_8$ crystals by c-axis magnetoresistance measurements. These c-axis transport measurements demonstrate an alternative technique to THz measurements of the JPR for determining the structure and correlations in a vortex system in the liquid phase of the magnetic phase diagram. Chapter 4 introduces the theory of the JPR with and without a c-axis magnetic field, followed by the experimental results of the JPR. These are the first observation of the JPR in a high-T_c

superconducting material in transmission. The strength of the JPR using THz spectroscopy is that measurements can be obtained in the entire phase diagram, and without causing artifacts. The experiments include angular dependence of the JPR to study the excitation mechanism, temperature and magnetic field dependence of the JPR to study the phase diagram, and the dependence of the JPR when driving the vortex lattice with a current to study the order in the vortex system. Using the JPR as a tool to study the interlayer phase coherence I find direct evidence that the vortex lattice melts into a liquid of vortex lines at the melting transition. Without a magnetic field the JPR is presented in both the time-domain and the frequency-domain. The c-axis quasiparticle conductivity as well as the symmetry of the order parameter is extracted from this data. Chapter 5 presents time-resolved optical-pump terahertz-probe studies of hole-doped transition metal oxides. The relaxation dynamics is studied in the high-T_c superconductor $YBa_2Cu_3O_7$ at different dopings. The second material investigated is from another class of hole doped transition metal oxides, namely the mixed valence manganites - $La_{0.7}Ca_{0.3}MnO_3$ and $La_{0.7}Sr_{0.3}MnO_3$.

CHAPTER 2

Terahertz Time-Domain Spectroscopy

THz-TDS is a very powerful technique for materials studies which covers a frequency range from below 100 GHz to several THz. THZ-TDS bridges the gap between microwave and infrared techniques. The coherent generation and detection of ultrafast pulses of terahertz radiation allows for extraction of the complex material parameters [23]. Thus, THz spectroscopy finds application in the study of a wide variety of materials [24]. In condensed matter systems THz-TDS is of great importance as terahertz photons are resonant with bound states such as excitons in semiconductors, Cooper pairs in superconductors, and low energy excitations of the hole doped transition metal oxides including high-T_c superconductors and mixed valence manganites. Importantly, tunneling and quasiparticle scattering rates of many materials lie also in the terahertz regime. In liquids, the terahertz regime coincides with typical time scales for intermolecular interactions. Most polar gases exhibit characteristic pure rotational spectral lines in the far infrared, and can be studied (or recognized, e.g., multiple gas sensing) using THz-TDS. In simple dielectrics, THz-TDS provides the index of refraction and the absorption coefficient [25]. As a final example, THz-TDS can be used to study artificially grown structures, such as quantum wells which have confinement energies which lie in the terahertz regime.

In spite of its importance, spectroscopy in the terahertz regime has been difficult due to a lack of efficient emitters and detectors. Fourier Transform Infrared

spectroscopic (FTIR) techniques are limited by the lack of brightness of incoherent sources and by the need for cooling of bolometric detectors. Furthermore, the main drawback of FTIR is measuring only the power spectrum with no information available on the spectral phase. However, THz-TDS which is a relatively new spectroscopic technique, developed in the past 10−15 years, circumvents these difficulties in a radical way.

2.1 Terahertz Time-Domain Spectrometers

Subpicosecond terahertz radiation can be generated and detected via opto-electronic or electro-optic techniques (or a combination of both) triggered by femtosecond laser pulses. Regardless of the source of radiation, the duration of these terahertz waveforms is close to a single-cycle oscillation of the electromagnetic field, and consequently will have a high bandwidth, spanning the spectral range from a few tens of gigahertz to several terahertz. With an optical gating pulse much shorter than the THz pulse, the electric field profile of the THz pulse is directly recorded as a function of time simply by varying the delay between the excitation and detection laser pulses. The time resolution is on the order of a fraction of a picosecond. The signal-to-noise ratio (SNR) improves with the square root of the repetition rate of the emitted THz pulses, and the gated detection scheme improves the SNR in the opto-electronic detector by a factor of the duty cycle of the laser system (100 fs/10 ns = 10^{-5}) in comparison to a CW detector, e.g. a bolometer or a photodiode. In practice, SNRs on the order of 10^4 to 10^5-times for opto-electronic detection, and at least 10^4 for electro-optic detection are easily achievable with averaging times of 15−20 minutes for a total scan. *Van Exter and Grischkowsky* [26] have estimated an average power of ∼10 nW with a peak power 10^4-times higher.

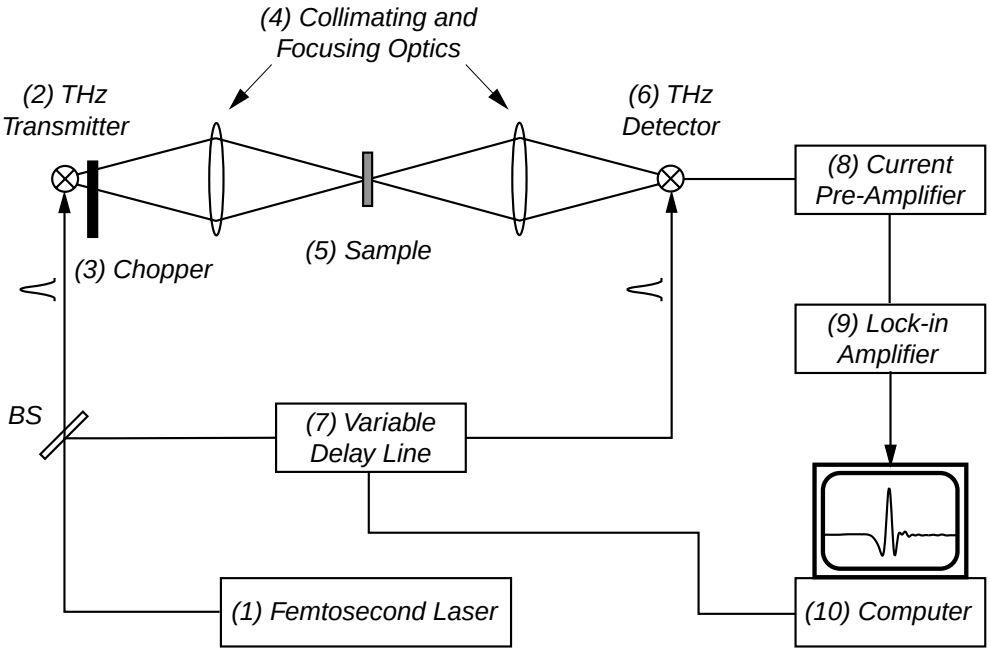

Figure 2.1: Schematic diagram of a THz-TDS spectrometer using a femtosecond laser source and THz transmitters and receivers.

In THz-TDS the terahertz waveform is either transmitted through or reflected by the sample, producing a reshaped waveform in accordance with the characteristic dispersion and absorption of the sample. THz-TDS in transmission is suited for measurements on relatively nonabsorbing samples (i.e. thin metal films less than $\sim$100 nm), while measurements in reflection are preferred for highly reflecting or absorbing materials. The critical measure in transmission is the precise thickness of the sample compared to a reference. In reflection the critical measure is the sample position compared to a reference, where a difference in optical path length gives rise to a shift in phase between sample and reference signals. THz-TDS in reflection will not be discussed any further as the experiments described in this dissertation are in transmission.

Figure 2.1 shows a schematic diagram of a Terahertz Time-Domain Spectrometer. It consists of (1) a femtosecond laser source, (2) a THz transmitter, (3) a

chopper, (4) collimating and focusing optics, (5) the sample, (6) a THz detector, (7) a variable delay line, (8) a current pre-amplifier, (9) a lock-in amplifier, and (10) a computer. The THz transmitter radiates a THz pulse when triggered by a laser pulse. The THz pulse is then collimated and focused onto the sample, and the transmitted THz pulse is refocused onto the THz detector. A portion of the laser beam is split off at the beam splitter and gates the THz detector to measure the waveform voltage. The resulting photocurrent from the THz detector is then detected by the current pre-amplifier and the lock-in amplifier which is referenced to the chopper. The THz detector is gated synchronously with the THz transmitter, and by varying the variable delay line one can map out the entire time dependent electric field of the transmitted THz pulses.

2.1.1 Photoconductive generation and detection of THz Pulses

Using ultrafast lasers for photoconductive switching was pioneered by *D. H. Austin* in the 1970's [27]. In the 1980's these photoconductive Austin switches were then utilized and developed further for the generation of freely propagating THz pulses [28]. Such a high-efficiency transmitter structure is shown in Figure 2.2. The antenna consists of two $5-10$ μm wide conductive metal striplines (standard mixture is gold-germanium-nickel) lithographically deposited on a semi-insulating GaAs substrate wafer, and separated by $10-100$ μm [29]. The applied field of typically $9-90$ Volts across the striplines serves to accelerate the photo-generated free carriers produced by an incoming laser pulse with a photon energy larger than the bandgap. The transient current through the switch gives rise to a time-varying macroscopic electric dipole moment, $\mathbf{P}(t)$. The resulting electric field from the oscillating dipole in the far-field limit is given by

$$\mathbf{E}(\mathbf{r},t) = \frac{1}{4\pi\epsilon_o c^2 r}\hat{\mathbf{r}} \times \left(\hat{\mathbf{r}} \times \frac{d^2\mathbf{P}(t)}{dt^2}\right). \tag{2.1}$$

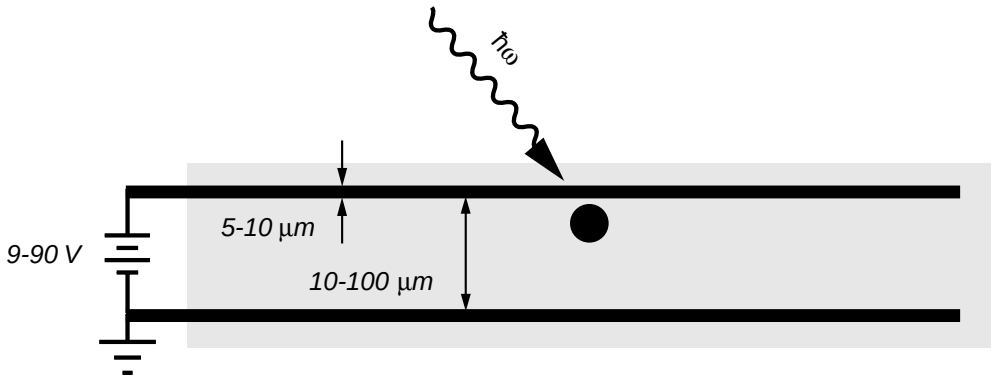

Figure 2.2: The Austin switch configured as a THz emitter. The laser is focused near the positive electrode where the electric field is maximized. The THz emitter is typically biased with 9−90 Volts.

The radiated electric field, $\mathbf{E}(\mathbf{r},t)$, i.e. the terahertz pulse, thus has the same polarization as the applied electric field across the striplines.

The efficiency of the emitted terahertz radiation with a high bandwidth depends on a number of parameters. In particular the dynamical properties of the semiconductor substrate determines the time evolution of the electric dipole moment, $\mathbf{P}(t)$. A high carrier mobility ensures a sharp rising edge of the transient photocurrent which dominates the radiation, $E(t) \propto \partial J(t)/\partial t$. The most effective semi-insulating substrate is chromium compensated gallium arsenide grown by the Czochralski method [29] or low temperature gallium arsenide (LT-GaAs). The applied electric field creates a strong field concentration near the anode which is further enhanced by ionization of deep acceptor traps [30]. The femtosecond laser pulses are then focused tightly to a spot diameter of $\sim$10 μm in the high field region near the anode in order to create the strongest and fastest terahertz pulses. It has been found that focusing the laser beam through a cylindrical lens to an oblong shape along the anode further enhances the THz radiation [29].

In order to effectively couple the terahertz radiation into free space in a forward direction a small hemispherical substrate lens is directly attached to the

back of the emitter substrate [31]. It is important to place the lens in direct contact with the substrate to avoid Fresnel losses and multiple reflections from an air interface. An excellent lens material is high-resistivity crystalline silicon which is highly transparent and dispersion free in the terahertz region with a very low absorption. The refractive index ($n = 3.4177$) is practically constant in the THz regime and matches the index of the most common antenna substrates (sapphire, GaAs, Si).

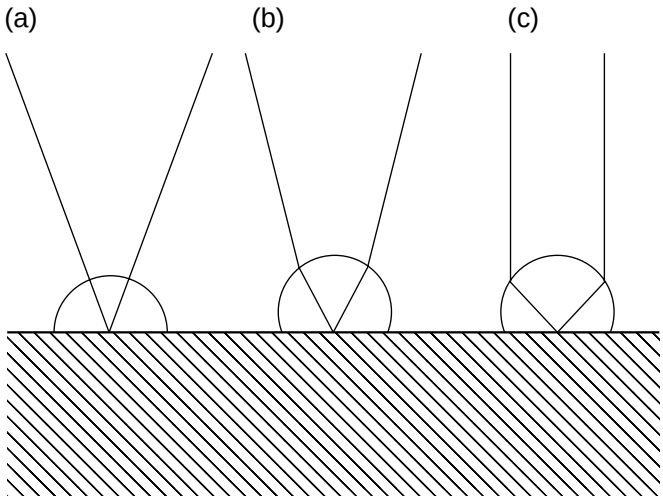

Figure 2.3: Refraction of rays from three different substrate lens designs. (a) The non-focusing hemispherical, (b) the aplanatic hyper-hemispherical, and (c) the focusing hyper-hemispherical substrate lenses.

Figure 2.3 shows three possible substrate lens designs. These are the non-focusing hemispherical, the aplanatic hyper-hemispherical, and the focusing hyper-hemispherical lenses. Typical lens diameters are $2-10$ mm. The design specifications are given by the lens diameter r, the refractive index n, and the distance from the center of the lens to the focal point ρ. In the hemispherical design ($\rho = 0$) all rays exit the lens at normal incidence. Like the hemispherical design, the aplanatic hyper-hemispherical design ($\rho = r/n$) has no spherical aberration or coma, as well as no chromatic abberations [32], when using a lens material

such as silicon with a constant refractive index. The rays are slightly collimated, which allows the remaining optical system to be designed with higher f-numbers. The focusing hyper-hemispherical lens design ($\rho = r/(n-1)$) collimates the rays fully. However, diffraction effects become important in this design because of the long wavelength of the terahertz radiation (1 THz $\sim$ 0.3 mm) compared to the output beam.

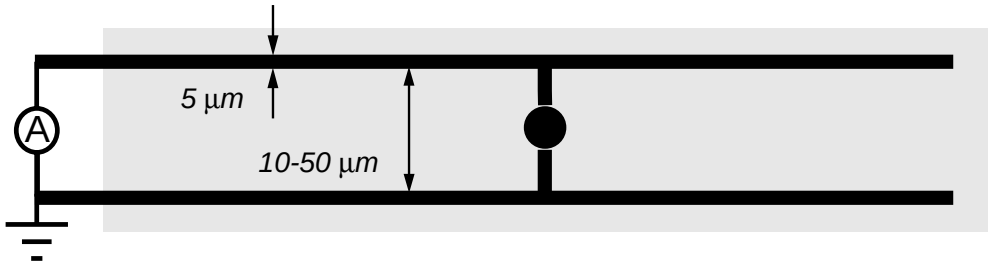

Figure 2.4: The Austin switch configured as a THz detector. The laser is focused in the photoconductive gap bridging the two striplines.

The detector consists of the same building blocks as the emitter with the replacement of the voltage bias with a current meter connected across the striplines as shown in Figure 2.4. The detection of the terahertz radiation is based on the same principles as for the generation described above. However, in this case the driving field for the photocarriers is provided by the electric field of the incident terahertz pulse. The femtosecond laser pulse opens the photoconductive switch, but no current will flow through the switch until both the terahertz field and the photocarriers are present. The current across the striplines will then be directly proportional to the instantaneous THz field. With the photocarrier lifetime, τ much shorter than the THz pulse, the photoconductive Austin switch will act as a sampling gate which samples the terahertz field within the time τ. By varying the time delay between the excitation and detection pulses, a sampled replica of the THz waveform is then recorded as a function of time.

The bandwidth of the detection process is determined by the frequency-dependence of the antenna structure which governs the low-frequency cutoff, and by the photocurrent response which governs the high-frequency cutoff. For a Hertzian dipole antenna with dimensions much less than the wavelength of the incident radiation, the collection efficiency becomes proportional to the radiation frequency, ω. This corresponds to a differentiation of the signal in the time-domain. The photocurrent response, $J(t)$ is described by the convolution of the transient photoconductivity, $\sigma(t)$ and the electric field, $E(t)$ of the terahertz waveform

$$J(t) = \int \sigma(t - t')E(t')dt'. \tag{2.2}$$

The current waveform reproduces $E(t)$ accurately when the photocurrent transient is much shorter than the terahertz waveform, ideally a delta function. Thus, to obtain a high detection bandwidth the antenna must first of all be small. The striplines (standard mixture is titanium-aluminum) are typically 5 μm wide and separated by $10-50$ μm. Secondly, the substrate must have a very short carrier lifetime. Suited materials are Ion implanted silicon on sapphire (RD-SOS) [33] and LT-GaAs, both with carrier lifetimes less than 0.5 ps.

Terahertz spectrometers based on photoconductive dipole antennas driven by sub-100 fs laser pulses can produce terahertz pulses with a bandwidth up to 5 THz [34].

2.1.2 Collimating and Focusing Optics

In order to perform spectroscopic measurements, the THz transmitter and detector are incorporated into a millimeter wave optical system such as shown in Figure 2.5. In Figure 2.5(a) off-axis paraboloid mirrors are used to collimate and focus the THz radiation to a diffraction-limited spot at the sample position.

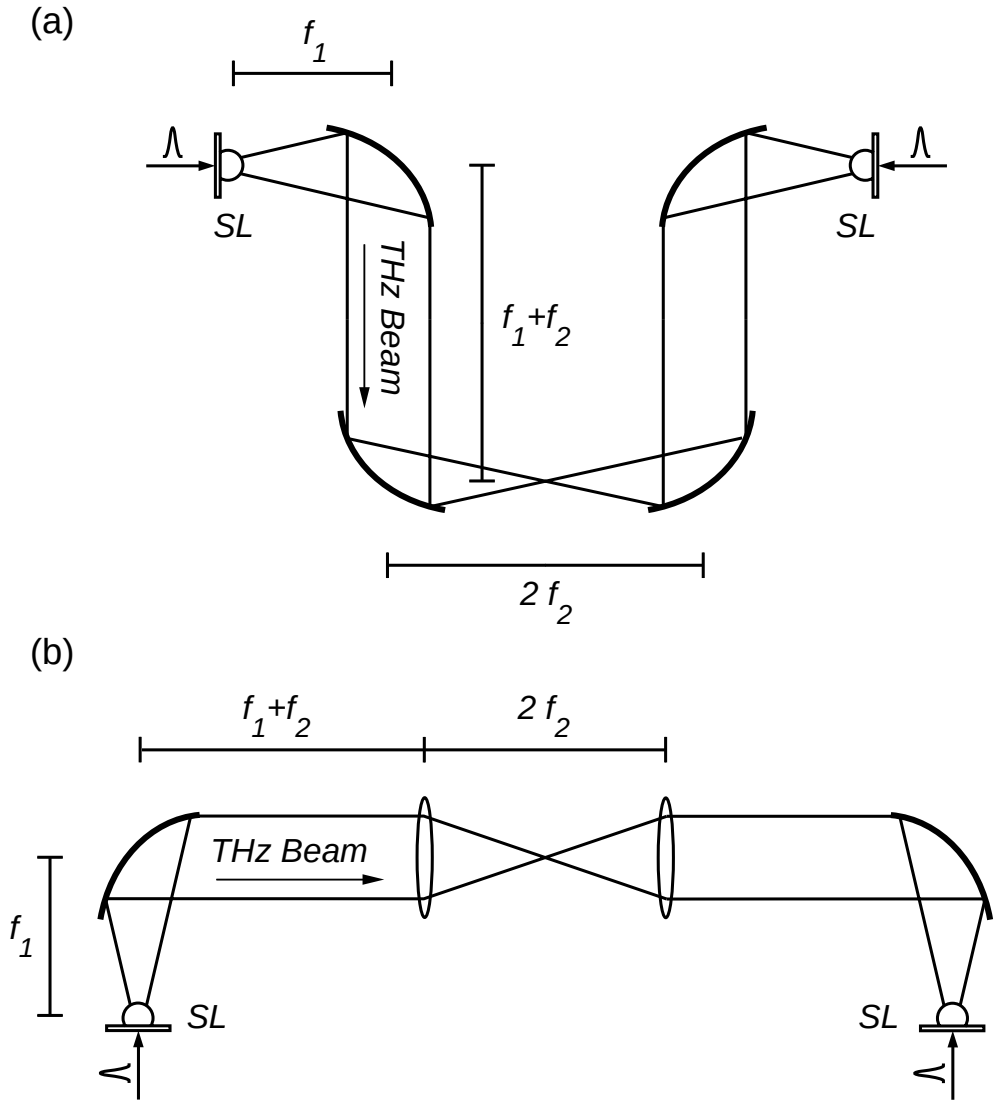

Figure 2.5: Typical designs for THz optical systems. The THz radiation is coupled in and out of the photoconducting dipole antenna using substrate lenses (SL). In (a) off-axis paraboloid mirrors are used to collimate and focus the THz radiation, and in (b) off-axis paraboloid mirrors are used to collimate the THz beam and a set of lenses to focus the THz beam.

Alternatively, Figure 2.5(b) uses off-axis paraboloid mirrors to collimate the THz beam and a set of lenses to focus the THz beam. Gold-coated paraboloids offer high reflectivity and achromatic operation over the entire THz range, and can easily be aligned with a laser beam. High-resistivity silicon ($n \sim 1.4$) is an excellent lens material and may be used up to ∼10 THz, but does not allow for optical alignment with a visible laser beam. The collimating and focusing optics are typically 2−inch−diameter optics with focal lengths in the range from 60 mm to 150 mm depending on the application. A focal spot less than 1 mm is readily achieved.

The emitter and receiver antennas are positioned with the substrate lens at the focal spot of the first and last paraboloid mirrors, respectively. The THz beam is a near Gaussian beam [35], and in the design considerations it is important to distance two adjacent THz guiding optics the added focal lengths apart ($f_1 + f_2$). This is well known to increase the performance of the system by ∼1.5 times or more. It is furthermore of critical importance to position the substrate lenses precisely centered at the emitter and detector within a tolerance of ± 5 μm to obtain the most intense and highest bandwidth THz pulses [29].

The absorption of ambient water vapor can lead to ringing of the THz pulses and the THz beam should be enclosed in a nitrogen purged atmosphere to avoid distortion of the THz pulses.

2.1.3 Electro-optic generation and detection of THz Pulses

In recent years, the prospect of a bandwidth extending beyond 5 THz has stimulated an interest in developing electro-optic techniques for the generation and detection of ultrafast broadband THz pulses. The THz pulses are generated by optical rectification (or the inverse optical effect) in semiconductors [36] or

nonlinear dielectric crystals [37] by use of femtosecond optical pulses. Difference-frequency mixing produces a low frequency polarization that follows the envelope of the incident laser pulse. The nonlinear polarization at the difference frequency is given by

$$P_i^{(2)}(\omega) = \chi_{ijk}^{(2)} \int E_j(\omega_{opt}) E_k(\omega_{opt} - \omega) d\omega_{opt}. \tag{2.3}$$

The second-order nonlinear susceptibility χ_{ijk} is related to the electro-optic tensor r_{ijk} by the expression

$$\chi_{ijk} = -\frac{1}{4} n_i^2 n_j^2 r_{ijk}. \tag{2.4}$$

In the time-domain Equation (2.3) yields

$$P_i^{(2)}(t) = \chi_{ijk}^{(2)} E_j(t) E_k(t). \tag{2.5}$$

This polarization is not stationary, however, but moves with the group velocity of the optical pulse. The contribution from the infrared lattice vibrations to the low-frequency dielectric response causes the velocity of the source to exceed the radiation velocity. This restricts the bandwidth available for efficient phase matching. The phase matching condition for the optical rectification process is given by

$$\Delta k = k(\omega_{opt} + \omega_{THz}) - k(\omega_{opt}) - k(\omega_{THz}) = 0, \tag{2.6}$$

where ω_{opt} and ω_{THz} are the optical and THz frequencies, respectively [38, 39]. Developing this condition up to first order in the frequency, gives the following expression for the inverse THz phase velocity

$$\frac{k(\omega_{THz})}{\omega_{THz}} \approx \frac{(\omega_{opt} + \omega_{THz}) - \omega_{opt}}{\omega_{THz}} \left(\frac{\partial k}{\partial \omega} \right)_{opt} = \left(\frac{\partial k}{\partial \omega} \right)_{opt}. \tag{2.7}$$

This relation implies that phase matching is achieved when the phase of the THz wave travels at the same speed as the optical pulse envelope, i.e., the optical group

velocity, v_g. After the optical laser pulse and the THz wave have copropagated through a material of thickness d, the accumulated group velocity mismatch (GVM) time is

$$\delta(\omega_{THz}) \approx \frac{n_g(\lambda_{opt}) - n(\omega_{THz})}{c} d, \tag{2.8}$$

assuming a monochromatic THz wave and a delta-function like optical pulse centered at λ_{opt}. $n_g(\lambda_{opt})$ is the optical group index, $n(\omega_{THz})$ the THz phase index, and d the crystal thickness. A trade-off clearly exists between a broadband response and a long interaction length. The THz bandwidth is ultimately limited only by the THz phase mismatch and phonon resonances of the nonlinear crystal.

Several considerations determine the selection of the electro-optic material. The material should both have a large electro-optic coefficient, and be transparent to the optical pulse having low absorption. It should also have good transparency in the far-infrared with low attenuation. Furthermore, the static birefringence in both the optical and the far infrared regions of the spectrum should be small. The generation of terahertz radiation through optical rectification has been demonstrated in a variety of materials, such as the ionic crystals, $LiNbO_3$ and $LiTaO_3$ [40], covalent zincblende crystals such as ZnTe, GaAs, GaP [41] and InP [42], and organic crystals [43].

Ionic crystals have large electro-optic coefficients, but their static dielectric constants are too high for efficient phase matching [44]. Furthermore, their ionic nature exhibit strong dispersion and absorption in the THz regime. Covalent zincblende crystals have moderate electro-optic coefficients, relatively low dielectric constants and zero intrinsic birefringence. Particularly ZnTe has shown excellent optical-group-velocity THz-phase-velocity matching within the tuning range of Ti:sapphire lasers with a maximum sensitivity at 2 THz [38]. However, in ZnTe there is a broad TA-phonon absorption line centered at 1.6 THz and one

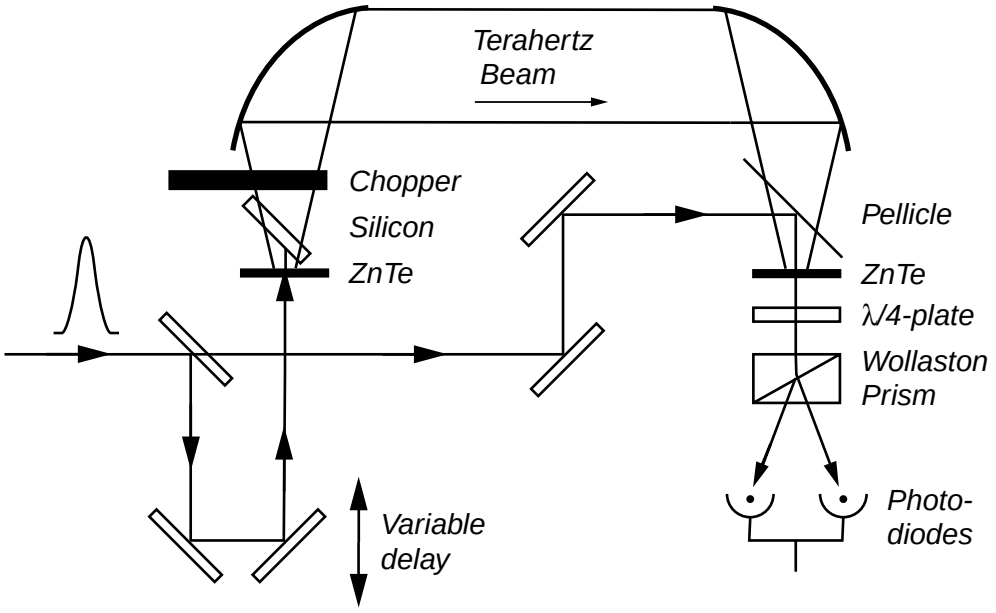

Figure 2.6: Typical optical set-up of a THz-TDS spectrometer using electro-optic techniques for the generation and detection of THz pulses without any focusing optics.

stronger at 3.7 THz in addition to a TO-phonon resonance at 5.3 THz limiting the bandwidth to below 5 THz [45] with a typical crystal thickness of 1 mm. GaAs, GaP, InP have higher lying TO-phonon lines at 8, 9 and 11 THz, respectively. However, the electro-optic coefficients are somewhat smaller [42].

The detection of the THz pulses is based on the linear electro-optic effect (Pockels effect). Since terahertz optical rectification originates from the second order nonlinear susceptibility, which also determines the electro-optic effect, terahertz generation and detection in electro-optic crystals are merely two inverse processes. Thus the same considerations concerning phase matching, etc. apply to the detection side, where a laser probe pulse travels collinear with the incident THz waveform.

Figure 2.6 shows a typical experimental set-up for the generation of THz pulses via optical rectification and coherent detection via free-space electro-optic sampling without any focusing optics. The terahertz radiation is generated in a

$\langle 110 \rangle$ oriented ZnTe crystal with the polarization of the laser pulses parallel to the $\langle 100 \rangle$ axis for maximum coupling to the electro-optic coefficient r_{41}. A high-resistivity silicon or teflon filter is used to block the generating laser beam. It is positioned at Brewster angle to allow maximum transmittance of the THz radiation. The THz radiation is imaged into an identical ZnTe crystal using two off-axis paraboloidal mirrors. A $2-\mu$m$-$thick 50% pellicle beamsplitter is interposed in the THz beam to allow an optical probe pulse with circular polarization to travel collinear with the THz pulse through the ZnTe crystal. The pellicle beamsplitter has a negligible effect on the THz beam and the laser pulse width. The electric field of the linearly polarized THz pulse modulates the optical refractive index of the probe pulse via the Pockels effect and thereby induces an ellipticity of the probe polarization. To convert the field-induced ellipticity modulation into an intensity modulation, the probe pulse is analyzed by a compensator ($\lambda/4$-plate) and a polarizer (Wollaston prism), then detected by a pair of balanced identical photodiodes. This detection scheme effectively reduces common-mode laser noise, so that the detection is primarily shot-noise limited. Peak-to-peak noise is routinely reduced to as small as 1.0×10^{-8}. It is fine adjusted by rotating the $\lambda/4$-plate appropriately. The temporal waveforms are then sampled by varying the time delay between the optical pump and probe pulses.

It has been demonstrated that, with this technique, frequencies as great as 37 THz can be measured [46]. In this experiment a Ti:sapphire laser delivered 12 fs pulses at 800 nm and an average power of 500 mW. A 0.45$-$mm$-$thick $\langle 110 \rangle$ oriented GaAs wafer was used as emitter and a $30-\mu$m$-$thick $\langle 110 \rangle$ ZnTe crystal as the electro-optic sensor. These thin crystals effectively minimize the optical and terahertz dispersion, absorption, phonon-polariton coupling, and GVM, resulting in high bandwidth. However, the trade-off is with the sensitivity and with the reflection-free time window. The reflection-free time window can be in-

creased by attaching a $\langle 100 \rangle$ plate of the same crystal, which has null transverse electro-optic effect, to the back of each of the $\langle 110 \rangle$ crystals to delay the THz reflection.

2.2 Time-Domain Analysis

To extract the complex material parameters of the sample under study THz-TDS requires two measurements. In the first measurement, a set of averaged scans of the temporal profiles $E_{\text{sig}}(t)$ of the THz pulses transmitted through the sample are recorded. In the second measurement, a set of averaged scans of the temporal profiles $E_{\text{ref}}(t)$ of the THz pulses transmitted through a reference with known parameters are recorded. After appropriate time-windowing and zero padding, the Fourier transform of the sample measurement is divided by the Fourier transform of the reference measurement. This ratio gives the complex transmission coefficient of the sample as a function of frequency. The final step involves performing a complex fit of the measured transmission coefficient to the theoretical transmission coefficient. This yields the complex refractive index, dielectric function or conductivity.

2.2.1 Time-Windowing of Data

An optically thick sample is defined as a sample for which the echoes of the THz pulse, caused by multiple reflections in the sample, are temporally well separated. In other words, when the transit time of the THz pulse is much larger than its duration, the THz signal drops to zero between two echoes. In this case it is possible to keep only the first directly transmitted THz pulse by temporally windowing out the echoes. In THz-TDS, the spectral resolution is the inverse of

the total scan time. However, since the measurement is performed in the time-domain, it is much more convenient to window out reflections in the raw data than to remove the reflections in the frequency-domain.

Even when there are no reflections the THz pulse is often windowed to smooth the data to prevent spectral leakage. The finite-length data is multiplied by a window whose amplitude varies smoothly and gradually goes to zero at the edges. This reduces the discontinuity at each period of the sampled data. In the case of THz pulses with a sampling period of $t_s = 40$ fs, the sampling rate is $f_s = 25$ THz, and the Nyquist frequency is $f_s/2 = 12.5$ THz. The duration of a THz pulse is typically only a few ps, and a scan is typically 10 ps or longer, giving plenty of room to bring the edges to zero. In most cases it is sufficient to gently window the data with a weakened Hanning window, or to exponentially bring the edges to zero on the first and last $20-30$ data points.

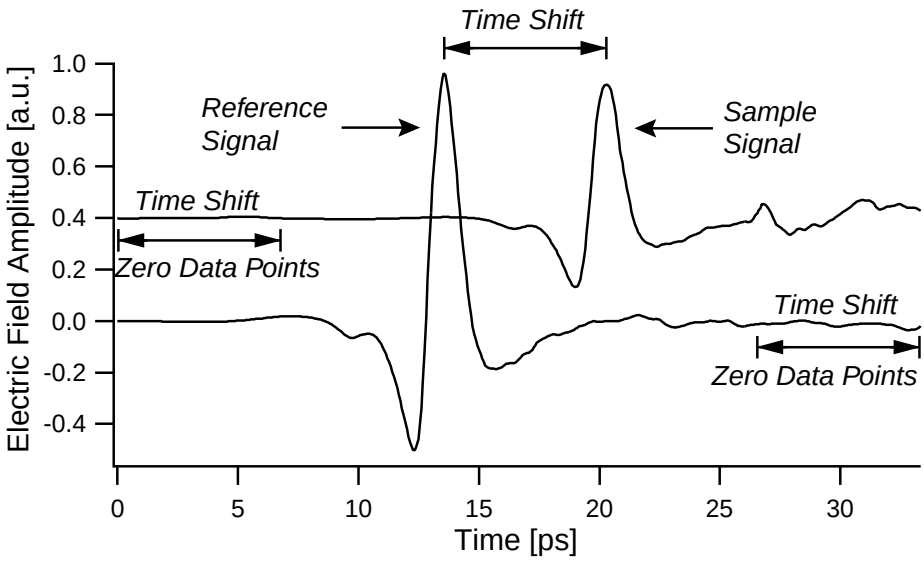

Figure 2.7: Measured THz waveforms of a 0.5 mm $LaAlO_3$ substrate as the sample scan and air as reference displaying the time delay between the two scans. The sample scan is displaced vertically with respect to the reference scan for clarity.

The sample signal and reference signal are typically shifted in time (see Figure 2.7), where the reference arrives before the signal. Intuitively, the time shift roughly determines the real index ($c/n = L/t$), and the decrease in amplitude determines the imaginary index of the sample. Here, t is the time shift, c the speed of light, L the distance the light travels, and n the real index of the sample. It is important that the window is centered at the center of the THz pulse for each of the sample and reference signal to avoid introducing artifacts. Furthermore, data points at the beginning of the sample signal should be zeroed corresponding to the time shift between the sample and reference signal, and data points at the end of the reference signal should be zeroed equivalently. This ensures that the same bumps and other characteristics of the scan are present in both sample and reference. In the case of a noticeable phase change in the THz pulse (i.e. high-T_c superconductors below T_c) the time shift is not as well defined and requires special considerations.

Zero padding is used to increase the frequency resolution of the Fourier transformed input signal ($\Delta f = f_s/N$) by artificially increasing the number of samples or data points, N. The input sequence size is made equal to a power of two by adding zeros to the end of the sequence. This simplifies the fast Fourier transform (FFT) algorithm as well.

In summarizing, the window process involves the following steps. Firstly, any offset is subtracted from the THz pulse in each of the sample and reference which brings the beginning and the end of each scan close to zero. Data points at the beginning of the sample and at the end of the reference scans are then zeroed according to the time shift. Finally, the sample and reference scans are windowed, and zero padded before performing an FFT.

2.2.2 Complex Transmission Coefficients

The theoretical complex transmission coefficient of the sample as a function of frequency is obtained by dividing the complex transmission coefficient of the sample by the complex transmission coefficient of the reference, $T(\omega) = E_{\text{sig}}(\omega)/E_{\text{ref}}(\omega)$, where $E_{\text{sig}}(\omega)$ and $E_{\text{ref}}(\omega)$ are the FFT of the time-domain pulses.

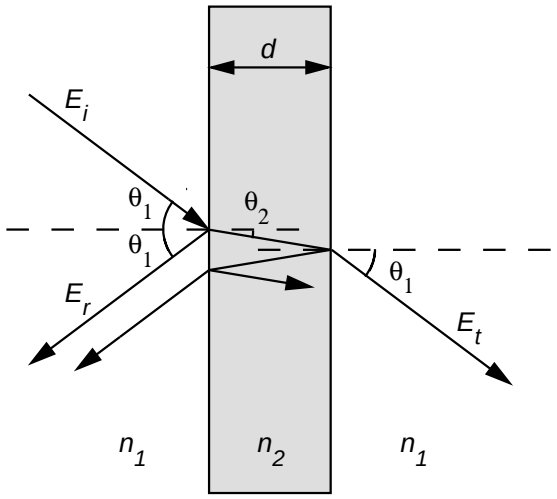

Figure 2.8: Propagation of a plane wave in a slab of material of thickness d illustrating the incident, reflected, and transmitted waves at the interfaces.

Figure 2.8 illustrates the incident, reflected, and transmitted fields of the THz radiation at the interfaces of a medium of thickness d. The Fresnel equations for the transmission coefficients in s-, and p-polarizations are

$$T_{12}^{s} = \frac{2\tilde{n}_1 \cos\theta_1}{\tilde{n}_1 \cos\theta_1 + \tilde{n}_2 \cos\theta_2}, \tag{2.9}$$

$$T_{12}^{p} = \frac{2\tilde{n}_1 \cos\theta_1}{\tilde{n}_2 \cos\theta_1 + \tilde{n}_1 \cos\theta_2}, \tag{2.10}$$

and the Fresnel equations for the reflection coefficients in s-, and p-polarizations are

$$R_{12}^{s} = \frac{\tilde{n}_1 \cos\theta_1 - \tilde{n}_2 \cos\theta_2}{\tilde{n}_1 \cos\theta_1 + \tilde{n}_2 \cos\theta_2}, \tag{2.11}$$

$$R_{12}^{p} = \frac{\tilde{n}_2 \cos\theta_1 - \tilde{n}_1 \cos\theta_2}{\tilde{n}_2 \cos\theta_1 + \tilde{n}_1 \cos\theta_2}. \tag{2.12}$$

Here, θ_1 and θ_2 are the angles of incidence in medium 1 and 2, respectively. $\tilde{n}_1$ and $\tilde{n}_2$ are the frequency-dependent complex refractive index, $\tilde{n} = n + i\kappa = \sqrt{\epsilon}$ in medium 1 and 2, respectively. n is the refractive index and κ is the extinction coefficient. The propagation coefficient (or phase shift) in medium 2 over a distance d is given by

$$P_2 = exp\left[i\frac{\omega d}{c}\tilde{n}_2 \cos\theta_2\right], \tag{2.13}$$

where ω is the angular frequency and c is the speed of light. In the case of an optically thin medium with multiple reflections of the THz pulses superimposed the propagation coefficient P_2 is multiplied by a Fabry-Perot term [32] F,

$$FP_2 = \frac{exp\left[i\frac{\omega d}{c}\tilde{n}_2 \cos\theta_2\right]}{1 + R_{12}R_{21} \cdot exp\left[2i\frac{\omega d}{c}\tilde{n}_2 \cos\theta_2\right]}. \tag{2.14}$$

This expression is good for both s-, and p-polarizations.

2.2.2.1 Thin Crystal

For a thin crystal (see Figure 2.8) $E_{\text{sig}}(\omega)$ is given by

$$E_{\text{sig}}(\omega) = T_{12}FP_2T_{21} = \frac{T_{12}T_{21} \cdot exp\left[i\frac{\omega d}{c}\tilde{n}_2 \cos\theta_2\right]}{1 + R_{12}R_{21} \cdot exp\left[2i\frac{\omega d}{c}\tilde{n}_2 \cos\theta_2\right]}. \tag{2.15}$$

For air as reference ($n_1 = 1$) $E_{\text{ref}}(\omega)$ is given by

$$E_{\text{ref}}(\omega) = P_1 = exp\left[i\frac{\omega d}{c}n_1 \cos\theta_1\right]. \tag{2.16}$$

Isotropic Thin Crystal

The complex transmission coefficient of a thin isotropic crystal as a function of frequency is given by

$$T(\omega) = \frac{E_{\text{sig}}(\omega)}{E_{\text{ref}}(\omega)} = \frac{T_{12}T_{21} \cdot exp\left[i\frac{\omega d}{c}\left[\tilde{n}_2\sqrt{1-\frac{n_1^2}{\tilde{n}_2^2}\sin^2\theta_1} - n_1\cos\theta_1\right]\right]}{1 + R_{12}R_{21} \cdot exp\left[2i\frac{\omega d}{c}\tilde{n}_2\sqrt{1-\frac{n_1^2}{\tilde{n}_2^2}\sin^2\theta_1}\right]}, \quad (2.17)$$

where for p-polarization

$$T_{12}^p = T_{21}^p = \frac{2n_1\cos\theta_1}{\tilde{n}_2\cos\theta_1 + \sqrt{1-\frac{n_1^2}{\tilde{n}_2^2}\sin^2\theta_1}}, \quad (2.18)$$

and

$$R_{12}^p = -R_{21}^p = \frac{\tilde{n}_2\cos\theta_1 - \sqrt{1-\frac{n_1^2}{\tilde{n}_2^2}\sin^2\theta_1}}{\tilde{n}_2\cos\theta_1 + \sqrt{1-\frac{n_1^2}{\tilde{n}_2^2}\sin^2\theta_1}}. \quad (2.19)$$

At normal incidence $T(\omega)$ simplifies to

$$T(\omega) = \frac{\frac{4}{(\tilde{n}_2+n_1)^2} \cdot exp\left[i\frac{\omega d}{c}(\tilde{n}_2 - n_1)\right]}{1 - \left(\frac{\tilde{n}_2-n_1}{\tilde{n}_2+n_1}\right)^2 \cdot exp\left[2i\frac{\omega d}{c}\tilde{n}_2\right]}. \quad (2.20)$$

Anisotropic Thin Crystal

The complex transmission coefficient of a thin anisotropic crystal (see Appendix (A.2.1)) for p-polarization as a function of frequency is given by

$$T(\omega) = \frac{E_{\text{sig}}(\omega)}{E_{\text{ref}}(\omega)} = \frac{T_{12}T_{21} \cdot exp\left[i\frac{\omega d}{c}\tilde{n}_{ab}\left[\sqrt{1-\frac{n_1^2}{\tilde{n}_c^2}\sin^2\theta_1} - n_1\cos\theta_1\right]\right]}{1 + R_{12}R_{21} \cdot exp\left[2i\frac{\omega d}{c}\tilde{n}_{ab}\sqrt{1-\frac{n_1^2}{\tilde{n}_c^2}\sin^2\theta_1}\right]}, \quad (2.21)$$

where T_{12}, T_{21}, R_{12}, and R_{21} are given in Appendix (A.2.1). For s-polarization $T(\omega)$ is given by Equation (2.18) with $\tilde{n}_2 = \tilde{n}_{ab}$, where $\tilde{n}_{ab}$ is the complex in-plane index. $\tilde{n}_c$ is the complex out-of-plane index. T_{12}^s, and T_{21}^s are given by Equation

(2.9), and R^s_{12}, and R^s_{21} are given by Equation (2.11). At normal incidence $T(\omega)$ simplifies to

$$T(\omega) = \frac{\frac{4}{(\tilde{n}_{ab}+n_1)^2} \cdot exp\left[i\frac{\omega d}{c}(\tilde{n}_{ab}-n_1)\right]}{1-\left(\frac{\tilde{n}_{ab}-n_1}{\tilde{n}_{ab}+n_1}\right)^2 \cdot exp\left[2i\frac{\omega d}{c}\tilde{n}_{ab}\right]}. \tag{2.22}$$

2.2.2.2 Thick Crystal

For a thick crystal (see Figure 2.8) $E_{\text{sig}}(\omega)$ is given by

$$E_{\text{sig}}(\omega) = T_{12}P_2T_{21} = T_{12}T_{21} \cdot exp\left[i\frac{\omega d}{c}\tilde{n}_2\cos\theta_2\right]. \tag{2.23}$$

For air as reference ($n_1 = 1$) $E_{\text{ref}}(\omega)$ is given by

$$E_{\text{ref}}(\omega) = P_1 = exp\left[i\frac{\omega d}{c}n_1\cos\theta_1\right]. \tag{2.24}$$

Isotropic Thick Crystal

The complex transmission coefficient of a thick isotropic crystal as a function of frequency is given by

$$T(\omega) = \frac{E_{\text{sig}}(\omega)}{E_{\text{ref}}(\omega)} = T_{12}T_{21} \cdot exp\left[i\frac{\omega d}{c}\left[\tilde{n}_2\sqrt{1-\frac{n_1^2}{\tilde{n}_2^2}\sin^2\theta_1} - n_1\cos\theta_1\right]\right]. \tag{2.25}$$

At normal incidence $T(\omega)$ simplifies to

$$T(\omega) = \frac{4}{(\tilde{n}_2+1)^2} \cdot exp\left[i\frac{\omega d}{c}(\tilde{n}_2-1)\right]. \tag{2.26}$$

Anisotropic Thick Crystal

The complex transmission coefficient of a thick anisotropic crystal (see Appendix (A.2.1)) for p-polarization as a function of frequency is given by

$$T(\omega) = \frac{E_{\text{sig}}(\omega)}{E_{\text{ref}}(\omega)} = T_{12}T_{21} \cdot exp\left[i\frac{\omega d}{c}\left[\tilde{n}_{ab}\sqrt{1-\frac{n_1^2}{\tilde{n}_c^2}\sin^2\theta_1} - n_1\cos\theta_1\right]\right], \tag{2.27}$$

where T_{12}, and T_{21} are given in Appendix (A.2.1). For s-polarization $T(\omega)$ is given by Equation (2.25) with $\tilde{n}_2 = \tilde{n}_{ab}$. T^s_{12}, and T^s_{21} are given by Equation (2.9). At normal incidence $T(\omega)$ simplifies to

$$T(\omega) = \frac{4}{(\tilde{n}_{ab}+1)^2} \cdot exp\left[i\frac{\omega d}{c}(\tilde{n}_{ab}-1)\right]. \tag{2.28}$$

2.2.2.3 Thin Film on Thick Substrate

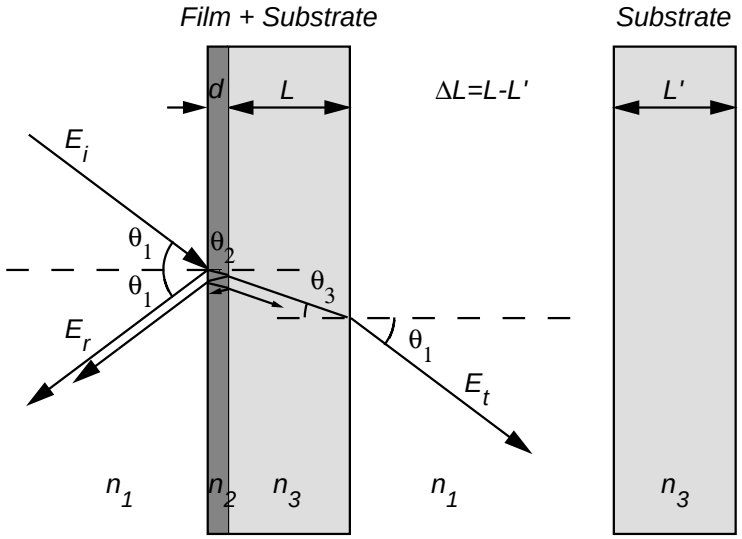

Figure 2.9: Propagation of a plane wave in a thin film on a thick substrate illustrating the incident, reflected, and transmitted waves at the interfaces.

For a thin film on a thick substrate (see Figure 2.9) $E_{\rm sig}(\omega)$ is given by

$$\begin{aligned} E_{\rm sig}(\omega) &= T_{12}FP_2T_{23}P_3T_{31} \\ &= \frac{T_{12}T_{23}\cdot exp\left[i\frac{\omega d}{c}\tilde{n}_2\cos\theta_2\right]}{1+R_{12}R_{23}\cdot exp\left[2i\frac{\omega d}{c}\tilde{n}_2\cos\theta_2\right]} \cdot exp\left[i\frac{\omega L}{c}\tilde{n}_3\cos\theta_3\right] T_{31}. \end{aligned} \tag{2.29}$$

For a thick substrate as reference $E_{\rm ref}(\omega)$ is given by

$$\begin{aligned} E_{\rm ref}(\omega) &= P_1T_{13}P'_3T_{31}P_{\Delta L} \\ &= exp\left[i\frac{\omega d}{c}n_1\cos\theta_1\right] T_{13}\cdot exp\left[i\frac{\omega L'}{c}\tilde{n}_3\cos\theta_1\right] T_{13} \\ &\quad exp\left[i\frac{\omega \Delta L}{c}n_1\cos\theta_1\right]. \end{aligned} \tag{2.30}$$

ΔL accounts for the difference in the thickness of the sample substrate and the reference substrate ($\Delta L = L - L'$).

Isotropic Thin Film on Thick Substrate

The complex transmission coefficient of an isotropic thin film on a thick substrate as a function of frequency is given by

$$T(\omega) = \frac{E_{\text{sig}}(\omega)}{E_{\text{ref}}(\omega)} = \frac{\frac{T_{12}T_{23}}{T_{13}} \cdot exp\left[i\frac{\omega d}{c}\left[\tilde{n}_2\sqrt{1-\frac{n_1^2}{\tilde{n}_2^2}\sin^2\theta_1} - n_1\cos\theta_1\right]\right]}{1 + R_{12}R_{23} \cdot exp\left[2i\frac{\omega d}{c}\tilde{n}_2\sqrt{1-\frac{n_1^2}{\tilde{n}_2^2}\sin^2\theta_1}\right]} exp\left[i\frac{\omega\Delta L}{c}\left[\tilde{n}_3\sqrt{1-\frac{n_1^2}{\tilde{n}_3^2}\sin^2\theta_1} - n_1\cos\theta_1\right]\right]. \quad (2.31)$$

At normal incidence $T(\omega)$ simplifies to

$$T(\omega) = \frac{\frac{2(\tilde{n}_3+1)}{(\tilde{n}_2+1)(\tilde{n}_3+\tilde{n}_2)} \cdot exp\left[i\frac{\omega d}{c}(\tilde{n}_2-1)\right]}{1 + \frac{(\tilde{n}_2-1)(\tilde{n}_3-\tilde{n}_2)}{(\tilde{n}_2+1)(\tilde{n}_3+\tilde{n}_2)} \cdot exp\left[2i\frac{\omega d}{c}\tilde{n}_2\right]} \cdot exp\left[i\frac{\omega\Delta L}{c}(\tilde{n}_3-1)\right]. \quad (2.32)$$

Assuming $\frac{\omega}{c}d\tilde{n}_2 \ll 1$ and $\tilde{n}_2 \gg \tilde{n}_3 > 1$ Equation (2.31) reduces to the simple form (see Appendix (A.1))

$$T(\omega) = \frac{1+\tilde{n}_3}{1+\tilde{n}_3+Z_o\tilde{\sigma}(\omega)d} \cdot exp\left[i\frac{\omega\Delta L}{c}(\tilde{n}_3-1)\right], \quad (2.33)$$

where Z_o represents the impedance of free space. Equation (2.33) can be solved analytically for the complex conductivity $\tilde{\sigma}(\omega)$ given the measured complex transmission coefficient $T(\omega)$.

Anisotropic Thin Film on Thick Substrate

The complex transmission coefficient of an anisotropic thin film on a thick substrate (see Appendix (A.2.1)) for p-polarization as a function of frequency is given

by

$$T(\omega) = \frac{E_{\rm sig}(\omega)}{E_{\rm ref}(\omega)} = \frac{\frac{T_{12}T_{23}}{T_{13}} \cdot exp\left[i\frac{\omega d}{c}\left[\tilde{n}_{ab}\sqrt{1-\frac{n_1^2}{\tilde{n}_c^2}\sin^2\theta_1} - n_1\cos\theta_1\right]\right]}{1 + R_{12}R_{23} \cdot exp\left[2i\frac{\omega d}{c}\tilde{n}_{ab}\sqrt{1-\frac{n_1^2}{\tilde{n}_c^2}\sin^2\theta_1}\right]}$$
$$exp\left[i\frac{\omega\Delta L}{c}\left[\tilde{n}_3\sqrt{1-\frac{n_1^2}{\tilde{n}_3^2}\sin^2\theta_1} - n_1\cos\theta_1\right]\right]. \quad (2.34)$$

Here T_{13} is given by Equation (2.10). T_{12}, T_{23}, R_{12}, and R_{23} are given in Appendix (A.2.1). For s-polarization $T(\omega)$ is given by Equation (2.31) with $\tilde{n}_2 = \tilde{n}_{ab} = \tilde{n}_c$. T_{12}^s, T_{23}^s and T_{13}^s are given by Equation (2.9), and R_{12}^s, and R_{23}^s are given by Equation (2.11). At normal incidence $T(\omega)$ simplifies to Equation (2.32) with $\tilde{n}_2 = \tilde{n}_{ab}$. Assuming $\frac{\omega}{c}d\tilde{n}_2 \ll 1$ and $\tilde{n}_2 \gg \tilde{n}_3 > 1$ Equation (2.32) reduces to the simple form given in Equation (2.33) with $\tilde{n}_2 = \tilde{n}_{ab}$.

2.2.3 Extraction of Material Parameters

The measured transmission coefficient of the sample as a function of frequency contains information of both the amplitude and phase of the THz field. Thus, this allows the extraction of both the real and imaginary part of the dielectric function by performing a complex fit to the theoretical transmission coefficient, without having to resort to the Kramers-Kronig relations. Given the complex dielectric function $\tilde{\epsilon} = \epsilon_1 + i\epsilon_2$, the complex refractive index $\tilde{n} = n + i\kappa$, or the complex conductivity $\tilde{\sigma} = \sigma_1 + i\sigma_2$, or the absorption coefficient α are easily calculated. For a plane monochromatic wave $\mathbf{E}=\mathbf{E_0}e^{i(\mathbf{k}\cdot\mathbf{r}-\omega t)}$ traveling in an anisotropic medium Maxwell's equations [47] yield the following relation between the dielectric function and the conductivity tensor

$$\begin{aligned} \text{(CGS)} \qquad \tilde{\epsilon}_{ij}(\mathbf{k},\omega) &= \delta_{ij} + \frac{4\pi i}{\omega}\tilde{\sigma}_{ij}(\mathbf{k},\omega) \\ \text{(SI)} \qquad \tilde{\epsilon}_{ij}(\mathbf{k},\omega) &= \delta_{ij} + \frac{i}{\epsilon_o\omega}\tilde{\sigma}_{ij}(\mathbf{k},\omega), \end{aligned} \quad (2.35)$$

where

$$\hat{\epsilon} = \begin{pmatrix} \epsilon_\perp & 0 & 0 \\ 0 & \epsilon_\perp & 0 \\ 0 & 0 & \epsilon_\parallel \end{pmatrix}$$

for a uniaxial anisotropic crystal (see Appendix (A.2)). In the case of a transverse wave traveling in a homogeneous isotropic medium **E** is perpendicular to **k** and ϵ is a scalar. Thus,

$$k = \frac{\omega}{c}\tilde{n}; \qquad \tilde{n}(\mathbf{k},\omega) = \sqrt{\epsilon(\mathbf{k},\omega)}. \tag{2.36}$$

The real part and the imaginary part of ϵ are related to the refractive index n, and the extinction coefficient κ by

$$\epsilon_1 = n^2 - \kappa^2, \tag{2.37}$$

$$\epsilon_2 = 2n\kappa. \tag{2.38}$$

The absorption coefficient α is defined by

$$\alpha = \frac{2\omega\kappa}{c} = \frac{\omega\epsilon_2}{nc}, \tag{2.39}$$

and the real part and the imaginary part of the conductivity σ are given by

$$\text{(CGS)} \qquad \sigma_1 = \frac{n\kappa\omega}{2\pi} = \frac{\epsilon_2\omega}{4\pi}$$

$$\text{(SI)} \qquad \sigma_1 = 2n\kappa\epsilon_o\omega = \epsilon_o\epsilon_2\omega, \tag{2.40}$$

$$\text{(CGS)} \qquad \sigma_2 = \frac{\omega(1-n^2+k^2)}{4\pi} = \frac{(1-\epsilon_1)\omega}{4\pi}$$

$$\text{(SI)} \qquad \sigma_2 = \epsilon_o\omega(1-n^2+k^2) = \epsilon_o(1-\epsilon_1)\omega. \tag{2.41}$$

Figure 2.10 shows the measured THz waveforms in the time-domain of an optimally doped 50 nm YBCO thin film on a 0.5 mm MgO substrate and a 0.5 mm MgO substrate reference at normal incidence, and at $T = 50$ K. The corresponding Fourier transforms are shown in Figure 2.11. The measured complex

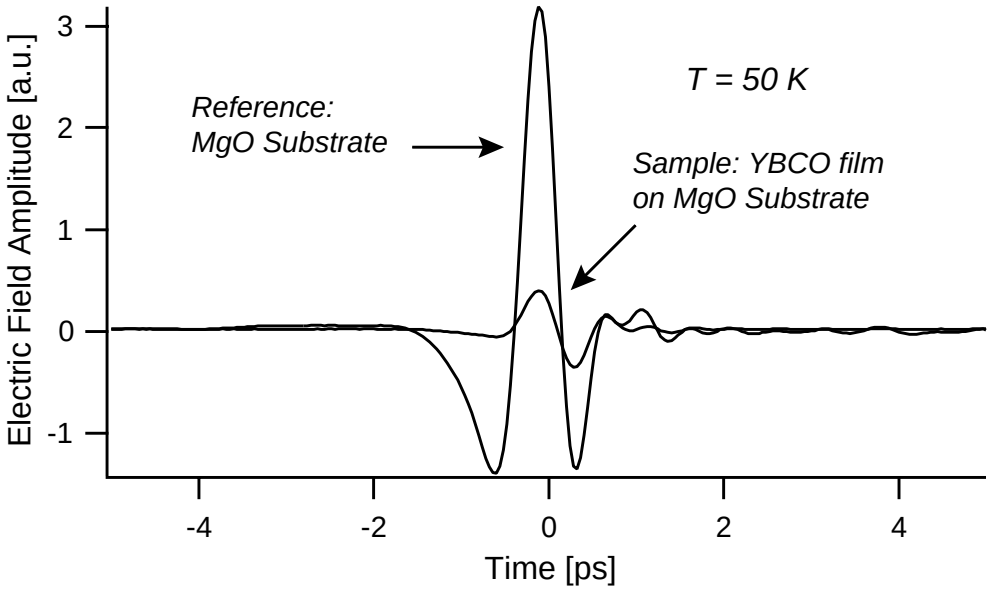

Figure 2.10: Measured THz waveforms of an optimally doped 50 nm YBCO thin film on a 0.5 mm MgO substrate and a 0.5 mm MgO substrate reference at normal incidence.

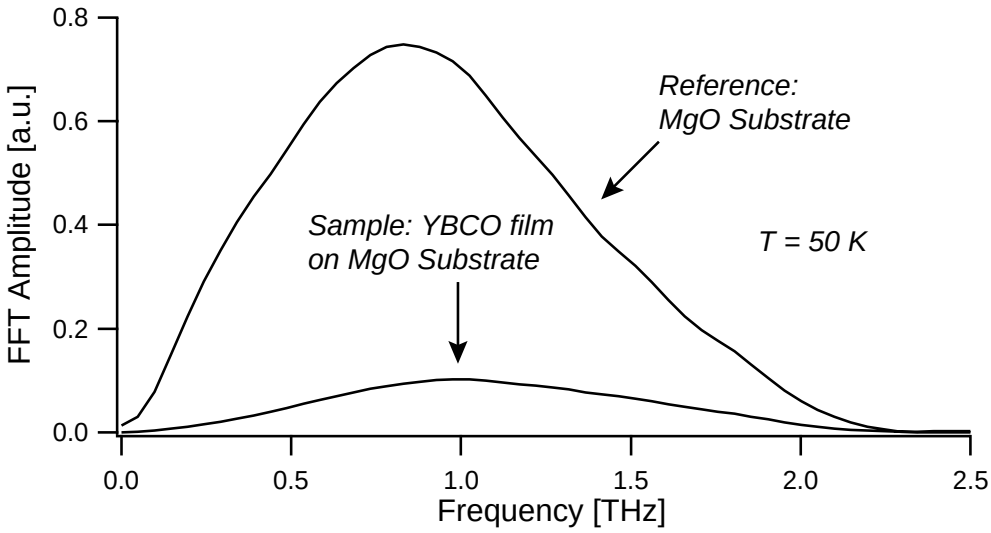

Figure 2.11: FFT amplitude of the measured THz waveforms shown in Figure 2.10.

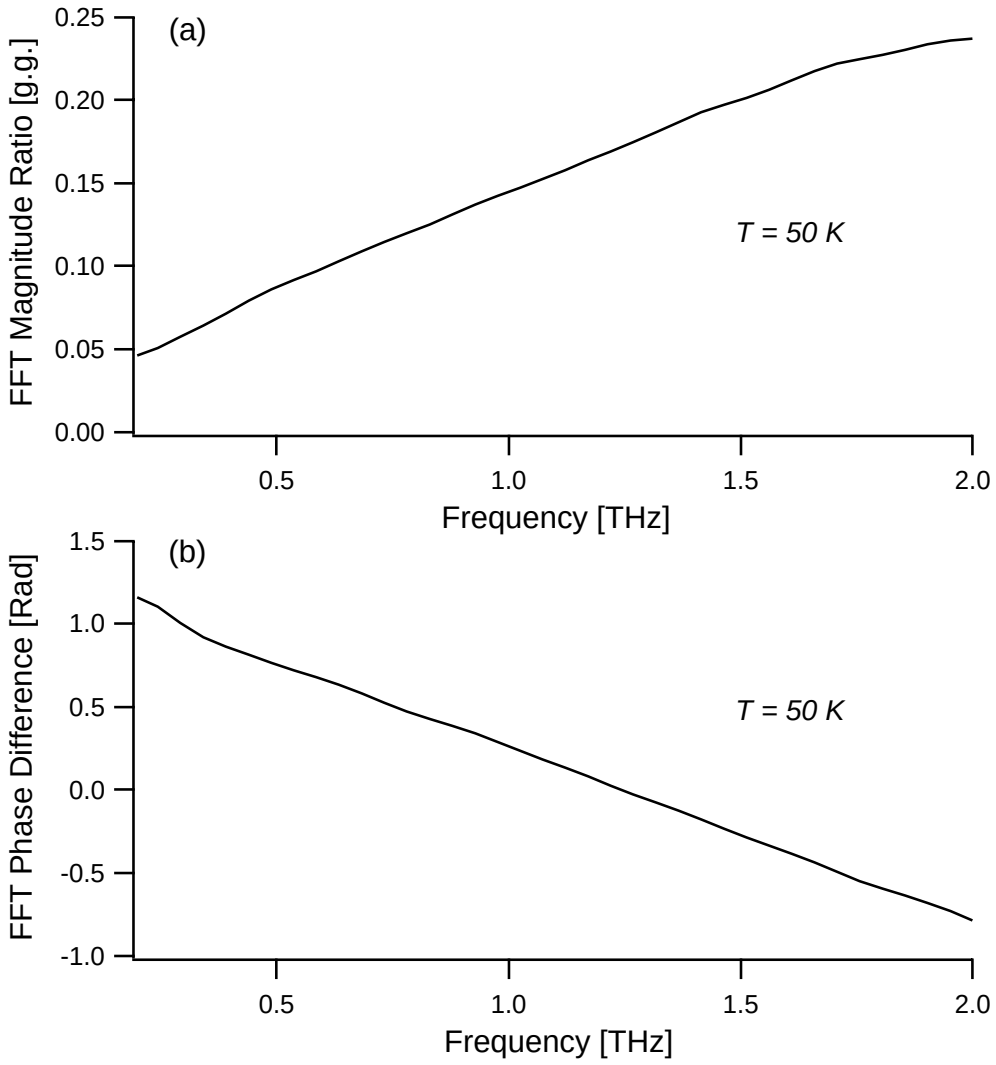

Figure 2.12: Complex transmission coefficient of the YBCO film obtained from the measured THz waveforms shown in Figure 2.10. (a) FFT magnitude ratio. (b) FFT phase difference.

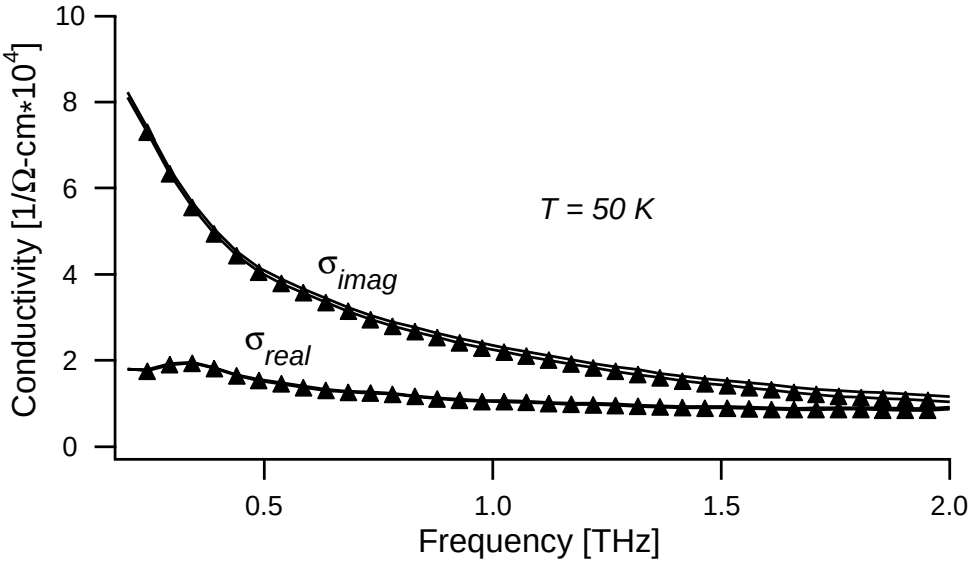

Figure 2.13: Complex conductivity of the YBCO film obtained from the measured THz waveforms shown in Figure 2.10 by a complex fit to Equation (2.32) (solid lines), and to the simplified Equation (2.33) (triangles) for comparison.

transmission coefficient of the sample as a function of frequency is shown in Figure 2.12. Finally, Figure 2.13 shows the real part and the imaginary part of the conductivity, obtained from a complex fit of the measured transmission coefficient to the theoretical transmission coefficient $T(\omega)$ given by Equation (2.32). For comparison, a fit to the simplified Equation (2.33) also shown in Figure 2.13 produces the same real and imaginary conductivities.

2.3 Time-Resolved Optical-Pump Terahertz-Probe Spectroscopy

Time-resolved optical measurements are of extreme importance in condensed matter systems because they can resolve dynamical processes at the fundamental timescales at the electronic and nuclear motion. In typical time-resolved pump-probe measurements, a short laser pulse is split into an intense pump pulse and

a much weaker probe pulse. The pump pulse induces a change in the sample and the probe pulse measures the induced change in the sample. By varying the delay between the pump pulse and the probe pulse one can follow the temporal development of the induced change in the sample. This development, which is typically measured in either transmission, $\Delta T/T$, or reflection, $\Delta R/R$, contains information of the relaxation dynamics in the sample. These measurements have found applications in various disciplines, such as chemistry where chemical reaction dynamics are studied by pump induced changes in absorbance. In semiconductors, measurements of the dynamics of hot-electron relaxation give important information of the physics of nonequilibrium phenomena in these materials, and information about the carrier-phonon and carrier-carrier interactions, which are of fundamental interest in semiconductor physics [48]. In the study of thin metal films, and more recently in metallic nanoparticles [49], time-resolved techniques are a powerful tool to monitor the electron-thermalization dynamics [50, 51]. As a final example, all optical pump-probe experiments have provided some insight into the ground state and nonequilibrium properties of high-T_c superconductors [52−56]. These time-domain experiments have the ability to temporally distinguish dynamics related to superconductivity, which can be difficult to resolve in the frequency-domain, given the multiplicity of similar energy scales in high-T_c superconductors.

The transiently induced change in transmission $\Delta T/T$ (or in reflection $\Delta R/R$) for small perturbations is related to the induced changes in the dielectric function $\tilde{\epsilon} = \epsilon_1 + i\epsilon_2$ of the sample by

$$\Delta T/T = \frac{\partial lnT}{\partial \epsilon_1}\Delta\epsilon_1 + \frac{\partial lnT}{\partial \epsilon_2}\Delta\epsilon_2 \tag{2.42}$$

which embodies the electronic properties of the material. Here $\Delta\epsilon_1$ ($\Delta\epsilon_2$) is the induced change in the real (imaginary) part of $\tilde{\epsilon}$.

The physics of ultrafast electron dynamics in metallic systems is most easily captured by considering a simple picture of the excitation and equilibration processes involved as depicted in Figure 2.14. The large difference between the electronic and lattice specific heat ($C_e \ll C_l$) allows for the preferential excitation of the electron gas by absorption of a femtosecond laser pulse, resulting in a nonequilibrium condition, $T_e > T_l$, where T_e is the temperature of the electron distribution and T_l is the lattice temperature. The initial rise in $\Delta T/T$ (see Figure 2.15) is associated with the equilibration of nonequilibrium electrons relaxing to a hot Fermi distribution through electron-electron interactions following optical excitation. In the second time regime, after electron thermalization, $\Delta T/T$ decays due to electron-phonon processes as the electron gas loses its energy and thermalizes with the lattice. After a few picoseconds, a local equilibrium will be reached at a slightly higher temperature than the initial temperature, $T_e = T_l > T_o$. The final step in the relaxation process involves thermal diffusion of phonons into the substrate and in the transverse direction on a 100 ps time scale as the electrons and phonons return to the original temperature T_o.

The temporal evolution of the electron and lattice temperatures can be described by a set of coupled differential equations. This two-temperature model treats the electrons and phonons as coupled subsystems with well defined temperatures at all times, where the electrons are described by a Fermi-Dirac distribution, and the phonons by a Bose-Einstein distribution. The model describes the energy flow between the coupled subsystems, but neglects the changes in occupation numbers. However, since this model assumes that all the optical energy is absorbed by the electrons which thermalize instantaneously to a hot Fermi distribution, but actually occurs over some few 100 fs, the two-temperature model must be modified to include the nonthermal electrons as a separate subsystem. Thus, the evolution of the electron-phonon coupled system is described by an

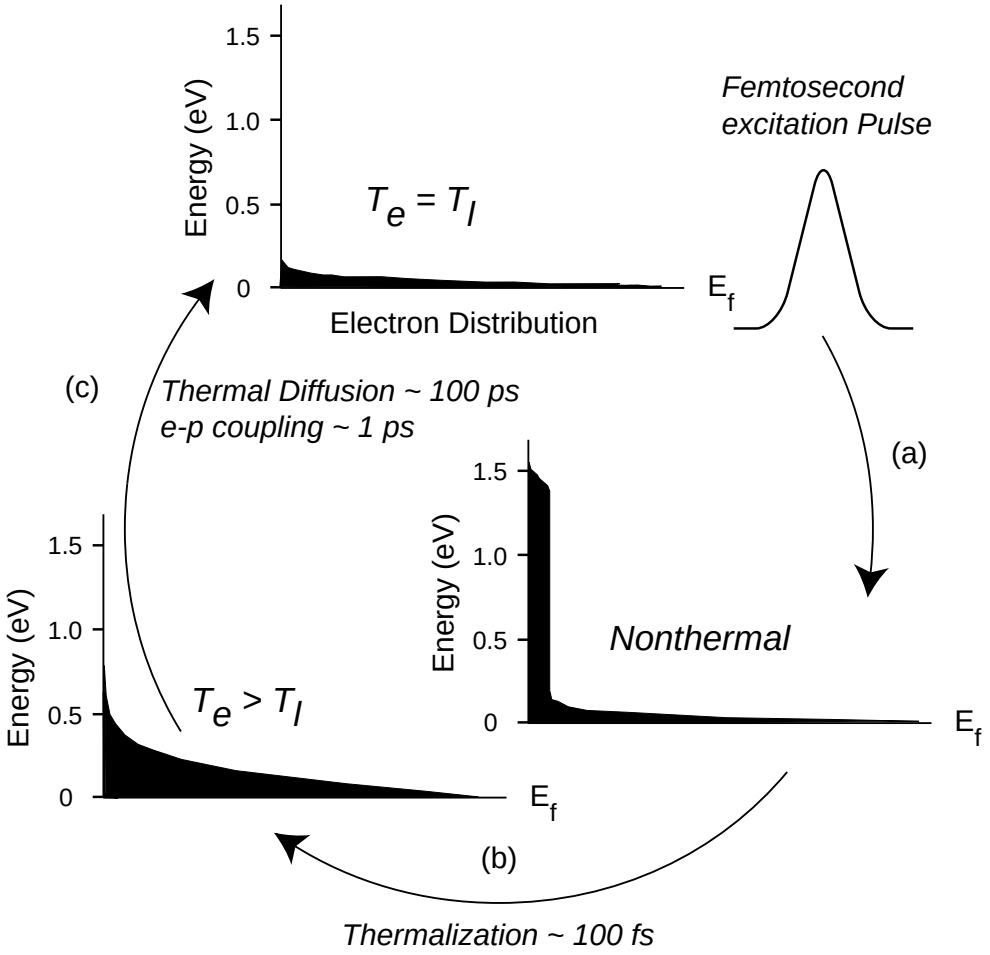

Figure 2.14: Ultrafast electron dynamics in metals. (a) A femtosecond pulse creates a nonthermal electron distribution. (b) The nonthermal electron distribution thermalizes to a hot Fermi distribution. (c) Electron-phonon coupling and heat diffusion cools the electrons and the lattice back to equilibrium.

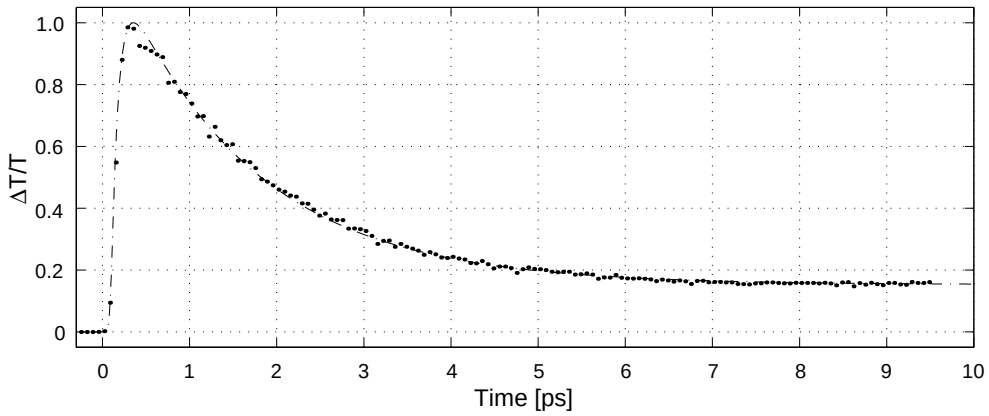

Figure 2.15: Illustration of the behavior of $\Delta T/T$ as a function of time in a metallic system.

effective two-temperature model given by

$$\frac{\partial N}{\partial t} = -\alpha N - \beta N, \tag{2.43}$$

$$C_e(T_e)\frac{\partial T_e}{\partial t} = -G(T_e - T_l) + \alpha N, \tag{2.44}$$

$$C_l(T_l)\frac{\partial T_l}{\partial t} = G(T_e - T_l) + \beta N, \tag{2.45}$$

where N is the energy density initially stored in the nonthermal electron distribution, α is the rate of energy transfer from the nonthermal population to the hot Fermi distribution, $\beta = G/C_e$ is the electron-phonon coupling rate, $C_e(T_e)$ and C_l are the electron and lattice specific heat, respectively, and G is the electron-phonon coupling constant. T_e and T_l are the electron and lattice temperatures, respectively. For small pertubative temperature changes ($\Delta T_e \ll T_o$) C_e and G can be considered as constants, and the temperature change in the Fermi part of the electron distribution as a function of time is found to be

$$\Delta T_e \propto \left[1 - exp\left(-\frac{t}{\tau_r}\right)\right] exp\left(-\frac{t}{\tau_d}\right), \tag{2.46}$$

where $\tau_r = 1/\alpha$ and $\tau_d = 1/\beta = C_e/G$. The induced change in transmission $\Delta T/T$ corresponds quantitatively to this functional form, where the temperature

of the electron distribution is described by an exponential rise time τ_r which is related to the relaxation of the nonthermalized distribution, followed by an exponential decay τ_d due to electron-phonon coupling.

Ultrafast optical pump-probe spectroscopy is an invaluable tool to investigate time-dependent or nonequilibrium phenomena in solid state materials that cannot be accessed by conventional techniques such as dc transport measurements. However, a potential drawback of all optical pump-probe experiments is that the probe energy, typically 1.5 eV or greater, is much larger than the relevant energy scales in many systems, such as the d-wave superconducting gap or pseudogap in high-T_c superconductors. Alternatively, combining THz-TDS with optical excitation one can measure the evolution of optically induced changes in the real and imaginary induced conductivity with a probe energy much closer to the relevant energy scales in the material. This technique also allows one to temporally discriminate processes such as electron-electron, electron-phonon and spin-lattice interactions by their different relaxation time scales. This can provide new insight into the low-lying excitations of complex systems such as the hole doped transition metal oxides, examples being high-T_c superconductors [57] or mixed valence manganites [58].

A time-resolved optical-pump THz-probe experiment is shown in Figure 2.16. An intense optical pump pulse, derived from the same laser beam that triggers the THz transmitter and detector, photoexcites the sample. Using a mechanical delay line, the optically induced changes in the transmitted electric field can be measured with subpicosecond resolution.

The complex transmission coefficient of the sample as a function of frequency and pump-probe delay time τ is given by

$$T(\omega,\tau) = \frac{FFT(E_{eq}(t) + \Delta E(t,\tau))}{FFT(E_{ref}(t))} = \frac{E_{sig}(\omega,\tau)}{E_{ref}(\omega)}. \tag{2.47}$$

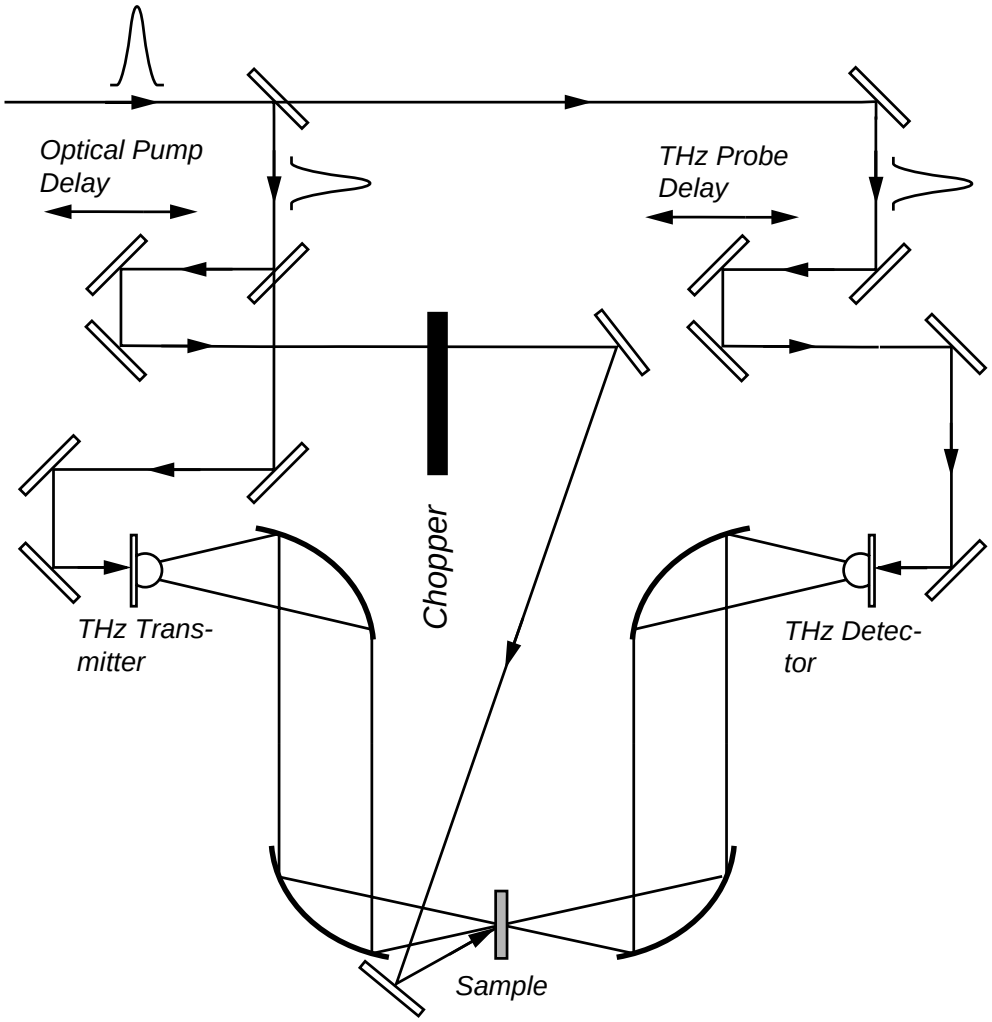

Figure 2.16: Typical optical set-up of an optical-pump THz-probe experiment. An optical pump pulse directly excites the sample, and the focused THz beam probes the far-infrared properties of the sample as a function of time after optical excitation.

Here $E_{eq}(t)$ is the equilibrium scan of the sample in the time-domain without optical excitation. $\Delta E(t,\tau)$ is the induced changes in the electric field, $\Delta E(t,\tau) = E_{ex}(t,\tau) - E_{eq}(t)$, where $E_{ex}(t,\tau)$ is the scan of the sample with optical excitation. The induced change in the electric field is related to the induced changes in the conductivity of the sample by

$$\Delta\sigma(\omega,\tau) = -\frac{\Delta T(\omega,\tau)}{T(\omega,\tau)}\frac{1}{T(\omega,\tau)}\frac{(1+n_3)e^{i\frac{\omega}{c}\Delta L(n_3-1)}}{Z_o d} \tag{2.48}$$

$$= -\frac{\Delta E(\omega,\tau)}{E_{sig}(\omega,\tau)}\frac{E_{ref}(\omega)}{E_{sig}(\omega,\tau)}\frac{(1+n_3)e^{i\frac{\omega}{c}\Delta L(n_3-1)}}{Z_o d} \tag{2.49}$$

for a thin film on a thick substrate using Equation (2.33) (see Appendix A.1.1).

Experimentally, $\Delta E(t,\tau=\tau_i)$ is obtained by scanning the THz probe delay line and mechanically chopping the optical pump delay line which is positioned at a specific pump-probe delay time $\tau = \tau_i$. This procedure measures the difference between $E_{ex}(t,\tau=\tau_i)$ and $E_{eq}(t)$ at the rate of the chopper frequency immediately yielding $\Delta E(t_r,\tau=\tau_i)$ at each THz probe delay time t_r. Alternatively, by chopping and scanning the THz probe delay line one would collect the data for first $E_{ex}(t,\tau=\tau_i)$ (i.e. pump on) and then $E_{eq}(t)$ (i.e. pump off) in separate scans. The former procedure allows for increased signal sensitivity as it is more robust to system drift, particularly when the difference between $E_{ex}(t,\tau=\tau_i)$ and $E_{eq}(t)$ is small. After obtaining $\Delta E(t,\tau=\tau_i)$, $E_{eq}(t)$ and $E_{ref}(t)$ are measured by chopping and scanning the THz probe delay line. The real and imaginary conductivity are then obtained from Equation (2.47), and the induced conductivity from Equation (2.49). $\Delta E(t,\tau=\tau_i)$ must be measured at each pump-probe delay time as the optical excitation can induce changes in both the phase and amplitude of the THz electric field. This is particularly true for high-T_c superconductors where the imaginary conductivity changes dramatically (see Chapter 5.1). However, for samples in which the optical excitation causes changes primarily in the THz electric field amplitude (i.e. $\Delta\sigma_{imag} \ll 1$) an alter-

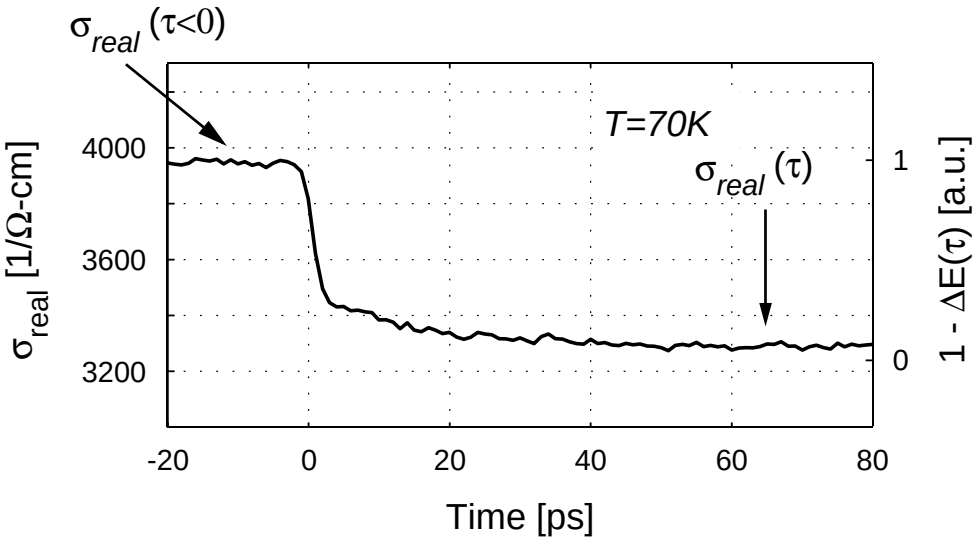

Figure 2.17: Illustration of the conductivity dynamics in a metallic system where $\sigma_{imag} \ll 1$. σ_{real} is obtained by scaling $1 - \Delta E(t = t_{peak}, \tau)$ to $\sigma_{real}(\tau < 0)$ and $\sigma_{real}(\tau)$.

native method can be employed. $\Delta E(t = t_{peak}, \tau)$ as a function of τ is obtained in a single scan by chopping and scanning the optical pump delay line while the THz probe delay line is positioned at the peak THz electric field. $1 - \Delta E(t = t_{peak}, \tau)$ can then be scaled to the absolute conductivity by measuring σ before the arrival of the excitation pulse ($\tau < 0$), and at a later pump-probe delay time in a stable regime but before complete recovery has occured (see Figure 2.17). This method, if applicable, provides considerable time savings in measuring the conductivity dynamics. One example where this method is justifiable is in the studies of colossal magneto resistance thin films (see Chapter 5.2.2). It must be kept in mind that this method is an approximation that can be employed only when the induced change in σ_{imag} is small or the phase of the THz pulse does not change with optical excitation (i.e. $\sigma_{imag} \ll 1$). In other words, it is useful for measuring σ_{real} under special circumstances.

CHAPTER 3

Introduction to Vortex Physics in High-T_c Superconductors

An applied magnetic field induces a vortex lattice in a high-T_c superconductor in the mixed-state which responds to changes in temperature and magnetic fields, and to applied currents. A sufficiently strong magnetic field or will cause the superconductor to return to the normal state. Vortex dynamics are of great importance because it determines both the transport and magnetic properties of high-T_c superconductors.

3.1 Properties of the Superconducting State

The phenomenon of superconductivity occurs below a critical temperature T_c exhibiting zero dc electrical resistivity, and diamagnetic response to an applied magnetic field. The microscopic mechanism responsible for superconductivity is qualitatively explained by the Bardeen, Cooper, and Schrieffer (BCS) theory [59]. Electrons near the Fermi surface condense into a superconducting ground state formed of Cooper pairs. A Cooper pair consists of two electrons with equal and opposite momentum and opposite spin. The two electrons are coupled via a phonon mediated attraction. An energy gap in the electronic spectrum opens up at the Fermi energy with a width $2\Delta(T)$, which is the energy required to

break a Cooper pair and create a pair of quasiparticle excitation above the gap. The energy gap is closed above T_c. Below T_c it opens up increasing in size with decreasing temperature leveling off at its maximum value $2\Delta(0)$. In the weak coupling limit of the BCS theory the transition temperature can be estimated from $2\Delta(0) \approx 3.5 K_B T_c$ [60].

The phenomenology of superconductivity is based on the Ginzburg-Landau theory [61] which provides a variational functional of the free energy describing the superconducting state. The two fields determining the physics of the system are the complex superconducting order parameter Ψ and the vector potential $\mathbf{A}$. The order parameter vanishes above T_c and its magnitude describes the degree of superconducting order at position $\mathbf{r}$ below T_c. The order parameter $\Psi(\mathbf{r})$ has the property that $\Psi^*(\mathbf{r})\Psi(\mathbf{r}) = n_s(\mathbf{r})$, the local concentration of superconducting electrons. The Ginzburg-Landau equations define two length scales. The first is a coherence length ξ that sets the scale for spatial variations of the order parameter Ψ. The second length is the London penetration depth λ_L that sets the length scale for variations in the magnetic induction inside the superconductor.

Low-T_c superconductors are well described by the BCS theory with a simple complex order parameter $\Psi(\mathbf{k}) = \phi_L(\mathbf{k})\chi_{spin}$ describing the quantum mechanical collective wave function of the Cooper pairs. The phonon-mediated short range interaction leads to a spherically symmetric pairing (Angular momentum $L = 0$) and the spin state must then be a singlet. Such a superconductor where the density of Cooper pairs is uniform in momentum space has s-wave symmetry (see Figure 3.1(a)), i.e. Ψ is direction independent and the superconducting gap $\Delta(\mathbf{k})$ is independent of $\mathbf{k}$.

Although the symmetry of the order parameter in high-T_c superconductors is still controversial, the majority of experimental evidence support d-wave sym-

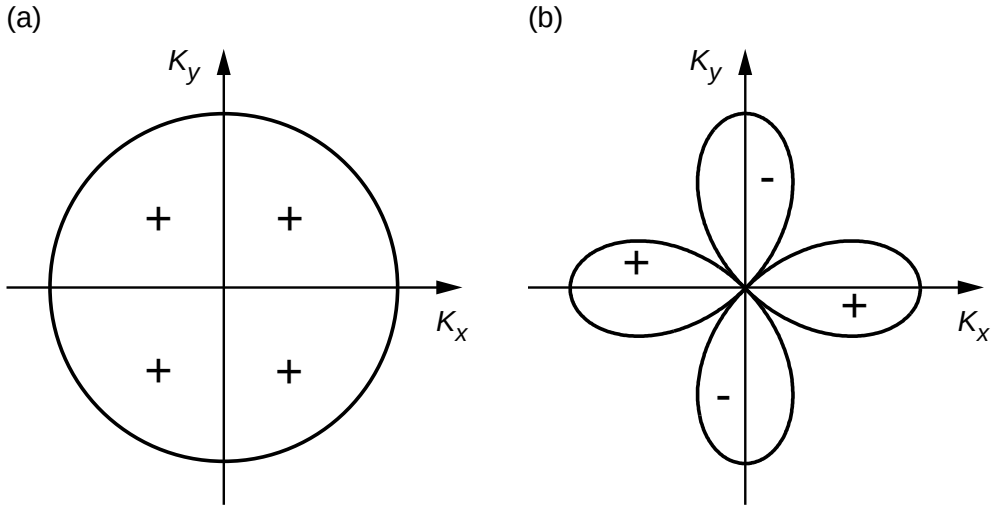

Figure 3.1: Schematic representation of the symmetry of the superconducting order parameter in k-space. In (a) is shown the situation for an isotropic s-wave order parameter which is direction independent. In (b) is depicted the situation for a d-wave order parameter which changes sign upon going through a node.

metry (see Figure 3.1(b)) [62, 63]. For a d-wave superconductor Ψ is direction dependent ($\Delta(\mathbf{k}) \propto (k_x^2 - k_y^2)) \propto \cos(2\theta)$) and the superconducting gap has four nodes in its spectrum. Monthoux et al. [64] proposed a strong-coupling theory using a phenomenological spin-fluctuation spectrum. This theory produces d-wave pairing, a relatively high transition temperature, and an anisotropic gap with nodes.

3.1.1 Magnetic Properties

The earliest studies of the magnetic properties of superconductors were performed on elemental metals (e.g. Hg, Pb, Al, Sn). These metals, now referred to as type I superconductors exhibit perfect diamagnetism regardless of whether they are cooled in a magnetic field or weather the field is applied after the sample is in the superconducting state. A type I superconducting material cooled below its transition temperature in an applied magnetic field below H_c will expel all

magnetic flux from its interior due to surface Meissner currents that set up a counter magnetic field exactly canceling the magnetic field in the interior. The applied magnetic field decreases exponentially within a surface layer λ_L (the London penetration depth). For the Meissner effect to occur $B = 0$. Thus the superconductor displays perfect diamagnetism $\chi = M/H = -1/4\pi$.

Now, as the applied magnetic field is increased beyond H_c magnetic flux will completely penetrate a type I superconductor, and it enters the normal state. By contrast, quantized flux lines will partially penetrate a type II superconductor at the lower critical field H_{c1}, and it enters a mixed superconducting state or vortex state. The surface energy between normal and superconducting metals is given by the ratio of the penetration depth and the coherence length $\kappa = \lambda_L/\xi$. For $\kappa < 1/\sqrt{2}$ the surface energy is positive corresponding to a type I superconductor. However, for $\kappa > 1/\sqrt{2}$ the surface energy is negative and it becomes favorable for magnetic flux to penetrate the superconductor in the form of quantized vortices.

The magnetization of a type I and a type II superconductor versus applied field is shown in Figure 3.2. The density of flux lines increases with increased applied field between H_{c1} and the upper critical field H_{c2} for a type II superconductor. Above H_{c2} the superconductivity is quenched. In the vortex state the flux arranges itself in a triangular array of flux tubes or vortex lines, each carrying a quantum of flux

$$\Phi_o = \frac{hc}{2e}. \tag{3.1}$$

To see that the magnetic flux in the superconductor is quantized integrate the superconducting current along a closed path within the superconductor. Using the superconducting current density from the Ginzburg-Landau theory

$$\mathbf{j} = \frac{e}{m}\left[\hbar\nabla\phi - \frac{2e}{c}\mathbf{A}\right]|\Psi|^2, \tag{3.2}$$

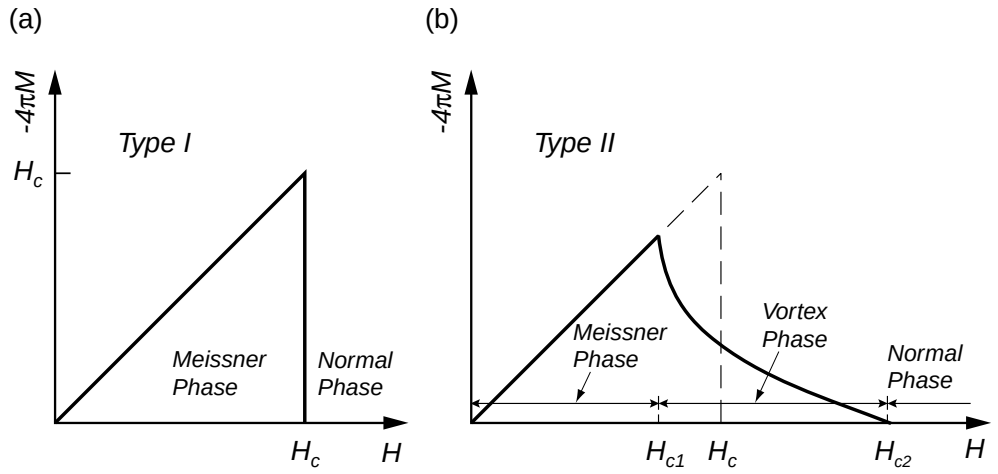

Figure 3.2: (a) Magnetization versus applied magnetic field for a type I superconductor exhibiting perfect diamagnetism in the Meissner phase where no field penetrates. Above the single critical field H_c a type I superconductor enters the normal state. (b) Magnetization versus applied magnetic field for a type II superconductor. A type II superconductor has a lower critical field H_{c1} and a higher critical field H_{c2} boundaring a vortex phase where flux penetrates the superconductor.

where $\Psi(\mathbf{r})$ is the complex order parameter, $\Psi = |\Psi|e^{i\phi}$, and $\mathbf{A}$ is the vector potential, yields

$$0 = \oint \mathbf{j} \cdot \mathbf{dl} = \oint \left(\hbar \nabla \phi - \frac{2e}{c} \mathbf{A} \right) \cdot \mathbf{dl}. \tag{3.3}$$

If we take the line integral around a circuit in the superconductor where the current density is zero this integral vanishes. Evaluating the first integral in Equation (3.3) yields the flux enclosed

$$\int \mathbf{A} \cdot \mathbf{dl} = \int \nabla \times \mathbf{A} \cdot \mathbf{dS} = \int \mathbf{B} \cdot \mathbf{dS} = \Phi. \tag{3.4}$$

In the second integral of Equation (3.3) the order parameter is single valued and the phase changes by 2π when going around the path

$$\oint \nabla \cdot \mathbf{dl} = \triangle \phi = 2\pi n. \tag{3.5}$$

Thus, the flux enclosed by the path must be quantized

$$\Phi = \frac{hc}{2e} n = \Phi_o n. \tag{3.6}$$

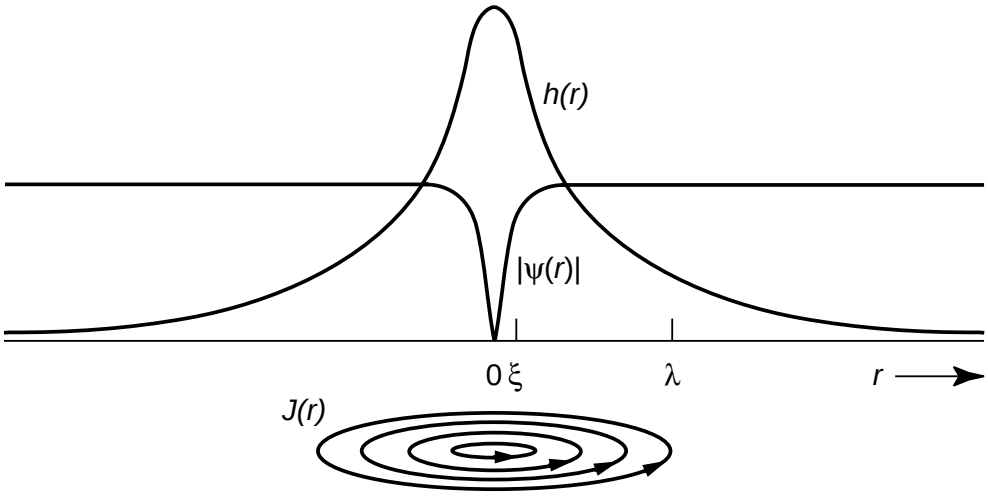

Figure 3.3: Schematic representation of the structure of an isolated Abrikosov vortex in a high-T_c superconductor. The magnetic field is concentrated in the center of the vortex. The order parameter goes to zero in the core region.

The structure of a vortex in the mixed-state is shown in Figure 3.3. Each vortex consists of a superconducting current, and it creates a magnetic field which is concentrated towards the center. The superconducting order parameter $\Psi(\mathbf{r})$, which describes the strength of superconductivity or the density of Cooper pairs, goes to zero at the center of the core of the vortex and then recovers with increasing radius over the length scale ξ (the coherence length). As an approximation, the core region of radius ξ is often taken to be in the normal state. The supercurrent circulates around the core and extends from ξ to λ. The free energy per unit length is found from the field energy and kinetic energy of the currents (neglecting the core) [60]

$$\epsilon = \frac{1}{8\pi}\int (h^2 + \lambda^2 |\nabla \times \mathbf{h}|^2) dS = \frac{\Phi_o}{8\pi} h(\xi) \approx \left(\frac{\Phi_o}{4\pi\lambda}\right)^2 ln\kappa = \frac{H_c^2}{8\pi} 4\pi\xi^2 ln\kappa. \quad (3.7)$$

The condensation energy lost in the core is only a factor $4ln\kappa$ smaller. When $H = H_{c1}$ one can calculate the lower critical field by considering the free energy per unit length of the first vortex line. The Gibbs free energy has the same value whether the first vortex is in or out of the sample ($G = F - \frac{H}{4\pi}\int h dr$)

$G_s|_{no\ flux} = G_s|_{first\ vortex}$

$$G = F = F + \epsilon L - \frac{H_{c1}\int hdr}{4\pi} = F + \epsilon L - \frac{H_{c1}\Phi_o L}{4\pi}. \tag{3.8}$$

The lower critical field is then given by

$$H_{c1} = \frac{4\pi\epsilon}{\Phi_o} \approx \frac{\Phi_o}{4\pi\lambda^2} ln\kappa. \tag{3.9}$$

The lower critical field H_{c1} is mainly determined by the London penetration depth. The upper critical field H_{c2} is determined by the coherence length of the superconductor

$$H_{c2} = \frac{\Phi_o}{2\pi\xi^2}. \tag{3.10}$$

At H_{c2} the vortices are spaced roughly ξ apart. $H_{c1}(T)$ and $H_{c2}(T)$ are shown in the simple magnetic phase diagram in Figure 3.4.

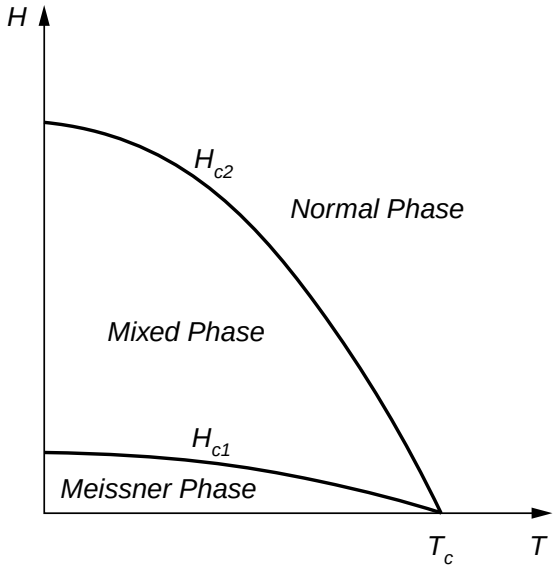

Figure 3.4: Schematic magnetic phase diagram of a high-T_c superconductor showing the temperature dependence of the lower and higher critical fields.

In the mixed-state the flux arranges itself into a hexagonal closed packed array or Abrikosov vortex lattice because of the repulsive forces between the vortices

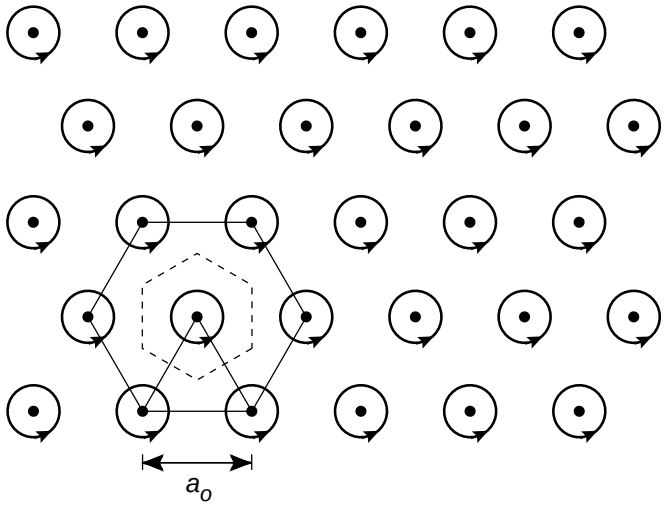

Figure 3.5: Schematic diagram of an Abrikosov vortex lattice.

(see Figure 3.5). The increase in total free energy per unit length when two vortices are brought together can be written

$$\Delta\epsilon = \frac{\Phi_o}{8\pi}\left[h_1(r1) + h_1(r_2) + h_2(r_1) + h_2(r_2)\right] = 2\left[\frac{\Phi_o}{8\pi}h_1(r_1)\right] + \frac{\Phi_o}{4\pi}h_1(r_2). \quad (3.11)$$

The first term is the sum of the individual line energies, and the second term is the interaction energy

$$\epsilon_{12} = \frac{\Phi_o h_1(r_2)}{4\pi} = \frac{\Phi_o^2}{8\pi^2\lambda^2}K_o\left(\frac{r_{12}}{\lambda}\right). \quad (3.12)$$

This falls off as $r_{12}^{-\frac{1}{2}}e^{-\frac{r_{12}}{\lambda}}$ at large distances and varies logarithmically at small distances. Thus, the interaction is repulsive when the vortices have the same sense. The force on vortex line 2 in the x direction is then given by

$$f_{2x} = -\frac{\partial\epsilon_{12}}{\partial x_2} = -\frac{\Phi_o}{4\pi}\frac{\partial h_1(r_2)}{\partial x_2} = \frac{\Phi_o}{c}J_{1y}(r_2), \quad (3.13)$$

using Ampère's law $\nabla \times \mathbf{h} = 4\pi\mathbf{J}/c$. In vector form

$$\mathbf{f}_2 = \mathbf{J}_1(\mathbf{r}_2) \times \frac{\mathbf{\Phi}_o}{c}. \quad (3.14)$$

Generalizing to an arbitrary array of vortices

$$\mathbf{f} = \mathbf{J}_s \times \frac{\mathbf{\Phi}_o}{c}, \tag{3.15}$$

where now $\mathbf{J}_s$ is the total supercurrent density due to all other vortices including any transport current at the location of the vortex in question.

3.2 Flux Flow, Flux Creep, and Pinning

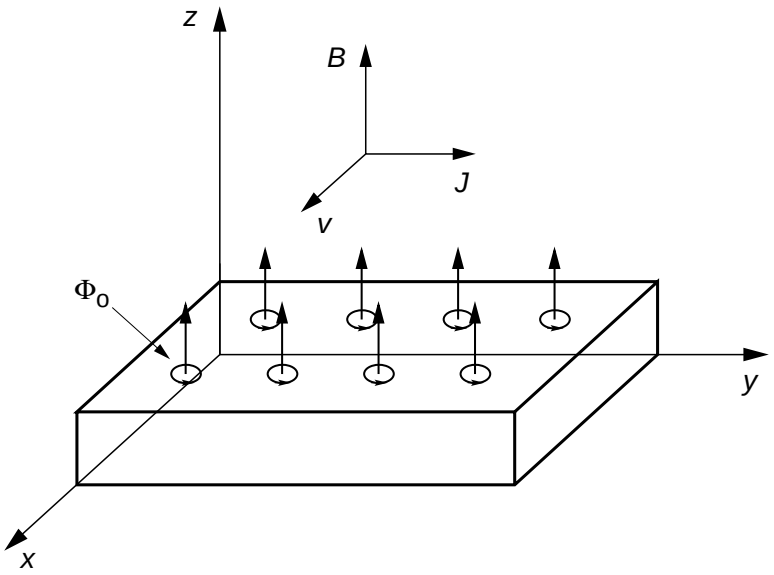

Figure 3.6: A schematic view of the flux-flow state with a transport current in a magnetic field. The vortex lines move with velocity v along the x direction due to the Lorentz force.

For practical applications, a superconductor must be able to carry a high current in the presence of a strong penetrating magnetic field without resistance or dissipation of energy. The origin of the dissipation stems from the Lorentz force

$$\mathbf{F}_L = \frac{1}{c}\mathbf{J} \times \mathbf{B} \tag{3.16}$$

between the current in the superconductor and the flux lines ($B = n\Phi_o$).

Figure 3.4 gives a view of the flux-flow state with an external current density $\mathbf{J}$ applied to the vortex system. The flux lines move in the x direction under the action of the Lorentz force. Within a perfectly homogenous system the driving lorentz force is counteracted only by the friction force $\mathbf{F}_\eta = -\eta\mathbf{v}$, where $\mathbf{v}$ is the steady-state velocity of the vortex system

$$\mathbf{v} = \frac{1}{\eta c}\mathbf{J} \times \mathbf{B}, \tag{3.17}$$

and η is the friction coefficient. This motion leads to the generation of an electric field

$$\mathbf{E} = \frac{1}{c}\mathbf{B} \times \mathbf{v} = \frac{\mathbf{B}^2}{\eta c_2}\mathbf{J} \tag{3.18}$$

which then with $\mathbf{E}$ and $\mathbf{J}$ running parallel gives rise to power dissipation in the system given by

$$P = \frac{1}{\eta c^2}\left(\mathbf{J} \times \mathbf{B}\right)^2 \approx \rho_n J^2 \frac{B}{H_{c2}}, \tag{3.19}$$

and electric resistance

$$\rho = \frac{E}{J} = \frac{B^2}{\eta c^2} \approx \rho_n \frac{B}{H_{c2}}, \tag{3.20}$$

where ρ_n is the normal-state resistivity [65]. In order to recover the desired property of dissipation-free current flow the flux lines have to be pinned to prevent flux motion, i.e. $\mathbf{v} = 0$. Pinning results from any spatial inhomogeneity of the material such as impurities, grain boundaries, point defects (i.e. oxygen defects), etc. The most effective pinning sites are artificially introduced into the material by irradiating it with very fast heavy ions [66]. These columnar defects are roughly 5 nm in diameter and 10's of microns long. They are ideal for pinning a vortex because a given defect absorbs all the free energy of the vortex core, and forms a very deep potential well for the vortex. The vortex lattice sees the

pinning centers as potential reliefs separated by potential barriers. Figure (3.7) depicts a segment of a vortex line pinned by point defects, and acted upon by the Lorentz force.

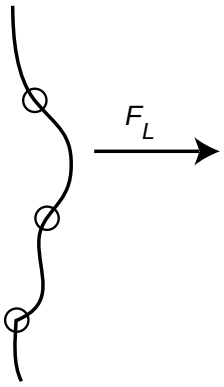

Figure 3.7: A single vortex line segment pinned by point defects and acted upon by the Lorentz force.

In the presence of pinning the Lorentz force is always accompanied by a density gradient of vortices. Inside the superconductor the current density and the vortex density gradient are intrinsically interrelated, $J \propto dB/dx \propto dn/dx$ where $B = n\Phi_o$. This is illustrated in Figure 3.8 where a net current $J = J_{right} - J_{left}$ flows in one direction along a pinned vortex array with a density gradient. The critical current density is defined as the current density which makes the driving Lorentz force equal to the pinning force acting on a vortex

$$J_c = \frac{cF_{pin}}{B}. \tag{3.21}$$

Increasing the current density beyond J_c leads to the depinning of the vortices and hence to the reappearance of dissipation. Even for current densities below J_c the vortex lines can jump over the pinning barriers to adjacent pinning sites due to thermally activated motion of the vortices resulting in slow changes in trapped magnetic fields and measurable resistivities. Thermal fluctuations produce a creep-type motion of the vortex system for current densities $J < J_c$. This

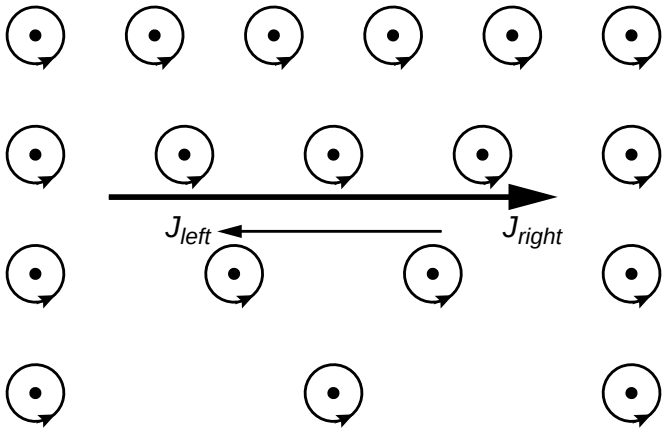

Figure 3.8: A vortex density gradient and a current density are always intrinsically related.

phenomena in type II superconductors is called flux creep. The rate of hopping between wells in the Anderson-Kim model [67] is presumed to be proportional to $R = \omega_o e^{-\frac{E_b}{K_b T}}$, where ω_o is a characteristic frequency of flux line vibration, and E_b is the activation or barrier energy.

Figure 3.9 illustrates the reduction in the barrier potential with increased applied current density. This model is called the tilted-washboard. Any flux creep that occurs will relieve the vortex density gradient, hence increases the barrier potential, and slows down the flux motion with a logarithmic time dependence.

Vortices tend to hop in bundles with the bundle size increasing with decreased current density. There are three energy scales determining the correlated motion of the vortices. The pinning energy tends to hold a vortex into place. The interaction between the vortices tend to make them move coherently as bundles. The third is the Lorentz force which tends to lower the barrier potential and unpin the vortices. At the critical state where $J \sim J_c$ the Lorentz force dominates, overwhelming both the pinning force and the intervortex interaction. This is the single vortex limit where vortices can break loose and move somewhat independently. At lower current densities it is more favorable for the vortices to move

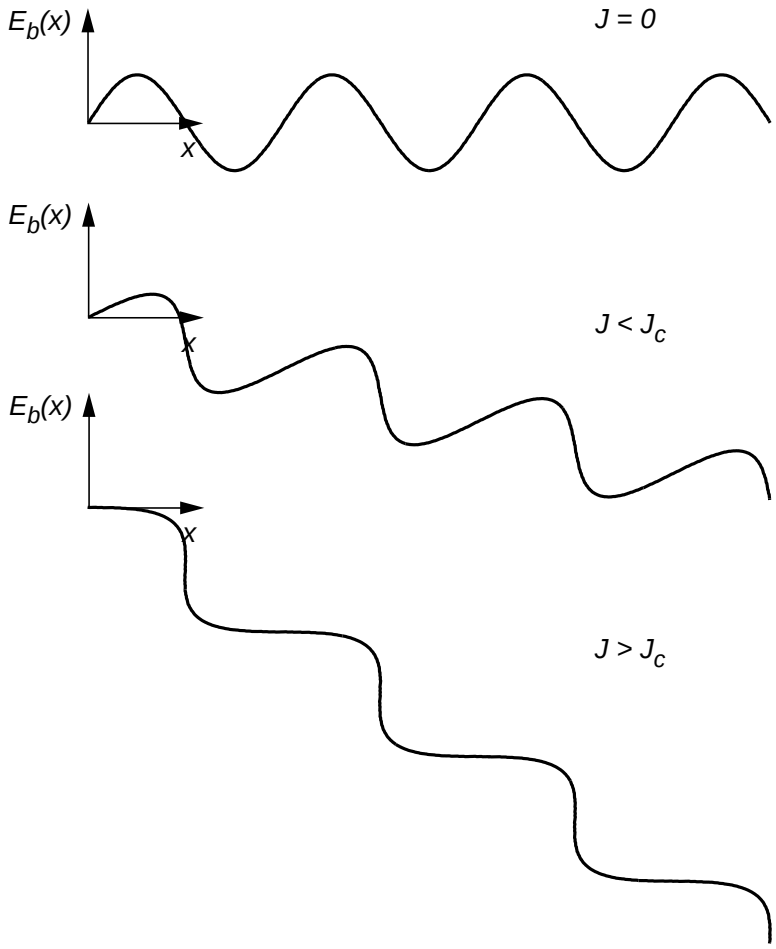

Figure 3.9: Flux pinning potential E_b with transport current density J which effectively reduces the pinning potential. A driving force due to current (or dB/dx) favors flux bundle jumps over barriers to adjacent pinning sites in a "downhill" direction.

in bundles. As a bundle moves it exerts a stress on the surrounding boundaries proportional to the perimeter of the bundle. There is an energy gain associated with moving downhill in the tilted washboard. At smaller current densities it becomes more favorable for the bundles to get larger to move, and at higher current densities the bundles are smaller. This theory is often referred to as collective creep [60].

If the Abrikosov vortex lattice was perfectly periodic and rigid it would not be effectively pinned by any random collection of pinning sites. Thus, the vortex lattice will always seek to arrange itself to take the most advantage of favorable pinning sites in order to lower its energy, but at the expense of increasing the elastic energy of the vortex lattice by deforming it. There is a frustration between the intervortex interactions and the pinning potential landscape. In the weak pinning limit with a dense array of weak pinning centers the equilibrium distorted vortex lattice that minimizes the sum of these two energies is described by the Larkin and Ovchinikov theory of collective pinning [68]. The key idea is that the ideal periodic vortex lattice works out this frustration by arranging itself into smaller sections of reasonable undistorted vortex lattice, where each domain (Larkin domain) can take advantage of the local pinning landscape more efficiently. Each segment will be rotated or displaced in some manner with respect to surrounding domains increasing the elastic energy at its surface which is the trade-off for the improved pinning energy. There is short-range order, but the long-range order is destroyed.

The elasticity of the vortex lattice, the shear modulus C_{66} and the bending modulus C_{44} are important considerations in determining the net pinning of the system. The more rigid the lattice the less pinned it is. The softer the lattice is the better it is pinned, but if it gets too soft it has no shear modulus and the

vortex lattice melts. If the pinning is very weak as in a clean crystal without defects the melting transition will be first order where the whole lattice melts suddenly close to homogeneously, and absorbs some latent heat. When stronger pinning is present the first order character of the melting vanishes, and a more gradual melting phenomena occurs over a wider range of temperature and fields, which implies a second order phase transition.

The critical current density decreases with increasing field or temperature. As the vortex lattice gets very close to melting the critical current density can suddenly shoot up as the vortex lattice becomes more deformable and adaptable to the pinning sites. Then it will go to zero as the vortex lattice finally melts completely. This peak effect is seen mostly in clean crystals with fairly weak pinning.

In the other extreme limit with a dilute array of very strong pinning centers, columnar defects, the pinning forces are so strong that they to some degree will overwhelm the forces between the vortices. The vortex lattice is pinned very effectively, and correlated-disorder prevails.

3.3 Magnetic Phase Diagram of High-T_c Superconductors

The high-temperature superconductors exhibit a very rich magnetic phase diagram with many new features and phase transitions still being investigated. The two main phases are the vortex solid and the vortex liquid which are separated by the irreversibility line. However, in highly anisotropic high-T_c superconductors such as $Bi_2Sr_2CaCu_2O_8$ the phase diagram is much more complicated and displays at least three distinct phases, a relatively ordered quasi-lattice or Bragg

glass, a highly disordered entangled vortex solid or vortex glass, and a vortex liquid phase. Part of the reason for the complicated phase diagram of these high-T_c superconductors, is shorter coherence length, high anisotropy, and higher operating temperatures and thereby the enhanced role of thermal fluctuations over large parts of the phase diagram leading first of all to vortex lattice melting and the two distinct vortex phases, vortex solid and vortex liquid [69]. The presence of disorder and its interplay with thermal fluctuations result in an even more complicated mixed-state phase diagram in layered high-T_c superconductors such as shown in Figure 3.12.

The layered structure of highly anisotropic high-T_c superconductors has a strong effect on the thermal destruction of the vortex lattice leading to some different features. Figure 3.10 shows the crystal structure of $Bi_2Sr_2CaCu_2O_8$ which is the most anisotropic superconductor known. The superconductivity is confined to the cuprate-oxide planes, which are separated by 12 Å of insulating layers of bismuth-oxide, strontium-oxide, and calcium-oxide layers. The thickness of the two superconducting cuprate-oxide layers is 3 Å and the coherence length ξ_c along the c-axis is only $\sim$0.3 Å, and hence a continuous anisotropic Ginzburg-Landau description for this system is inappropriate as the order parameter can change drastically from layer to layer. In the discrete Lawrence-Doniach model [70], layered superconductors are viewed as a stacked array of two-dimensional (2D) superconductors weakly coupled together by the Josephson effect between adjacent layers. The order parameter $\Psi_n(x, y)$ depends on the discrete variable n and is a 2D-function within each layer. A vortex line perpendicular to these layers is looked upon in this model as a stacking of 2D pancake shaped vortices with one in each layer as shown in Figure 3.11. The vortex current is confined to the layers, and two pancake vortices in adjacent layers are weakly coupled by Josephson interactions and magnetic interactions. The strength of the interlayer coupling

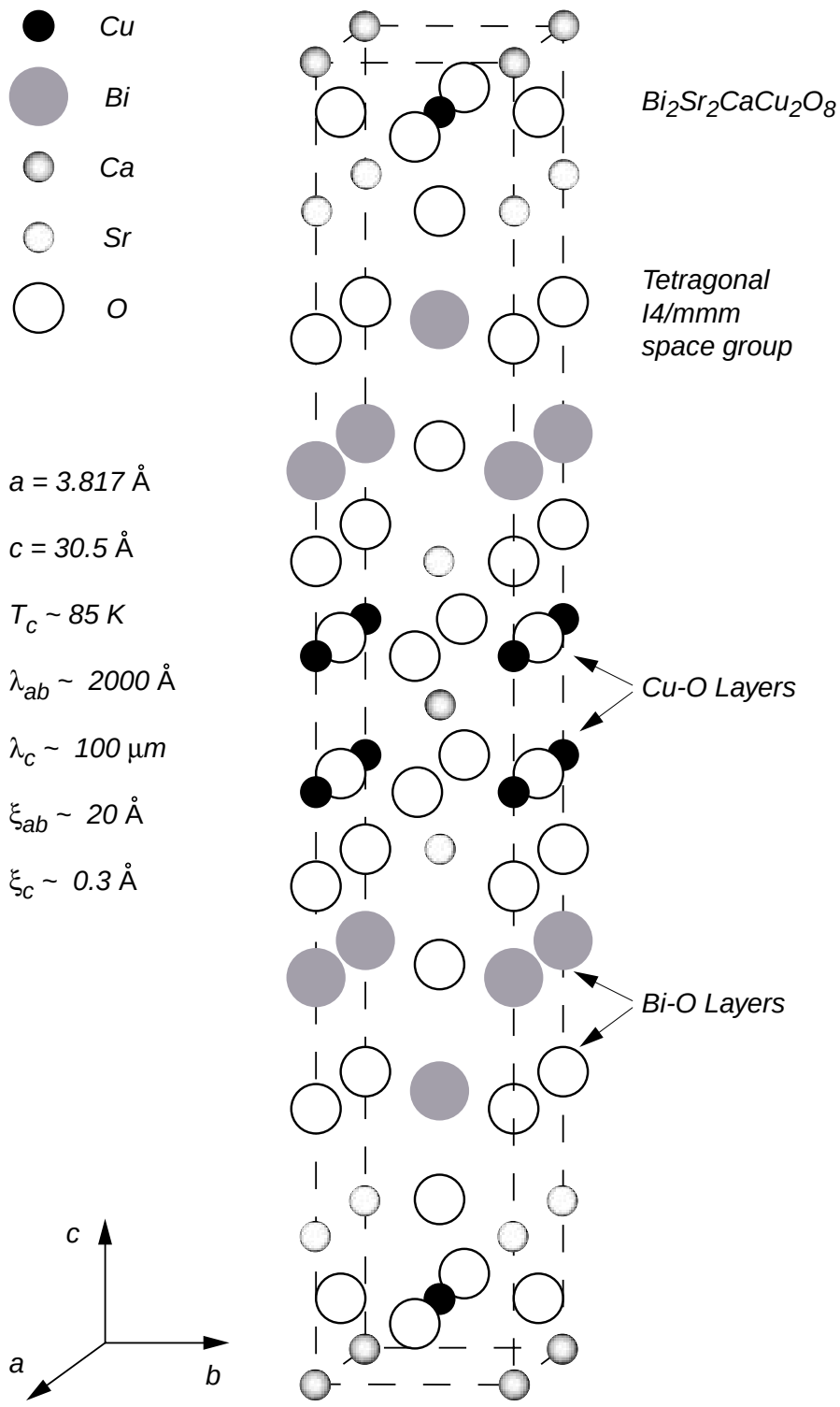

Figure 3.10: Crystal structure of $Bi_2Sr_2CaCu_2O_8$ superconducting compound.

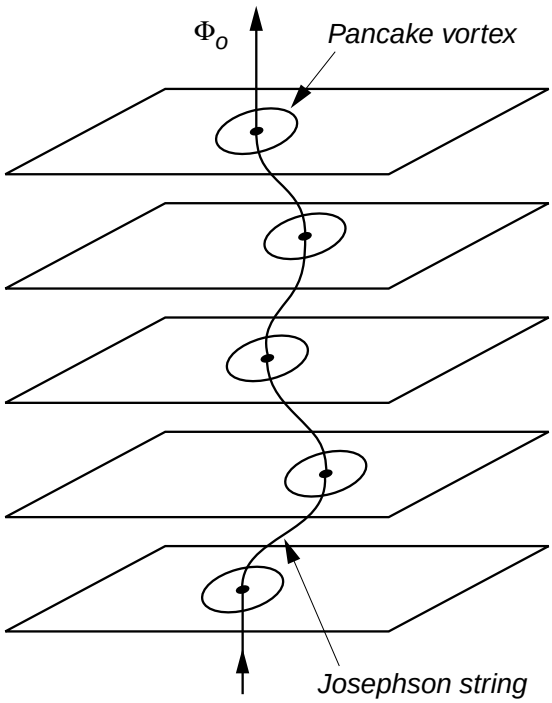

Figure 3.11: Illustration of a single flux line structure in a strongly layered high-T_c superconductor. The vortex line can be viewed as an array of pancake vortices in the superconducting CuO_2 planes interconnected by Josephson strings.

determines the degree of anisotropy in the magnetic properties with respect to fields applied along the c-axis and the ab-plane. The anisotropy is defined as the ratio of the c-axis penetration depth to the in-plane penetration depth $\gamma = \lambda_c/\lambda_{ab}$ assuming a close to uniaxial crystal structure. This anisotropy differs significantly for different families of materials. In $YBa_2Cu_3O_{7-\delta}$ the vortex system at the melting transition behaves as in a continuous anisotropic superconductor [71, 72]. In the other limit with a high degree of anisotropy such as for $Bi_2Sr_2CaCu_2O_8$, the coupling is very weak and the behavior of the vortex system depends strongly on the layered structure. In this material the vortex lattice melts at such low fields [73] that the in-plane penetration depth $\lambda_{ab} \approx 2000$ Å is comparable to the intervortex distance $a_o \approx (\Phi_o/B_z)^{1/2}$. The irreversibility line generally scales with the degree of anisotropy. It goes down to very low temperatures for materials

with a high degree of anisotropy. The vortex liquid phase occupies a significant portion of the phase diagram for $Bi_2Sr_2CaCu_2O_8$, whereas for $YBa_2Cu_3O_{7-\delta}$ it is much smaller.

A magnetic field applied along the *ab*-plane (parallel magnetic field) introduces a triangular lattice of Josephson vortices in between the layers [74, 75]. A Josephson vortex has no normal core. The vortex current flow pattern is approximately elliptical, and is limited by the interlayer Josephson coupling.

The mixed-state phase diagram for a pristine $Bi_2Sr_2CaCu_2O_8$ crystal with the magnetic field applied parallel to the *c*-axis is illustrated in Figure 3.12. In the Bragg glass phase elastic interactions govern the structure of the vortex solid at low fields, forming a well defined hexagonal lattice with long-range order only weakly destroyed. A characteristic of this phase is the presence of Bragg diffraction spots in small angle neutron diffraction (SANS) and the absence of topological defects (dislocations). Closer to the irreversibility line at higher temperatures the pinning gets weaker and the vortex lattice gets softer. Above the irreversibility line and below the melting line the vortex lattice is still solidified, but not pinned signifying the onset of the flux-flow state with a zero critical current density. Finally, above the melting line the vortex lattice melts completely due to thermal fluctuations. This phase transition has the nature of a first order phase transition with a discontinuity in heat capacity, resistivity, and local field B [73]. In the vortex glass at low temperatures and higher magnetic fields, disorder dominates, where vortex-pin interactions result in a lattice in which small vortex lattice segments are twisted and dislocations proliferate. The crossover from the Bragg glass occurs when the intervortex distance becomes comparable to the underlying disorder in the system as the magnetic field is increased at low temperatures. At this point pancake vortices are displaced when attracted

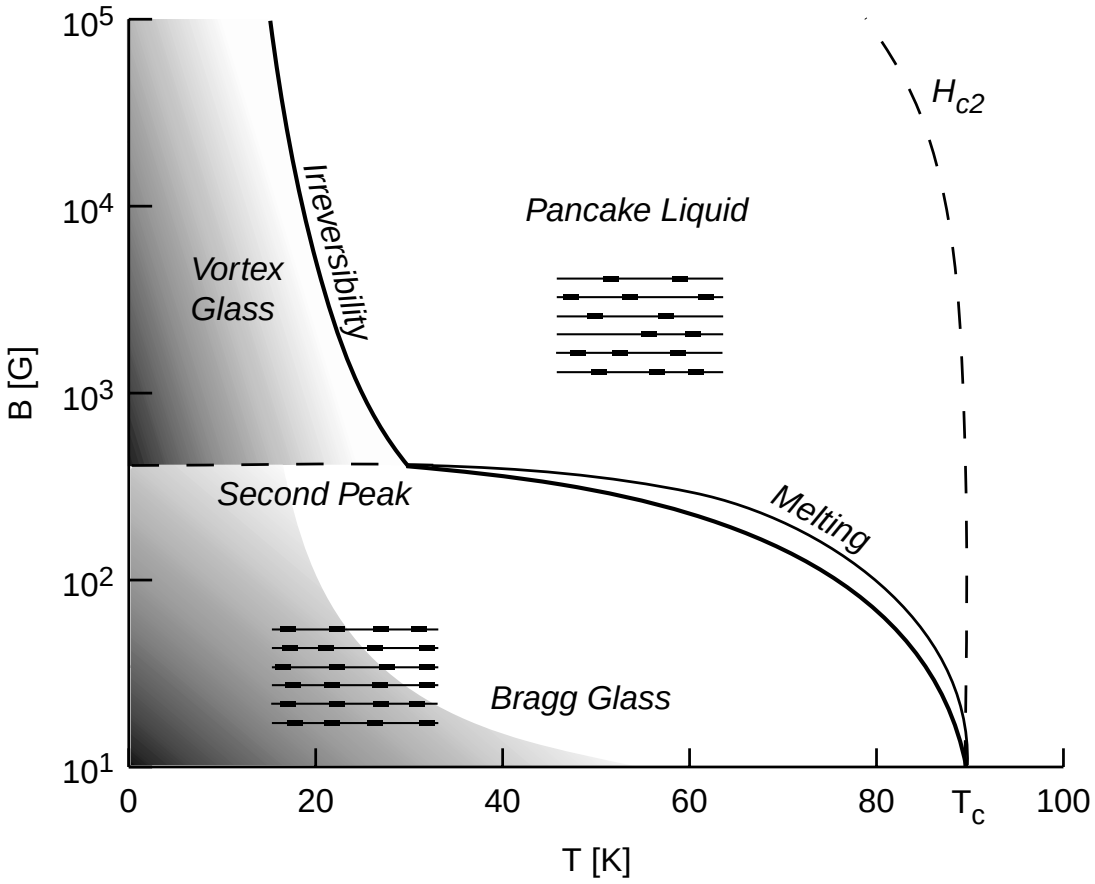

Figure 3.12: Mixed-state phase diagram of a pristine $Bi_2Sr_2CaCu_2O_8$ crystal with the magnetic field applied parallel to the c-axis, showing the three major phases, the Bragg glass, the vortex glass and the liquid phase.

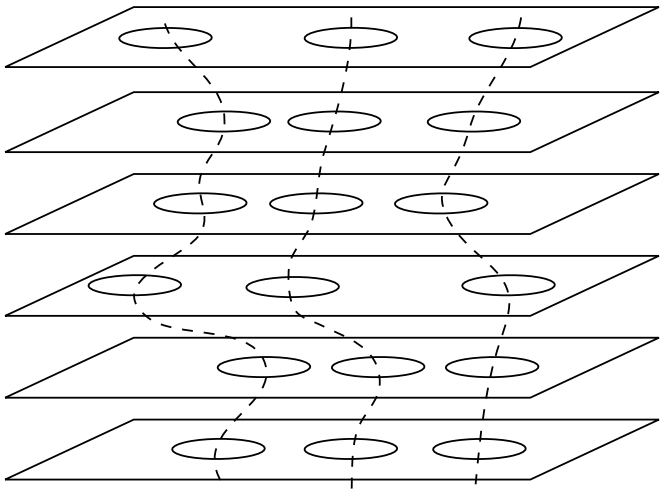

Figure 3.13: Illustration of the sudden disorder of pancake vortices at the second peak.

to defects and to pancake vortices from neighboring lines of pancake vortices in adjacent layers, and the close-to long-range order is destroyed [76]. This melting phenomena is similar to the Lindemann criteria, which is responsible for melting of the vortex lattice thermally. When the displacements become some fraction c_L^2 of the vortex lattice separation a_o then the vortex lattice melts. The nature of this phase transition remains somewhat controversial. The phase transition between the vortex glass and the vortex liquid is of second order.

The second peak effect [77], a pinning driven phase transition, occurs in a narrow temperature window and shows in the magnetic hysteresis loop as a sudden sharp feature when increasing the magnetic field into the glassy state due to a sudden increased disorder of the pancake vortices along the c-axis as depicted in Figure 3.13. Interestingly, the critical current density is increased in the ab-plane because of improved pinning, while it is decreased along the c-axis due to increased disorder.

The mixed-state phase diagram for an irradiated $Bi_2Sr_2CaCu_2O_8$ crystal with

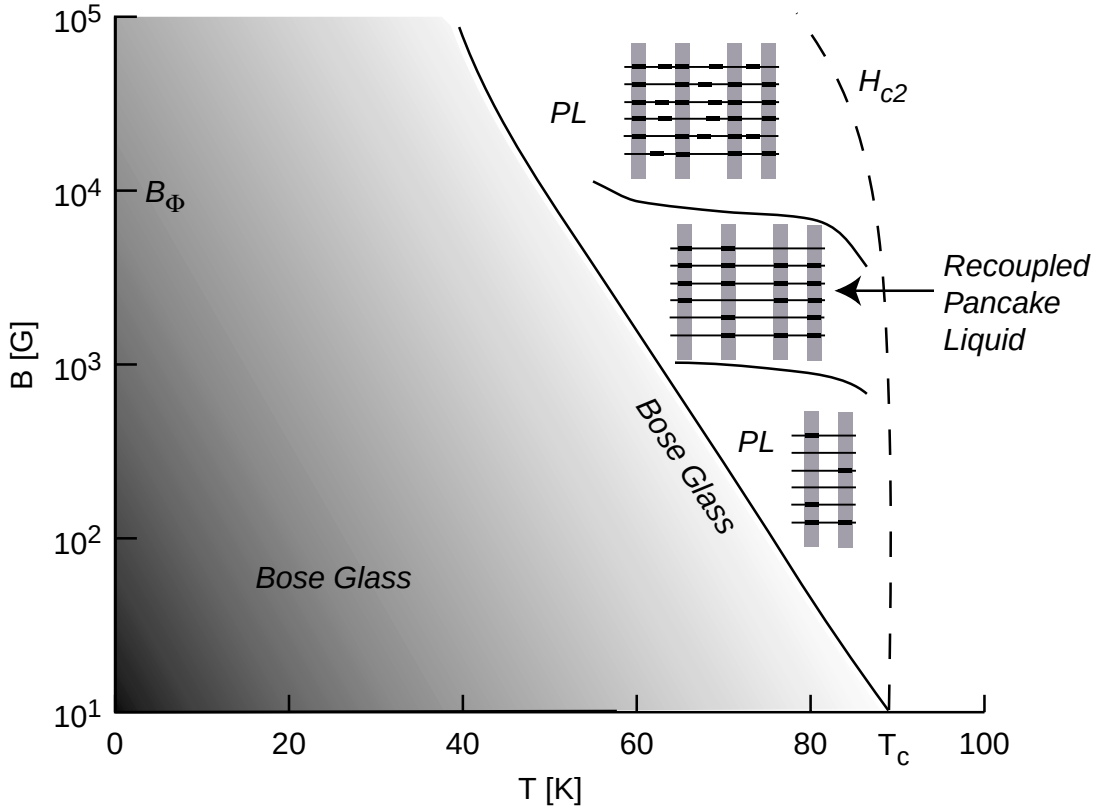

Figure 3.14: Mixed-state phase diagram of an irradiated $Bi_2Sr_2CaCu_2O_8$ crystal with the magnetic field applied parallel to the c-axis, showing the two major phases, the Bose glass, and the liquid phase.

the magnetic field applied parallel to the c-axis is illustrated in Figure 3.14. Columnar defects introduced by irradiation with very energetic heavy ions are expected to be the most effective pinning centers for vortices aligned parallel to the defect structure. The correlated disorder induced by the columnar defects acting as a coherent pinning force over an extended pinning structure largely improves the pinning properties of the material. The pancake vortices are located on the columnar defects at low temperatures, forming a so-called Bose glass phase. The trapping of the pancake vortices by the columnar defects suppresses the thermal fluctuations, which drive the melting transition, and moves it up in phase space creating a large region with a substantial critical current density. It is predicted that the Bose glass melts into an entangled liquid through a second order phase transition [65].

An anomalous peak effect has been observed in magnetic hysteresis measurements in irradiated $Bi_2Sr_2CaCu_2O_{8+\delta}$ occuring in the temperature range ∼50 K to ∼60 K at a peak field $B_{peak} \sim B_\Phi/3$ in the Bose glass regime, accompanying the reentrant behavior of the Bose Glass melting line [78]. B_Φ is the matching field defined as the equivalent dose, where the density of vortices is equal to the defect density.

It has been found using magnetoresistance measurements that even in the pancake liquid phase pancake vortices are localized mostly on the columnar defects, and that the columnar defects promote formation of lines as shown in Figure 3.14. There is a recoupling of the pancake liquid in a narrow range of field and temperature [79], which will be further discussed in Chapter 3.6.

3.4 Zero Field Cooling and Field Cooling

To fully appreciate the vortex dynamics in a magnetic phase diagram such as shown in Figure 3.12 it is important to understand the difference between zero field cooling and field cooling when applying a magnetic field. When zero field cooling (ZFC), the high-T_c superconductor is cooled down before applying a magnetic field. In field cooling (FC), it is cooled in a magnetic field. The different behavior of the vortex system is best illustrated with a magnetization measurement on a high-T_c superconductor such as a $Bi_2Sr_2CaCu_2O_8$ single crystal shown in Figure 3.16. This data was obtained with a standard SQUID magnetometer.

The superconductor is first zero field cooled to 5 K, whereafter a 10 Oe field is applied along the c-axis. The increasing applied magnetic field will, in the presence of pinning, create a vortex density gradient in the sample as vortices are being pushed into the material from outside. The slope of the vortex density gradient resembles the forefront of a sandpile being pushed forward by a bulldozer. In the Bean critical state model this slope is considered to be linear and proportional to the critical current density, which is related to the vortex density gradient (see Figure 3.15). The Lorentz force pushes vortices in and the pinning force is a reaction force pushing back and stabilizing. The maximum pinning force defines the critical state equation $\mathbf{F}_{pin} = \frac{1}{c}\mathbf{J}_c \times \mathbf{B}$, which also gives the definition of $J_c = \frac{cF_{pin}}{B}$.

Starting out in ZFC mode at 10 Oe and 5 K denoted by 1 in the magnetization measurement in Figure 3.16 the sample is still in the Meissner state as illustrated in Figure 3.16(c) Bean model 1. As the temperature is increased the flux penetrates in the mixed-state creating a vortex density gradient. The Bean slope is steeper at lower temperatures because the Lorentz force required to overcome the pinning is strong. The slope then gets flatter with increased temperature as

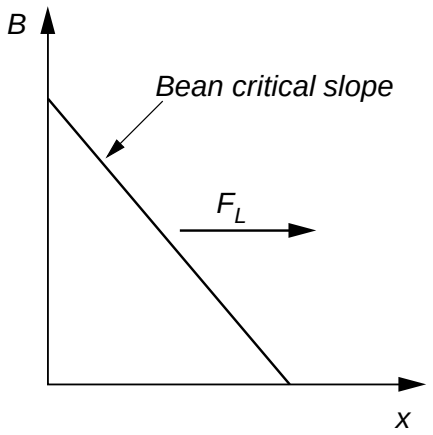

Figure 3.15: The flux density profiles are straight lines in the Bean model, and the slope is proportional to the pinning force and critical current density.

the pinning gets weaker (see Bean model 3). When crossing the irreversibility line the pinning disappears and the slope flattens out which is seen in Figure 3.16(b) as a merging of the ZFC and FC curves. Above T_c, the sample is completely penetrated and the vortices have disappeared according to the mean field approximation.

The sample is now field cooled, still with an applied magnetic field of 10 Oe. The vortices reappear as the temperature is decreased below T_c. The part where ZFC and the FC curves are merged, just below T_c, is reversible. Then, as the temperature is lowered below the irreversibility line pinning sets in and the two modes deviate. The pinning prevents expulsion of flux from the sample. Thus, the magnetization does not change, even below H_{c1}. However, a little flux is expelled at the surface, but doesn't affect the bulk magnetization much. In the Bean model it results in a small dome shaped flux density profile at the surface. The pinning only gets stronger and stronger as the temperature is lowered, and even entering the Meissner state does not expel the flux. Even though the mixed-state doesn't provide the lowest energy for the system, there is no mechanism to annihilate them.

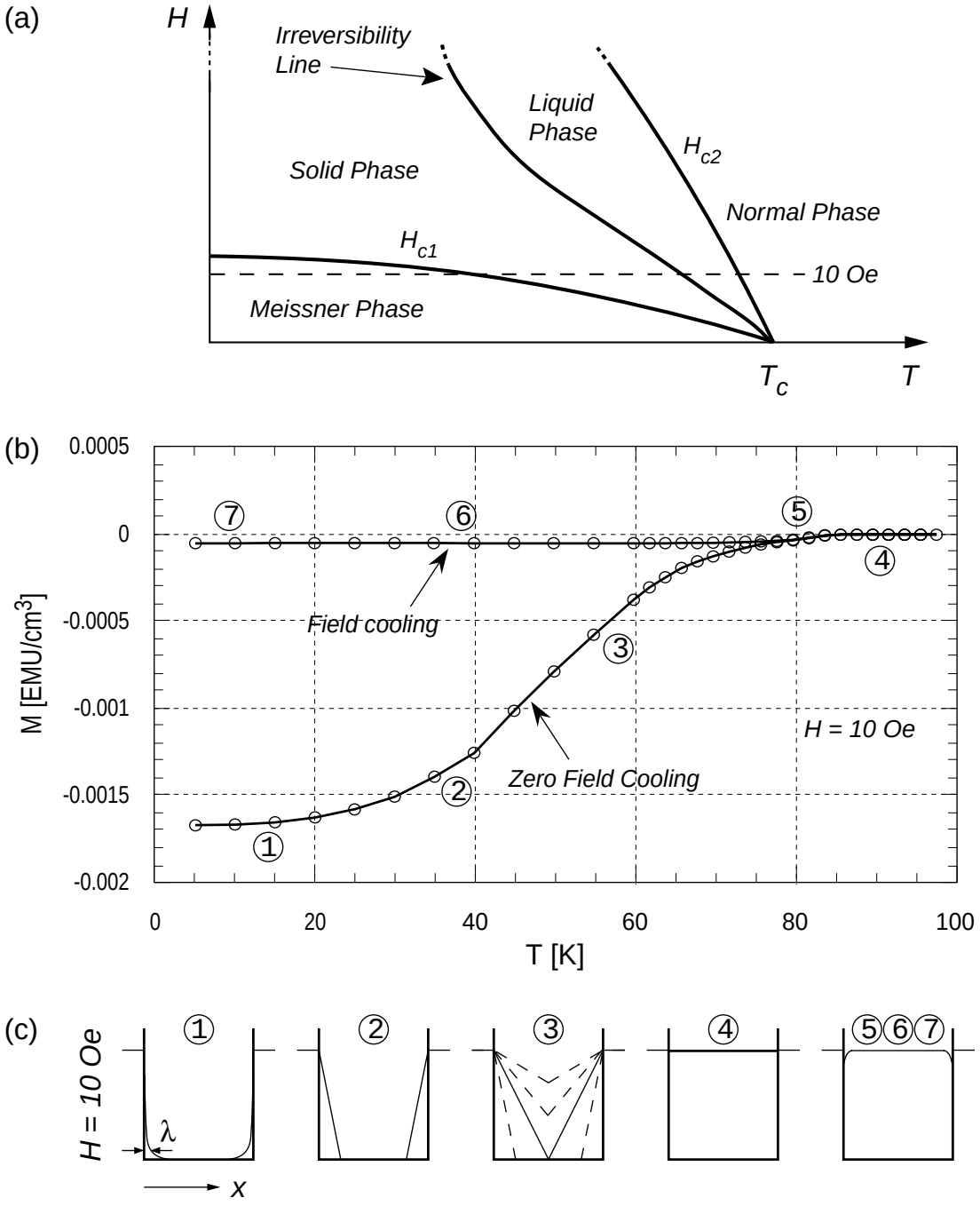

Figure 3.16: Zero field and field cooling on $Bi_2Sr_2CaCu_2O_8$ single crystal ($B||c$). (a) Phase diagram showing a 10 Oe field in the various phases. (b) Zero field and field cooled curves with a 10 Oe field. (c) Corresponding Bean flux profiles.

3.5 Magnetization Hysteresis

Magnetization hysteresis measurements of high-T_c superconductors is a valuable experimental tool to gain insight into features or phases of the magnetic phase diagram. The basic behavior of the vortex dynamics during the hysteresis is illustrated in Figure 3.17 on a $Bi_2Sr_2CaCu_2O_8$ single crystal with corresponding Bean model flux density profiles. The data was obtained in a standard SQUID magnetometer with the magnetic field along the c-axis at 5 K.

Starting at zero field the magnetization follows the virgin curve up to the lower critical field H_{c1}. This part is reversible since no flux enters in the Meissner phase, except for a negligible surface layer within the London penetration depth ($\lambda_L \sim$ 2000 Å). When exceeding H_{c1} flux enters the sample in the form of quantized vortices creating flux density profiles as depicted in Bean model 2. The field value for which the Bean slopes meet in the middle, and the virgin curve merges with the hysteresis loop, is denoted by H_p. As the field increases further, more and more vortices are introduced into the sample, and the whole flux density profile picture simply lifts as shown in Bean model 3. Because of the shielding Meissner currents, there is always a little jump from the applied external field outside to the Bean slope profiles inside the sample. When the external field is reversed the Bean slopes reverses beginning at the surface (see Bean model 4). This is required for the Lorentz force to now push vortices out of the system. At the field H_o the magnetization changes sign which means there is now more flux in the interior than outside. The magnetization is the average B-field inside minus the applied field $4\pi M = B - H$. Close to zero applied field there is still plenty of trapped flux inside, and there is a small region where before the first negative vortices enters there are no vortices leaving the system. This causes the difference between the external field and the internal average field to keep

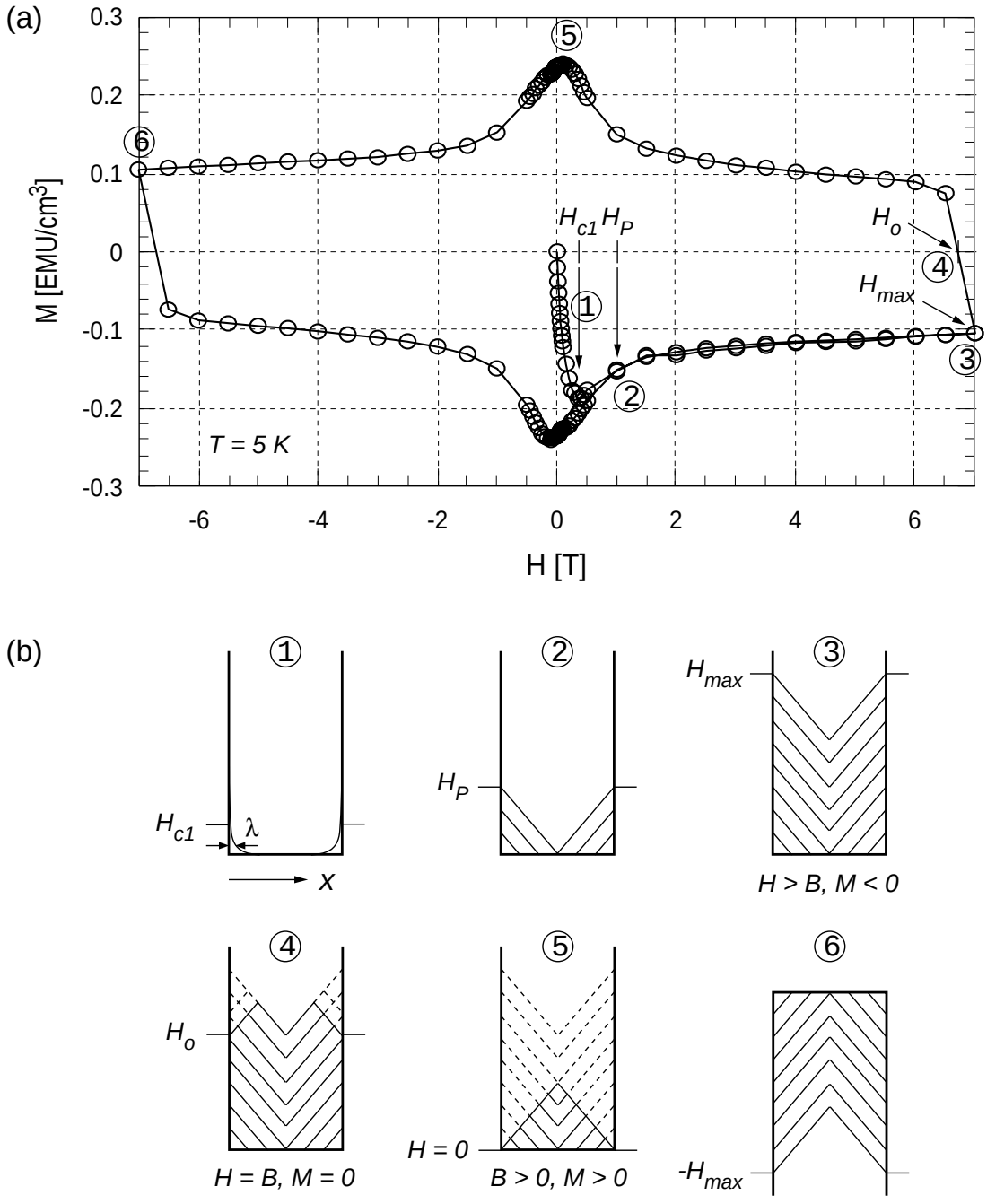

Figure 3.17: Magnetic hysteresis measurement on a $Bi_2Sr_2CaCu_2O_8$ single crystal ($B||c$). (a) Magnetic hysteresis loop. (b) Corresponding Bean flux profiles.

increasing as the external field is driven through zero. This magnetization peak is due partly to demagnetization factors for the plate-like geometry of the sample [80], and partly to the inherent field dependence of the critical current density. The magnetization curve in the negative external field repeats the sequence of the positive region.

The magnetization curve is not quite symmetric about zero field, but is symmetric about the reversible line which is always implicitly present in the flux profiles. The critical state occurs on top of the equilibrium magnetization, and at much higher fields the hysteresis loop will merge with the reversible line. It will simply collapse due to lack of pinning in the liquid state. At higher temperatures the pinning is weaker and the hysteresis loop will merge with the reversible equilibrium line much sooner, shrinking in both amplitude and width. The critical current density at a given field in the loop is proportional to the positive magnetization minus the negative magnetization, multiplied by the diameter of the sample perpendicular to the field.

Figure 3.18(a) shows a series of hysteresis loops of the same sample at 5 K, 10 K, and 15 K in a field from -7 T to +7 T. These hysteresis loops illustrate the fact that the pinning gets weaker with increased temperature as seen from the shrinking hysteresis loops. Figure 3.18(b) shows hysteresis loops for the same sample at yet higher temperatures at 30 K, 40 K, and 50 K in a field from -3000 Oe to $+3000$ Oe. Here, as seen from the 40 K loop, all pinning vanishes when approaching 40 K in a small field of 600 Oe. The point where the loop collapses and merges with the reversible line is associated with the melting line.

The 30 K hysteresis loop in Figure 3.18(b) shows a hint of the second peak effect mentioned earlier in Section 3.3. The second peak effect is a pinning driven phase transition, and occurs at a precise B-field at low temperatures. The ramp-

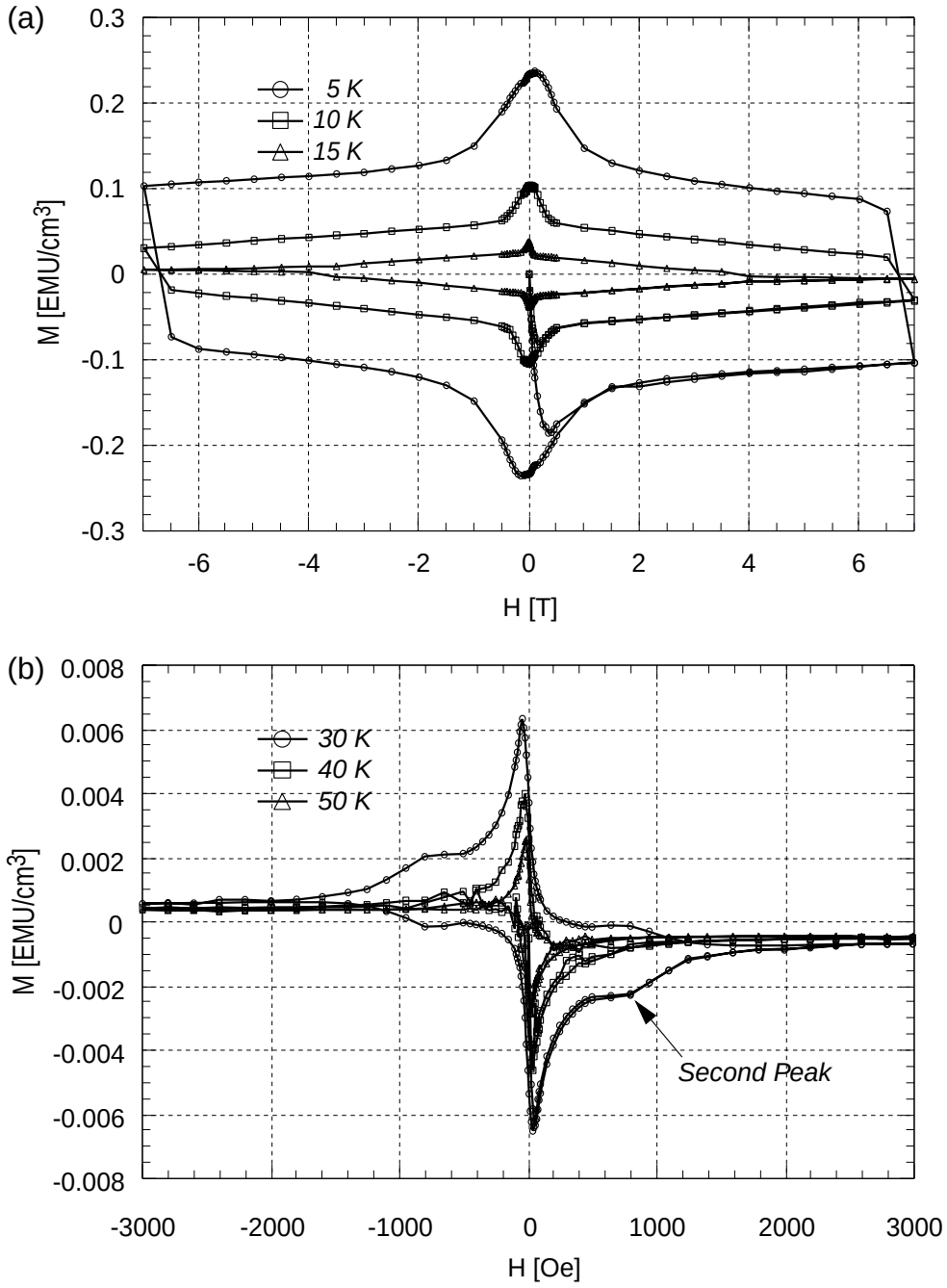

Figure 3.18: Magnetic hysteresis measurements on a $Bi_2Sr_2CaCu_2O_8$ single crystal ($B||c$). (a) Magnetic hysteresis loops at 5 K, 10 K, and 15 K. (b) Magnetic hysteresis loops at 30 K, 40 K, and 50 K.

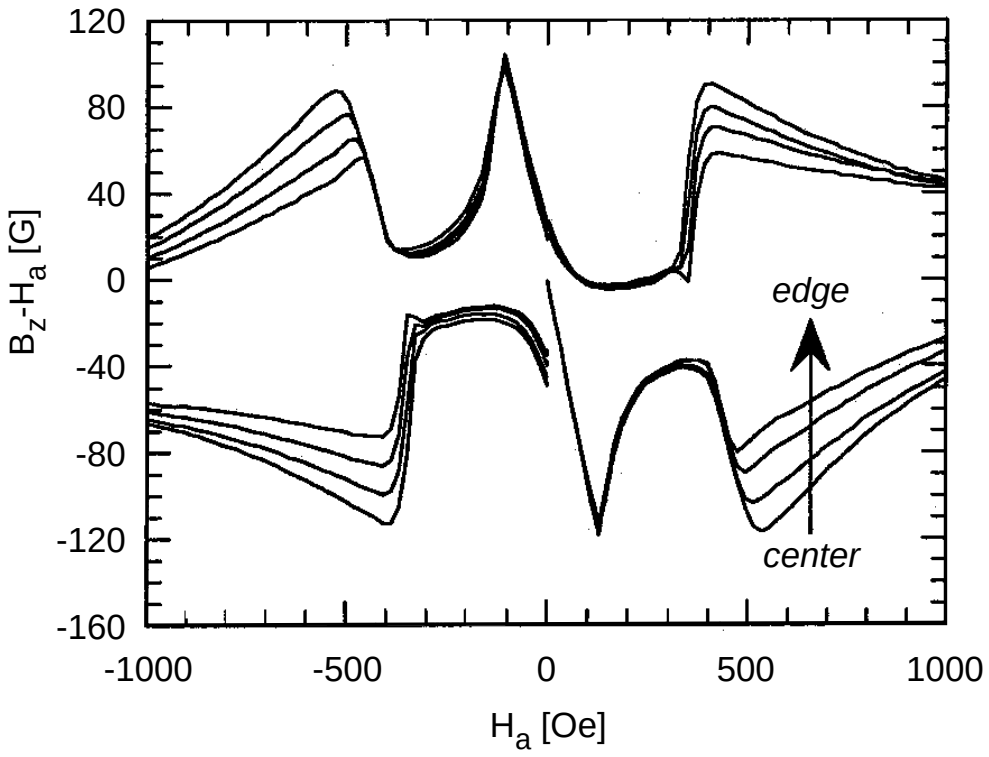

Figure 3.19: Hysteretic loops of the local magnetization on a $Bi_2Sr_2CaCu_2O_{8+\delta}$ single crystal at $T = 25.6$ K at various locations on the sample surface ($B||c$). The distance between consecutive sensors is 18 μm. ((© Copyright (1997) by Elsevire Science. Figure 1 in Reference 1).

ing up of the applied field causes a vortex density gradient with a location dependent B-field. Thus, the transition occurs at different locations in the sample. However, the standard SQUID magnetometer measures the average B-field in the sample thereby smearing out the sharp feature characteristic of the second peak effect as seen in Figure 3.18(b). Using a Hall-sensor array capable of measuring the magnetic induction in the sample at local positions one can record the local magnetic field profile for each sensor. Such local magnetic relaxation measurements were performed by Berry *et al.* [81] on $Bi_2Sr_2CaCu_2O_{8+\delta}$ single crystals at $T = 25.6$ K clearly showing the sharp feature characteristic of the second peak effect shown in Figure 3.19.

The second peak effect can alternatively be probed with the Josephson Plasma Resonance which is sensitive to the abrupt disorder in the pancake vortices along the c-axis associated with the phase transition.

3.6 Structure of Vortex Liquid Phase in Irradiated $Bi_2Sr_2CaCu_2O_{8-\delta}$ Crystals

The structure of the vortex liquid in highly anisotropic layered superconductors with columnar defects (CDs) produced by heavy ion irradiation is one of the most intriguing questions in the current study of the vortex state in high temperature superconductors. For the most anisotropic $Bi_2Sr_2CaCu_2O_{8-\delta}$ (Bi-2212) superconductor without strong disorder, neutron scattering and Josephson plasma resonance (JPR) data provide evidence in favor of a pancake liquid with very weak correlations of pancakes in different layers [82−85]. When CDs are introduced into these crystals a large decrease in the reversible magnetization is observed [86], indicating that pancakes are predominantly situated on the CDs, even in the liquid state. Recent studies of the JPR [87, 88] and c-axis transport [89, 90] in irradiated Bi-2212 crystals reveal enhancement of c-axis correlations in some interval of out-of-plane magnetic fields, $B_\perp$, below the matching field, B_Φ, at temperatures $T \sim 70$ K. In other words, pancakes at these fields and temperatures appear to form aligned segments of vortex lines inside CDs, while outside of this region they are better described as a liquid of weakly c-axis-correlated pancakes, as in pristine crystals. Both c-axis transport and JPR involve the flow of Josephson currents and are thus sensitive to the misalignment of pancake vortices between adjacent planes. CDs aligned with the c-axis will promote interplane pancake alignment in a region of temperature where pancakes remain largely localized on CDs. Even in the liquid state, where pancakes are mobile,

filling of the available CD sites should lead to enhanced c-axis correlation from statistical considerations alone. In previous c-axis transport measurements [89], a dip in the magnetoresistance, $\rho(B_\perp)$, of a Bi-2212 crystal was observed at a magnetic field corresponding to a filling factor of CDs, $f = B_\perp/B_\Phi \approx 1/3$.

So far there has been no technique available for providing quantitative information on the degree of c-axis correlation or on the length of pancake line segments. In addition, it is unclear whether vortex interactions play a significant role in enhancing correlation in the liquid state. Previously, a method was proposed, but not yet realized, to extract the pancake density correlation function using data for the JPR frequency as a function of $B_\parallel$ at fixed $B_\perp$ [91]. Here we determine the average length of vortex line segments as a function of $B_\perp$, i.e., of the filling factor f from transport measurements on single crystals of Bi-2212 with and without CDs. For this we have developed a method for extracting the phase difference correlation function along the layer from measurements of the c-axis conductivity, σ_c, as a function of the magnetic field component parallel to the layers, $B_\parallel$, at fixed $B_\perp$. The component $B_\perp$ establishes the vortex state to be studied, while the component $B_\parallel$ serves as a probe of this state, as described below. Knowing the phase difference correlation length, we estimate the pancake density correlation length along the c-axis.

In Josephson coupled superconductors in the presence of a c-axis current, voltage is induced by slips of the phase difference between layers, $\varphi_{n,n+1}(\mathbf{r},t)$, as described by the Josephson relation $V_{n,n+1} = (\hbar/2e)\dot{\varphi}_{n,n+1}$. Here n labels layers, $\mathbf{r} = x, y$ are coordinates in the ab-plane, and t denotes time. The c-axis conductivity in the vortex liquid state is determined by the Kubo formula [85]

$$\sigma_c(B_\perp, B_\parallel) = (s\mathcal{J}_o^2/2T)\int_0^\infty dt \int d\mathbf{r} G(\mathbf{r},t), \tag{3.22}$$

$$G(\mathbf{r},t) \;=\; 2\langle \sin\varphi_{n,n+1}(0,0)\sin\varphi_{n,n+1}(\mathbf{r},t)\rangle$$

$$\approx \quad \langle \cos[\varphi_{n,n+1}(\mathbf{r},t) - \varphi_{n,n+1}(0,0)] \rangle, \tag{3.23}$$

where $\mathcal{J}_o$ is the Josephson critical current and s is the interlayer distance. Time variations of the phase difference are caused by mobile pancakes [92] induced by $B_\perp$ and by mobile Josephson vortices induced by the parallel component $B_\parallel$. In the lowest order in Josephson coupling we split $[\varphi_{n,n+1}(0,0) - \varphi_{n,n+1}(\mathbf{r},t)]$ into the contribution induced by pancakes and that caused by the unscreened parallel component $B_\parallel$. Assuming that $B_\parallel$ is along the x-axis, we obtain a simple expression for the contribution of the parallel component to the phase difference,

$$\begin{aligned} &\varphi_{n,n+1}(0,0) - \varphi_{n,n+1}(\mathbf{r},t) \approx \\ &[\varphi_{n,n+1}(0,0) - \varphi_{n,n+1}(\mathbf{r},t)]_{B_\parallel=0} - 2\pi s B_\parallel y/\Phi_o. \end{aligned} \tag{3.24}$$

Inserting this expression into Equations (3.22) and (3.23) we obtain

$$\sigma_c(B_\perp, B_\parallel) = (\pi s \mathcal{J}_o^2/T) \int dr r \tilde{G}(r, B_\perp) J_o(\alpha B_\parallel r), \tag{3.25}$$

where $J_o(x)$ is the Bessel function, $\alpha = 2\pi s/\Phi_o$, and

$$\tilde{G}(\mathbf{r}, B_\perp) = \int_0^\infty dt G(\mathbf{r}, t, B_\perp). \tag{3.26}$$

The function $G(\mathbf{r},t)$ describes the dynamics of the phase difference caused by mobile pancakes. If $g(B_\perp, B_\parallel) = \sigma_c(B_\perp, B_\parallel)/\sigma_c(B_\perp, 0)$ is known in the vortex liquid, the correlation function $G(r) = \tilde{G}(r)\mathcal{J}_o^2\Phi_o^2/4\pi s T \sigma_c(B_\perp, 0)$ may be found using the inverse Fourier-Bessel transform,

$$G(r, B_\perp) = \int dB_\parallel B_\parallel g(B_\parallel, B_\perp) J_o(\alpha B_\parallel r). \tag{3.27}$$

The correlation lengths R and R_1 of this function are defined by the relations

$$R^2 = \int_0^\infty dr \frac{rG(r)}{G(0)}, \quad R_1^2 = \int_0^\infty dr \frac{r^3 G(r)}{R^2 G(0)}. \tag{3.28}$$

Note that R_1 is related to the coefficient of the $B_\parallel^2$ term in the expansion of $g(B_\perp, B_\parallel)$ in $B_\parallel^2$,

$$g(B_\perp, B_\parallel) \approx 1 - [\pi s R_1(B_\perp)/\Phi_o]^2 B_\parallel^2. \tag{3.29}$$

Thus $R_1(B_\perp)$ can be obtained independently from data for $\sigma_c(B_\perp, B_\parallel)$ at small $B_\parallel$.

Such a procedure to obtain the function $G(r, B_\perp)$ is valid if the vortex state depends weakly on the Josephson coupling and hence on the probe field $B_\parallel$ (which affects Josephson coupling). Then this method is nondestructive. Let us check first under what conditions we can neglect the effect of Josephson coupling on the equilibrium vortex state. The energy of Josephson coupling in the correlated area πR^2 is $\pi E_o R^2/\lambda_J^2$, which should be much smaller than the temperature T to be treated as a perturbation [91]. Here $E_o(T) = \Phi_o^2 s/16\pi^3\lambda_{ab}^2(T)$. For Bi-2212, with $\gamma \approx 300$ and $\lambda_{ab}(0) \approx 2000$ Å, the Josephson coupling in the correlated area is $\sim 0.2T$ at the maximum value of R found below and at $T > 60$ K. Thus the effect of Josephson coupling, and hence $B_\parallel$, on the equilibrium vortex state may be neglected. For dynamical parameters, such as σ_c, higher order terms in Josephson coupling describing dynamic screening of $B_\parallel$ omitted in Equation (3.24), may be important. This will be discussed below.

We anticipate that in the pancake vortex liquid state in pristine crystals the characteristic lengths R and R_1 of the correlation function $G(r)$ are on the order of the intervortex distance, $a = (\Phi_o/B_\perp)^{1/2}$, because each pancake here is mobile and induces phase slippage as described in Reference 92. In irradiated crystals with CDs we anticipate much bigger R and R_1 if pancakes form long segments of lines inside CDs. Then only ends of segments contribute significantly to the phase difference $\varphi_{n,n+1}(\mathbf{r}, t)$ and lead to suppression of Josephson coupling and σ_c, while the effect of pancakes in neighboring layers inside the segments is much

smaller.

In our experiments, high quality Bi-2212 crystals ($T_c \simeq 85$ K) of about $1\times1.5\times 0.02$ mm^3 were used. The irradiation by 1.2 GeV U^{238}-ions was performed on the ATLAS accelerator (Argonne National Lab.). According to TRIM calculations these ions produce in Bi-2212 crystals continuous amorphous tracks with diameter $4-8$ nm and length $25-30$ μm. Below, we present the results for the samples irradiated with a density of CDs corresponding to a matching field $B_\Phi = 2$ T and for a reference pristine sample.

Our c-axis conductivity measurements were carried out in a cryostat with *two* superconducting magnets providing magnetic fields in orthogonal directions. The magnets are controlled independently and provide fields in orthogonal directions. The magnets are controlled independently and provide fields up to 8 T in one direction and up to 1.5 T in the other direction. Samples can be oriented along the axis of either magnet. Misalignment of the crystal c-axis with respect to the perpendicular component $B_\perp$ was detected by the asymmetry of $\rho_c(B_\parallel)$ with respect to the sign of $B_\parallel$. We adjusted the direction of the field components, providing asymmetry below 5% at $B_\parallel > 2$ T and below 10% at lower fields. The normalized conductivity $g(B_\parallel)$ was calculated using the average resistivity $\overline{\rho}_c(B_\parallel) = [\rho_c(B_\parallel) + \rho_c(-B_\parallel)]/2$. Two Silver contact pads were deposited on both sides of the sample using a mechanical shadow mask. The mask provided a clean surface rim $\sim$0.1 mm from the sample edges and 25 μm separation between current and potential pads. The area of the contact was $\sim$0.75 mm^2 for current and $\sim$0.05 mm^2 for potential terminals. The resistance of the current pads at room temperature was ~2 Ω. A current of 1 mA, driven through the sample, provides an ohmic I-V regime. For the very anisotropic Bi-2212, in our range of the magnetic fields and temperatures, in-plane conductivity, $\sigma_{ab} \sim 10^3\sigma_c$ [93],

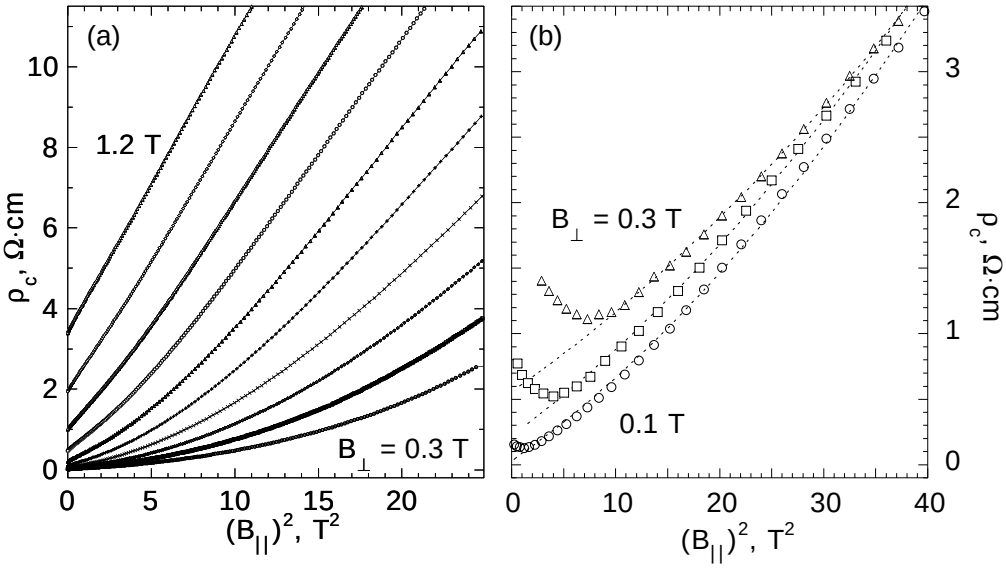

Figure 3.20: Dependence of resistivity ρ_c versus $B_\parallel^2$ for perpendicular components $B_\perp$, increasing sequentially with 0.1 Tesla steps in irradiated (a) and pristine (b) crystals.

provided nearly equipotential current distribution in the *ab*-plane, at least in the central area of the sample. Thus the contribution of σ_{ab} to the anisotropic conductivity is weak and can be neglected, in the limit of small pad separation. Thus a standard 4-probe method can be used for ρ_c measurements instead of the complicated multiterminal Montgomery analysis. The temperature was stabilized within an accuracy of ± 50 mK. The resistivity $\rho_c(B_\parallel)$ was measured in the $B_\perp$ interval where g at maximum $B_\parallel$ drops with $B_\parallel$ at least to the value 0.2.

In Figure 3.20 we present ρ_c as a function of $B_\parallel^2$ at different $B_\perp$ for (a) irradiated and (b) pristine crystals. For irradiated crystals at low $B_\parallel$ the resistance increases quadratically with $B_\parallel$ as prescribed in Equation (3.29). In contrast, for the pristine crystal we observed that ρ_c increases quadratically at high $B_\parallel$, but exhibits a minimum at low fields that is not described by Equation (3.29). This low field behavior is caused by dynamic screening of $B_\parallel$ that results in additional dissipation at low fields, due to the combined effects of motion of Josephson vor-

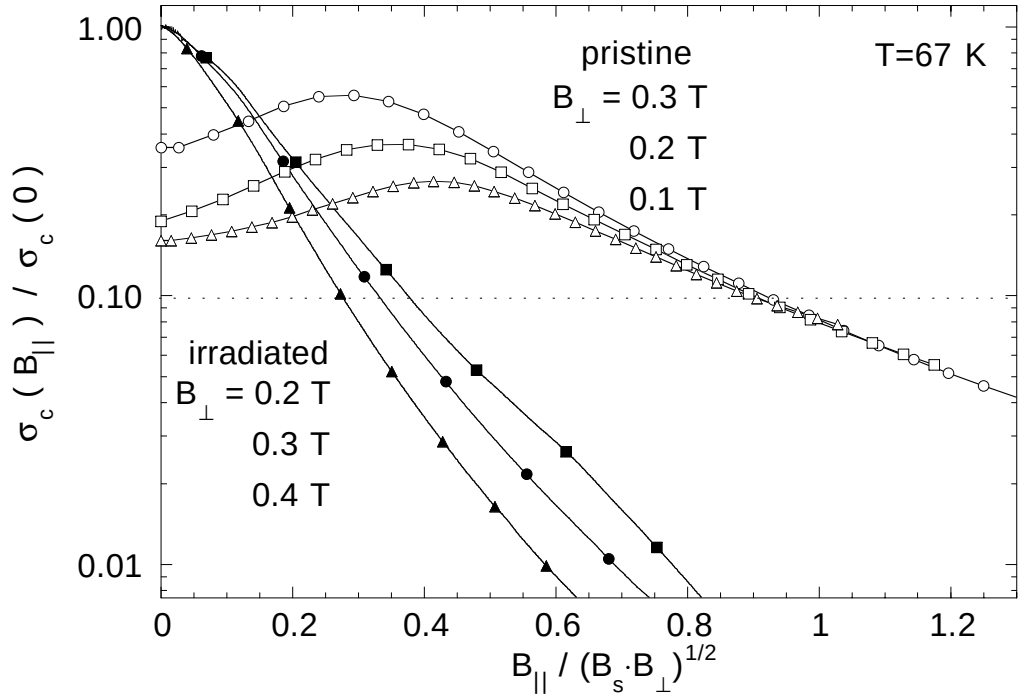

Figure 3.21: Dependence $g(B_\parallel) = \sigma_c[B_\parallel/(B_s B_\perp)^{1/2}]/\sigma_c(0)$ in irradiated and pristine crystals.

tices induced by $B_\parallel$ and of pancake vortices. These effects are not important at high fields. They do not appear in the irradiated crystal due to pinning of the Josephson vortices.

In Figure 3.21 we show the dependence $g = \sigma_c(b)/\sigma_c(0)$ at different $B_\perp$ on $b = B_\parallel/(B_s B_\perp)^{1/2}$ for irradiated and pristine samples at different $B_\perp$. Here $B_s = \Phi_o/2\pi s^2$. For the pristine crystal the values $\sigma_c(B_\perp)$ at $B_\parallel = 0$ were determined by extrapolation of $\rho_c(B_\parallel)$ from the high field quadratic dependence to zero as shown in Figure 3.20(b) by the dashed lines. Note that for the pristine crystal all three curves coincide at high fields, demonstrating scaling of the correlation length R with a. Such a scaling is not observed for the irradiated crystal at $B_\perp \leq 1.2$ T, because the average distance between CDs, $a_\Phi = (\Phi_o/B_\Phi)^{1/2}$, gives another length scale in addition to a. More importantly, we see that g drops with

$B_\parallel$ much faster for the irradiated sample. The correlation length $R(B_\perp)$ is related via $R \approx \Phi_o/\tilde{B}_\parallel s$ to the magnetic field $\tilde{B}_\parallel$ which characterizes the scale of the drop of σ_c with $B_\parallel$. Here $\tilde{B}_\parallel$ is the magnetic field at which flux in the area Rs is $\sim\Phi_o$. If we define the characteristic field $\tilde{B}_\parallel$ as given by $g(\tilde{B}_\parallel) = 0.1$, then from Figure 3.21 at $B_\perp = 0.2$ T, we estimate for the pristine crystal $R/a \approx 2.5$, while for the irradiated one $R/a \approx 8$. As one can see from Figure 3.21, at high $B_\parallel$ fields used in our measurements, the dependence $g(B_\parallel)$ is close to exponential, and we use this to extrapolate $g(B_\parallel)$ to higher fields. Then we determine $G(r)$ in the interval $r < r_m \approx 0.5$ μm by use of Equation (3.27). The accuracy of our experimental data and of the inverse Fourier-Bessel transformation is not sufficient to obtain $G(r)$ at $r > r_m$.

In Figure 3.22(a) we show the functions $G(r/a)$ and in Figure 3.22(b) the same data versus $x = r/R$, where the scaling length $R(B_\perp, B_\Phi)$ is defined by Equation (3.28). For the pristine crystal at $B_\perp = 0.1$ and 0.2 T we obtain $R(B_\perp) \approx a$. The curve for $B_\perp = 0.2$ T is plotted with a dashed line, and it practically coincides with $B_\perp = 0.1$ T. For the irradiated sample we show the curves corresponding to regions below, above, and at the position at the dip in the magnetoresistance curve, $\rho_c(B_\perp, 0)$ from Reference 89 as shown in the inset. It is evident from Figure 3.22(a) that the rate of decay of correlations with distance is not a monotonic function of $B_\perp$ but has a minimum at a value corresponding to the dip in $\rho_c(B_\perp)$. Notably, all these curves merge quite accurately in Figure 3.22(b), providing *a universal function* $G(x)$ for both pristine and irradiated samples with a single scaling length R, although the irradiated sample is characterized generally by two lengths a and a_Φ. In comparison with pristine crystals CDs simply diminish the effective concentration of pancakes acting on Josephson coupling by a factor a^2/R^2.

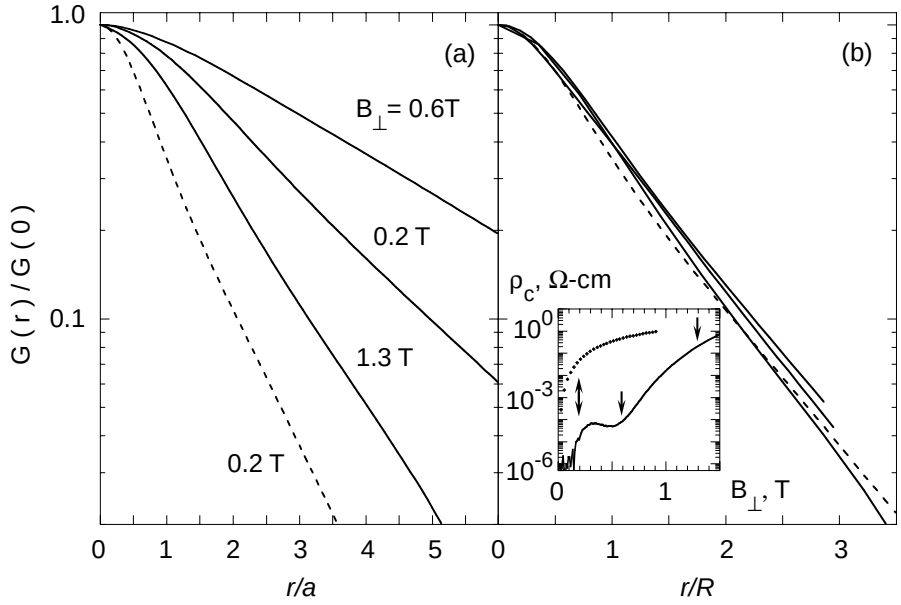

Figure 3.22: The functions $G(r/a)$ (a), and $G(r/R)$ (b) as extracted from $g(B_\parallel)$ for irradiated (solid) and for pristine (dashed) samples. Inset: $\rho_c(B_c)$ at $B_\parallel = 0$ from Reference 89. Arrows indicate $B_\perp$ values for the presented $G(r)$ curves.

The correlation length R as a function of $B_\perp$ is shown in Figure 3.23. It exhibits a distinct maximum, $R/a \approx 4$, at $f \approx 0.35$, again coinciding with the position of the dip in $\rho_c(B_\perp)$. At $f = 0.35$ the ratio of $R(B_\perp)$ for irradiated and pristine crystals is about 4 times.

The length R_1 obtained from the function $G(r)$ using Equation (3.28) is $\sim$2R for all studied values of $B_\perp$. The same length determined directly from the function $g(B_\parallel)$ for small $B_\parallel$ using Equation (3.29) is $\sim$3R. Thus we estimate the accuracy of extracting $G(r)$ to $\sim$30%.

In order to determine the c-axis correlations of pancakes and to explain scaling, we note that at small f pancakes are positioned mainly inside CDs and hence the drop in phase difference correlations is caused by interruptions in the pancake arrangement inside CDs. Namely, we suppose that the phase difference $\phi_{n,n+1}(\mathbf{r})$ is induced when a columnar defect in the layer n is occupied by a pancake, but

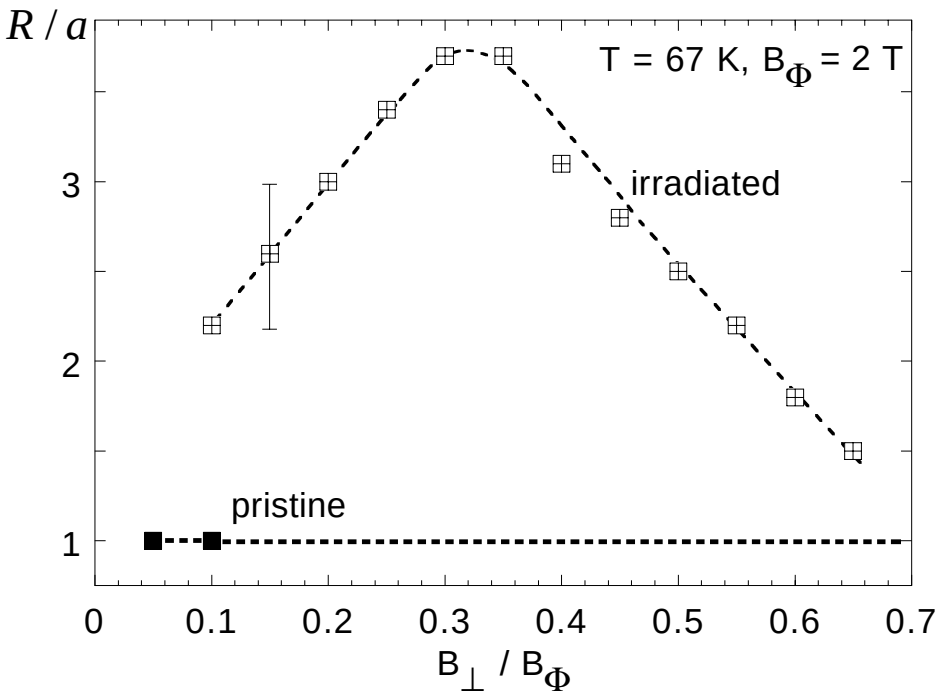

Figure 3.23: Dependence of the correlation length R as a function of filling factor, $f = B_\perp/B_\Phi$ of columnar defects for irradiated and pristine samples. Dashed lines are guides.

the site inside the same CD in the layer $n+1$ is empty (and vice versa). At larger f the unpinned pancakes also contribute to the decay of correlations. Scaling for both pristine and irradiated crystals means that ends of vortex segments inside CDs act on the phase difference correlations as unpinned pancakes. The net concentration of interruptions and unpinned pancakes is $1/R^2$, i.e., the average length of vortex segments is $L/s \approx R^2/a^2$. In the most aligned vortex liquid, at $f \approx 0.35$, we estimate $L/s \approx 15$. This is much larger than $L_o/s \approx 1/(1-f) \approx 1.5$ in the model of noninteracting pancakes positioned randomly on CDs. Thus we conclude that interaction of pancakes is important for enhanced alignment inside CDs.

In the hierarchy of interactions in the presence of CDs, both the pinning energy per pancake and the intralayer repulsion energy of pancakes are characterized by

the same energy scale E_o. The scale of magnetic pair attraction of pancakes in different layers is smaller by a factor s/λ_{ab}. The random distribution of CDs is important. Repulsion between vortices in the same layer leads to a significant increase of pancake energy inside CDs situated near those already occupied by pancakes [94]. As $B_\perp$ increases, some CDs become more favorable for filling by pancakes, while others remain unoccupied. Another important point is that favorable configurations are similar in all layers due to the geometry of the CDs. Thus repulsion of pancakes inside randomly positioned CDs in the same layer leads to enhancement of c-axis correlations. Another mechanism for pancake alignment inside CDs is magnetic attraction of pancakes in adjacent layers.

In conclusion, we extract the universal phase difference correlation function using c-axis resistivity measurements as a function of the parallel component of the magnetic field at fixed perpendicular component. We estimated the correlation length of the pancake density correlation function along the c-axis as a function of the filling factor f of columnar defects. It first increases with f, reaches a maximum at $f \approx 0.35$, and then drops as pancakes start to occupy positions outside the CDs. We argue that enhancement of the alignment of pancakes inside columnar defects is caused by the interaction of pancakes confined inside columnar defects.

CHAPTER 4

Josephson Plasma Resonance in High-T_c Superconductors

The c-axis JPR in highly anisotropic layered cuprate superconductors originates from the interlayer tunneling of Cooper pairs. Measurements of the JPR in these Josephson-coupled layered systems have received much interest in recent years because of its direct relation to the London penetration depth along the c-axis, λ_c. The JPR is thus a fundamental probe of the superconducting state and an excellent tool with which to study these highly anisotropic systems. The JPR in zero magnetic field is given by

$$\omega_{pc} = \frac{c}{\lambda_c \sqrt{\epsilon_\infty^c}} = \frac{c}{\gamma \lambda_{ab} \sqrt{\epsilon_\infty^c}} \tag{4.1}$$

Here ϵ_∞^c is the high frequency dielectric constant along the c-axis, and γ is the anisotropy parameter. For $T \ll T_c$, the temperature dependence of λ_c is related to the symmetry of the order parameter [21]. For T close to T_c, the appearance of the JPR probes the onset of interlayer phase coherence [20]. Furthermore, the JPR linewidth is a measure of the quasiparticle scattering rate, assuming no other broadening mechanisms. In addition, the JPR probes the tunneling mechanism and provides information about the validity of the interlayer tunneling model [19, 95]. In a magnetic field, the JPR probes the correlation of pancake vortices along the c-axis and is a tool with which to study the B-T phase diagram [87, 96]. The advantage of using THz-TDS to map the phase diagram is that this technique

allows measurements to be made over a broad frequency range at fixed magnetic field and temperature. The terahertz regime is very important because it overlaps both the JPR and the quasiparticle scattering rates of high-T_c superconductors with extreme anisotropy such as the bismuth-, thallium-, and mercury-based high-T_c superconductors.

Earlier JPR experiments included microwave cavity experiments on $Bi_2Sr_2CaCu_2O_8$ at a fixed frequency on the order of 30−90 GHz and made use of the fact that the microwave absorption resonance peak can be tuned by temperature and magnetic field [84, 87, 97]. Although these measurements demonstrated the existence of the JPR and are useful in probing the system over a narrow range of temperature and fields, the changing pancake vortex density in a swept field mode alters the system. Recently, Gaifullin *et al.* [22] overcame this shortcoming and probed the vortex system of underdoped $Bi_2Sr_2CaCu_2O_8$ in a waveguide by sweeping the frequency continuously from 20 to 150 GHz at constant magnetic field and temperature. However, in order to measure the JPR of less anisotropic high-T_c superconductors such as the thallium, and mercury compounds, one needs optical techniques. Tsvetkov *et al.* [19] used a grazing incidence reflectivity technique and measured the JPR in $Tl_2Ba_2CuO_6$ and $Tl_2Ba_2CaCu_2O_8$ thin films to be ∼840 GHz and ∼780 GHz, respectively, for $T \ll T_c$ in zero field.

4.1 Theory of the Josephson Plasma Resonance

The model for a highly anisotropic high-T_c superconductor with a layered structure, as discussed in Chapter 3.3, is a stack of superconducting sheets weakly coupled by the Josephson effect (see Figure 4.1). The order parameters are suppressed between the layers, and the Cooper pairs have to tunnel through the insulating barriers to make up the interlayer Josephson current. The Josephson

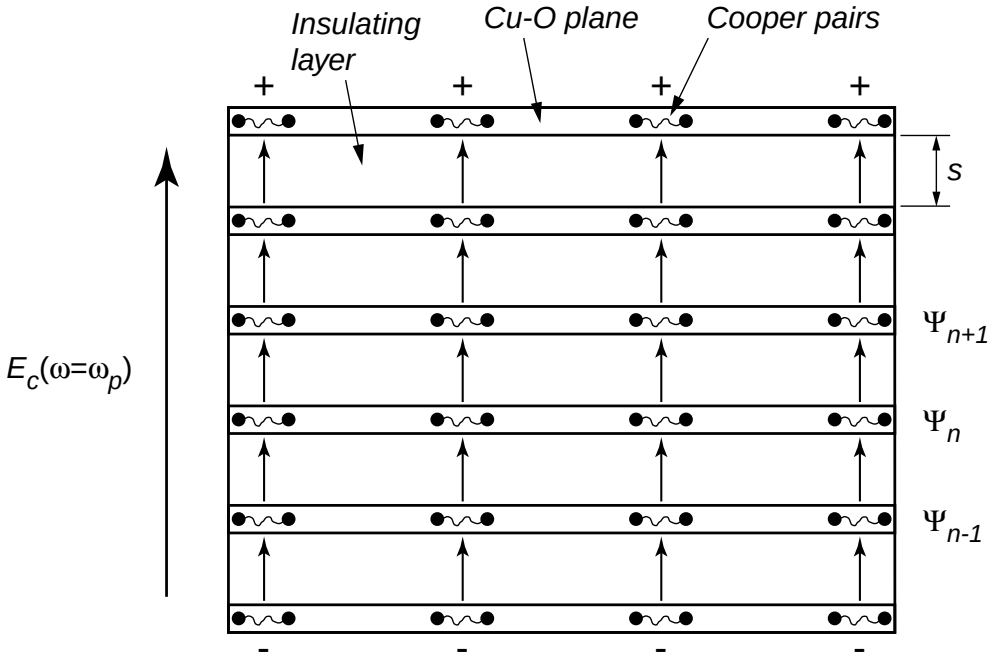

Figure 4.1: Structure of highly anisotropic High-T_c superconductor with Josephson coupled CuO_2 layers and interstitial insulating layers.

current between two adjacent layers is determined by the Josephson current in a single junction

$$J = J_o \sin(\varphi_{n+1} - \varphi_n), \tag{4.2}$$

where $\varphi_{n,n+1} = \varphi_{n+1} - \varphi_n$ is the phase difference between the order parameters $\Psi_{n+1}(\mathbf{r}) = |\Psi_{n+1}(\mathbf{r})|e^{i\varphi_{n+1}(\mathbf{r})}$ and $\Psi_n(\mathbf{r})$ in layer $n+1$ and n, respectively, and $\mathbf{r} = (x, y)$ is the in-plane coordinate.

The electrodynamics in a single junction is described by the sine-Gordon equation [98] for the gauge-invariant phase difference $\varphi(\mathbf{r}, t)$

$$\frac{1}{c_o^2}\frac{\partial^2\varphi}{\partial t^2} - \nabla^2\varphi + \frac{1}{\lambda_J^2}\sin\varphi = 0 \tag{4.3}$$

which, if the phase is spatially independent, reduces to

$$\frac{d^2\varphi}{dt^2} + \omega_J^2 \sin\varphi = 0, \tag{4.4}$$

where

$$\omega_J^2 = \frac{2e}{\hbar C} J_o = \frac{c_o^2}{\lambda_J^2}. \tag{4.5}$$

Here, $c_o = cs/\lambda_{ab}$ is the Swihart velocity, λ_J is the Josephson penetration length, and C is the junction capacitance per unit area, $C = \epsilon_r/4\pi s$, where s is the barrier thickness. The plasma oscillations come from a pulsating interchange of energy between the coupling energy $\frac{J_o \Phi_o}{2\pi}(1 - \cos\varphi_{n,n+1})$ and the charging energy $\frac{(2en)^2}{2C}$. Josephson [99] considered the small-amplitude oscillations of $\varphi(\mathbf{r}, t)$ in the sine-Gordon equation and obtained the dispersion relation

$$\omega^2(\mathbf{k}) = \omega_J^2 + c_o^2 \mathbf{k}^2. \tag{4.6}$$

This Josephson plasmon was observed first (1968) by Dahm *et al.* [100] as a resonance in a Josephson tunneling junction with dimensions of a point junction (i.e. $\mathbf{k} = 0$).

The Josephson plasmon in a layered superconductor is similarly a charge oscillation between the Josephson coupled layers. It is excited by an ac electric field perpendicular to the layers, and is provided by the oscillation of tunneling interlayer Josephson currents in a phase collective mode. The JPR frequency is determined by this interlayer Josephson current.

The time dependent equation for the phase difference $\varphi_{n,n+1}(\mathbf{r}, t)$ for a multi-layered system describing the c-axis Josephson plasma resonance in the presence of an external electric field [75] is given by

$$\frac{1}{c_o^2}\frac{\partial^2}{\partial t^2}\varphi_{n,n+1} - \sum_m L_{nm}\nabla^2\varphi_{m+1,m} + \frac{1}{\lambda_J^2}\sin\varphi_{n,n+1} = \frac{\hbar}{8\pi e E_J}\frac{\partial D_z}{\partial t}. \tag{4.7}$$

Here, $\lambda_J = \gamma s$ is the Josephson length, D_z is the external electric field applied along the c-axis, $E_J = E_o/\lambda_J^2$ is the Josephson energy per unit area, and $E_o = s\Phi_o^2/16\pi^3\lambda_{ab}^2$ is the characteristic pancake energy. s is the interlayer spacing.

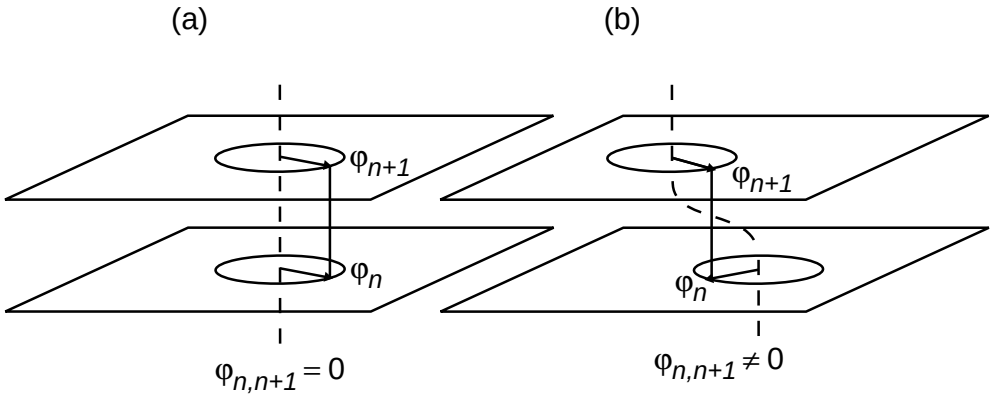

Figure 4.2: Phase difference induced by pancake vortices in neighboring layers. (a) Pancake vortices perfectly aligned induces no phase difference. (b) Misaligned pancake vortices contributes a phase difference.

$L_{nm} \approx (\lambda_{ab}/2s)exp(-|n-m|s/\lambda_{ab})$ is the mutual inductance between the layers nm.

In the presence of a magnetic field, which introduces pancake vortices in the layers, $\varphi_{n,n+1}(\mathbf{r},t) = \varphi^o_{n,n+1}(\mathbf{r},t) + \varphi'_{n,n+1}(\mathbf{r},t)$. $\varphi'_{n,n+1}(\mathbf{r},t)$ is the phase difference due to the external electric field which drives the Josephson plasma resonance, and $\varphi^o_{n,n+1}(\mathbf{r},t)$ is an additional contributing phase difference due to the misalignment of pancake vortices between adjacent layers. This last contribution is most easily seen by considering Figure 4.2. The phase changes by 2π when going around a given pancake vortex one time, and the angle is then represented by the polar angle in the plane. If two pancake vortices in adjacent layers are aligned as in Figure 4.2(a) the phase difference is zero. However, if they are misaligned as in Figure 4.2(b) there will be a phase difference contribution. The Josephson current is then $J = J_o\langle\sin(\varphi^o_{n,n+1} + \varphi'_{n,n+1})\rangle$, where the average is over the entire plane (The intervortex distance $a_o = (\Phi_o/B_z)^{1/2} \ll \lambda_J$). Thus, assuming the pancake vortices move slowly (i.e. $\omega_\nu \ll \omega_{pc}$) and $\varphi'_{n,n+1} \ll \varphi^o_{n,n+1}$,

$$J = J_o\langle\sin(\varphi^o_{n,n+1} + \varphi'_{n,n+1})\rangle \approx J_o\langle\cos(\varphi^o_{n,n+1})\rangle\varphi'_{n,n+1}. \tag{4.8}$$

Therefore $J_o \to J_o\langle\cos(\varphi^o_{n,n+1})\rangle$ and $\omega_p^2 \propto J_o\langle\cos(\varphi^o_{n,n+1})\rangle$ depends on the alignment of pancake vortices along the c-axis. This method is nondestructive because the Josephson current does not affect the vortex structure in the liquid phase. Equation (4.7) can then be put in the form of a Schrödinger equation for the small oscillations of the phase difference $\varphi'_{n,n+1}(\mathbf{r},\omega)$ induced by an external ac electric field along the c-axis with amplitude D_z

$$\left[\frac{\omega^2}{\omega_o^2} + \lambda_J^2\hat{L}\nabla^2 - \cos\varphi^o_{n,n+1}(\mathbf{r},0)\right]\varphi'_{n,n+1} = -\frac{\hbar i\omega D_z}{8\pi e E_J}. \tag{4.9}$$

This simplified equation essentially captures the physics of the JPR. Here,

$$\omega_o(T) = \frac{c}{\lambda_c(T)\sqrt{\epsilon^c_\infty}} = \frac{c}{\gamma\lambda_{ab}(T)\sqrt{\epsilon^c_\infty}} \tag{4.10}$$

is the zero field Josephson plasma resonance frequency. The inductive matrix $\hat{L}$ is defined as $\hat{L}A_n = \sum_m L_{nm}A_m$. Equation (4.9) assumes the time variations of the pancake vortices to be small during the time $1/\omega$, and neglects charging effects [101] and quasiparticle dissipation. The Josephson plasma resonance depending on both c-axis magnetic field and temperature is given by

$$\omega_{pc}^2(B_z,T) = \omega_o^2(T)\langle\cos(\varphi^o_{n,n+1}(\mathbf{r},B_z))\rangle, \tag{4.11}$$

or

$$\omega_{pc}^2(B_z,T) = \frac{8\pi^2 cs}{\epsilon^c_\infty\Phi_o}J_m(B_z,T), \tag{4.12}$$

where the maximum interlayer Josephson current is given by

$$J_m(B_z,T) = J_o\langle\cos(\varphi^o_{n,n+1}(\mathbf{r},B_z))\rangle. \tag{4.13}$$

$\langle\cdots\rangle$ denotes averages over thermal and disorder displacement of pancake vortices in adjacent layers, and J_o characterizes the strength of the interlayer Josephson coupling at $B_z = 0$,

$$J_o(T) = \frac{c\Phi_o}{8\pi^2 s\lambda_{ab}^2(T)\gamma^2(T)}. \tag{4.14}$$

4.1.1 Temperature and C-axis Magnetic Field dependence of the Josephson Plasma Resonance

The JPR $\omega_{pc}(T) = \frac{c}{\lambda_c(T)\sqrt{\epsilon_\infty^c}} = \frac{c}{\gamma\lambda_{ab}(T)\sqrt{\epsilon_\infty^c}}$ depends strongly on temperature because it depends on the concentration of superconducting electrons. It provides a very direct measurement of the c-axis superfluid density n_c via $\omega_{pc}^2 = \frac{4\pi n_c e^2}{\epsilon_\infty^c m_c^*}$, where m_c^* is the effective electron mass along the c-axis. For Bi-2212 with a high degree of anisotropy, $\gamma \sim 500$, the plasma frequency lies in the range of $\sim$150$-$200 GHz at low temperatures, and decreases then with increasing temperature to about 20 GHz just below T_c. For the thallium compounds which are less anisotropic, $\gamma \sim 150$, the JPR frequency lies in the range 150 GHz to 800 GHz. For the YBCO compounds with a low degree of anisotropy, $\gamma \sim 10$, the JPR frequency lies in the range of $\sim$7 THz at low temperatures. For comparison, the plasma frequency in a usual isotropic metal is on the order of $\sim 10^{15}$ Hz. The temperature dependence of the JPR in zero field is illustrated in Figure 4.5(a).

(A) The Josephson Plasma Resonance as a Probe to study the Symmetry of the Superconducting Order Parameter

The JPR is directly related to the c-axis penetration depth $\lambda_c(T)$ which provides information about the symmetry of the superconducting order parameter. In the BCS theory the temperature dependent normal carrier fraction $x_n(T)$ is exponentially activated, whereas d-wave pairing predicts $x_n(T)$ to follow a power law [102] of the form

$$x_n(T) \propto \left(\frac{T}{T_c}\right)^{\alpha}. \tag{4.15}$$

For the in-plane penetration depth component $\lambda_{ab}(T)$, $\alpha = 1$ for d-wave pairing in a high-T_c superconductor, at least at low temperatures [103], and $\alpha = 2$

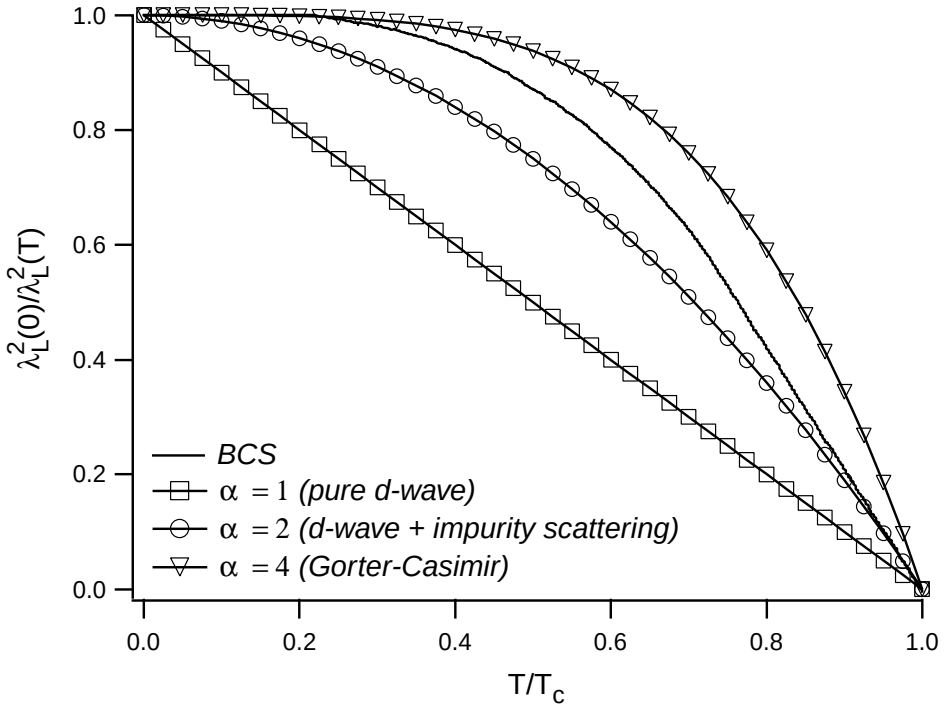

Figure 4.3: Normalized London penetration depth $\lambda_L^2(0)/\lambda_L^2(T)$ versus reduced temperature T/T_c. The values of α corresponds to the in-plane penetration depth component $\lambda_{ab}(T)$.

for d-wave pairing with strong impurity scattering [104]. Because $\lambda_L(T)$ and the superconducting fraction $x_s(T)$ are related through $x_s = 1 - x_n = [\lambda_L(0)/\lambda_L(T)]^2$ [105], d-wave theories predict that

$$\frac{\lambda_{ab}^2(0)}{\lambda_{ab}^2(T)} = 1 - \left(\frac{T}{T_c}\right)^{\alpha}. \tag{4.16}$$

Figure 4.3 shows the theoretical curves for $\lambda_L^2(0)/\lambda_L^2(T)$ as a function of reduced temperature T/T_c for d-wave pairing following the power law behavior in Equation (4.16) for $\lambda_{ab}(T)$. Also plotted is the s-wave curve for the BCS theory, and the curve for the classical Gorter-Casimir two-fluid model ($\alpha = 4$ in Equation (4.16)) [106].

The temperature dependence of the out-of-plane penetration depth component $\lambda_c(T)$ is complicated by the Josephson interaction between the layers, and

depends strongly on doping, anisotropy and electronic structure. A much weaker temperature dependence of $\lambda_c(T)$, as compared to $\lambda_{ab}(T)$, has been observed in a number of materials, e.g. Y-123 [107], Hg-1201, Hg-1223 [108], and La-214 [109]. It has been suggested that this weaker temperature dependence is a consequence of the in-plane anisotropy of the c-axis hopping integral $t_\perp \propto (\cos k_x - \cos k_y)^2$ where the zeros of $t_\perp$ coincides with the node directions of $d_{x^2-y^2}$ symmetry [21]. This in-plane momentum dependence of $t_\perp$ originates from the wave function overlap between the Cu $4s$ orbital and the O $2p$ orbital and is a common feature of high-T_c superconductors without Cu-O chain bands. This coherent tunneling mechanism where parallel momentum is conserved between the layers leads to a T^5 dependence at low temperatures [21]. The T^5 contribution is small and has been observed in clean tetragonal samples of relatively low anisotropy compounds, e.g. Hg-1201 [108] (although, it has also been observed in Bi-2212 [110]), where the coherent hopping of holes is the main contribution to the superfluid response. However, the incoherent conduction process with anisotropic impurity scattering (impurity assisted hopping) is expected to vary as T^2 at low temperatures [21, 111]. This is because the anisotropic impurity scattering enhances the contribution of the node directions, which in turn enhances the temperature dependence. When disorder effects are important in the c-axis superfluid response, the T^5 behavior of $\lambda_c(T)$ will be completely masked by the T^2 behavior. The temperature dependence of $\lambda_c(T)$ can be expressed as

$$\frac{\omega_{pc}^2(T)}{\omega_{pc}^2(0)} = \frac{\lambda_c^2(0)}{\lambda_c^2(T)} = 1 - A\left(\frac{T}{T_c}\right)^\alpha . \tag{4.17}$$

Here α determines the temperature dependence and the parameter A depends strongly on the ratio of T_c and Δ_o [108].

(B) Dissipation and Dispersion Effects of the Josephson Plasma Resonance

The intrinsic JPR linewidth $\Delta\omega_{pc}$ is due to interlayer tunneling of quasiparticles, and thus provides a direct measurement of the c-axis quasiparticle conductivity σ^c_{qp}. The quasiparticle dissipation is determined by the imaginary part of the dielectric function, $I(\omega) \propto Im[1/\epsilon_c(\omega)]$. When $\hbar\omega \ll \Delta$, the dielectric function can be expressed as

$$\epsilon_c(\omega) = \epsilon^c_\infty \left[1 - \frac{\omega^2_{pc}}{\omega(\omega + i0^+)} - \frac{\omega^2_{qp}}{\omega(\omega + i/\tau)}\right]. \tag{4.18}$$

ω_{qp} is the plasma frequency of the quasiparticles given by

$$\omega^2_{qp} = \frac{4\pi n_{qp} e^2}{\epsilon^c_\infty m^*_c}, \tag{4.19}$$

and τ is the quasiparticle scattering time. When $\omega\tau \ll 1$, $I(\omega, T)$ can be written as

$$I(\omega, T) \propto \frac{\frac{4\pi\sigma_{qp}(T)}{\epsilon^c_\infty}}{\left[1 - \frac{\omega^2_{pc}}{\omega^2}\right]^2 + \left[\frac{4\pi\sigma_{qp}(T)}{\epsilon^c_\infty \omega}\right]^2}, \tag{4.20}$$

where the quasiparticle conductivity [112, 113] is given by

$$\sigma^c_{qp} = \frac{\epsilon^c_\infty \omega^2_{pc} e^2 \tau}{4\pi}. \tag{4.21}$$

The JPR occurs at $\omega = \omega_{pc}$, and the linewidth is given by

$$\Delta\omega_{pc} = \frac{4\pi\sigma_{qp}}{\epsilon^c_\infty}. \tag{4.22}$$

When applying a magnetic field along the c-axis two additional mechanisms contribute to the linewidth, namely, inhomogeneous Josephson interaction in the presence of randomly positioned vortices (inhomogeneous broadening), and dissipation of the plasma mode into vortex oscillations [114]. In magnetic fields

below ∼7 T in Bi-2212 the linewidth was found to be determined mainly by inhomogeneous broadening, whereas in higher fields or lower pinning, dissipation of the plasma mode into vortex oscillations may become the dominant mechanism of line broadening [114].

It has been established, both experimentally [115] and theoretically [116], that there exists two Josephson plasma modes with very different dispersion relations. The longitudinal mode ($\mathbf{k}\|c$) displays a sharp resonance, and is excited by an oscillating electric field ($E\|c$), whereas the transverse mode ($\mathbf{k}\perp c$) has been found to display multipeaks, and is excited by an oscillating magnetic field ($H\|ab$) [115]. The dispersion relation for the longitudinal Josephson plasma propagating along the c-axis in the case of $\sigma_{qp}^{c} = 0$ [101] can be expressed as

$$\omega_{pc}^{L}(k_z) \simeq \omega_{pc}\sqrt{1 + \epsilon_{\infty}^{c}\mu^2\left[\frac{(s+D)^2}{sD}\right]k_z^2}. \tag{4.23}$$

μ is an effective charge screening length (Debye length) along the c-axis due to the superconducting carriers and quasiparticles ($\mu \ll \lambda_L$). s and D are the widths of the superconducting and insulating layers, respectively. Typical values for a high-T_c cuprate are $\mu \sim 2$ Å, $s \sim 6$ Å, and $\epsilon_{\infty}^{c} \sim 25$. Thus the dispersion of the longitudinal plasma is very weak, compared to the transverse one propagating along the layers, $\omega_{pc}^{T}(\mathbf{k}) \simeq \omega_{pc}\sqrt{1 + (\lambda_c\mathbf{k})^2}$, which shows a strong dispersion, and eventually tends to a linear dependence for $k \to \infty$ [116].

(C) The Josephson Plasma Resonance as a Probe to study the Vortex Structure

A magnetic field applied parallel to the c-axis introduces misaligned pancake vortices in the layers which suppresses the critical current density and the JPR as described in the previous section. The JPR, $\omega_{pc}^2(B_z, T) = \omega_o^2(T)\langle\cos(\varphi_{n,n+1}^{o}(\mathbf{r}, B))\rangle$,

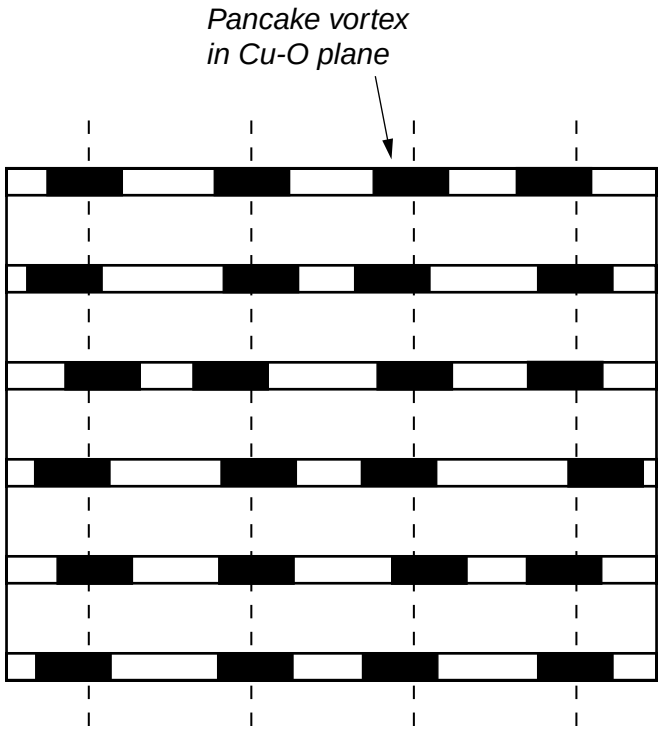

Figure 4.4: Magnetic and Josephson interactions between pancake vortices in adjacent layers strive to align the pancake vortices along straight lines, while thermal fluctuations and pinning effects cause misalignment.

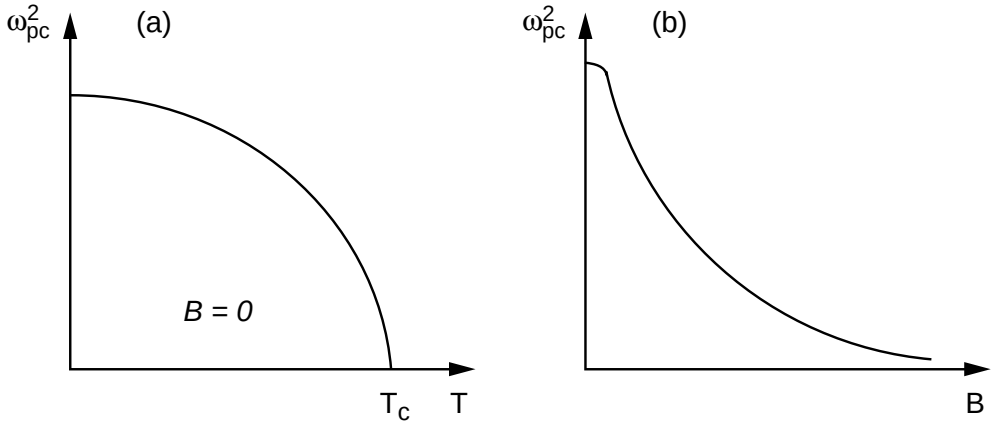

Figure 4.5: (a) JPR versus temperature in zero field. (b) JPR versus c-axis applied field at constant temperature in the liquid phase.

depends strongly on temperature because $J_o(T)$ drops with temperature ($\omega_o^2(T) \propto J_o(T)$). $\langle\cos(\varphi^o_{n,n+1}(\mathbf{r}, B))\rangle$, which describes the local thermal and disorder average of the cosine of the gauge-invariant phase difference between adjacent layers n and $n+1$, depends both on temperature and magnetic field. When the pancake vortices form straight lines perpendicular to the layers, $\langle\cos(\varphi^o_{n,n+1}(\mathbf{r}, B))\rangle$ is unity. However, when the pancake vortices are misaligned along the c-axis caused by either thermal fluctuations or pinning effects (see Figure 4.4), a nonzero phase difference is introduced which suppresses the interlayer Josephson coupling, and results in the reduction of $\langle\cos(\varphi^o_{n,n+1}(\mathbf{r}, B))\rangle$ from unity. Thus, the JPR is sensitive to the correlations of pancake vortices along the c-axis, and is an excellent tool with which to study the various vortex phases and phase transitions of the B-T vortex phase diagram. The magnetic field dependence of the JPR is illustrated in Figure 4.5(b). The stronger the field, the smaller is $\langle\cos(\varphi^o_{n,n+1}(\mathbf{r}, B))\rangle$, and the JPR frequency decreases approximately as $\omega_{pc}^2 \propto 1/B$ in the pancake liquid phase of Bi-2212 [117].

The majority of JPR measurements have been performed in microwave cavities at a fixed frequency (i.e. 45 GHz). The drawback of the microwave cavity technique is that the temperature and magnetic field have to be tuned to bring the Josephson plasma resonance into the resonant frequency of the cavity. This changes the phase of the vortex system, and makes it difficult to follow the continuous development of the vortex phase correlations.

These problems are illustrated in Figure 4.6, where the JPR is measured in a microwave cavity at a fixed frequency of 45 GHz in a $Bi_2Sr_2CaCu_2O_{8+\delta}$ single crystal [118]. The JPR is shown as a function of c-axis field for decreasing temperatures. Notice the resonance is shifting to higher fields from 83.0 K to 32.9 K. This is normal behavior because the disorder decreases by lowering the

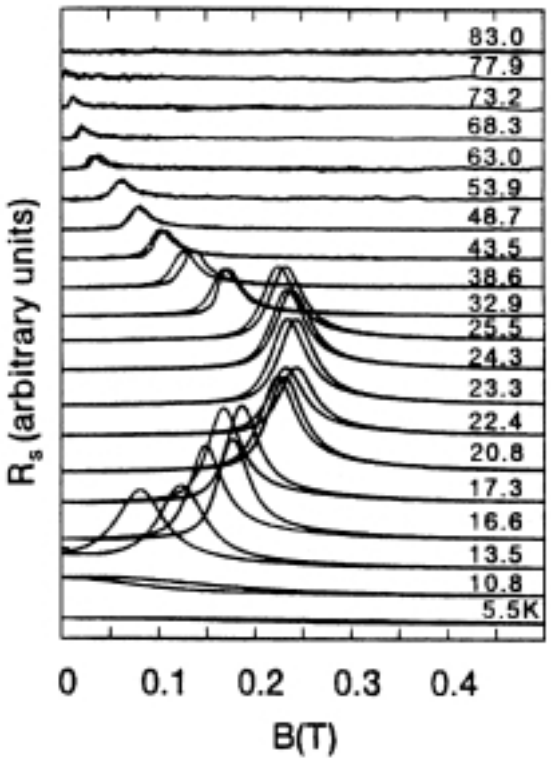

Figure 4.6: JPR measurements in a microwave cavity. Surface resistance R_s of $Bi_2Sr_2CaCu_2O_{8+\delta}$ single crystal at 45 GHz as a function of field ($B||c$) at different temperatures. R_s is measured with E_{ac} parallel to the c-axis. (© Copyright (1995) by The American Physical Society. Figure 3 in Reference 2).

temperature in the liquid state, and a bigger field is then needed to reduce the JPR into the resonant frequency of the cavity. However, below 25.5 K the system goes from the liquid phase into the vortex phase, and pinning sets in. A vortex density gradient then develops across the sample from ramping up the field in zero field cooled mode. This induces additional disorder, and the disorder only increases when further lowering the temperature because the pinning gets stronger, causing the JPR to shift to lower frequencies from 25.5 K to 5.5 K. This artifact is caused by the fact that the field was being swept.

4.2 C-axis Josephson Plasma Resonance Observed in Transmission in $Tl_2Ba_2CaCu_2O_8$ by use of Terahertz Time-Domain Spectroscopy

This section presents experimental data on the JPR in $Tl_2Ba_2CaCu_2O_8$ (Tl-2212) as a function of temperature in zero magnetic field, in both the time-domain and the frequency-domain. These are the first observations of the JPR in a high-T_c superconducting material in transmission. Measuring the JPR in transmission improves the SNR allowing measurements of the JPR and its linewidth closer to T_c than previous measurements performed in reflection using a grazing incidence reflectivity technique [19].

The experiments were performed using THz-TDS in transmission, with a bandwidth covering approximately 0.2−2.5 THz. A commercial-based regeneratively amplified Ti:AlO_2O_3 operating at 1 KHz provided nominally 1.0 mJ, ∼100 fs pulses for the experiment. The detailed experimental set-up is shown in Figure 4.7. Approximately 10% of the incoming beam is split off at the beam splitter and used for the electro-optic detection. The principle of operation of the THz-TDS spectrometer is explained in Chapter 2.1 (see Figure 2.1 and Figure 2.6). The beamspot at the sample position was roughly 3 mm in diameter. Tl-2212 has the same crystal structure as Bi-2212 shown in Figure 3.10 where Bi and Sr are exchanged with Tl and Ba, respectively [119]. The Tl-2212 film (700 nm) was grown on a 10 × 10 mm^2 MgO substrate in a two-step process. First an amorphous TBCCO film is deposited by laser ablation. Next it was annealed at high temperature in oxygen to form the 2212 phase. The film exhibited a sharp transition (0.2−K width) at a temperature of 103.4 K.

In order to excite the c-axis JPR a component of the electric field (E-field) of

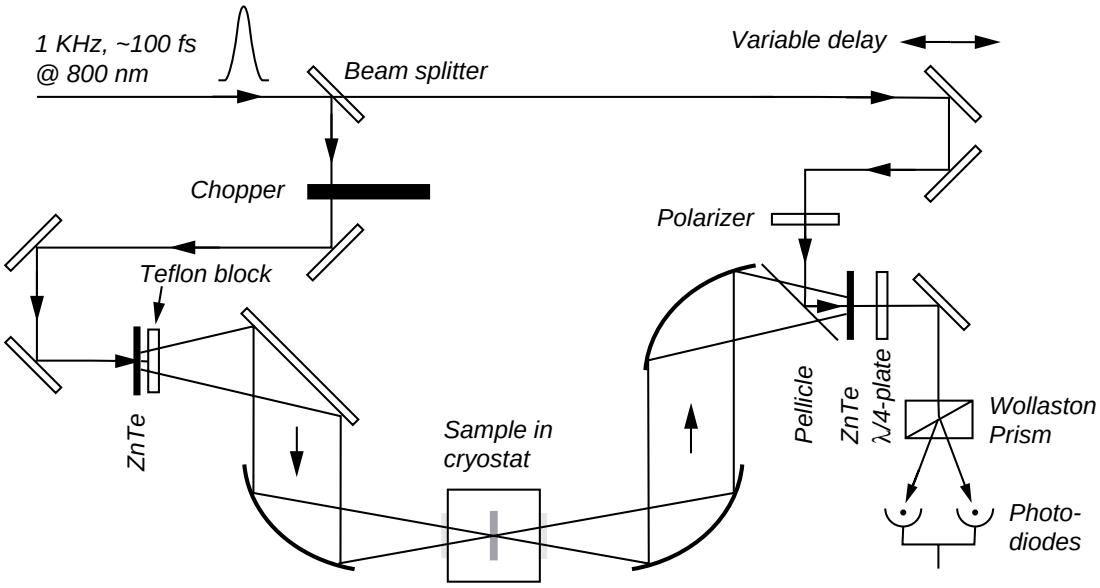

Figure 4.7: Experimental set-up of THz-TDS spectrometer. The sample is positioned in a cryostat with optical access.

the terahertz pulse has to be along the c-axis of the sample. The plasma frequency along the ab-plane is close to the metallic regime $\sim$1.5 eV, whereas the JPR along the c-axis lies in the terahertz range. Therefore, by tilting the sample at an angle incident p-polarized THz radiation will be transmitted at the JPR when there is an E-field component parallel to the c-axis and completely reflected when the E-field is parallel to the ab-plane. However, as will be discussed in Section 4.3, the angular dependence of the JPR does not entirely conform to this picture, and the JPR is also observed at smaller incident angles. The anisotropic dielectric function can be written as

$$\epsilon_{ab}(\omega) = \epsilon_{\infty}^{ab}\left(1 - \frac{\omega_{pab}^2}{\omega^2}\right), \qquad \epsilon_c(\omega) = \epsilon_{\infty}^{c}\left(1 - \frac{\omega_{pc}^2}{\omega^2} + \frac{4\pi i\sigma_c}{\epsilon_{\infty}^{c}\omega}\right). \tag{4.24}$$

Here ω_{pab} and ω_{pc} are the in-plane and out-of-plane plasma frequencies, respectively. Assuming $\omega \ll \omega_{pab}$, and not taking into account dissipation and c-axis dispersion effects [101, 120], we find that electromagnetic waves can only propa-

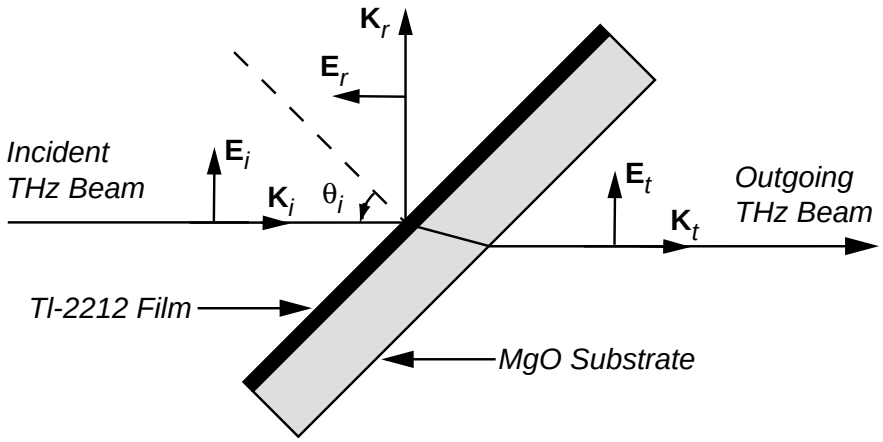

Figure 4.8: Configuration of the thin film plus substrate with respect to the terahertz beam. P-polarized THz radiation is transmitted through the sample.

gate in a narrow window above the plasma edge,

$$\omega_{pc} < \omega < \frac{\omega_{pc}}{\sqrt{1 - \frac{\sin^2\theta}{\epsilon_\infty^c}}} \approx \omega_{pc}\left(1 + \frac{\sin^2\theta}{2\epsilon_\infty^c}\right). \tag{4.25}$$

(See Appendix (A.2)). It is a well-known fact that the electromagnetic wave in an anisotropic media does not have a purely transverse character, but also has a longitudinal component, unless it travels along the principal axes.

The configuration of the sample with respect to the terahertz beam is shown in Figure 4.8. P-polarized THz radiation, incident at an angle of 45° to the surface normal, is transmitted through the sample. In order to minimize the effect of the substrate, two sets of averaged scans are performed at each temperature. The first set on the sample (film plus substrate), and the other set on a bare reference substrate. The FFT of the sample is then divided by the FFT of the reference. This ratio gives the complex transmission coefficient of the film as a function of frequency.

Figure 4.9(a)-(d) shows the electric field amplitude of the terahertz pulse in the time-domain transmitted through the sample at different temperatures.

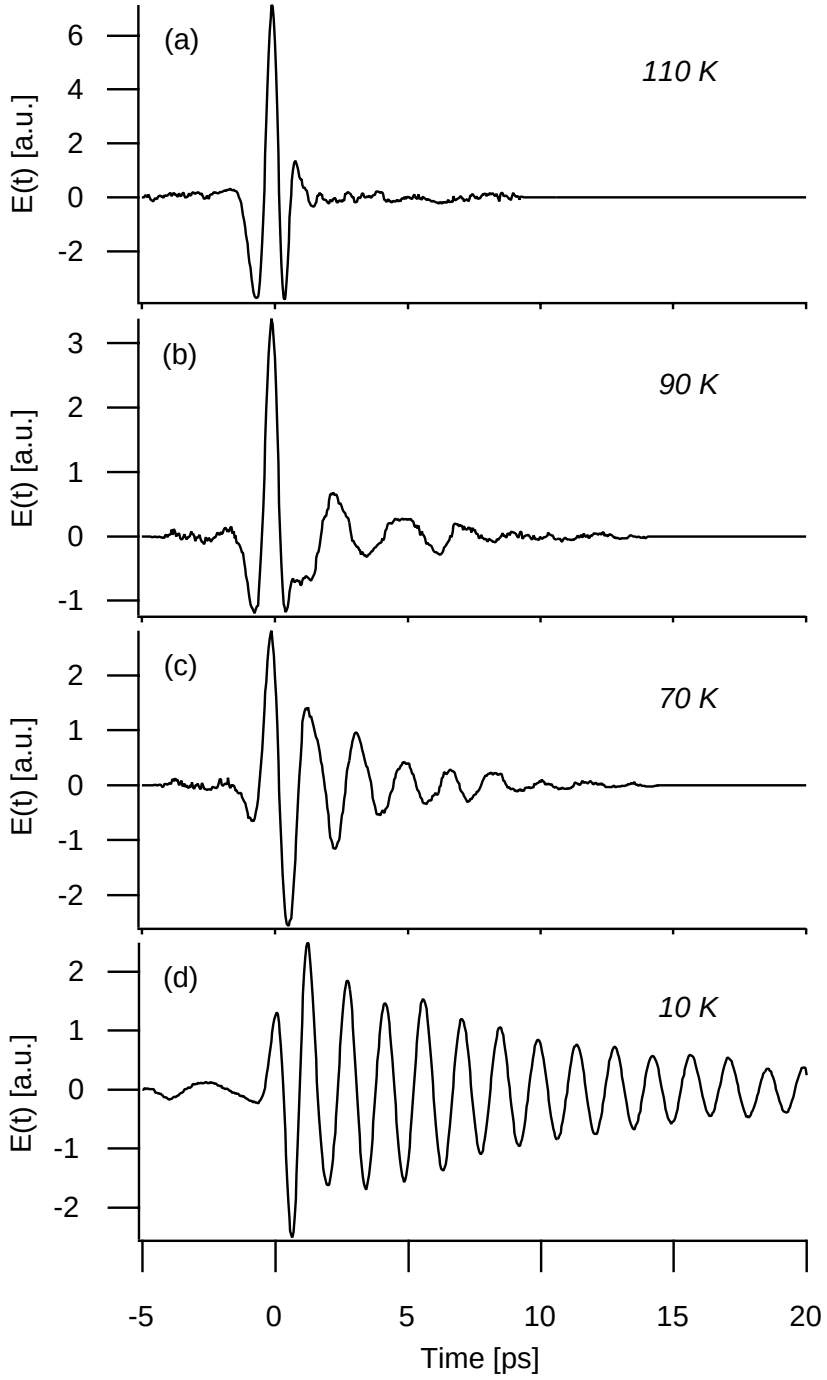

Figure 4.9: Electric field of the THz pulse in the time-domain transmitted through Tl-2212 film on MgO at (a) 110 K, (b) 90 K, (c) 70 K, and (d) 10 K, showing the development of the JPR with decreasing temperature.

Figure 4.9(a) shows the terahertz pulse transmitted through the sample at 110 K, above the onset of superconductivity. At 90 K, Figure 4.9(b), the onset of c-axis coherent tunneling is just perceptible as a slight oscillation following the main pulse. This damped ringing appears as a broad JPR peak in the frequency-domain (see Figure 4.10), where the damping is due to quasiparticle scattering. When the temperature is lowered to 70 K, Figure 4.9(c), the terahertz pulse displays an even stronger oscillation amplitude due to a reduction in scattering. This results in a narrowing of the JPR peak (see Figure 4.10). The terahertz pulse at 10 K, Figure 4.9(d), displays a pronounced ringing that lasts for at least 20 ps following the main pulse. These traces reveal how the oscillation frequency increases as the temperature is lowered, resulting in a shifting of the JPR to higher frequencies.

Figure 4.10 shows the transmission amplitude as a function of frequency for the Tl-2212 thin film for different temperatures. The figure clearly illustrates the temperature dependence of the JPR, which appears as a sharp peak at $\sim$705 GHz to 680 GHz for low temperatures (10$-$40 K) and decreases with temperature to $\sim$170 GHz at 98 K. The JPR vanishes close to 99 K which is $\sim$4 K below T_c (see Figure 4.10). The linewidth of the JPR peak increases with temperature, which indicates an increase in the quasiparticle scattering rate. The appearance of the JPR as a peak at the resonance in the transmission spectrum agrees with the electromagnetic analysis, in which propagation of the electromagnetic wave occurs only in a narrow window above the plasma edge. The decrease in the JPR frequency with temperature is consistent with a decreasing superconducting electron density on approaching T_c from below. Terminating the temporal scans of the THz pulses at 20 ps eliminates the effect of the first Fabry-Perot reflection that is due to the 1 mm MgO substrate. This truncation might cause a slight additional broadening of the JPR peaks in Figure 4.10 in the temperature range 10$-$40 K.

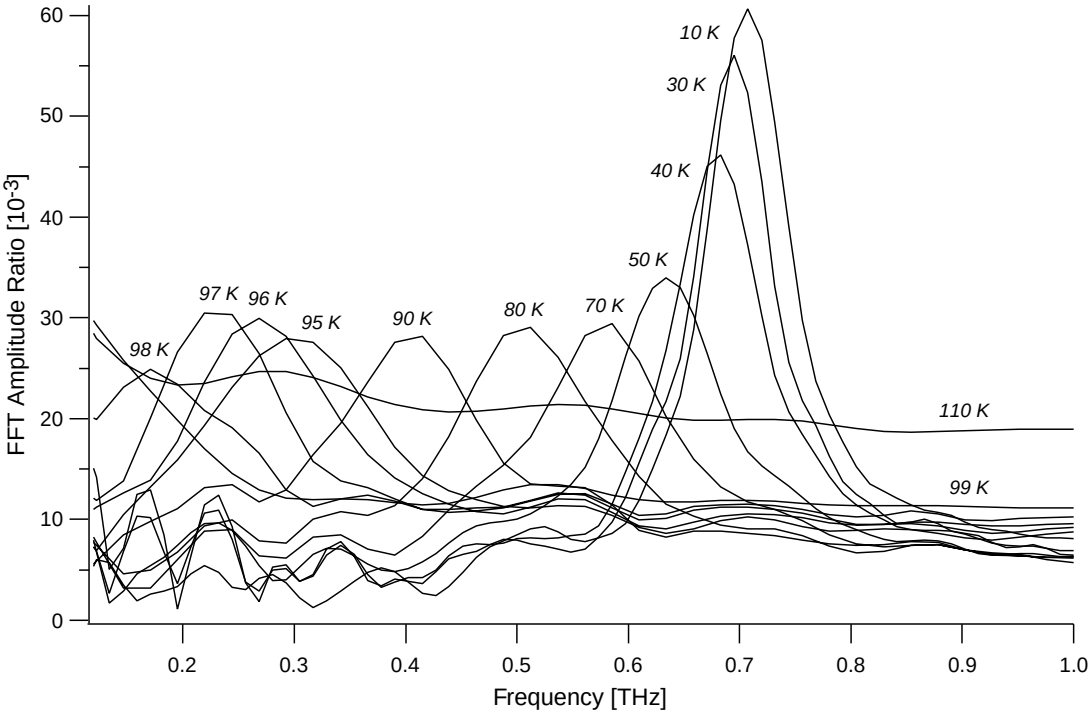

Figure 4.10: Transmission amplitude versus frequency for Tl-2212 film on MgO. The JPR peak broadens and shifts to lower frequencies with increased temperature. FFT, fast Fourier transform.

Using Equation (4.10), and taking $\epsilon_\infty^c = 9.1 \pm 0.7$ for the high frequency dielectric constant for the electric field along the c-axis [19], we obtain for the c-axis penetration depth, $\lambda_c(10K) = 22.4 \pm 0.6$ μm, and $\lambda_c(98\text{K}) = 94 \pm 9$ μm. Similar results were obtained on a 600 nm Tl-2212 film grown on LaO substrate ($T_c =$ 105 K). The temperature dependence of the JPR frequency, plotted in Figure 4.11 displays the same behavior as that of the Tl-2212 film on MgO substrate but with a higher lying JPR which could be attributed to a slight difference in the anisotropy. Here we obtain, for the c-axis penetration depth, $\lambda_c(10\text{K}) = 20.3 \pm 0.5$ μm ($\omega_{pc}/2\pi \approx 780 \pm 5$ GHz), and $\lambda_c(90\text{K}) = 35.2 \pm 1.4$ μm ($\omega_{pc}/2\pi \approx 450 \pm 10$ GHz).

To summarize, we have applied THz-TDS in transmission to measure the c-

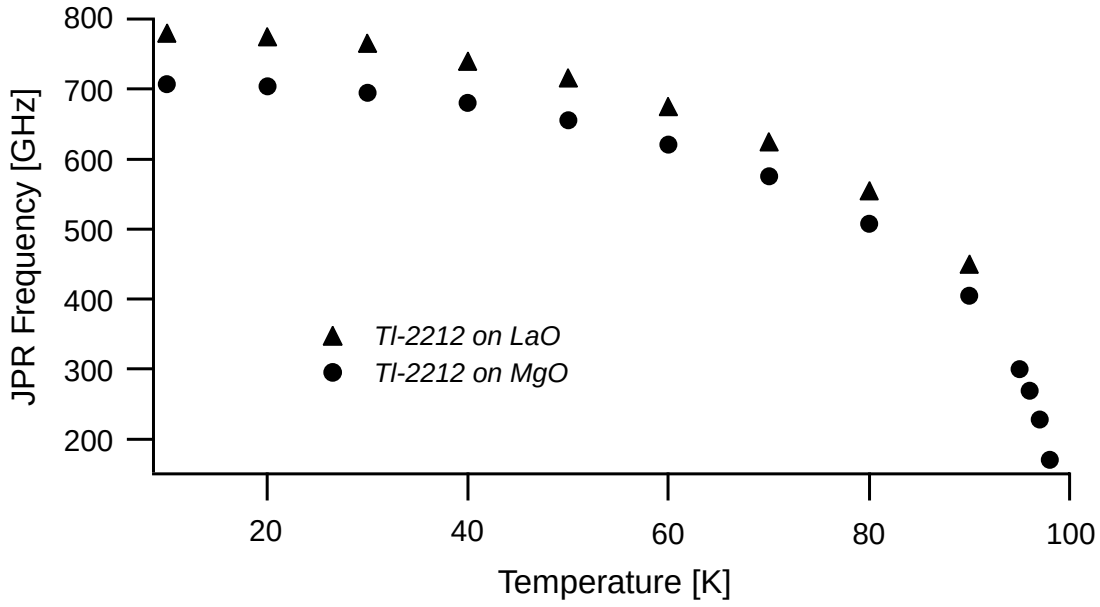

Figure 4.11: JPR frequency versus temperature for Tl-2212 film on both MgO (solid circles) and LaO (solid triangles) substrate.

axis JPR in Tl-2212 as a function of temperature. These measurements agree well with previous measurements of Tl-2212 by use of a grazing incidence reflectivity technique [19], and we were able to extend the measurements to temperatures approaching T_c. We probed the onset of the c-axis phase coherence to $\sim 0.95 T_c$. These measurements demonstrates THz-TDS as an improved technique to measure the JPR, with an improved SNR compared to the grazing incidence reflectivity technique, and without the need for a magnetic field to tune the JPR as in previous microwave cavity experiments.

4.2.1 Symmetry of the Superconducting Order Parameter

The temperature dependencies of $\lambda_c^2(10K)/\lambda_c^2(T)$, as determined from Equation (4.10), for both Tl-2212 grown on MgO substrate (T_c = 103.4 K) and Tl-2212 grown on LaO substrate (T_c = 105 K) are shown in Figure 4.12. $\lambda_c^2(10K)/\lambda_c^2(T)$

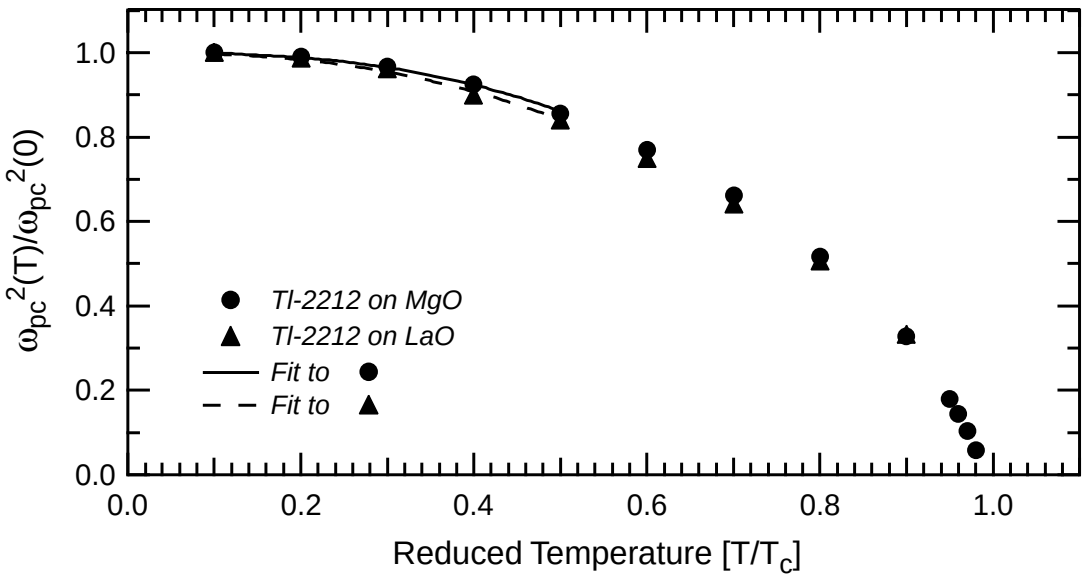

Figure 4.12: Superfluid fraction versus reduced temperature for Tl-2212 film on both MgO (solid circles) and LaO (solid triangles) substrate with T_c = 103.4 K and T_c = 105 K, respectively. The solid line, and the broken line represent $\omega_{pc}^2(T)/\omega_{pc}^2(0) = 1-A(T/T_c)^\alpha$ fitted to respectively Tl-2212 on MgO with $A = 1.0\pm0.1$ and $\alpha = 2.6\pm0.1$, and Tl-2212 on LaO with $A = 0.9\pm0.1$ and $\alpha = 2.4\pm0.1$.

is well expressed as $1-A(T/T_c)^\alpha$ with $A = 1.0\pm0.1$ and $\alpha = 2.6\pm0.1$ for Tl-2212 on MgO, and $A = 0.9\pm0.1$ and $\alpha = 2.4\pm0.1$ for Tl-2212 on LaO. The small difference in α may be due to the difference in anisotropy of the two films since the JPR for Tl-2212 on MgO is $\omega_{pc}(10K) = 705$ GHz, and $\omega_{pc}(10K) = 780$ GHz for Tl-2212 on LaO. This nearly quadratic temperature dependence in the c-axis penetration depth suggests that impurity assisted hopping [21] is the dominating tunneling mechanism in Tl-2212. A similar temperature dependence has been reported in $YBa_2Cu_3O_{7-\delta}$ [107], $Bi_2Sr_3CaCu_2O_{8+\delta}$ [121], $La_{1.85}Sr_{0.15}CuO_4$ [109], and $HgBa_2Ca_2Cu_2O_{8+\delta}$ [108]. However, a T^5 dependence has been observed in low anisotropic $HgBa_2CuO_{4+\delta}$ [108], and in slightly underdoped Bi-2212 [110] suggesting that the behavior is not entirely universal. Further theoretical investigations are needed to develop a comprehensive understanding of the behavior of the order parameter in high-T_c superconductors.

4.2.2 C-axis Quasiparticle Damping of the Josephson Plasma Resonance

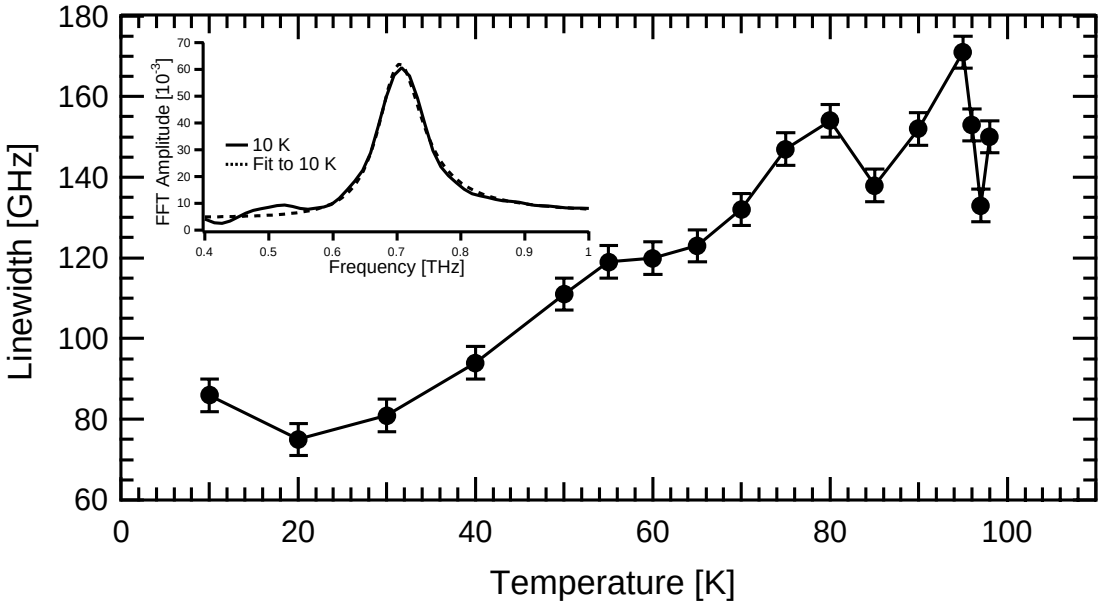

Figure 4.13: JPR linewidth versus temperature for Tl-2212 film on MgO substrate. The inset shows the JPR at 10 K fitted to a Lorentzian function, given by Equation (4.20), to obtain the linewidth.

Figure 4.13 shows the JPR linewidth as a function of temperature for Tl-2212 on MgO substrate obtained by fitting the JPR's in Figure 4.10 to Equation (4.20) at low temperatures (see inset to Figure 4.13), and directly from Figure 4.10 at higher temperatures (because the JPR's do not fit as well at higher temperatures). The corresponding quasiparticle conductivity along the c-axis is determined from Equation (4.22) and shown in Figure 4.14. Below T_c the quasiparticle conductivity σ_{qp}^c falls rapidly, and then increases slightly below 20 K. The temperature dependence of σ_{qp}^c is qualitatively different from the temperature behavior of the ab-plane conductivity σ_{qp}^{ab} usually observed in high-T_c superconductors below T_c [122]. σ_{qp}^{ab} generally increases below T_c displaying a broad peak at lower temperatures. This increase below T_c has been attributed to a rapid increase in the

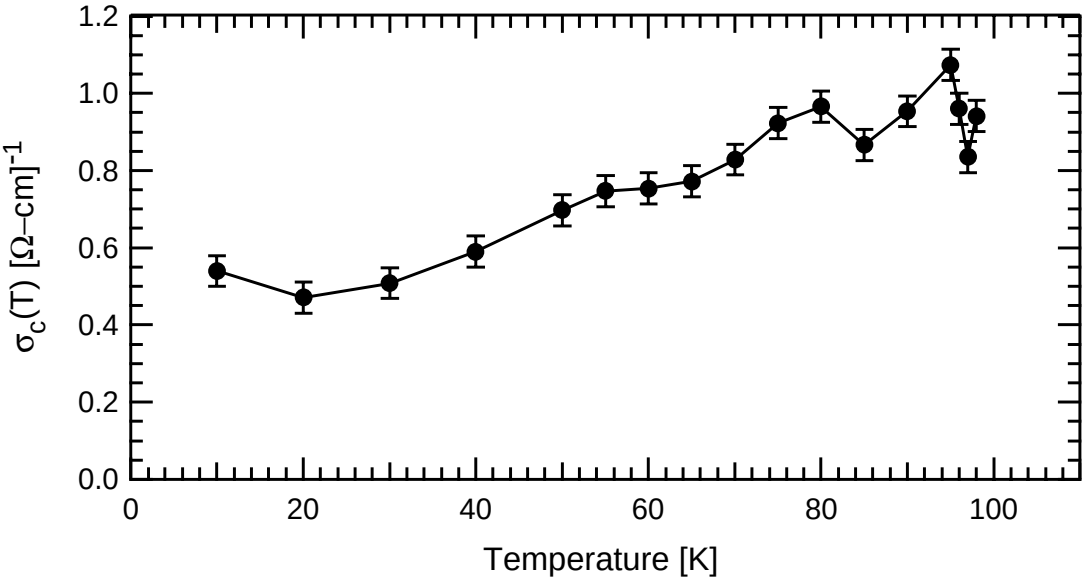

Figure 4.14: C-axis quasiparticle conductivity versus temperature for Tl-2212 film on MgO substrate ($T_c = 103.4$ K).

quasiparticle lifetime in the superconducting state. The absence of such a peak in σ_{qp}^c presented here indicates that the c-axis transport is not influenced by the development of the long transport lifetimes observed in the ab-plane. The fact that σ_{qp}^c remains finite at low temperatures further implies d-wave symmetry because of a finite quasiparticle density of states at the Fermi level, which has also been observed in Bi-2212 [123]. However, it is unclear whether the quasiparticle conductivity σ_{qp}^c can be obtained accurately from the linewidth, because superconducting films might have normal regions, and no definite conclusions can be made from this data.

Comparing σ_{qp}^c for Tl-2212 obtained here to σ_{qp}^c obtained for Y-123 by Hosseini *et al.* [124], and for Bi-2212 by Gaifullin *et al.* [110] one sees the same qualitative behavior. The values for Y-123 with anisotropy ∼10 lies in the range ∼100 $(\Omega-\text{cm})^{-1}$ while Bi-2212 with anisotropy ∼500 lies in the range ∼0.02 $(\Omega-\text{cm})^{-1}$. σ_{qp}^c for Tl-2212 with anisotropy ∼150 lies a factor of ∼50

higher than Bi-2212, and a factor of ∼100 below Y-123. It is interesting to note that σ_{qp}^{c} approximately scales with ω_{pc}^{2} as Bi-2212:Tl-2212:Y-123 [110, 124]. This relationship was established with $La_{2-x}Sr_xCuO_4$ as well [125].

4.3 Angular Dependence of the Josephson Plasma Resonance in $Tl_2Ba_2CaCu_2O_8$

The JPR is excited by an ac electric field applied perpendicular to the CuO_2 layers. According to linear electrodynamic wave theory for a uniaxial anisotropic crystal (see Appendix A.2) the JPR FFT amplitude should decrease with decreasing incident angle and completely vanish at 0 degrees. Furthermore, the transmitted wave and the JPR is expected to decrease with increasing thickness of the Tl-2212 superconducting film, and vanish for a thickness on the order of ∼300 nm. However, the JPR in Tl-2212 is perfectly observable in transmission at a thickness of 700 nm, and also at 0 degrees incidence. Consequently, this behavior makes it impossible to extract parameters of the sample such as the dielectric function, etc. by fitting the JPR data to the complex transmission coefficient given by Equation (2.34). Thus, other mechanisms leading to the excitation or generation of the JPR seem to be at play.

Extensive X-ray diffraction measurements [126] reveal a rotation and tilt of the grains in the Tl-2212 films typically ranging from 0.1 to 0.5 degrees, and in extreme cases as much as 2 degrees. Thus, these films are considered nearly single crystals, and it is appropriate to commence an investigation of additional excitation or generation mechanisms of the JPR besides the E-field of the THz pulse. Such mechanisms could possibly be attributed to the magnetic field component of the THz pulse, nonlinear effects in the Tl-2212 film, or even the distribution,

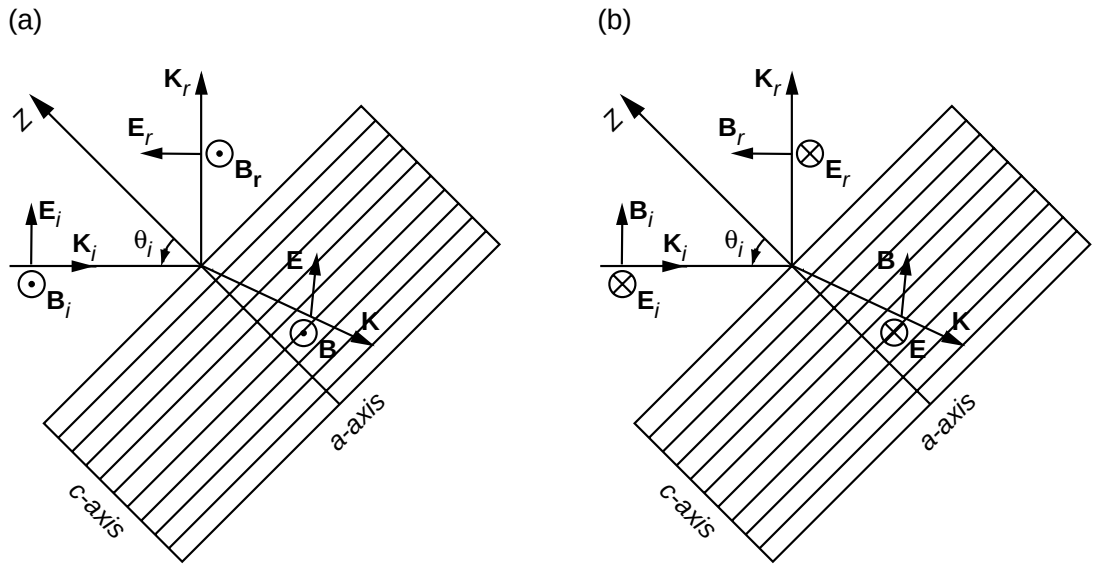

Figure 4.15: Configuration of the Tl-2212 film with respect to the THz beam for (a) *p*-polarization, and (b) *s*-polarization.

orientation, or size of the grains.

The effect of the magnetic field (B-field) component of the THz pulse, compared to the E-field component, is examined in the following two experiments. The configuration of the Tl-2212 film with respect to the THz beam is shown in Figure 4.15. Incident *p*-polarized THz radiation, Figure 4.15(a), has the E-field component in the plane of incidence while the B-field component is parallel to the *ab*-plane for all incident angles.

The optical path length of the THz radiation traveling in the film increases, for both configurations, somewhat with increasing incident angle according to Snell's law. However, since the additional path length is close to negligible if the refractive index of the superconducting film is much greater than the index for air, this effect can safely be neglected.

Figure 4.16 shows the JPR for *p*-polarized THz radiation at 0, 15, 30, and 45 degrees incidence. The JPR peak increases monotonically $\sim$10% in going from

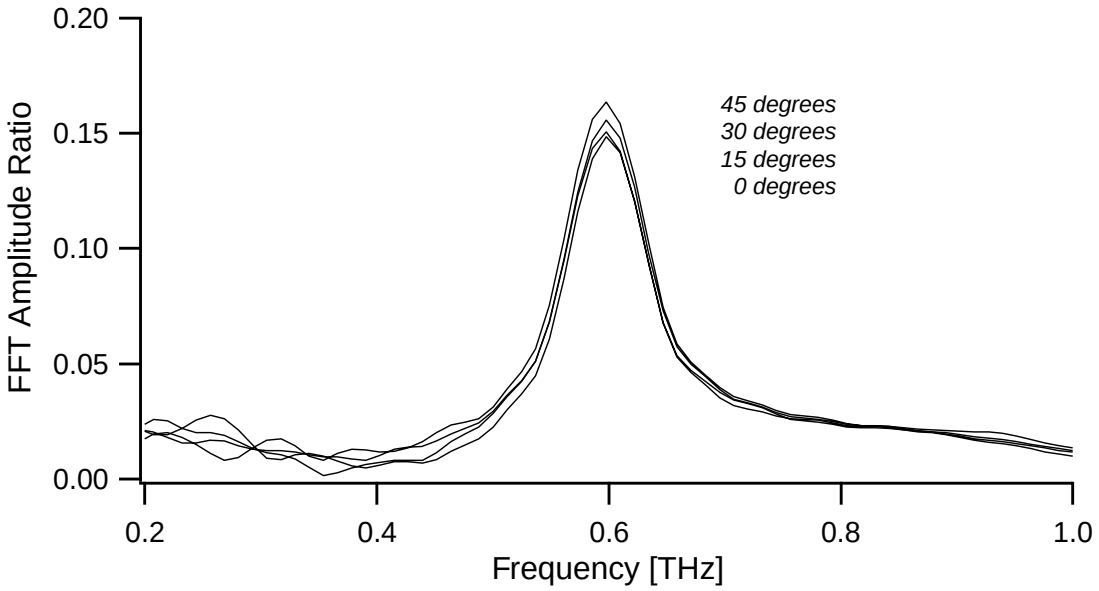

Figure 4.16: JPR at 0, 15, 30, and 45 degrees angles for p-polarization in Tl-2212 at 20 K ($T_c = 105.4$ K). The JPR peak increases with an increasing angle of incidence.

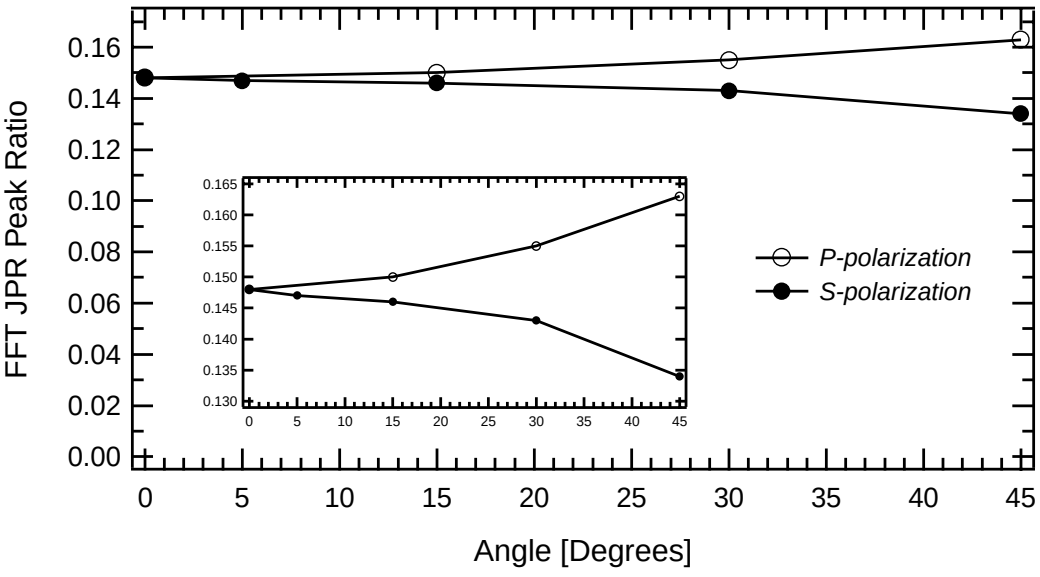

Figure 4.17: JPR versus angle for both p- and s-polarizations in Tl-2212 at 20 K ($T_c = 105.4$ K).

0 degrees, with no E-field component along the c-axis, to 45 degrees with ∼70% of the E-field parallel to the c-axis. This is shown in Figure 4.17. For incident s-polarized THz radiation (see Figure 4.15(b)), the B-field component is in the plane of incidence while the E-field component is parallel to the ab-plane for all incident angles. The decrease of the JPR peak for s-polarization as a function of angle is shown in Figure 4.17 for comparison with the p-polarized case. The JPR peak decreases monotonically ∼10% in going from 0 degrees, with maximum B-field component along the ab-plane, to 45 degrees angle with ∼70% of the B-field parallel to the ab-plane. These results indicates that the B-field component of the THz radiation is at least as influential as the E-field component. Roughly the same behavior is observed at 70 K (Not shown here).

Consider the following for a plausible explanation of the JPR dependence on the B-field component of the THz radiation, and hence the observed lack of dependence on the angle of incidence. Figure 4.18 illustrates an oscillating B-field applied along the y-axis of a layered system with dimensions L along the x-axis, and infinity along y and z. If uniformly applied within the ab-plane a screening current J is induced which gives rise to an electric field E_z along the c-axis in accordance with Maxwell's equations and the London equation as follows.

$$\frac{4\pi}{c}\mathbf{J} = -\frac{1}{\lambda_c^2}\mathbf{A}, \tag{4.26}$$

$$\nabla \times \mathbf{B} = \frac{4\pi}{c}\left(\mathbf{J} + \sigma_{qp}\mathbf{E}\right) + \frac{\epsilon}{c}\frac{\partial}{\partial t}\mathbf{E}, \tag{4.27}$$

$$\nabla \times \mathbf{E} = -\frac{1}{c}\frac{\partial}{\partial t}\mathbf{B}, \tag{4.28}$$

where $\mathbf{J} = (0,0,J_z)$, $\mathbf{A} = (0,0,A_z)$, $\mathbf{B} = (0,B_y,0)$, and $\mathbf{E} = (0,0,E_z)$. The current parallel to the c-axis penetrates much deeper than the one parallel to the ab-plane because $\lambda_c/\lambda_{ab} \sim 150$ for Tl-2212. This current along the c-axis drives

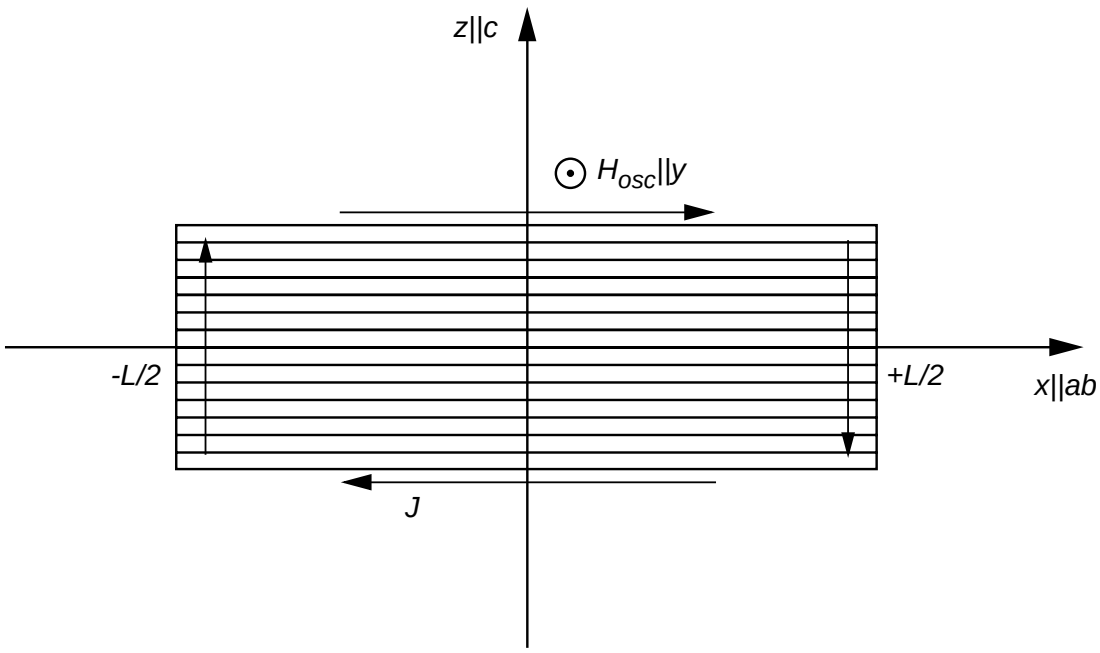

Figure 4.18: Schematic diagram of a layered high-T_c superconductor with B-field component $B_{osc}\|y$. B_{osc} induces a screening current J which gives rise to an E-field along the c-axis at the edges for the transverse plasma excitation.

the oscillating electric field E_{osc} which excites the transverse Josephson plasma [115]. The normal mode of the electromagnetic wave inside the superconductor is obtained by setting $B_y \propto exp[ikx - i\omega t]$, resulting in the condition

$$k^2 + \frac{1}{\lambda_c^2} - \frac{4\pi}{c^2} i\omega\sigma_{qp} - \frac{\epsilon}{c^2}\omega^2 = 0, \tag{4.29}$$

where $k = k_1 + ik_2 = \omega/c\sqrt{\epsilon(\omega)}$. Using the boundary conditions for $B_y(x = \pm L/2) = B_{osc}$, B_y is expressed as

$$B_y = B_{osc} e^{-i\omega t} \left(\frac{e^{ikx} + e^{-ikx}}{e^{i\frac{kL}{2}} + e^{-i\frac{kL}{2}}} \right), \tag{4.30}$$

and the electric field E_z is then given by

$$E_z = -i\frac{\omega}{c} \int^x B_y dx = -\frac{\omega B_{osc}}{ck} e^{-i\omega t} \left(\frac{e^{ikx} + e^{-ikx}}{e^{i\frac{kL}{2}} + e^{-i\frac{kL}{2}}} \right). \tag{4.31}$$

E_z, thus represents an oscillating E-field along the c-axis which is due to the screening currents induced by the oscillating B-field component of the incident

THz pulse. The induced screening current is a surface phenomena and penetrates only weakly into the layered high-T_c superconductor at the edges. The dimensions of the Tl-2212 superconducting thin film are 10×10 mm^2, and 700 nm thick. The THz beam diameter is $\sim$3 mm, and interacts only with a portion of the film. $\lambda_c \sim 20$ μm for Tl-2212, and $\lambda_{ab} \sim 170$ nm at 20 K. However, the THz radiation is transmitted through the Tl-2212 film and the B-field component creates a more complicated current flow pattern as the THz pulse propagates into the film. The results do show evidence of dependence on the B-field component of the THz radiation, and it is plausible that the current flow is also influenced by the distribution and size of the grains. In fact, a picture of the surface of the Tl-2212 film, obtained using atomic force microscopy (AFM), reveals a rough surface with grain sizes on the order of 1 to 1.5 μm (see Figure 4.19). Furthermore, channels with diameters up to $\sim$2 μm and hundreds of nm deep are distributed throughout the thin film. Thus, providing an alternative flow pattern for the induced screening current enabling it to excite the JPR within the interaction area of the THz beam. Nonetheless, the observed behavior of the B-field component in Figure 4.17 cannot account for the entire missing angular dependence of the JPR.

In order to continue to look for the origin of the generation mechanism of the JPR in the Tl-2212 film, and hence the observed lack of dependence on the angle of incidence, the polarization of the emitter and receiver are crossed. The JPR as an emission resonance could be indicated by circularly polarized THz radiation emitted from the Tl-2212 film. Figure 4.20 shows the JPR for s-polarized THz radiation at 0, 15, 30, and 45 degrees incidence with the receiver set up to detect p-polarized THz radiation. The extinction ratio of the polarizers is $\sim$1:50. The FFT amplitude ratio is obtained by dividing by a reference with emitter and receiver both set up for p-polarization. The JPR peak decreases monotonically

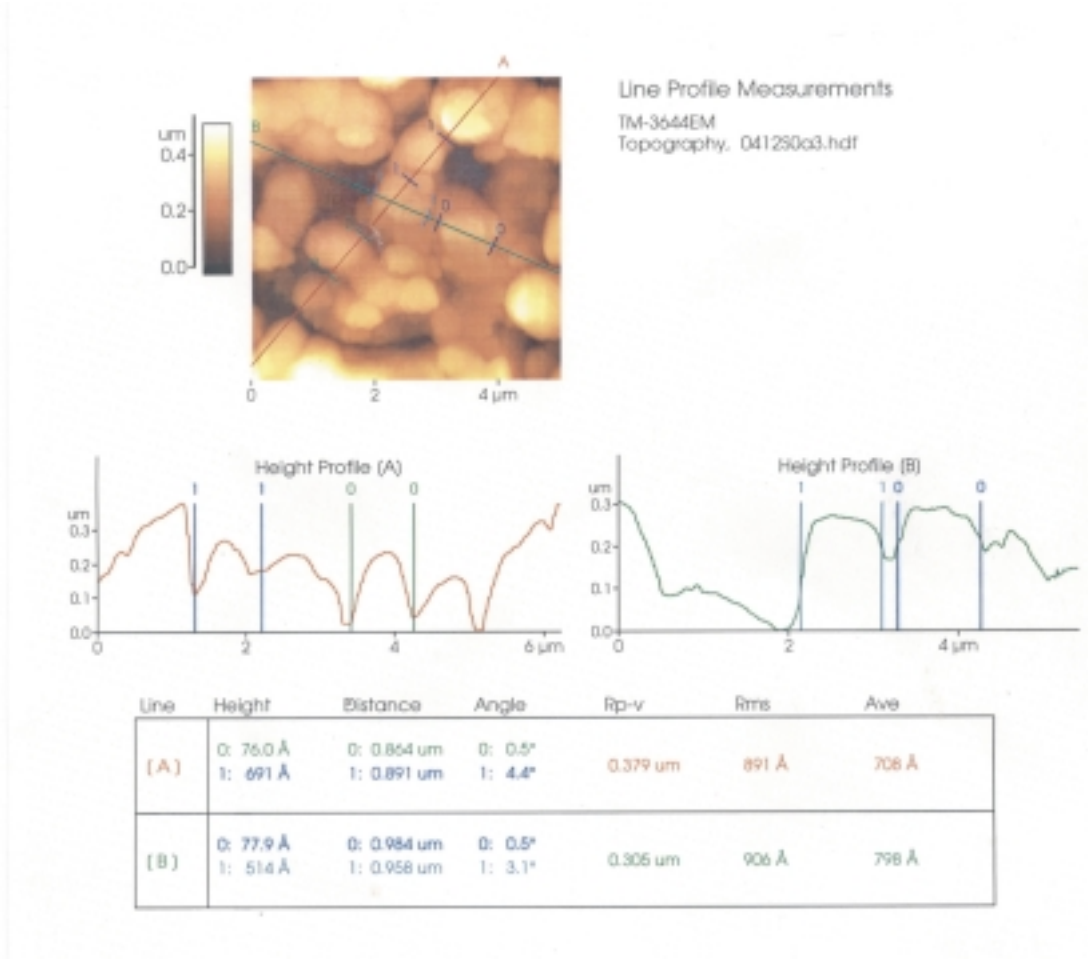

Figure 4.19: Atomic force microscopy surface picture of 700 nm thick Tl-2212 thin film showing height profiles along line A and B.

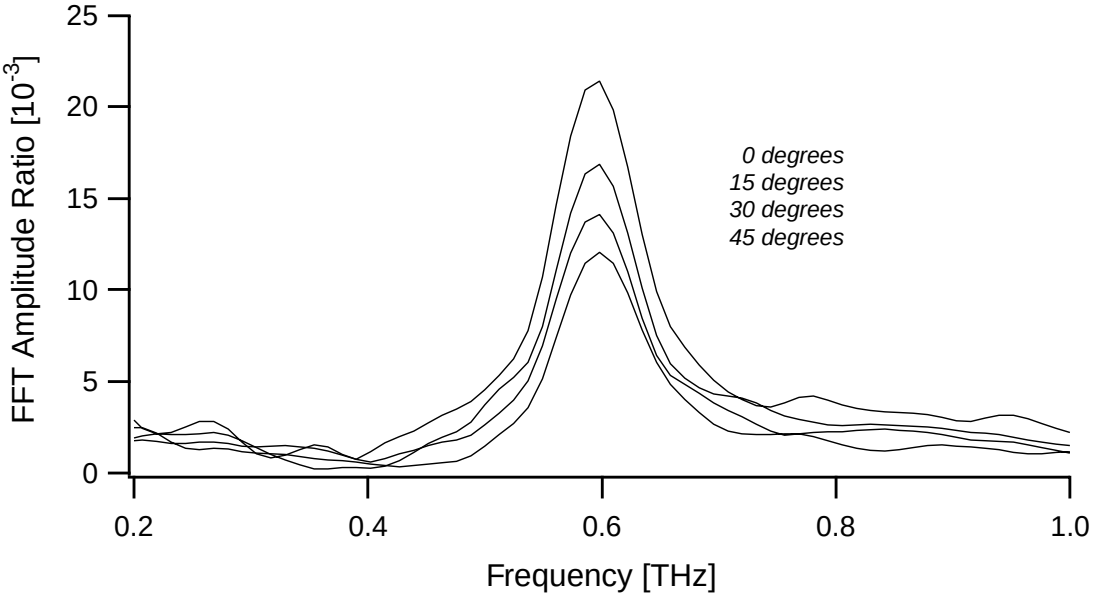

Figure 4.20: JPR at 0, 15, 30, and 45 degrees angles in Tl-2212 at 20 K ($T_c = 105.4$ K). The polarizations of emitter and receiver are crossed: Emitter s-polarized, Receiver p-polarized. The JPR decreases with increasing angle.

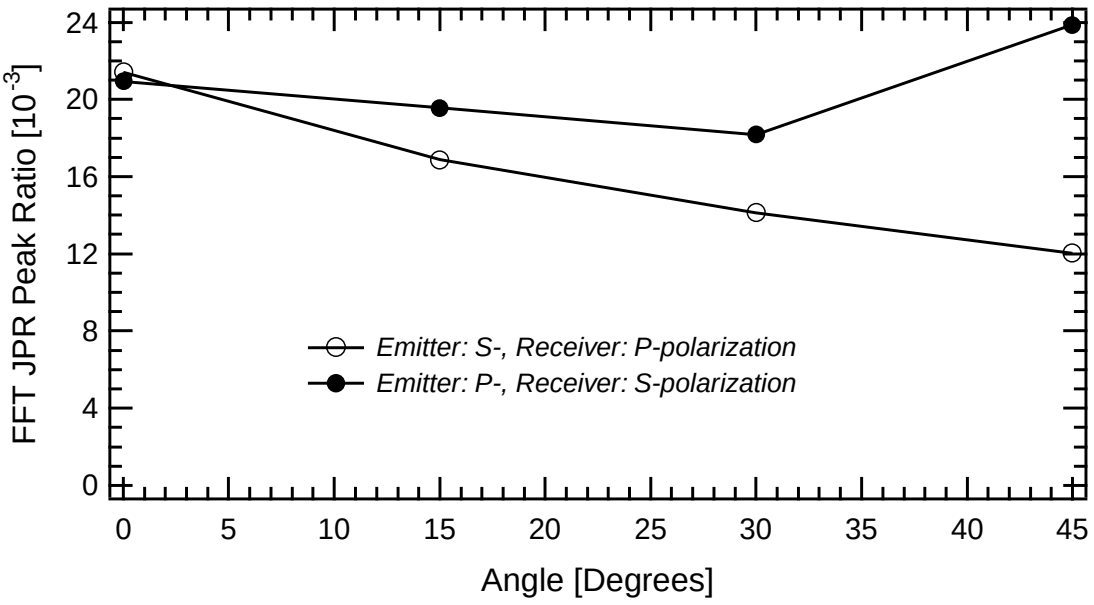

Figure 4.21: JPR versus angle for crossed polarizations in Tl-2212 at 20 K ($T_c = 105.4$ K).

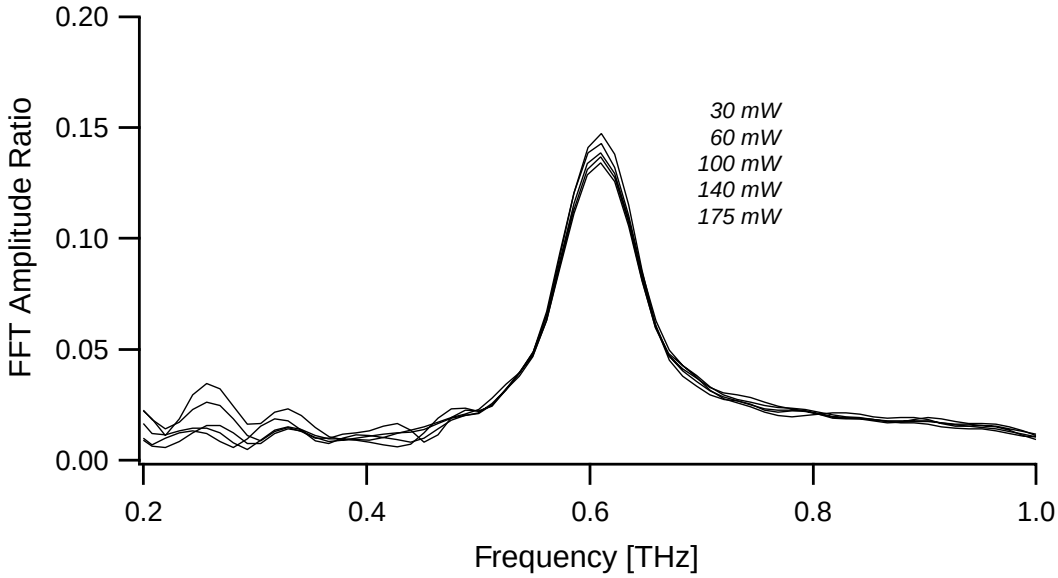

Figure 4.22: JPR at 30, 60, 100, 140 and 175 mW optical power at the ZnTe emitter for p-polarization at 0 degrees incidence in Tl-2212 at 20 K (T_c = 105.4 K).

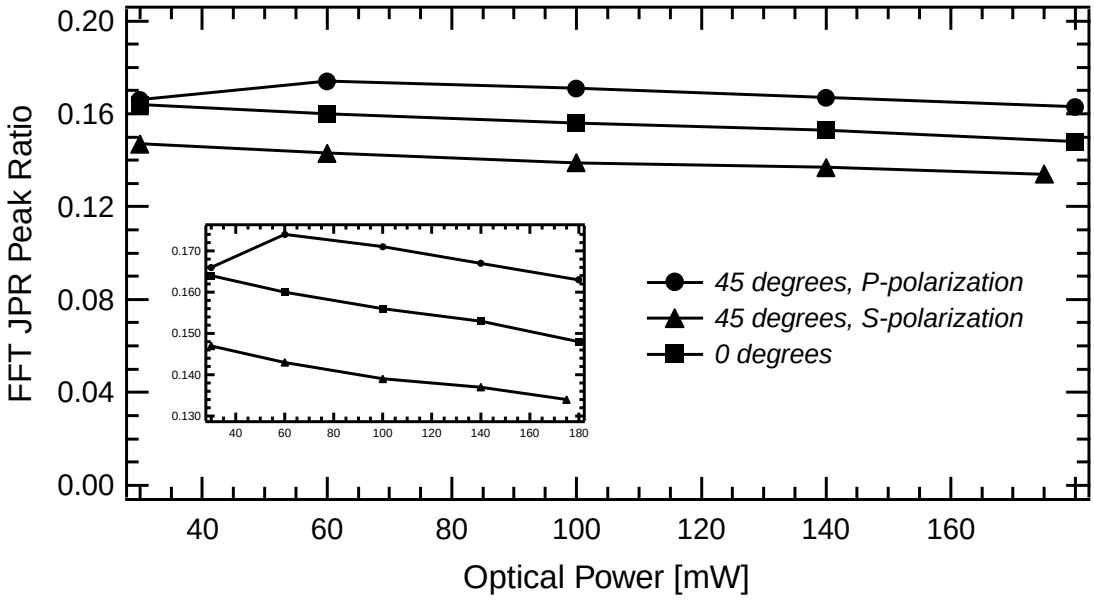

Figure 4.23: JPR versus optical power for both p- and s-polarizations at 45 degrees, and at 0 degrees incidence at the Tl-2212 film (T_c = 105.4 K).

by ∼40% in going from 0 degrees, with maximum B-field component along the ab-plane, to 45 degrees angle with ∼70% of the B-field parallel to the ab-plane. The FFT amplitude ratio for the JPR for p-polarized incident THz radiation with the receiver set up to detect s-polarized THz radiation is obtained by dividing by a reference with emitter and receiver both set up for s-polarization. The extinction ratio is ∼1:30. The JPR peak as a function of angle is shown in Figure 4.21 for both cases of crossed polarizations. The JPR peaks are generally ∼10−15% of the value when the polarizations are not crossed (see Figure 4.17). The observation of the JPR with crossed polarizations might partly be caused by imperfect extinction ratios, and is too weak to substantially support evidence of generation of the JPR in the Tl-2212 film.

In a continued search for the excitation mechanism of the JPR, and the missing angular dependence we now look for nonlinear effects in the film. Figure 4.22 shows the JPR at 30, 60, 100, 140 and 175 mW optical power at the ZnTe emitter for p-polarization at 0 degrees incidence at the Tl-2212 film. Figure 4.23 shows the JPR peak versus optical power for both p- and s-polarizations at 45 degrees, and at 0 degrees incidence at the Tl-2212 film. There is a slight decline in the JPR peak ∼6% with increasing power from 30 to 180 mW for all three cases, but the angular dependence is unaffected by the optical power.

In conclusion, we speculate that the missing (or very weak) angular dependence of the JPR is attributed to the roughness of the film which is shown in Figure 4.19. The incident THz radiation will always have an E-field component along the c-axis by random scattering in the film as inferred from Figure 4.17. Furthermore, the B-field component of the THz radiation induces a screening current, which runs in the channels of the film, and gives rise to an E-field along the c-axis. The contribution from the B-field component seems, according to

Figure 4.17, to be as important as the E-field component of the THz radiation in generating the JPR which is observed for all angles between 0 and 45 degrees incidence.

4.4 Direct Evidence for Linelike Vortex Liquid Phase in $Tl_2Ba_2CaCu_2O_8$ Probed by the Josephson Plasma Resonance

The structure of the different vortex phases and the nature of the phase transitions in the magnetic phase diagram of high-T_c superconductors has been the subject of intense study over the past several years [65]. It has been established rather conclusively, both experimentally [73, 127] and theoretically [128], that there exists a first-order phase transition at which the vortex lattice melts into a vortex liquid where at least in-plane long-range order is lost. This melting transition depends strongly on the anisotropy of the superconductor [129]. The anisotropy is defined as $\gamma = \lambda_c/\lambda_{ab}$, where λ_c and λ_{ab} are the London penetration depths along the c-axis and ab-plane, respectively. In $YBa_2Cu_3O_{7-\delta}$ (Y-123), which has a low degree of anisotropy $\gamma \sim 8$, the vortex lattice melts by a first-order phase transition into a linelike liquid [128, 130] up to rather high magnetic fields $\sim 10^4 - 10^5$ G [127] (see Figure 4.24(c)). In the case of extreme anisotropy $\gamma \sim 500$ and $\gamma \sim 150$ as in, respectively, Bi- and Tl-based high-T_c superconductors a model has been introduced, whereby the vortices are stacks of two-dimensional "pancake" vortices in the CuO_2 layers, which are weakly coupled by Josephson and magnetic interactions [131]. Such a vortex lattice of pancake vortices has close to long-range order at low magnetic fields and temperatures, where the pancake vortices form aligned stacks (vortex lines). However, the interactions between

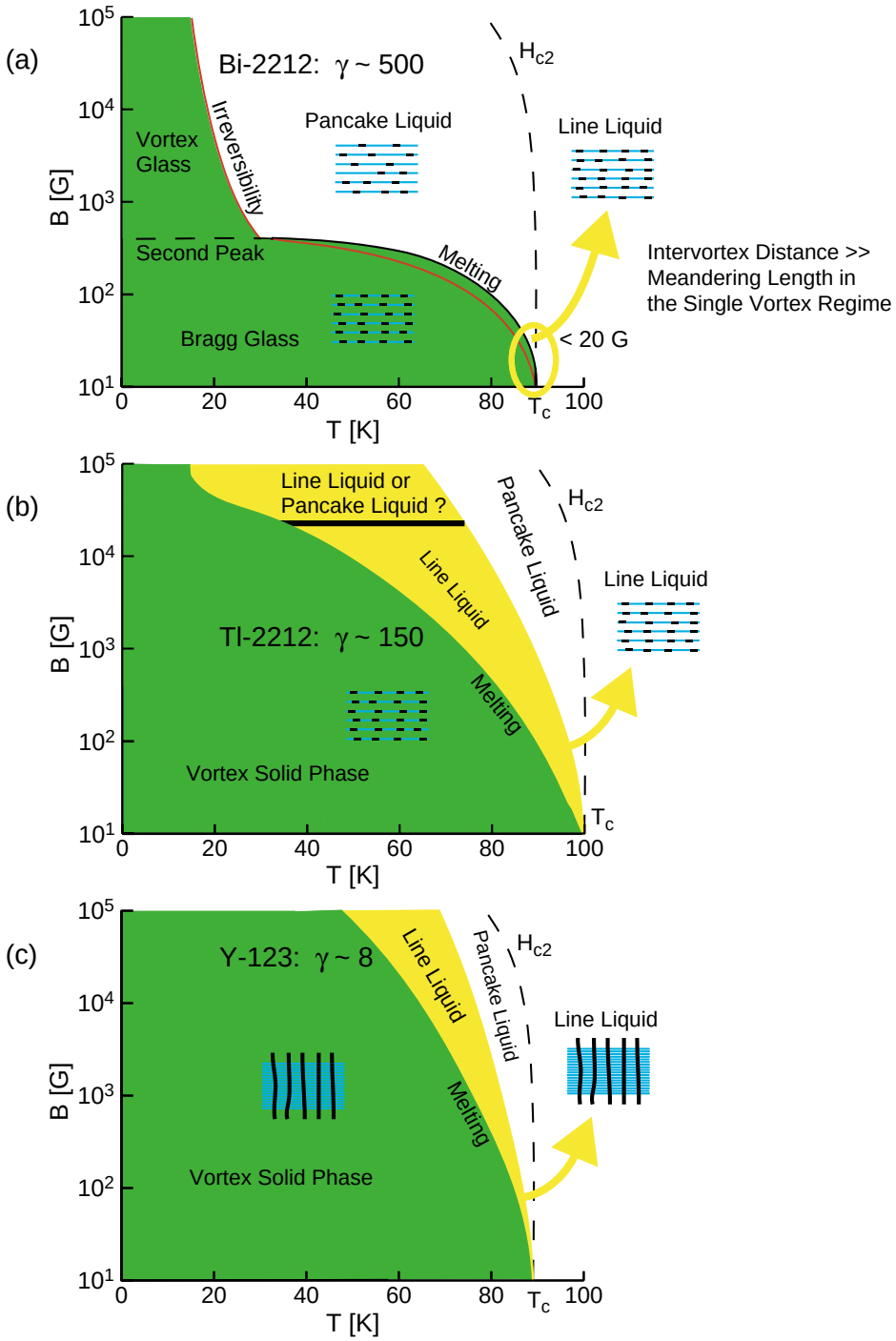

Figure 4.24: Illustration of the mixed-state phase diagram of (a) Bi-2212, (b) Tl-2212, and (c) Y-123. The focus of these phase diagrams is to see the effect of the anisotropy on the structure of the vortex liquid phase.

the pancake vortices in adjacent layers are very weak and these vortex lines are easily destroyed due to misalignment of the pancake vortices by either thermal fluctuations at higher temperatures, or by random pinning. In $Bi_2Sr_2CaCu_2O_{8+\delta}$ (Bi-2212), which is the most anisotropic superconductor known, the vortex lattice undergoes a first-order melting at magnetic fields below ∼500 G [129] (see Figure 4.24(a)).

The structure of the vortex liquid phase in the anisotropic superconductors Y-123 and Bi-2212 has been the focus of numerous experimental and theoretical studies [22, 130, 132]. It has been found that at the melting transition in Bi-2212 vortex lines are disintegrated into a liquid of pancakes [22, 132], in contrast to Y-123, where vortex lines are preserved above the melting line [130]. Here we report on the structure of the vortex liquid in Tl-2212 which has an intermediate anisotropy in between Bi-2212 and Y-123. We show that with respect to melting Tl-2212 behaves as Y-123.

The most direct way to clarify the nature of these vortex phases and the phase transitions between them is to measure the interlayer phase coherence in each vortex phase. One of the most powerful experimental probes for the interlayer phase coherence in highly anisotropic layered superconductors is the c-axis Josephson plasma resonance [20, 22], which is directly related to the c-axis correlations of pancake vortices in the mixed-state [117]. The JPR is a Cooper pair charge oscillation mode perpendicular to the CuO_2 layers. In zero magnetic field the JPR is a direct probe of the Josephson coupling between the layers [110]. The JPR frequency is given by $\omega_0(T) = c/\left(\lambda_c(T)\sqrt{\epsilon_0}\right) = c/\left(\gamma\lambda_{ab}(T)\sqrt{\epsilon_0}\right)$. Here, c is the speed of light, and ϵ_0 is the high-frequency dielectric constant along the c-axis. In the presence of a c-axis magnetic field B, the JPR can be written as

[117]

$$\omega_p^2(B,T) = \omega_0^2(T)\langle\cos(\varphi_{n,n+1}(\mathbf{r},B))\rangle. \tag{4.32}$$

Here, $\langle\cos(\varphi_{n,n+1}(\mathbf{r},B))\rangle$ is the local thermal and disorder average of the cosine of the gauge-invariant phase difference between adjacent layers n and $n+1$, and $\mathbf{r}$ is the in-plane coordinate. When the pancake vortices form straight lines perpendicular to the layers, $\varphi_{n,n+1}(\mathbf{r},B)$ vanishes. However, when the pancake vortices are misaligned along the c-axis, due to either thermal fluctuations or pinning effects, a nonzero phase difference is induced which suppresses the interlayer Josephson coupling, and results in the reduction of $\langle\cos(\varphi_{n,n+1}(\mathbf{r},B))\rangle$ from unity. Thus, the JPR probes the correlations of pancake vortices along the c-axis, and provides information on various vortex phases and phase transitions between them.

Recent JPR microwave cavity measurements in a Bi-2212 crystal by Shibauchi *et al.* [132] show a jump in the interlayer phase coherence factor, $\langle\cos\varphi_{n,n+1}\rangle$ from $\approx$0.7 to $\approx$0.3 at the first-order melting transition (see Figure 4.25). These data together with magnetization measurements, suggest that the melting of the vortex lattice is accompanied by disintegration of vortex lines into a pancake liquid, where c-axis correlations are lost. Recently Gaifullin *et al.* [22] probed the vortex system of a slightly underdoped $Bi_2Sr_2CaCu_2O_{8+x}$ crystal by sweeping the frequency in the range $20-150$ GHz in a waveguide at constant magnetic field. They found a similar change in the interlayer phase coherence factor $\langle\cos\varphi_{n,n+1}\rangle$ from $\approx$0.7 to $\approx$0.4 at the first-order melting transition. Quantitative analysis [117] of the JPR data confirmed that correlations of pancake vortices between neighboring layers in the liquid phase in Bi-2212 far away from T_c are practically absent.

However, Bulaevskii *et al.* [133] found, by analyzing JPR data [22, 132] evidence for a line liquid phase in Bi-2212 for small melting fields ($<$ 20 G) near

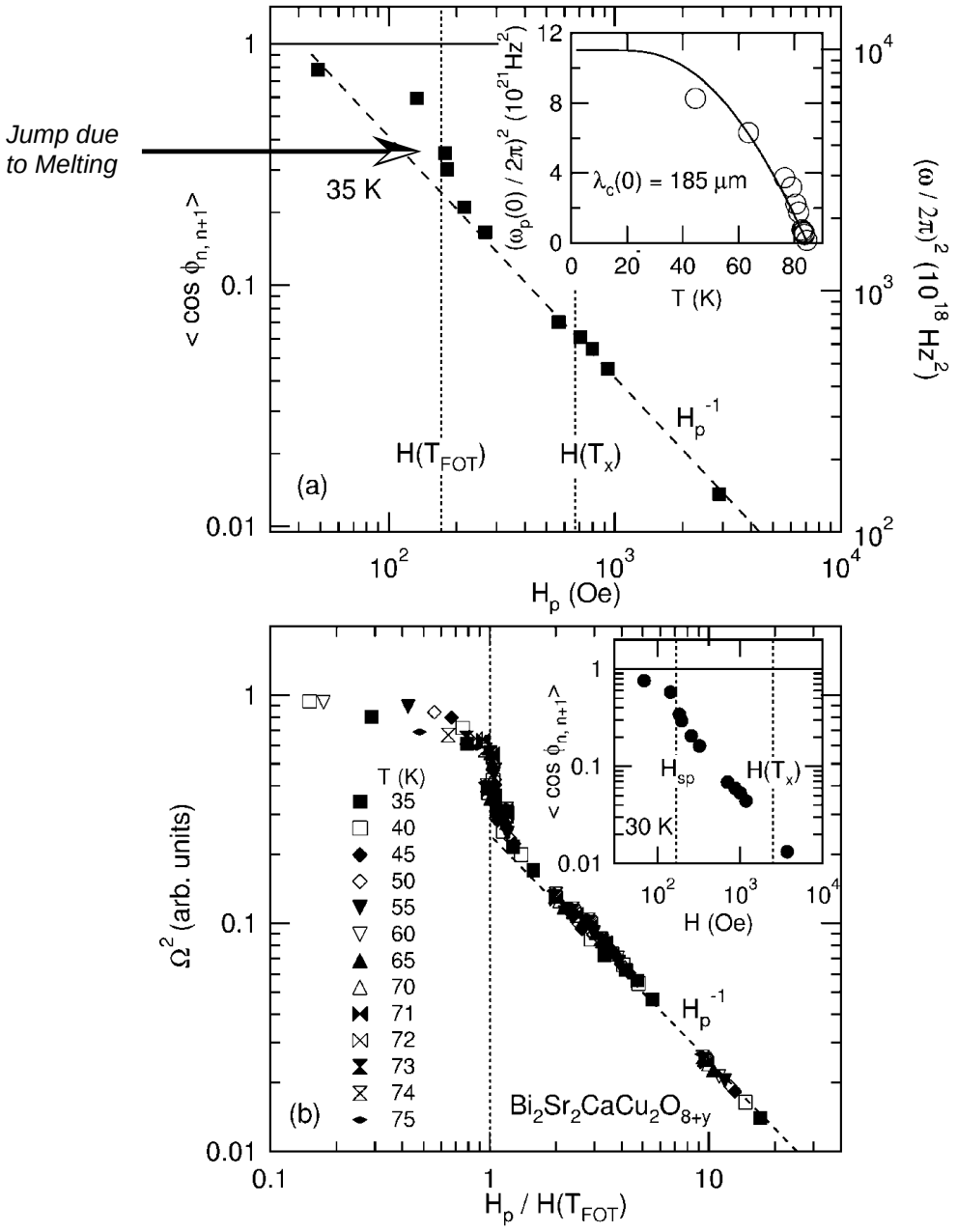

Figure 4.25: (a) Jump in the interlayer phase coherence factor in Bi-2212 single crystal at the melting transition as a function of magnetic field. The jump in the factor illustrates the simultaneous melting and decoupling of the vortex lattice. (b) A scaling of the factor as a function of normalized field. (© Copyright (1999) by The American Physical Society. Figure 4 in Reference 3).

T_c (see Figure 4.24(a)). At low magnetic fields, $B_m < B_J = \Phi_0/\lambda_J^2$ ($\lambda_J = \gamma s$ is the Josephson length where s is the interlayer distance), the intervortex distance is much larger than the meandering length. The meandering length r_w is defined as the average in-plane distance between two pancake vortices in adjacent layers which belong to the same vortex line (stack of pancake vortices). In this single vortex regime the Josephson coupling in the region occupied by a given vortex stack is not suppressed by other vortices. The pancake vortices are thus well correlated in neighboring layers both below and above the melting line.

To probe c-axis correlations in less anisotropic high-T_c superconductors such as thallium and mercury compounds, where the JPR lies in the THz range, one needs optical techniques. Demonstrated techniques are either the grazing incidence reflectivity technique [19], or terahertz time-domain spectroscopy (THz-TDS) in transmission [20]. Here we measure the JPR by use of THz-TDS in transmission. THz-TDS has a better SNR, in comparison to the grazing incidence reflectivity technique, allowing measurements close to T_c [20]. The experimental set-up of the THz-TDS spectrometer is shown in Figure 4.7. The Tl-2212 film (700 nm) was grown on a 12×12 mm^2 MgO substrate as described in Section 4.2, and exhibited a sharp transition temperature ($0.2-$K width) at $T_c = 103.4$ K. The sample was positioned inside an optical cryostat with optical access, between a pair of permanent magnets with the magnetic field oriented along the c-axis. All experiments were performed in field cooled mode. In order to excite the JPR, p-polarized THz radiation, incident at an angle of 45° to the surface normal, is transmitted through the sample [20]. To obtain the transmission amplitude of the Tl-2212 film, we performed two sets of averaged scans at each temperature and field. The first set was performed on the sample (film plus substrate), and the other set was performed on a bare reference substrate. The fast Fourier transform of the sample was then divided by the fast Fourier transform of the

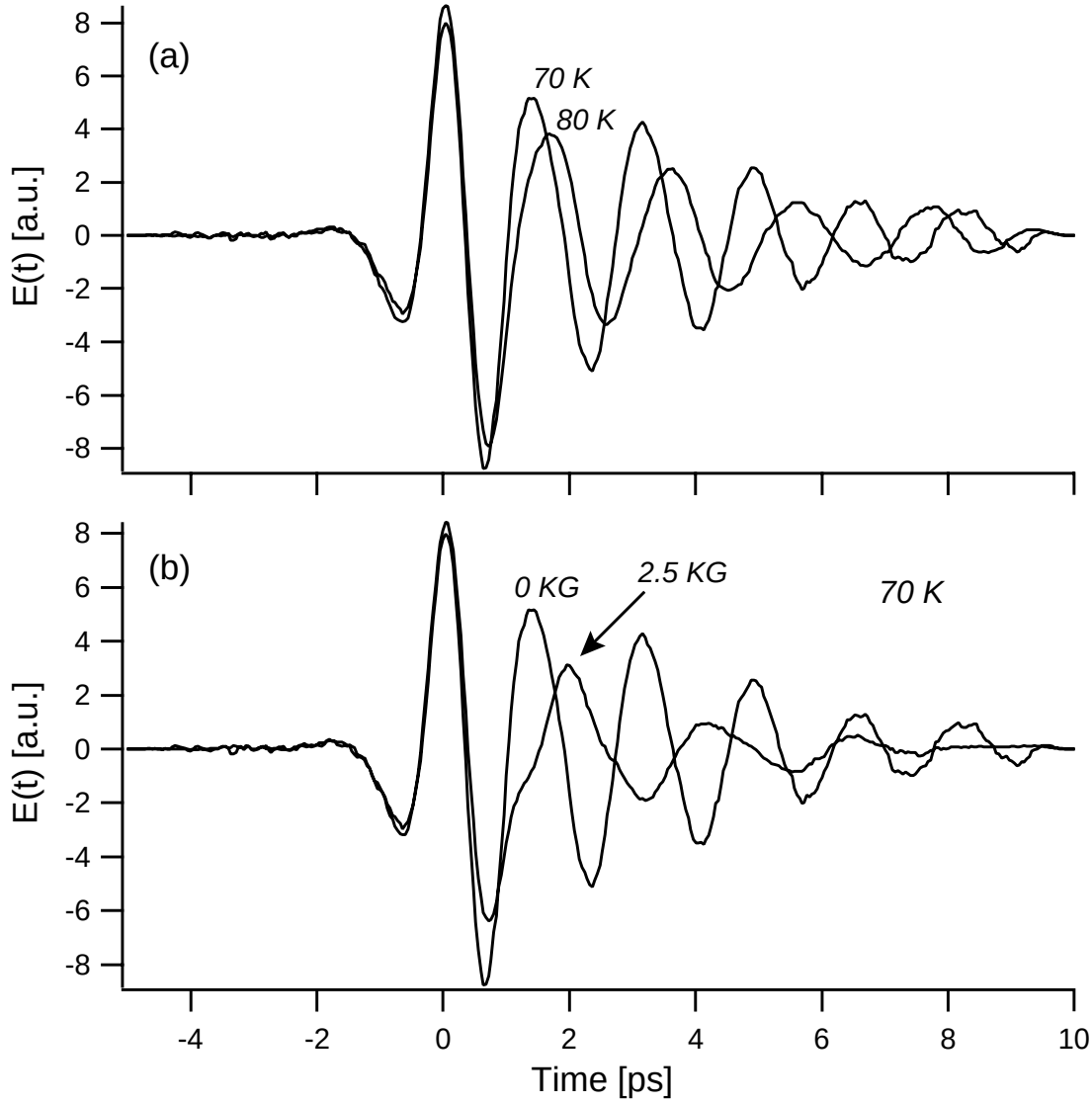

Figure 4.26: Electric field of THz pulse in the time-domain transmitted through Tl-2212 thin film on MgO substrate at (a) 70 K and 80 K, and at (b) 70 K with and without a 2.5 kG c-axis applied field.

reference. This ratio gave the complex transmission coefficient of the Tl-2212 film as a function of frequency.

Figure 4.26 shows the electric field of the THz pulse transmitted through the sample. Figure 4.26(a) shows the JPR in the time-domain at 70 K and 80 K. This clearly illustrates a downward shift in the oscillation frequency as the temperature is increased from 70 K to 80 K. Figure 4.26(b) shows the JPR in the time-domain at 70 K in zero magnetic field and in a 2.5 kG c-axis applied field. In the time-domain, the effect of the magnetic field is clearly seen to both shift the oscillation frequence downward, due to the induced disorder of the pancake vortices, and also to distort the THz pulse caused by inhomogeneous broadening of the pancake vortices, which is seen as an increase of the linewidth in the frequency-domain (see Figure 4.27).

In the frequency-domain, Figure 4.27 shows the transmission amplitude as a function of frequency for the Tl-2212 film (a) in zero field from 70 to 100 K, and (b) in a 2.5 kG field applied along the c-axis. The JPR frequency is seen to decrease with increasing temperature, and a drastic drop in frequency is observed for each of these temperatures when applying the 2.5 kG field along the c-axis.

In Figure 4.28(a) we show the decrease of the JPR frequency with temperature at $B = 0$ and $B = 2.5$ kG. The drop in the JPR frequency due to the applied c-axis field, shown in Figure 4.28(b), is seen to increase from $\sim$115 GHz at 70 K to $\sim$185 GHz at 85 K. This increase indicates the crossover from the vortex solid phase to the vortex liquid phase. The corresponding decrease of the interlayer phase coherence factor $\langle \cos \varphi_{n,n+1} \rangle$ with temperature is shown in the inset in Figure 4.28(b). We see here a very smooth and gradual reduction of this factor without any abrupt changes, which is in contrast to what was observed for Bi-2212 (see Figure 4.25).

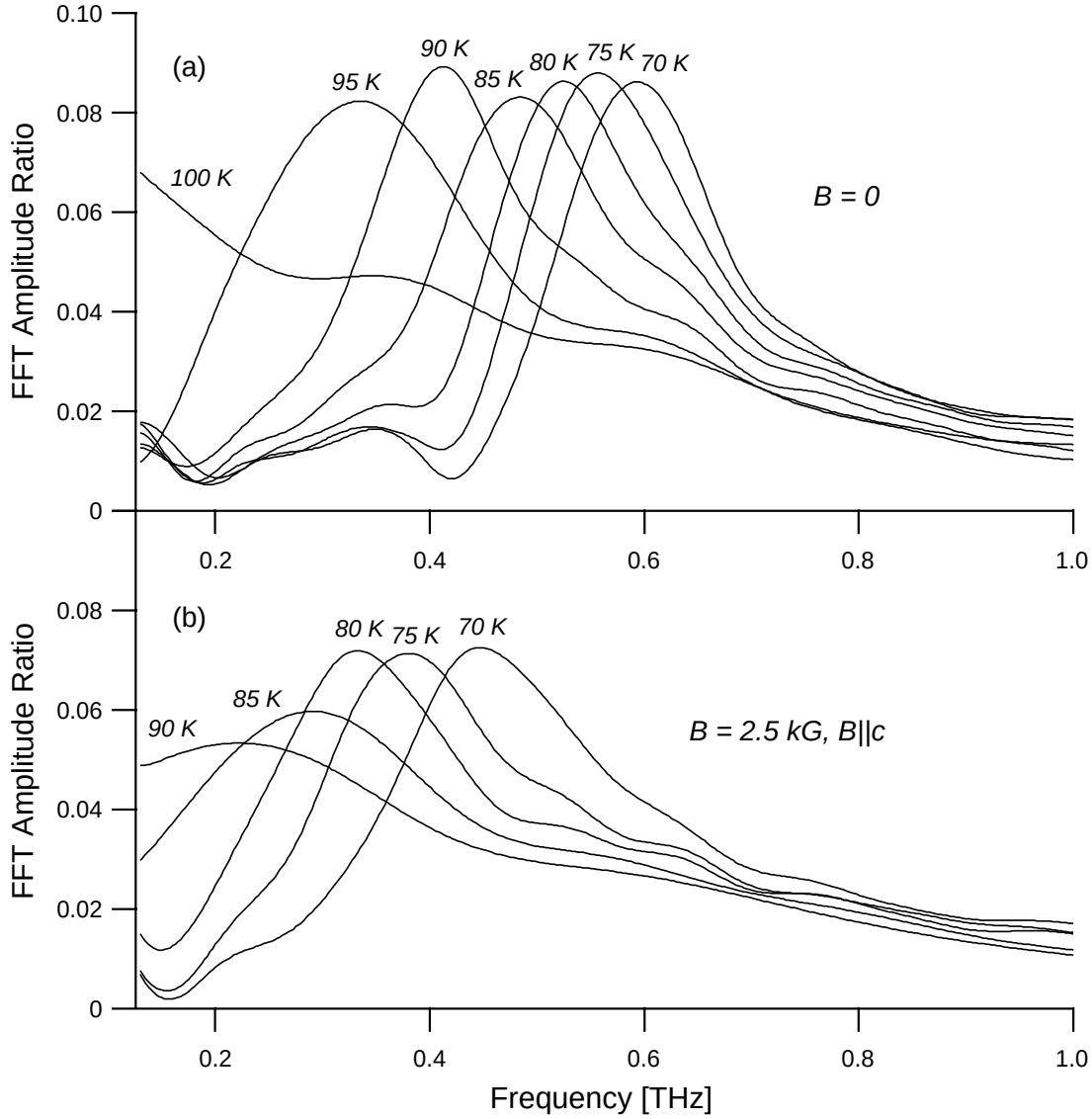

Figure 4.27: Transmission amplitude versus frequency for Tl-2212 thin film. (a) JPR in zero field from 70 K to 100 K. (b) JPR in 2.5 kG field applied along the c-axis from 70 K to 90 K.

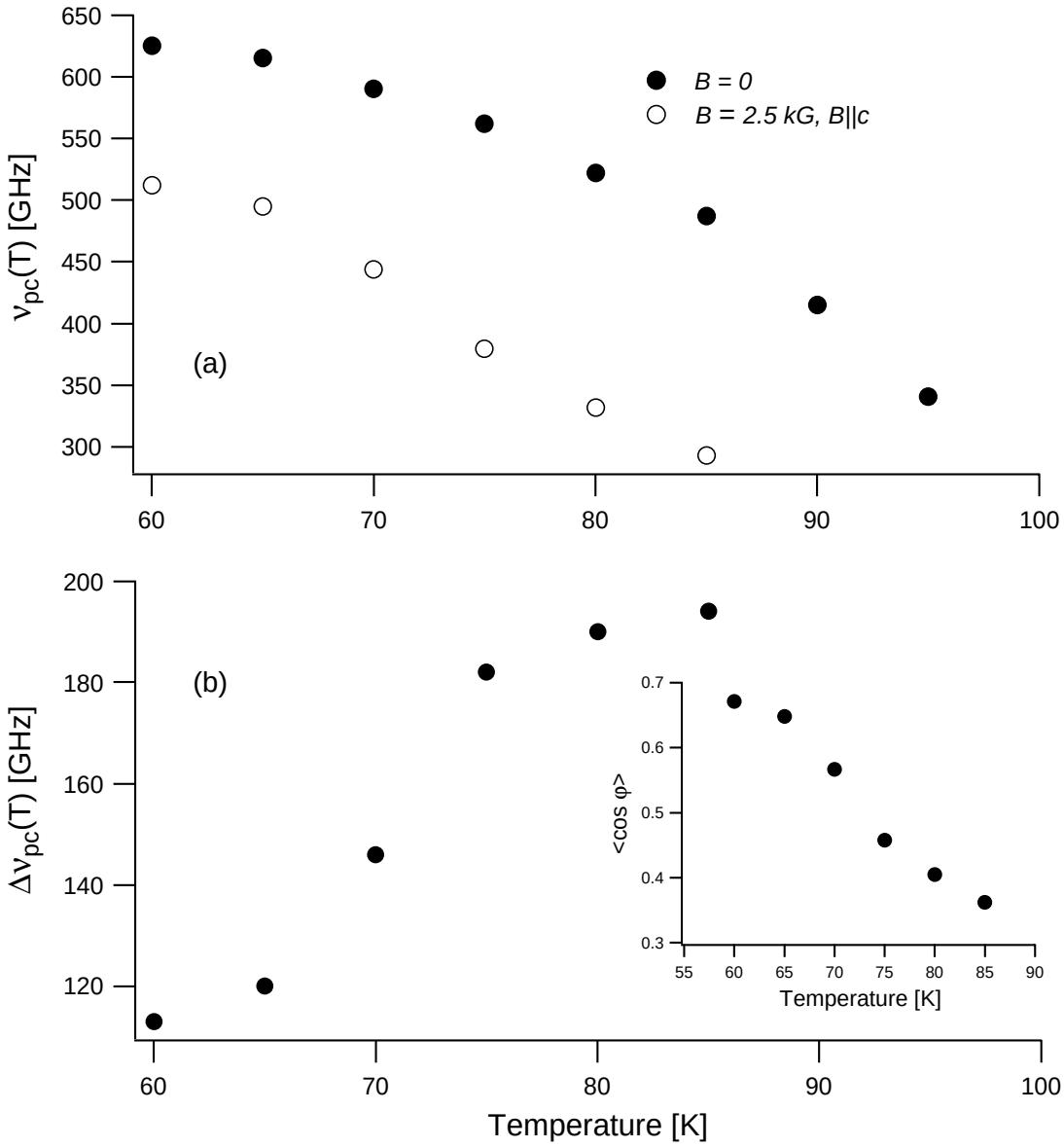

Figure 4.28: (a) JPR frequency versus temperature in Tl-2212 with and without c-axis applied field of 2.5 kG. (b) Drop in JPR frequency due to c-axis field of 2.5 kG versus temperature. The inset shows the interlayer phase coherence factor $<\cos\varphi_{n,n+1}>$ versus temperature.

The interlayer phase coherence factor, $\langle \cos \varphi_{n,n+1} \rangle = \omega_p^2 (B,T) / \omega_0^2 (0, 20K)$, as a function of temperature at different magnetic fields is shown in Figure 4.29. This factor is practically temperature independent from 20 to 70 K at B = 0.4 kG, and from 20 to 50 K at B = 1.8 kG. This suggests that the pancake vortices are well pinned and largely unaffected by thermal fluctuations at lower temperatures in the vortex solid phase. $\langle \cos \varphi_{n,n+1} \rangle$ decreases approximately linearly with field at low temperatures from 20 to 50 K (see Figure 4.30). Such a field dependence was also observed in the vortex solid phase in Bi-2212 [22, 132]. At higher temperatures the drop of $\langle \cos \varphi_{n,n+1} \rangle$ with magnetic field becomes stronger, in agreement with theoretical predictions [134]. We note that Dulić *et al.* [135] did not observe a change in the field dependence of the JPR frequency, $\omega_p(B)$, with temperature in grazing incidence reflectivity measurements up to 70 K. The important point is that there is no indication of a sudden change of the field dependence as a function of temperature, which would have signaled a disintegration of vortex lines into a liquid of pancake vortices at the melting transition.

Suppression of the Josephson coupling due to pinning-induced meandering of vortex lines at low temperatures has been considered in Reference 136. At small fields the coherence factor decreases linearly with field, $\langle \cos \varphi_{n,n+1} \rangle = 1 - B/B_w$, where the typical field B_w is a measure of the meandering length r_w, $B_w \approx \Phi_0 / \pi r_w^2 \ln(\gamma s / r_w)$, and the meandering length, in turn, is determined by a balance between the pinning energy U_p and the Josephson energy, E_J, $r_w^2 \sim U_p / E_J$. Our data give $B_w \approx 7.4$ kG corresponding to $r_w \approx 20$ nm. This value for B_w has to be compared with the lower value $B_w \approx 1.2$ kG for the more anisotropic Bi-2212 [22], the similar value of B_w for a different Tl-2212 film $B_w \approx 14$ kG [135], and the much higher value $B_w \approx 30$ T for the less anisotropic underdoped $YBa_2Cu_3O_x$ [135]. This confirms that B_w is mainly determined by the anisotropy

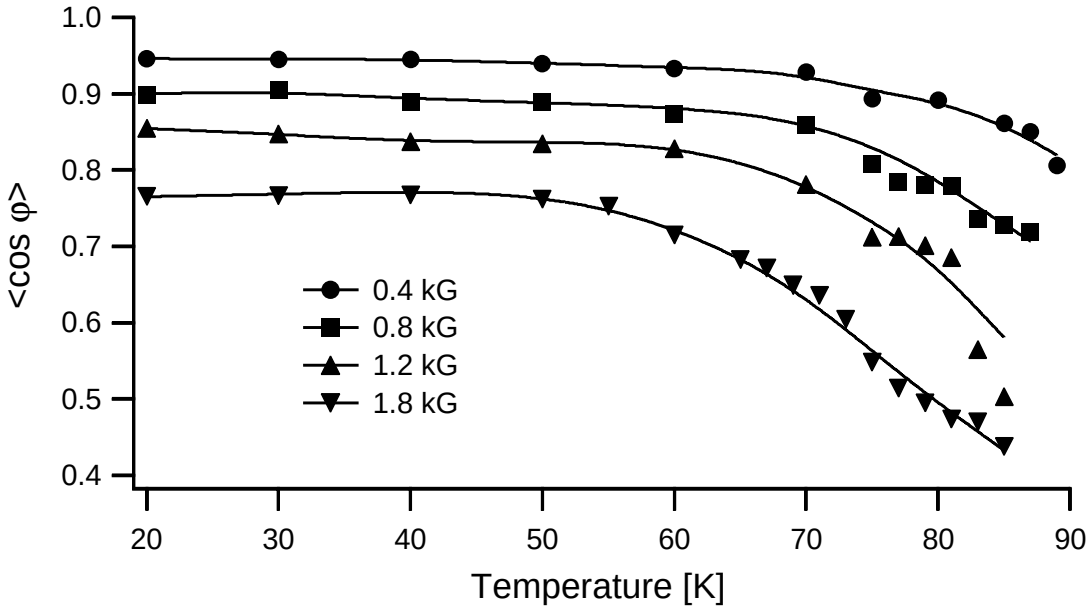

Figure 4.29: Interlayer phase coherence factor $<\cos\varphi_{n,n+1}>$ versus temperature in Tl-2212 with four different magnetic fields applied along the c-axis. The drop in the curves at high temperatures indicates the crossover from the vortex solid phase to the vortex liquid phase.

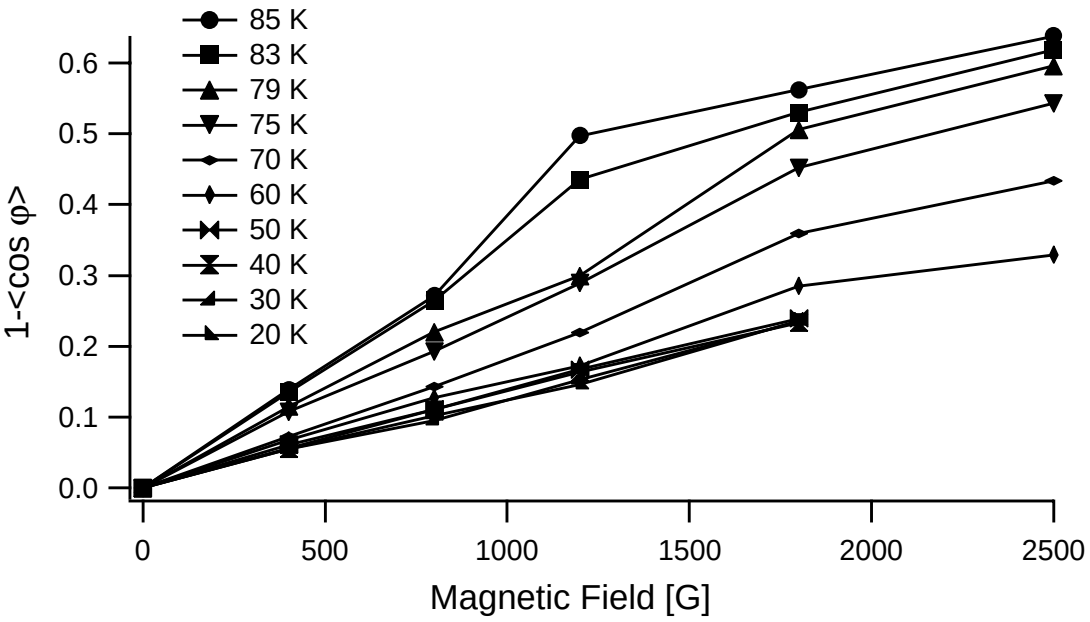

Figure 4.30: Interlayer phase coherence factor 1-$<\cos\phi_{n,n+1}>$ in Tl-2212 versus c-axis magnetic field at various temperatures.

of the material.

We will now discuss the role of thermal fluctuations on the suppression of $\langle \cos \varphi_{n,n+1} \rangle$ at higher temperatures. At all magnetic fields we find that thermal fluctuations start to contribute to the suppression of the Josephson coupling above a certain characteristic temperature. Although pinning probably has some influence even above this temperature, it is instructive to compare the observed behavior of the JPR frequency with its expected behavior in clean materials. The important feature, induced by thermal fluctuations, is the vortex lattice melting. Recent extensive numerical simulations of the anisotropic frustrated XY model [128, 137−140] and Bose model (interacting elastic strings) [141] allow us to reliably predict both the location of the melting transition and the nature of the liquid phase based only on the intrinsic superconducting parameters, s, λ_{ab}, and λ_c. These results are obtained within the "frozen field" approximation and are quantitatively valid for superconductors with not very high anisotropy, $\gamma < \lambda_{ab}/s$, and at sufficiently high fields, $B > \Phi_0/4\pi\lambda_{ab}^2$. In this regime the relevant properties of the melting transition in a pinning-free material can be summarized as follows: (i) the crossover between linelike and pancake regimes of melting takes place in the field interval $B = C\Phi_0/(\gamma s)^2$, where $C \approx 3 - 10$ [139]; (ii) in the linelike regime the melting temperature is given by $T_m \approx 0.13\epsilon_0 a/\gamma$ with $\epsilon_0 = \Phi_0^2/(4\pi\lambda_{ab}^2)$ and $a = \sqrt{\Phi_0/B}$ [142]; (iii) the latent heat of the transition per vortex per layer, Δe, is almost field-independent with $\Delta e \approx 0.015 s\varepsilon_0$; (iv) in the linelike regime the loss in the Josephson energy at the melting point constitutes half of the latent heat and the jump of the coherence factor is given by $\Delta\langle \cos \varphi \rangle \approx 0.05\gamma^2 s^2 B/\Phi_0$.

In the case of Tl-2212 the anisotropy factor $\gamma \approx 100 - 150$ is comparable with the ratio λ_{ab}/s and the magnetic coupling between pancake vortices in neighbor-

ing layers may influence the melting transition. We will estimate the shift of the melting point caused by the magnetic coupling using perturbation theory. Using the approach of Reference 143, we calculate the correction to the crystal free energy per vortex per layer due to the magnetic coupling as:

$$\delta f_M = -2\pi s\varepsilon_0 a^{-2} \sum_{\mathbf{Q}\neq 0} \frac{\exp\left(-Q^2 \left\langle u^2 \right\rangle /2\right)}{\left(1+\lambda^2 Q^2\right) Q^2}, \tag{4.33}$$

where $\mathbf{Q}$ are the reciprocal lattice vectors, and $\langle u^2 \rangle$ is the mean-squared fluctuation of the vortices. At the melting point $\langle u^2 \rangle \approx c_L^2 a^2$ with $c_L \approx 0.25$ [139, 141], and one can keep only the first 6 terms in the Q-sum corresponding to the smallest vectors $\mathbf{Q}_0$ with $Q_0^2 = \left(8\pi^2/\sqrt{3}\right) a^{-2}$. At high fields, $B > \Phi_0/\left(4\pi\lambda_{ab}^2\right)$, we obtain the following estimate for δf_M at the melting point:

$$\delta f_M(T_m) \approx -0.044 \frac{s\varepsilon_0 a^2}{4\pi\lambda_{ab}^2} \tag{4.34}$$

The shift of the relative melting temperature due to a small perturbation of the crystal free energy is given by

$$\delta \frac{T_m}{s\varepsilon_0} = -\frac{T_m}{s\varepsilon_0} \frac{\delta f_M}{\Delta e} \tag{4.35}$$

and, we obtain for the corrected melting point:

$$\frac{T_m}{s\varepsilon_0} \approx 0.13 \frac{a}{\gamma s} \left(1 + 0.23 \frac{a_2}{\lambda_{ab}^2}\right) \tag{4.36}$$

We calculate the temperature and field dependence of the interlayer phase coherence factor, $\langle \cos\varphi_{n,n+1} \rangle$, in the vortex solid phase neglecting pinning but accounting for Gaussian thermal fluctuations of pancakes [134], taking into account both Josephson and magnetic coupling between the layers. Calculations are based on the Lawrence-Doniach model in the London limit, which is completely defined by the components of the London penetration depth (λ_c and $\lambda_{ab} = \lambda_c/\gamma$), and the lattice parameter along the c-direction, $s = 15$ Å. We extract λ_c directly

from the JPR frequency assuming $\epsilon_0 = 9.1$ provided in Reference 144. We find that the best agreement between calculation and experiment is achieved using $\gamma = 150$. This value is consistent with the resistivity anisotropy of Tl-2212 single crystals near T_c [145]. The calculation results together with the experimental data, are shown in Figure 4.31. The position of the expected melting transition shown by arrows was estimated from Equation (4.36). Melting close to the arrows is supported by our recent dc transport measurements and magnetization measurements (unpublished). The field dependence is completely smooth near the expected melting transition. These results strongly implies that vortex lines are preserved across the melting transition, at least in the low magnetic field portion of the phase diagram.

In conclusion, we have measured the JPR in Tl-2212 thin films using THz-TDS in transmission. We used the JPR frequency measurements as a probe to study the interlayer phase coherence as a function of temperature and magnetic fields above and below the melting line. Our results show that in Tl-2212 vortex lines exist in the liquid state in magnetic fields below 2.5 kG. We conclude that Tl-2212, at least in the low magnetic field portion of the phase diagram, behaves as Y-123, and not as Bi-2212 despite the closer anisotropy ratios.

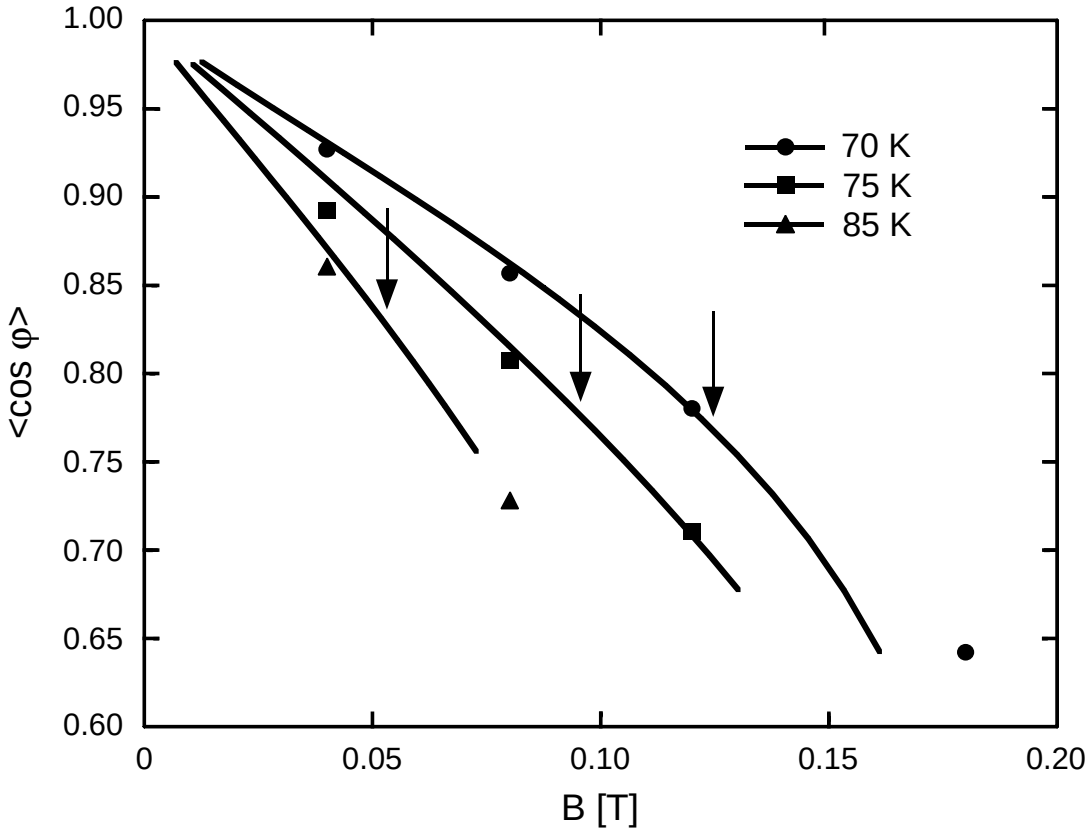

Figure 4.31: Comparison between experimental data (marks) for the interlayer phase coherence factor $<\cos\phi_{n,n+1}>$ in Tl-2212 at 70, 75, and 85 K, and numerical calculations (solid lines) based on Reference 134 across the melting transition. The arrows indicate the position of the melting transition estimated from Equation (4.36). Calculations were done using λ_c extracted directly from the JPR frequency with $\epsilon_o = 9.1$ and assuming the anisotropy factor to be $\gamma = 150$.

4.5 Current-driven Vortex State in $Tl_2Ba_2CaCu_2O_8$ Probed by the Josephson Plasma Resonance

The properties of driven periodic structures subject to quenched disorder, including charge-density waves, Wigner crystals and vortex lattices, have become one of the central issues in the phenomenology of nonequilibrium statistical mechanics [146−151]. In the context of the vortex lattice, Koshelev and Vinokur [147] predicts the driven system to undergo a dynamic phase transition at some threshold current between the fluidlike and crystallike moving states. In other words, an applied current puts forth a scenario where a pinned vortex lattice flows plastically at first as some vortices are depinned, and then becomes more ordered at higher applied currents as more vortices are depinned, possible forming a moving ordered vortex lattice. Thus, beyond some critical value a dynamic phase transition may occur to a more ordered state, characterized by a change from incoherent to coherent vortex motion.

Previous experimental techniques employed in studying the transformations of the moving states (dynamic phase transitions) include detection of anomalies in the I-V characteristics [151, 152], and changes in the correlation length which reflects the order of the moving lattice [153−155]. Until now, the most direct measurement is by neutron diffraction, where the continuous development of the order of the vortex lattice can be followed as long as Bragg diffraction spots are detectable [153].

Here we present the first studies of the current-driven vortex lattice in a high-T_c superconductor by directly probing the interlayer phase coherence with the JPR. The experiments were performed on Tl-2212 thin films using THz-TDS in transmission (see Figure 4.7) [20]. The Tl-2212 film (700 nm) was grown

on a 12 × 12 mm^2 MgO substrate as described in Section 4.2, and exhibited a sharp transition temperature (0.2−K width) at T_c = 102.5 K. Current leads were attached along the ends of two opposite sides, thus providing a homogeneous current flow across the film. The sample was positioned inside an optical cryostat with optical access, between a pair of permanent magnets with the magnetic field oriented along the *c*-axis. All experiments were performed in field cooled mode. The configuration of the sample with respect to the THz beam, and obtaining the complex transmission coefficient of the Tl-2212 film as a function of frequency is described in Section 4.2.

Figure 4.32 shows the interlayer phase coherence factor as a function of current in the *ab*-plane at 10, 60, 80, and 90 K in a 2.5 kG *c*-axis applied magnetic field. The current exerts a Lorentz force on the vortices. At 10 K the effect of the current is very small because the vortices are strongly pinned in the vortex solid phase. At 60 K the pinning is weaker, and the drop of the factor is more pronounced with increasing current. One sees a weak knee structure at approximately ∼20 mA, where the slope of the factor is increased. The scenario where some vortices are moving while others are still pinned is well described by the ice flow case. When a frozen river starts to melt, rivers of water will flow through where the ice is melted, while islands of unmelted ice is still stuck. At 80 K the first slope of the factor is approximately the same as for 60 K with increasing current up to the knee structure which is occuring approximately at ∼16 mA for 80 K. The second slope is slightly steeper than for 60 K. Then the 80 K factor displays a very pronounced increase at approximately ∼32 mA, which was not observed for 60 K. The pinning is even weaker for 80 K, and the vortex lattice is driven into the flux-flow state at higher currents. At the point where all the vortices flow, the order of the vortex lattice actually improves. This is the effect which was predicted by Koshelev and Vinokur [147] described earlier,

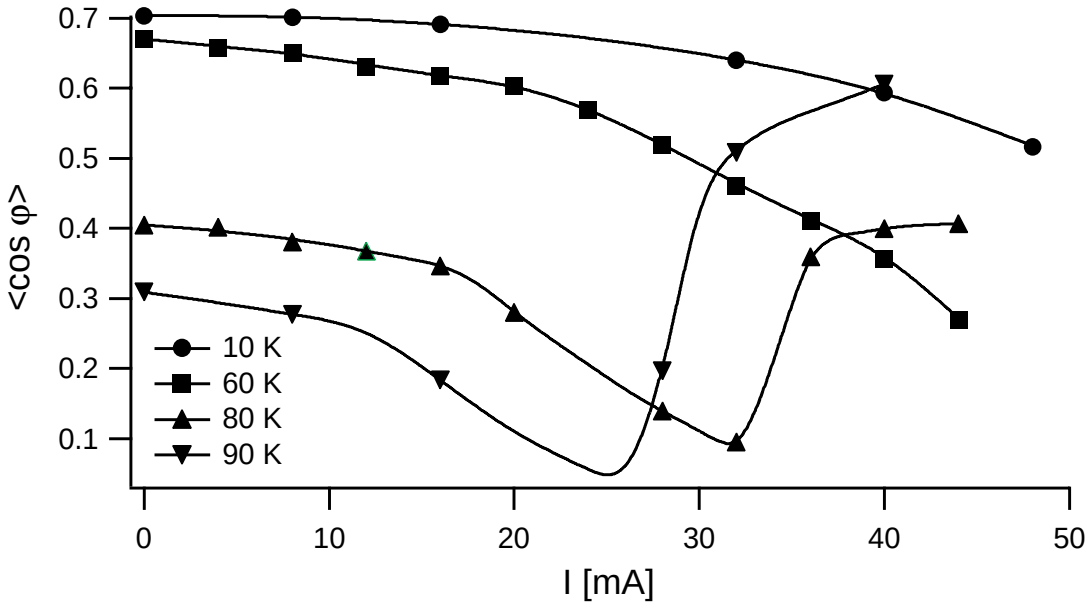

Figure 4.32: Interlayer phase coherence factor $<\cos\phi_{n,n+1}>$ versus applied ab-plane current in Tl-2212 in 2.5 kG c-axis magnetic field at 10, 60, 80, and 90 K.

where the vortex lattice is proposed to undergo a dynamic phase transition at some threshold current between the fluidlike and crystallike moving states. The same phenomenon is observed for 90 K, where the first knee structure occurs at approximately ∼9 mA, and the second at approximately ∼24 mA. The factor displays a third knee structure for both 80 K (∼36 mA) and 90 K (∼31 mA), which is observed to decrease in current and get steeper from 80 K to 90 K. Thus, this indicates pinning is not completely absent, even in the vortex liquid phase.

When the Tl-2212 film is field cooled in zero current, the system enters a disordered, pinned nonequilibrium state as it passes through H_{c2} and remains disordered as it is further cooled to 10 K because the pinning free energy barriers are to high to cross. As the applied current is then increased, the pinning potential is reduced and some vortices are depinned, resulting in a slight disorder of the vortex lattice. At 80 and 90 K, the pinning potential has been reduced so much that at a certain threshold current the system is completely driven into the flux-

flow state where the vortex-vortex interactions become important, resulting in the recrystalization of the vortex lattice. After the applied current is turned off, and the temperature raised, it is found that the order of the system has increased compared to when the system has not been subjected to the application of a current. It is interesting to note that the order of the vortex lattice depends on the history of the sample's current in addition to temperature and field.

CHAPTER 5

Ultrafast Conductivity Dynamics of Hole Doped Transition Metal Oxides

Ultrafast optical pump-probe experiments are a proven tool to temporally discriminate dynamic processes such as electron-electron, electron-phonon, and spin-lattice interactions to better understand the properties of materials. During the past several years these techniques have been increasingly applied to complex materials, such as hole doped transition metal-oxides including high-T_c superconductors and mixed valence manganites. In these materials even the ground state properties are strongly influenced by many body effects such as on-site coulomb repulsion, Hund's-rule coupling, and polaronic effects. Importantly, the defining characteristic of many of the hole doped transition metal oxides is the conductivity as a function of temperature, applied magnetic field, or frequency. As has been seen in Chapter 4, THz spectroscopy is an excellent tool to probe the low-lying excitations of materials. Therefore, by combining THz spectroscopy with optical excitation, dynamics can be resolved in the time-domain providing another experimental handle with which to understand material properties.

The experimental set-up of the time-resolved optical pump THz probe spectrometer in transmission, used for these experiments, is shown in Figure 5.1. The concepts of the experiment and how to obtain the induced conductivity as a function of pump-probe delay time is explained in Chapter 2.3.

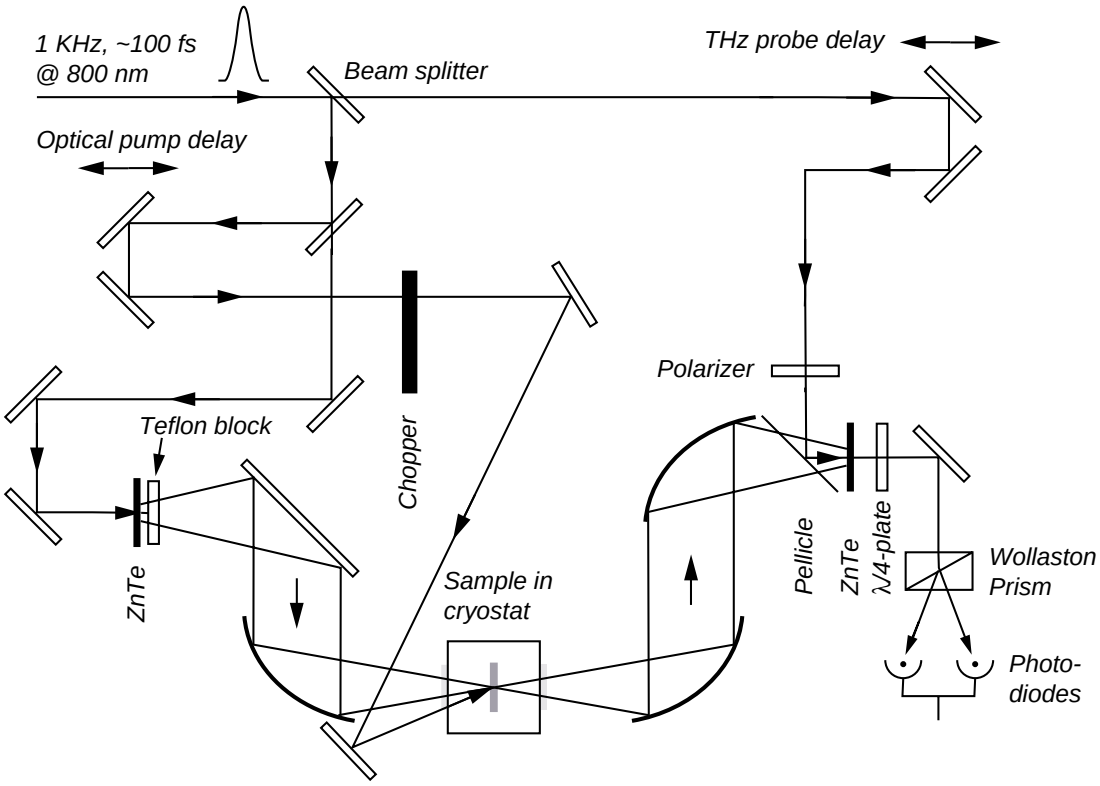

Figure 5.1: Experimental set-up of optical-pump terahertz-probe spectrometer in transmission.

5.1 Nonequilibrium Superconductivity in $Y_{1-x}Pr_xBa_2Cu_3O_7$ Thin Films

THz-TDS is an ultrafast optical technique that has found wide application in the study of many systems having far-infrared excitations. In the context of correlated electron materials, THz-TDS has been successfully applied to study high-T_c superconductors and, more recently, materials such as the ferromagnetic metal $SrRuO_3$ [156, 157]. We can expect an increase in the use of THz-TDS to study a variety of other correlated electron materials given its unique ability to directly and easily measure $\sigma_{re}(\omega) + i\sigma_{im}(\omega)$ from ∼50 GHz to several THz.

Importantly, the freely propagating THz pulses generated in THz-TDS are

temporally coherent with the generating optical pulses - this permits measurement of the THz conductivity with picosecond resolution following optical excitation of the sample. Several groups have been developing this technique, termed time-resolved THz spectroscopy (TRTS), to study various systems including photogenerated electrons in liquids such as hexane, or semiconductors such as GaAs or radiation damaged silicon-on sapphire [158−160]. Previous work in our group has focused on using TRTS to study high-T_c superconductors and colossal magnetoresistance manganites [57, 58, 161]. Here we present our most recent measurements on $Y_{1-x}Pr_xBa_2Cu_3O_7$ thin films.

Figure 5.2(a) and (b) show the conductivity at 60 K and 95 K respectively (T_c = 89 K) for the near optimally doped film. The phenomenological two-fluid model fits the data quite well (shown in dashed line in Figure 5.2(a)) below T_c where the imaginary conductivity is dominated by the $1/\omega$ dependence of the superfluid [57, 162]. Above T_c, a standard Drude model fits the data (dashed line Figure 5.2(b)). Upon optical excitation, there is a decrease in the imaginary conductivity due to superconducting pair breaking with a corresponding increase in the real component (not shown). The induced change in $\sigma_{im}(\omega)$ is shown at 60 K in figure 1(c). There is a decrease that rapidly recovers on a ps timescale that is due in large part to superconducting pair reformation. Figure 5.2(d) shows the induced change in $\sigma_{im}(\omega)$ at 95 K (above T_c) which is due quasiparticle relaxation.

The dynamics can be followed by plotting the induced change in the conductivity as a function of time at a specified frequency. The induced change in the imaginary conductivity (60 K) is shown in Figure 5.3. With increasing frequency, the lifetime decreases (see inset). In the limit of zero quasiparticle fraction, this induced change would be solely due to superconducting pair recovery. However, there are quasiparticles present (at 60 K the initial quasiparticle

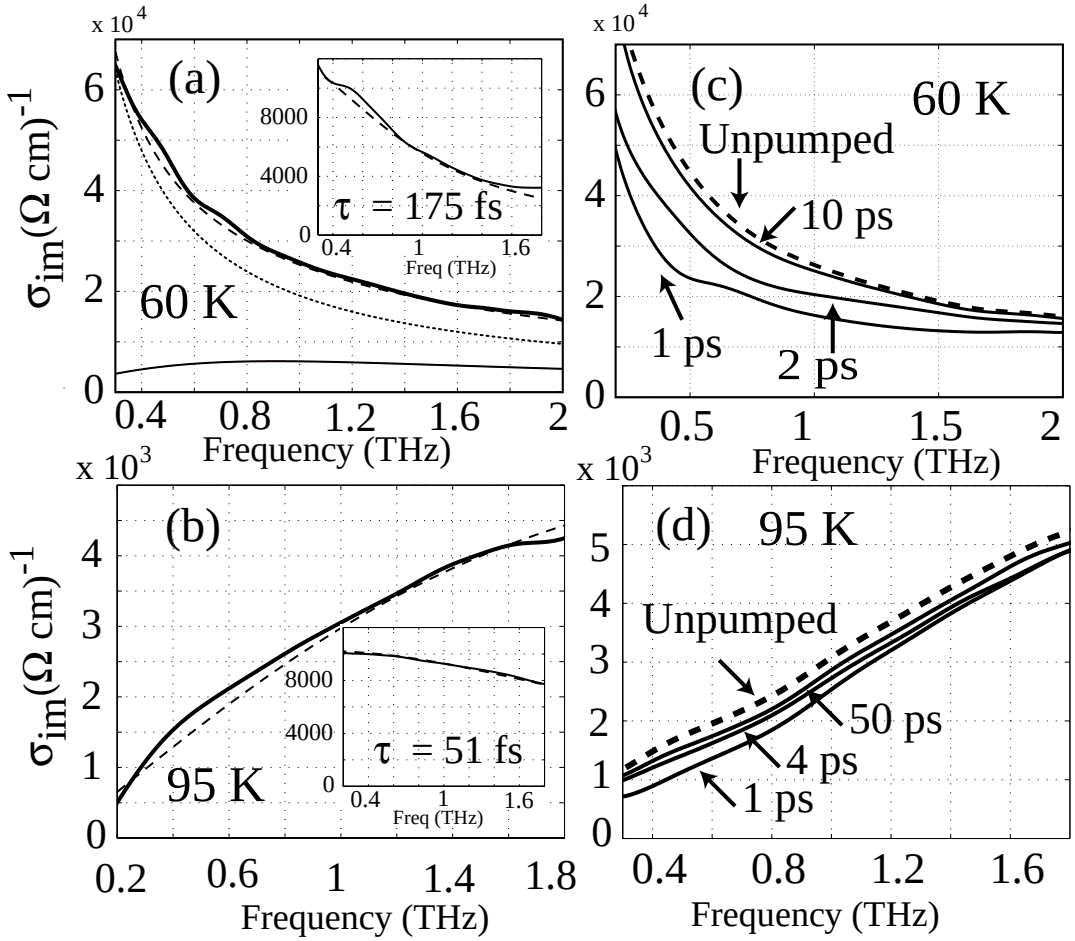

Figure 5.2: (a)-(b) Conductivity at 60 K and 95 K, respectively. The imaginary conductivity is shown with the real conductivity in the insets. Below T_c the data is fit using a two-fluid model. The thick solid line is the experimental data. The dashed lines are the overall fit to the data. In (a), the dotted line is the superconducting pair component and the thin solid line is the quasiparticle component. (c)-(d) Optically induced changes in the imaginary conductivity at 60 and 95 K.

fraction is ∼40%) so (see inset in Figure 5.2(b)) the quasiparticle fraction makes a nonnegligible contribution to $\sigma_{im}(\omega)$. Importantly, at higher frequencies this fraction becomes increasingly important since the superconducting pair fraction response goes as $1/\omega$. This offers a potential explanation for the decrease in the lifetime of $\sigma_{im}(\omega)$ with increasing frequency: at low frequencies $\sigma_{im}(\omega)$ is dominated by the superconducting pair recovery, but at higher frequencies the relaxation is increasingly influenced by an additional relaxation pathway associated with the quasiparticles. This is further supported in that the lifetime of $\sigma(\omega)_{re}$ is quite short (∼1.5 ps independent of frequency). Speculating on the origin of this additional relaxation pathway, it could be due to the relaxation of the excited quasiparticles into the nodes of the superconducting gap along $k_x = k_y$. Since this process is faster than the superconducting pair recovery, this would suggest that the excited quasiparticle relax into the nodes of the gap followed by pair recovery.

Finally, the results of the superconducting pair recovery time as a function of temperature are consistent with previous results [57]. For optimal doping, the lifetime at 20 K is about 1.5 ps (at 1.0 THz) increasing to 3.0 ps near T_c. Above T_c, the lifetime of $\sigma_{im}(\omega)$ (which is no longer a measure of the superconducting recovery time, but rather the initial quasiparticle cooling) drops to 1.5 ps (this is also consistent with the discussion in the previous paragraph). In contrast, in the $x = 0.3$ films the lifetime is ∼3.5 ps independent of temperature even above T_c. This lifetime is the same as that measured in our $YBa_2Cu_3O_{6.5}$ films. These results suggest that for the optimally doped films, the dynamics are influenced by the closing of the superconducting gap, and that for the underdoped films, the pseudogap plays a role in determining the observed dynamics. Further experiments are ongoing to more fully elucidate the observed dynamics as a function of temperature and doping.

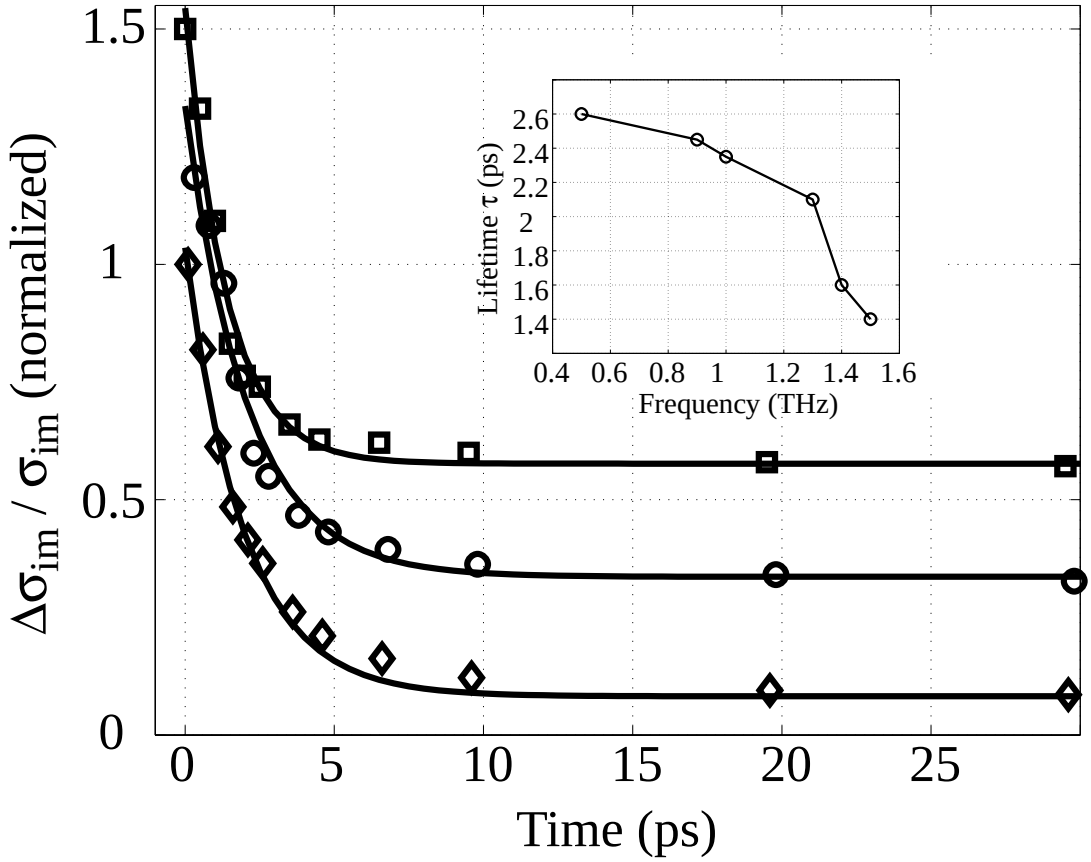

Figure 5.3: Normalized induced change in the imaginary conductivity (60 K) as a function of time at various frequencies. The curves are displaced vertically for clarity. The solid lines are fits to the function y = a×exp(-t/τ_σ) + b. The inset shows the measured lifetime as a function of frequency.

5.2 Colossal Magnetoresistance Manganites

5.2.1 Basic Theory of Colossal Magnetoresistance Manganites

Mixed valence manganites such as doped $La_{1-x}Ca_xMnO_3$ have been studied since the 1950's. Particularly, in the past 10 years research has intensified, primarily because of an increased interest in the colossal negative magnetoresistance observed for certain levels of doping (see Figure 5.4).

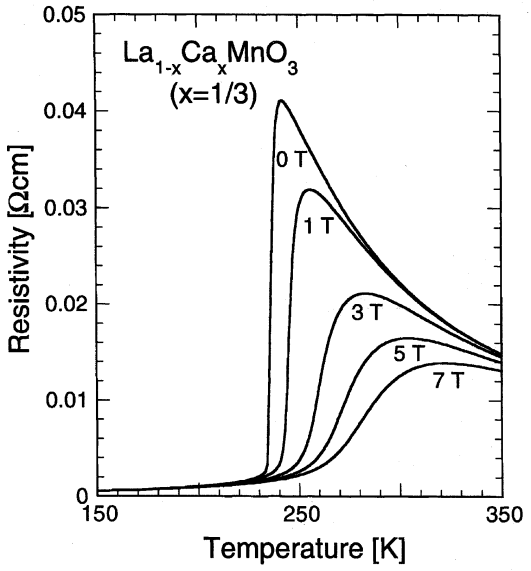

Figure 5.4: Temperature profile of resistivity of a $La_{1-x}Ca_xMnO_3$ ($x = 0.3$) single crystal at various magnetic fields. A strong negative magnetoresistance is observed close to the Curie temperature. (© Copyright (2000) OPA (Overseas Publishers Association) N. V. Figure 1, Chapter 1 in Reference 4).

The magnetic phase diagram of $La_{1-x}Ca_xMnO_3$ is shown in Figure 5.5. The parent compound is best described as an antiferromagnetic charge transfer insulator (typical of undoped transition metal oxides) with the relevant band originating from the manganese $3de_g$ orbital. With increasing doping with a divalent substituent such as Ca one gets a mixture of Mn^{3+} and Mn^{4+} (hence

the term "mixed valence manganites"). The magnetic phase diagram displays a richness of phases including a canted ferromagnet, crossing over to a ferromagnetic metal, etc. Eventually at all dopings with increased temperature there is a crossover to a paramagnetic phase. These experiments (Chapter 5.2.2) will focus on $La_{1-x}Re_xMnO_3$ (Re = Ca, Sr with $x = 0.3$) which displays ferromagnetic metallic behavior crossing over to a paramagnetic behavior at ∼260 K for Re = Ca and 350 K for Re = Sr.

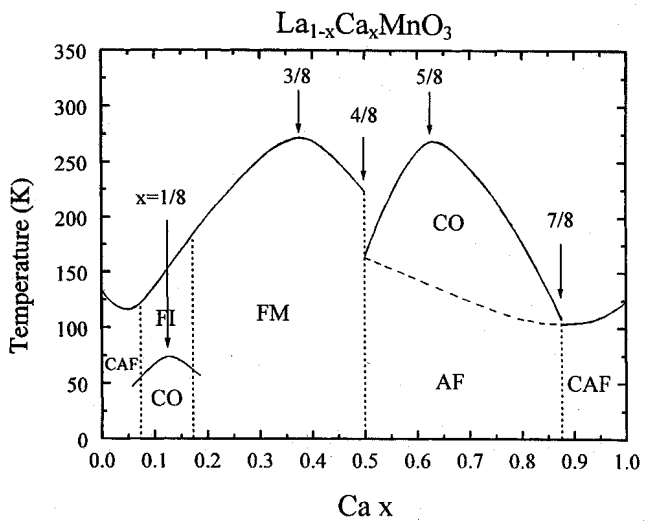

Figure 5.5: Magnetic phase diagram of $La_{1-x}Ca_xMnO_3$. The abbreviations mean ferromagnetic metal (FM), ferromagnetic insulator (FI), antiferromagnetism (AF), canted antiferromagnetism (CAF), and charge/orbital ordering (CO). (© Copyright (2000) OPA (Overseas Publishers Association) N. V. Figure 1, Chapter 7 in Reference 4).

The important entity of interest is the manganese atom. It is situated in an octahedrally coordinated environment surrounded by six oxygen ions. Its $3d$ electrons experience, due to crystal field effects, a splitting of the levels as shown in Figure 5.6. The t_{2g} levels comprise an electronically inert core of total spin 3/2. The higher level e_g electrons form the conduction band. Due to large Hund's-rule coupling the spins are all aligned on a given manganese, meaning the e_g spin is slaved to the t_{2g} spin.

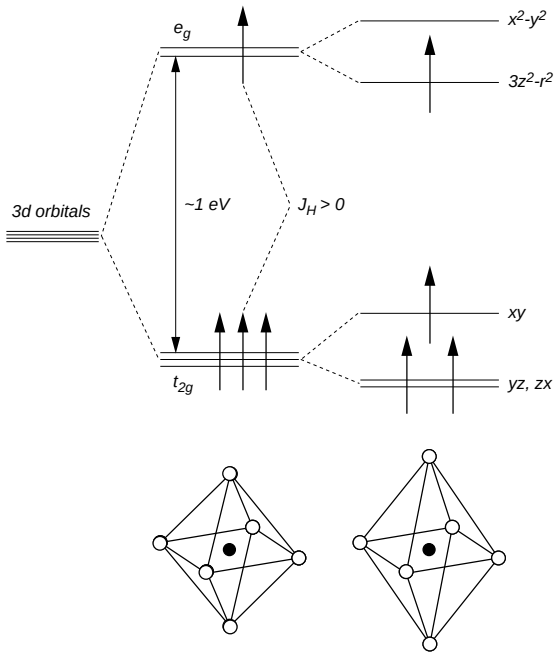

Figure 5.6: Crystal ligand-field splitting of five-fold degenerate atomic $3d$ levels into lower t_{2g} (triply degenerate) and higher e_g levels (doubly degenerate levels of Mn^{3+}). Jahn-Teller distortion of MnO_6 octahedron further lifts each degeneracy as shown in the figure.

Conduction proceeds via what is historically known as double-exchange (see Figure 5.7) in which transport is via hopping from one manganese to another via an intermediate oxygen. There is a hopping integral $t_{ij} = t\cos\theta_{ij}$ that characterizes the conductivity that depends on the relative angle of the spins between nearest neighbor Mn ions. In other words, in the paramagnetic phase where there is no spin alignment the hopping integral is much smaller than in the ferromagnetic regime where the spins are aligned, making it easier for an e_g electron on one Mn ion to jump to another Mn ion. However, magnetic scattering alone cannot account for the large values of the resistivity observed in the paramagnetic regime. Thus, the lattice degrees of freedom must also be considered. First, there can be a distortion of the Mn-O-Mn bond angle (see Figure 5.8) which is defined by a tolerance factor $f = (r_a + r_o)/\sqrt{2}(r_b + r_o)$. f measures the lattice

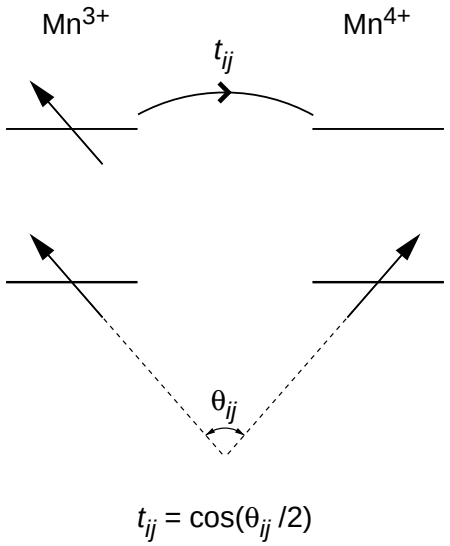

Figure 5.7: Illustration of the double-exchange mechanism via the transfer integral t_{ij} (hopping matrix).

mismatch between the AO-planes and the adjacent BO_2-planes, where r_a is the average A-site radius for La, Ca, or Sr, and r_b is the Mn ionic radius. So, in decreasing r_a the tolerance factor gets smaller which means the Mn-O-Mn bond angle is distorted from 180 degrees. The reduced overlap between the manganese and oxygen orbitals then reduces the hopping integral.

Perhaps even more important are the Jahn-Teller distortions of the O_6 octahedra surrounding the Mn ions. When the e_g orbital is occupied the orbital degeneracy of the e_g level is removed by the distortion of the ideal octahedral structure with this being a more favored energy state. With increasing doping with Ca^{2+} the long range coherent Jahn-Teller distortion is decreased, as there is no such distortion for Mn^{4+}. In this case the Jahn-Teller distortion is dynamic, traveling with the carriers. The paramagnetic phase has misaligned spins which lowers the hopping rate. This means the dynamic Jahn-Teller distortions can follow the electrons around as they hop. This results in the trapping of the electrons which causes an increased resistance in the paramagnetic phase. When the tem-

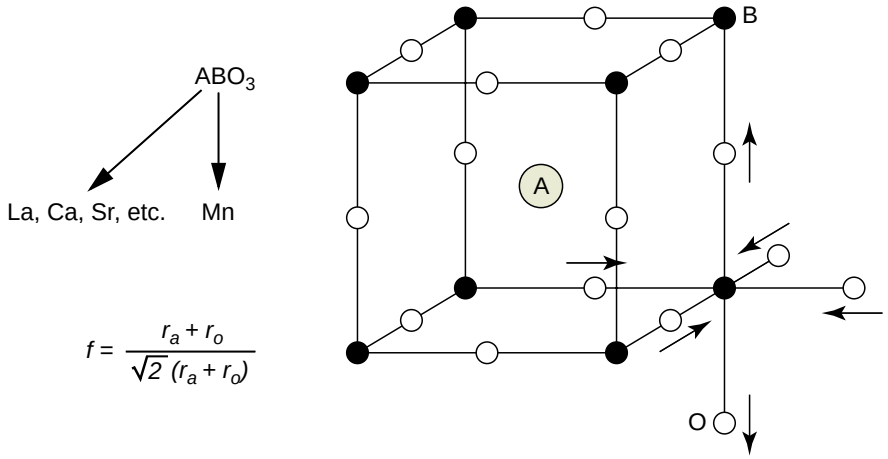

Figure 5.8: Schematic crystal structure of $La_{1-x}Ca_xMnO_3$. The tolerance factor f measures the distortion from the perovskite-based cubic structure. $f \sim 1$: ideal perovskite structure. $0.96 < f < 1.0$: rhombohedral structure. $f < 0.96$: orthorhombic structure.

perature is decreased below the Curie point the relative spin alignment increases, resulting in an increase in the hopping rate. That means that the Jahn-Teller distortion can no longer trap the carriers which means there is a large increase in conductivity in the ferromagnetic phase.

5.2.2 Ultrafast Conductivity Dynamics in Colossal Magnetoresistance Manganites

The observation of "colossal" negative magnetoresistance (CMR) in the hole-doped manganite perovskites ($R_{1-x}D_xMnO_3$ where, e.g., R = La, Nd and D = Ca, Sr) demonstrates the sensitivity of electronic conduction to the underlying magnetic structure in these materials [163, 164]. Experimental and theoretical work has also revealed the importance of the lattice and orbital degrees of freedom in determining the electronic properties of CMR materials above and below T_c [165, 166]. Nonetheless, it is still not clear, especially for $T \ll T_c$, what the relative importance of phonons is in comparison to double-exchange in determining σ.

Ultrafast optical spectroscopy has provided significant insight into electron dynamics in metals [167−169], and more recently, transition metal oxides [56, 170, 171]. Using similar ultrafast techniques, we address the relative contributions of spin fluctuations and phonons in determining the conductivity in the manganites from ∼10 K to $0.9T_c$.

THz-TDS is an ultrafast optical technique in which electric field transients are used to measure the complex conductivity of a material. Since this is a coherent technique, a sample can be optically excited and then probed with a terahertz pulse to measure induced conductivity changes with picosecond (ps) resolution. We use this method, known as time-resolved terahertz spectroscopy (TRTS), to measure ps conductivity transients in $La_{0.7}Ca_{0.3}MnO_3$ (LCMO) and $La_{0.7}Sr_{0.3}MnO_3$ (LSMO) thin films. The dynamics occur on two time scales. A fast, ∼2 ps, conductivity decrease arises from optically induced modification of the effective phonon temperature. The slower component, related to spin-lattice relaxation, has a lifetime that increases upon approaching T_c from below in accordance with an increasing spin specific heat. Our results demonstrate that, at low temperatures, $\partial\sigma/\partial T$ is primarily determined by thermally disordered phonons while spin fluctuations dominate close to T_c.

The TRTS experiments were performed on LCMO and LSMO epitaxial thin films grown on $LaAlO_3$ substrates using pulsed laser deposition [172]. For very thin films (∼150 Å), island growth can alter the film properties, but the thicker films used in these experiments (∼1000 Å) display bulk behavior [173]. Magnetization measurements yield T_c = 250, 360 K for the LCMO and LSMO films respectively. The experiments utilized a regeneratively amplified Ti:Al_2O_3 system operating at 1 KHz and producing nominally 1.0 mJ, 150 fs pulses at 1.5 eV. The absorbed fluence for LCMO (LSMO) was 170 (110) $\mu J/cm^2$ corresponding to an

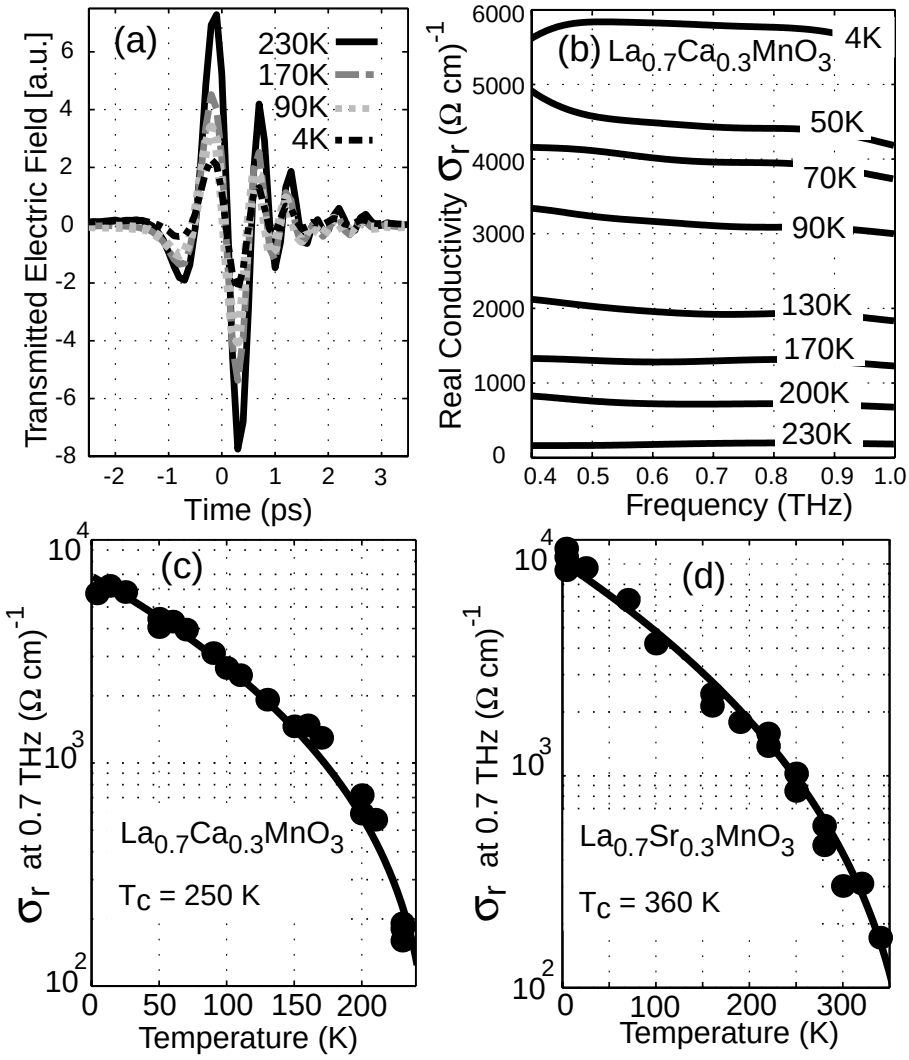

Figure 5.9: Temperature dependence of the THz transmission and real conductivity. (a) Transmitted electric field at various temperatures for a 90 nm thick LCMO film (see legend). (b) Real conductivity versus frequency for LCMO at various temperatures. (c and d) The value of the real conductivity at 0.7 THz as a function of temperature for LCMO and LSMO thin films. The lines are fits using Equation (5.1).

initially excited carrier density of $\sim 8{\times}10^{19}$ ($4{\times}10^{19}$) cm^{-3}. The THz pulses were generated and detected using electrooptic techniques. A He cryostat permitted temperature dependent measurements from 4−400 K. Further details of the film growth and TRTS experiments are described elsewhere [161, 172].

Figure 5.9(a) shows the THz electric field transmitted through a LCMO film at various temperatures without optical excitation. The magnitude decreases with decreasing temperature while the phase is relatively constant. This indicates an increase in the real conductivity as the temperature is lowered. Figure 5.9(b) displays the real conductivity versus frequency for the LCMO film at various temperatures as determined from the data in Figure 5.9(a). These conductivity measurements are in the regime $\omega\tau \ll 1$ (ω is the angular frequency and τ is the carrier collision time) as indicated by the flat frequency response. Figure 5.9(c and d) show the temperature dependence of σ_r at 0.7 THz for the LCMO and LSMO films respectively. The lines are fits to the conductivity using the following equation:

$$\sigma(T) = \sigma_o e^{M(T)/M_o} \tag{5.1}$$

where $M(T) \propto (1 - T/T_c)^{\beta}$ ($\beta \simeq 0.33$) is the magnetization and T_c is the transition temperature. This suggests, in agreement with dc resistivity measurements, that the conductivity is primarily determined by the magnetization below T_c [174]. However, this dependence on the magnetization cannot fully describe the nature of the conductivity in the manganites as indicated in more recent experiments [175, 176]. As shown below, our dynamic measurements also deviate from Equation (5.1).

Figure 5.10(a) shows the temporal evolution in the normalized peak THz electric field (plotted as 1 - ΔE where ΔE is the induced change in the transmitted electric field) transmitted through a LCMO film following optical excitation at

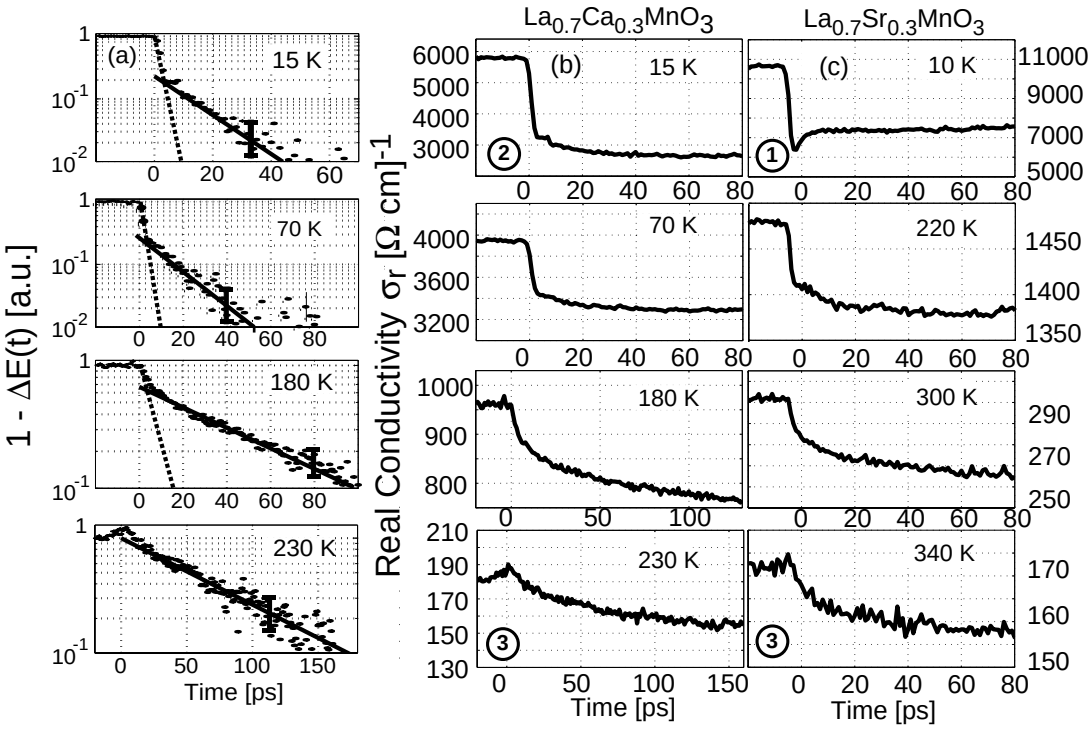

Figure 5.10: (a) One minus the normalized induced change in electric field ΔE versus time for LCMO film at various temperatures (dots). Two slopes are distinguishable - a shorter < 2 ps lifetime (dashed line) and a longer lifetime (solid line). (b and c) Real conductivity versus time at various temperatures. The circled numbers in (b) and (c) correspond to the description in the text using Figure 5.12(b). The uncertainty in the data is approximately given by the line thickness. There is also an absolute uncertainty of $\pm 5\%$ due to the uncertainty in the film thickness.

15, 70, 180, and 230 K. Two components characterize the increase in field transmission. The fast ∼2 ps component is resolution limited. However, the data in Figure 5.10(a) shows this component decreases in magnitude as the temperature is increased. The data in Figure 5.10(a) also reveal a slow component that increases in relative magnitude as the temperature is increased. As the temperature is increased the lifetime of the slow component increases.

In Figure 5.10(b and c) the temporal evolution of the optically induced change in absolute conductivity at various temperatures is plotted for the LCMO and LSMO films. In each sample the fast component decreases in absolute magnitude and in relative magnitude to the slow component as the temperature is increased. The lifetime of the slow component increases with temperature for both films. The plateau in the conductivity at longer times corresponds to equilibrium between the electrons, spins, and phonons, albeit at a higher temperature than before the arrival of the pump. On a ns time scale the film recovers to the initial temperature as the phonons leave the film via thermal transport to the substrate.

To understand the measured dynamics, we consider a model where the spins and lattice are coupled subsystems having well defined temperatures T_s and T_p respectively:

$$C_p \frac{\partial T_p}{\partial t} = -G_{sl}(T_p - T_s) \tag{5.2}$$

$$C_s \frac{\partial T_s}{\partial t} = +G_{sl}(T_p - T_s) \tag{5.3}$$

These differential equations describe the energy transfer between the phonons and spins. C_p (C_s) is the lattice (spin) specific heat and G_{sl} is the spin-lattice coupling constant. The initial optical excitation creates a distribution of excited electrons with the same spin orientation as in the ground state, since the initial and final states are coupled via dipole-allowed matrix elements which forbid spin flip transitions. Furthermore, most mechanisms which flip spins conserve total

spin. Thus, the initial 2 ps decrease in the conductivity is not related to an ultrafast demagnetization, but rather to a change in the phonon temperature as the excited electrons relax through electron-phonon coupling. Equations (5.2) and (5.3) describe the dynamics subsequent to this electron-phonon equilibration. On a longer time scale, spin reorientation occurs due to the combined effects of spin-orbit coupling and momentum scattering (i.e. a scattering process which breaks translational invariance is required in addition to spin-orbit coupling [177]). We attribute the longer time-scale conductivity dynamics to such a process and use Equations (5.2) and (5.3) to describe this spin-lattice relaxation.

Figure 5.11(a and b) shows the measured lifetimes of the slow component as a function of temperature for LCMO and LSMO. The solid lines are calculations from numerically solving Equations (5.2) and (5.3) using fits to the specific heat data of [178] (LCMO) and [179] (LSMO). The spin-lattice lifetime can be approximated as $\tau_{sl} = C_s/G_{sl}$ where G_{sl} is the spin-lattice coupling constant. For these calculations, G_{sl} was assumed independent of temperature. The agreement between experiment and theory in Figure 5.11 justifies this assumption yielding $G_{sl} = 2.5{\times}10^{15}$ ($5{\times}10^{15}$) W/(m^{3}K) for LCMO (LSMO).

The results of this two-temperature model can be extended to understand the induced change in conductivity ($\Delta\sigma$) as follows:

$$\Delta\sigma(t, T_p, T_s) = \frac{\partial\sigma}{\partial T_p}\Delta T_p(t) + \frac{\partial\sigma}{\partial T_s}\Delta T_s(t) \tag{5.4}$$

This equation shows that the temporal evolution of $\Delta\sigma$ depends on changes in the phonon $\Delta T_p(t)$ and spin $\Delta T_s(t)$ temperatures. It is important to have a measure of the relative importance of phonons and spins in determining σ. Such a measure is given by the quantity

$$\alpha \equiv \frac{\partial\sigma}{\partial T_s} \Big/ \frac{\partial\sigma}{\partial T_p}. \tag{5.5}$$

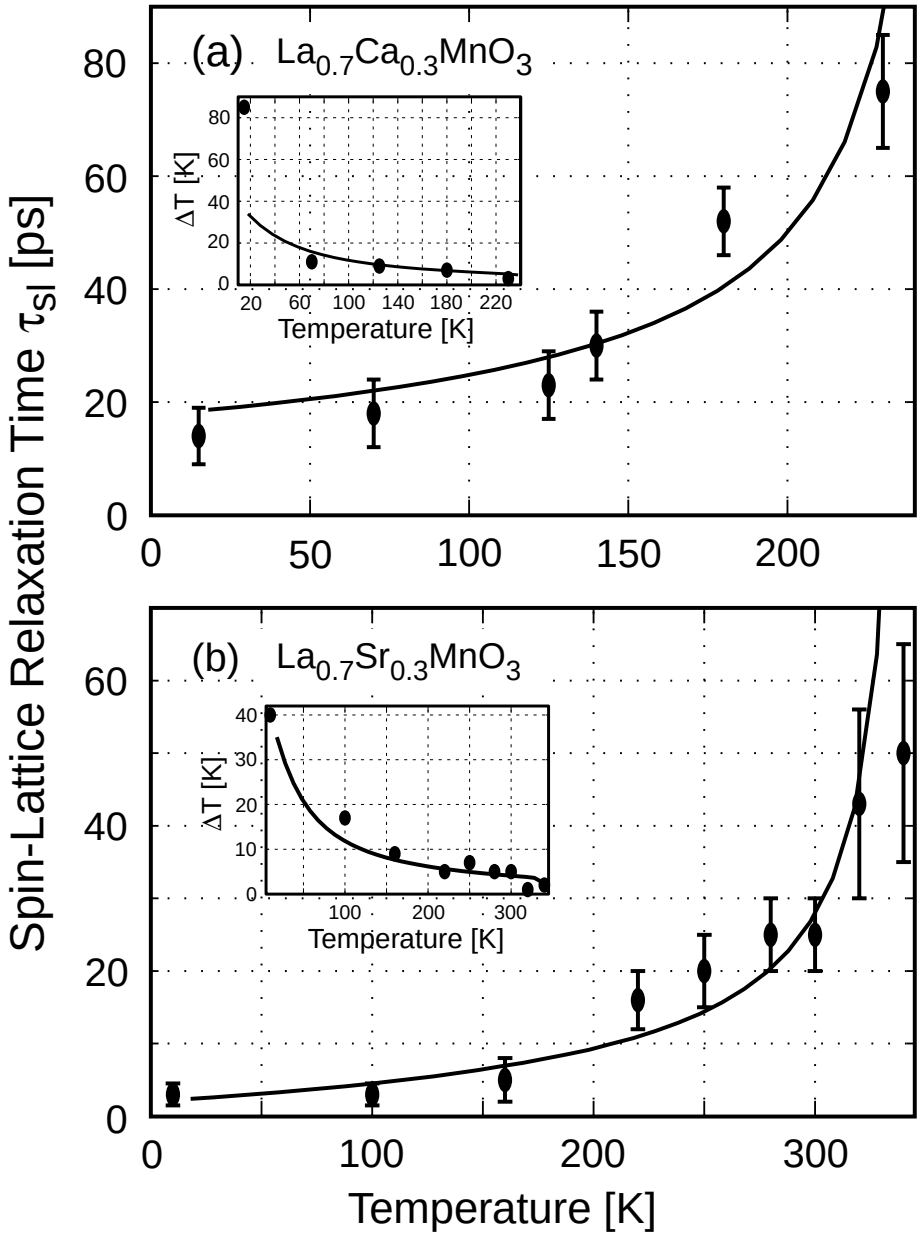

Figure 5.11: (a and b) Temperature dependence of the lifetime τ_{sl} of the slow component due to spin-lattice relaxation for LCMO and LSMO respectively. The solid line are fits as described in the text. The inset shows the induced temperature change as determined from the conductivity measurements (dots) and the calculations (solid line).

It can be shown that α is given by the ratio of the measured slow component amplitude divided by the fast component amplitude in the limit $C_s \ll C_p$. A plot of α is shown in Figure 5.12(a) for LCMO and LSMO as determined from the experimental data in Figure 5.10(b and c). For temperatures less than $\sim 0.5T_c$ ($0.7T_c$) for LCMO (LSMO), α is smaller than one indicating that phonons are the primary factor limiting hole transport in the e_g derived conduction band. In contrast, above these temperatures α is larger than one and continues to increase with temperature indicating that spin fluctuations predominantly determine σ. For LSMO, $\alpha < 1$ occurs at ~ 0.7 whereas for LCMO this occurs at ~ 0.5. This is consistent with other measurements which indicate that polaronic behavior persists to lower temperatures in LCMO than in LSMO.

The measured α places constraints on the dominant scattering mechanism. If holes are scattered primarily by thermally disordered ions, α would be small, as is observed at low temperatures. If they are scattered primarily by the simple double-exchange mechanism, α would be large, as is observed nearer to T_c. A more subtle case is a polaron / double-exchange scenario in which small polarons form only after the average hopping $<t>$ is reduced due to local spin misalignment. Although phonons are involved in this scenario, they are phonons that coherently form a polaron (not thermally disordered phonons), and $\partial\sigma/\partial T_s$ dominates $\partial\sigma/\partial T_p$, resulting in a large α.

It is possible to use the experimental data to extrapolate the conductivity in the T_s–T_p plane by expanding $\ln(\sigma(T_s,T_p))$ in a power series and performing a least-squares fit using the data in Figure 5.12(a) and Figure 5.9(c). This has been accomplished for LCMO by expanding $\ln(\sigma)$ to third order in T_s and T_p. The results are shown in Figure 5.12(b) as contours of constant $\ln(\sigma)$ in the T_s–T_p plane. Conventional measurement techniques (e.g. σ vs. T or H) do not

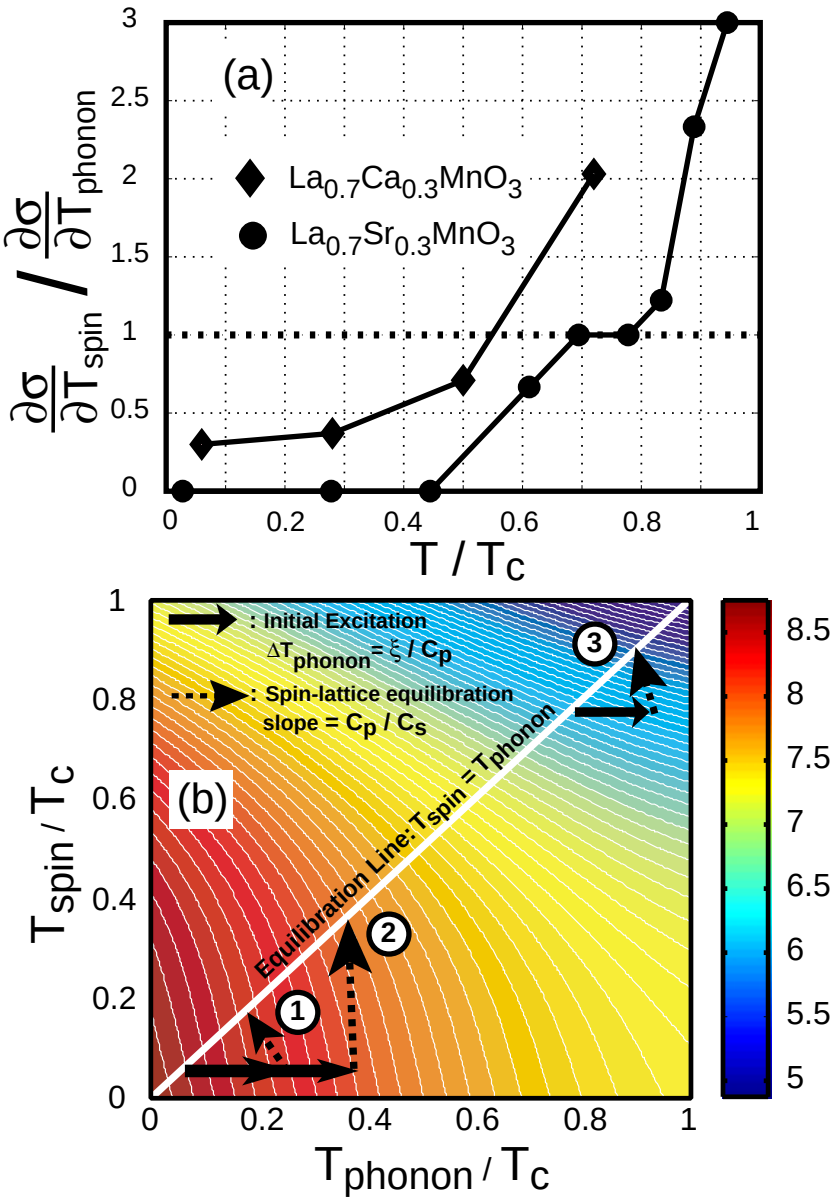

Figure 5.12: Temperature dependence of the THz transmission and real conductivity. (a) Transmitted electric field at various temperatures for a 90 nm thick LCMO film (see legend). (b) Real conductivity versus frequency for LCMO at various temperatures. (c and d) The value of the real conductivity at 0.7 THz as a function of temperature for LCMO and LSMO thin films. The lines are fits using Equation (5.1).

deviate from equilibrium as indicated by the white diagonal line in Figure 5.12(a). However, TRTS experiments, while starting from a point on the equilibrium line, allow for access to the portion of the $T_p - T_s$ plane below the diagonal equilibrium line since the excited electrons couple preferentially to the phonons during the initial 2 ps. This optically induced change in the phonon temperature is shown by the solid black arrow in Figure 5.12(b). The magnitude of this change is given by ξ/C_p where ξ is the deposited laser energy density. The system then returns to the equilibrium line as shown by the dashed arrows with the slope given by C_p/C_s. Depending on the initial temperature, ξ, and $C_{p,s}$, the observed conductivity decrease can depend predominantly on T_p, T_s, or both.

Figure 5.12(b) can be used to understand the dynamics shown in Figure 5.10 (b and c). The dynamics labeled by a 1 in Figure 5.12(b) show a decrease in σ as the lattice temperature increases followed by a slight recovery in the conductivity upon approaching the equilibrium line. In this case the change in σ depends primarily on the phonon temperature. In Figure 5.12(b) this is evident in that the contours of constant conductivity are nearly perpendicular to the phonon temperature axis. This is analogous to the data in the first panel of Figure 5.10(c), albeit for LSMO. Our model indicates that a slight cooling of the phonon distribution as it transfers heat to the spins accounts for the observed conductivity recovery (i.e. $\partial\sigma/\partial T$ remains negative as expected for the metallic behavior observed at these temperatures). Arrow 2 in Figure 5.12(b) again corresponds to a decrease in σ during the initial electron-phonon equilibration, followed by a further decrease in the conductivity as the spin temperature equilibrates with the lattice temperature. This two-component behavior is observed in LCMO at low temperatures (see Figure 5.10(b) panel 1) and indeed throughout most of the temperature range for LCMO and LSMO up to higher initial temperatures where, as arrow 3 in Figure 5.12(b) shows, the initial change in phonon temperature does

not result in a large change in σ: the decrease is due mostly to spin fluctuations. This is evident in that the contours of constant conductivity are now nearly perpendicular to the spin temperature axis. This is observed at higher initial temperatures in both LCMO and LSMO (see the bottom panels of Figure 5.10(b and c)).

In conclusion, we have measured the ultrafast conductivity dynamics in LCMO and LSMO thin films showing that $\partial\sigma/\partial T$ is determined primarily by thermally disordered phonons at low temperatures and by spin fluctuations at higher temperatures.

CHAPTER 6

Conclusions

The first measurements of the JPR in a high-T_c superconducting material in transmission have been demonstrated in Tl-2212 superconducting thin films using terahertz time-domain spectroscopy. Using this technique in zero field, the onset of the interlayer phase coherence is probed as close as $\sim$4 K below T_c. In addition, the c-axis quasiparticle conductivity was determined from the linewidth of the JPR's as a function of temperature, and I found indications of the superconducting order parameter to have d-wave symmetry in the dirty limit. Using the JPR as a tool to study the vortex structure, I found direct evidence for a linelike liquid phase in Tl-2212. The ordering of the vortex lattice probed by the JPR when driving it with a current in the ab-plane was studied at various temperatures. It was found that at higher temperatures, when driving the vortex lattice into the flux flow state, there is a threshold current above which the ordering improves with increasing current.

The JPR of high-T_c superconductors with extreme anisotropy such as the bismuth, thallium and mercury based high-T_c superconductors lies in the far-infrared and is thus amenable to study using THz-TDS. The advantage of using THz-TDS in transmission to measure the JPR, in comparison to the grazing angle reflectivity technique is an improved SNR which allows measurements close to T_c. Furthermore, the magnetic field dependence changes correctly with temperature, in contrast to the grazing angle reflectivity technique, where no change in the

field dependence was observed with temperature [135].

In this dissertation it was established that the vortex lattice in Tl-2212 melts into a linelike liquid phase for low magnetic fields ($B < 2.5$ kG). However, the structure of the vortex liquid phase at higher magnetic fields is still undetermined. Future JPR experiments at higher magnetic fields would aim to answer the questions of whether the vortex lattice melts directly into a disintegrated liquid of pancake vortices or if it is further subdivided into two liquid phases. Namely, a liquid of vortex lines immediately above the melting transition, and a disintegrated liquid of pancake vortices at higher temperatures.

In addition, the technique of THz-probe spectroscopy was shown to be a useful tool to study correlated electron materials such as Y-123 and $La_{0.7}Ca_{0.3}MnO_3$. In the case of the superconductors, phase coherent pair recovery occurs on a picosecond timescale following optical excitation. For the manganite films, it was found that $\partial\sigma/\partial T$ is determined primarily by thermally disordered phonons at low temperatures ($T \ll T_c$) and by spin fluctuations closer to T_c. It is expected that this technique will find application in a wide variety of other strongly correlated electron materials.

APPENDIX A

Derivation of Transmission Coefficients

A.1 Thin Film on Thick Substrate

At normal incidence the complex transmission coefficient $T(\omega)$ for a thin film on a thick substrate is given by Equation (2.31),

$$T(\omega) = \frac{\frac{T_{12}T_{23}}{T_13} \cdot exp\left[i\frac{\omega d}{c}(\tilde{n}_2 - 1)\right]}{1 + R_{12}R_{23} \cdot exp\left[2i\frac{\omega d}{c}\tilde{n}_2\right]} \cdot exp\left[i\frac{\omega \Delta L}{c}(\tilde{n}_3 - 1)\right], \tag{A.1}$$

where

$$T_{12} = \frac{2}{\tilde{n}_2 + 1}, \qquad T_{23} = \frac{2\tilde{n}_2}{\tilde{n}_3 + \tilde{n}_2}, \qquad T_{13} = \frac{2}{\tilde{n}_3 + 1}, \tag{A.2}$$

and

$$R_{12} = \frac{\tilde{n}_2 - 1}{\tilde{n}_2 + 1}, \qquad R_{23} = \frac{\tilde{n}_3 - \tilde{n}_2}{\tilde{n}_3 + \tilde{n}_2}. \tag{A.3}$$

Assuming $\frac{\omega}{c}d\tilde{n}_2 \ll 1$ and $\tilde{n}_2 \gg \tilde{n}_3 > 1$ Equation (A.1) can be reduced as follows (omitting the phase mismatch factor)

$$\begin{aligned} T(\omega) &= \frac{\frac{2\tilde{n}_2(\tilde{n}_3+1)}{(\tilde{n}_2+1)(\tilde{n}_3+\tilde{n}_2)} \cdot exp\left[i\frac{\omega d}{c}(\tilde{n}_2 - 1)\right]}{1 + \frac{(\tilde{n}_2-1)(\tilde{n}_3-\tilde{n}_2)}{(\tilde{n}_2+1)(\tilde{n}_3+\tilde{n}_2)} \cdot exp\left[2i\frac{\omega d}{c}\tilde{n}_2\right]} \\ &\simeq \frac{2\tilde{n}_2(\tilde{n}_3+1)(1+i\frac{\omega}{c}d\tilde{n}_2)}{\tilde{n}_2\tilde{n}_3 + \tilde{n}_2^2 + \tilde{n}_3 + \tilde{n}_2 + (\tilde{n}_2\tilde{n}_3 - \tilde{n}_2^2 - \tilde{n}_3 + \tilde{n}_2)(1 + 2i\frac{\omega}{c}d\tilde{n}_2)} \\ &\simeq \frac{\tilde{n}_3 + 1}{\tilde{n}_3 + 1 + (\tilde{n}_2\tilde{n}_3 + \tilde{n}_2^2 - \tilde{n}_3 + \tilde{n}_2)i\frac{\omega}{c}d} \\ &\simeq \frac{\tilde{n}_3 + 1}{\tilde{n}_3 + 1 - i\frac{\omega}{c}d\tilde{n}_2^2}. \end{aligned} \tag{A.4}$$

The refractive index of the superconducting film is given by

$$\tilde{n}_2 = \sqrt{1 + i\frac{\tilde{\sigma}}{\epsilon_o \omega}}, \tag{A.5}$$

and the impedance of free space is given by

$$Z_o = \sqrt{\frac{\mu_0}{\epsilon_o}} = \frac{1}{c\epsilon_o}. \tag{A.6}$$

The reduced expression for $T(\omega)$ (including the phase mismatch factor) can then be written as

$$T(\omega) = \frac{E_{\text{sig}}(\omega)}{E_{\text{ref}}(\omega)} = \frac{\tilde{n}_3 + 1}{\tilde{n}_3 + 1 + Z_o \tilde{\sigma}(\omega)\frac{\omega}{c} d} \cdot exp\left[i\frac{\omega \Delta L}{c}(\tilde{n}_3 - 1)\right]. \tag{A.7}$$

A.1.1 Induced Conductivity as a function of Induced Field

The induced change in conductivity as a function of induced change in electric field for a thin film on a thick substrate is obtained from Equation (A.7).

$$\frac{dT}{d\sigma} = \frac{-(1+\tilde{n}_3)e^{i\frac{\omega\Delta L}{c}(\tilde{n}_3-1)} Z_o d}{(1+\tilde{n}_3 + Z_o\sigma d)^2} = \frac{\Delta T}{\Delta \sigma} \tag{A.8}$$

$$\Rightarrow \Delta T = -T\frac{Z_o d \Delta\sigma}{(1+\tilde{n}_3 + Z_o\sigma d)} \tag{A.9}$$

$$\Rightarrow \Delta\sigma = -\frac{\Delta T}{T}\frac{1}{T}\frac{(1+\tilde{n}_3)e^{i\frac{\omega\Delta L}{c}(\tilde{n}_3-1)}}{Z_o d} \tag{A.10}$$

$$= -\frac{\Delta E}{E_{\text{sig}}}\frac{E_{\text{ref}}}{E_{\text{sig}}}\frac{(1+\tilde{n}_3)e^{i\frac{\omega\Delta L}{c}(\tilde{n}_3-1)}}{Z_o d}. \tag{A.11}$$

A.2 Optical Properties of Uniaxial Anisotropic Media

An electromagnetic wave incident at an angle, θ_i upon an anisotropic media (uniaxial crystal) will excite a wave inside the material, $\mathbf{E}=\mathbf{E_0}e^{i(\mathbf{k}\cdot\mathbf{r}-\omega t)}$ where each component of $\mathbf{E}$ and $\mathbf{k}$ can be complex. This is illustrated in Figure A.1 where the x-axis lies at the intersection of the plane of incidence and the z-axis

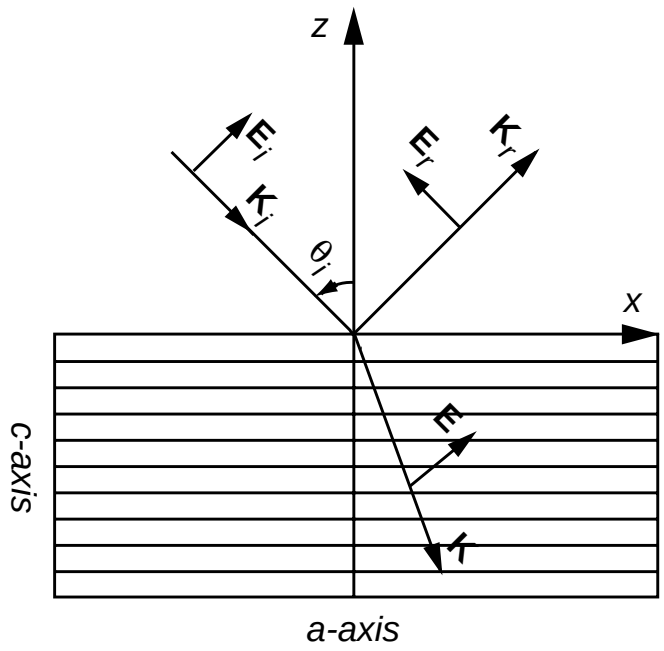

Figure A.1: Electromagnetic wave propagating in a uniaxial crystal.

is normal to the surface. The dielectric function in the anisotropic medium is a tensor

$$\hat{\epsilon} = \begin{pmatrix} \epsilon_\perp & 0 & 0 \\ 0 & \epsilon_\perp & 0 \\ 0 & 0 & \epsilon_\parallel \end{pmatrix},$$

and when solving Maxwell's equations [47] for the dispersion relation

$$\mathbf{k}(\mathbf{k}\cdot\mathbf{E}) - k^2\mathbf{E} + k_0^2\hat{\epsilon}\mathbf{E} = 0 \tag{A.12}$$

$$\Rightarrow \underbrace{\left[k^2 - k_0^2\epsilon_\perp\right]}_{ordinary}\underbrace{\left[\epsilon_\perp k_\perp^2 + \epsilon_\parallel k_\parallel^2 - \epsilon_\perp\epsilon_\parallel k_0^2\right]}_{extraordinary} = 0, \tag{A.13}$$

where

$$k = k_0 n, \qquad k_0^2 = \frac{\omega^2}{c^2}, \qquad k_\parallel = k_z, \qquad k_\perp^2 = k_x^2 + k_y^2 \tag{A.14}$$

we get two modes for the propagation of electromagnetic waves with a different value for the complex refractive index

$$\frac{1}{n} = \frac{1}{\epsilon_\perp}, \tag{A.15}$$

$$\frac{n_z^2}{\epsilon_\perp} + \frac{n_x^2 + n_y^2}{\epsilon_\parallel} = 1. \tag{A.16}$$

The complex refractive index for the ordinary and extraordinary waves are then given by

$$\frac{1}{n_o(\theta_o)} = \frac{1}{n_\perp}, \tag{A.17}$$

$$\frac{1}{n_e^2(\theta_e)} = \frac{\cos^2(\theta_e)}{n_\perp^2} + \frac{\sin^2(\theta_e)}{n_\parallel^2}, \tag{A.18}$$

respectively. If the incident wave is p-polarized the excited wave will propagate along the extraordinary axis at the angle, θ_e, and along the ordinary axis at the angle, θ_o when s-polarized [32].

To further understand the propagation of electromagnetic waves through a uniaxial anisotropic media we consider the x-component and z-component of the wave vectors. For the ordinary wave, $\sin\theta_i = n_\perp \sin\theta_o$. Therefore,

$$k_x = k\sin\theta_o = \frac{\omega}{c}\sin\theta_i, \tag{A.19}$$

and

$$k_z^2 = k^2\cos^2\theta_o = \frac{\omega^2}{c^2}\epsilon_{ab}\left(1 - \frac{\sin^2\theta_i}{\epsilon_{ab}}\right), \tag{A.20}$$

where $\epsilon_{ab} = \epsilon_\perp$ for the ab-plane (in-plane), and $\epsilon_c = \epsilon_\parallel$ for the c-axis (out-of-plane) dielectric functions given by

$$\epsilon_{ab}(\omega) = \epsilon_\infty^{ab}\left(1 - \frac{\omega_{pab}^2}{\omega^2}\right), \qquad \epsilon_c(\omega) = \epsilon_\infty^c\left(1 - \frac{\omega_{pc}^2}{\omega^2} + \frac{4\pi i\sigma_c}{\epsilon_\infty^c\omega}\right). \tag{A.21}$$

Here ω_{pab} and ω_{pc} are the in-plane and out-of-plane plasma frequencies, respectively. The x-axis wave vector depends only on the incident radiation, while the z-axis wave vector depends on the in-plane dielectric function. When substituting we find that the ordinary wave can only propagate above the in-plane plasma edge, $\omega > \omega_{pab}$.

For the extraordinary wave, $\sin\theta_i = n_e \sin\theta_e = n_x$. Therefore,

$$k_x = k \sin\theta_e = \frac{\omega}{c} \sin\theta_i. \tag{A.22}$$

From Equation (A.16), $n_x = \sin\theta_i$, and $n_y = 0$ we find

$$k_z^2 = \frac{\omega^2}{c^2} \epsilon_{ab} \left(1 - \frac{\sin^2\theta_i}{\epsilon_c} \right). \tag{A.23}$$

Thus, for the extraordinary wave, the z-axis wave vector depends on both the in-plane and out-of-plane dielectric functions. Assuming $\omega \ll \omega_{pab}$, and not taking into account dissipation and c-axis dispersion effects [101, 120], we find that the extraordinary wave can only propagate in a narrow window above the out-of-plane plasma edge,

$$\omega_{pc} < \omega < \frac{\omega_{pc}}{\sqrt{1 - \frac{\sin^2\theta}{\epsilon_\infty^c}}} \approx \omega_{pc} \left(1 + \frac{\sin^2\theta}{2\epsilon_\infty^c} \right). \tag{A.24}$$

A.2.1 Reflection and Transmission Coefficients at an Interface

The transmission and reflection coefficients for the ordinary wave at an interface between an anisotropic medium and an isotropic medium are given by the well known s-polarized Fresnel Equations (2.9) and (2.11), respectively.

The incident, reflected and transmitted waves for the extraordinary wave are given by

$$\mathbf{E}_i \;=\; \mathbf{E}^{(i)} exp\left[i(\mathbf{k}^{(i)} \cdot \mathbf{r} - \omega t) \right] \tag{A.25}$$

$$\mathbf{H}_i = n_1 \left(\hat{\mathbf{k}}^{(i)} \times \mathbf{E}_i \right), \tag{A.26}$$

$$\mathbf{E}_r = \mathbf{E}^{(r)} exp \left[i(\mathbf{k}^{(r)} \cdot \mathbf{r} - \omega t) \right] \tag{A.27}$$

$$\mathbf{H}_r = n_1 \left(\hat{\mathbf{k}}^{(t)} \times \mathbf{E}_r \right), \tag{A.28}$$

$$\mathbf{E}_t = \mathbf{E}^{(t)} exp \left[i(\mathbf{k}^{(t)} \cdot \mathbf{r} - \omega t) \right] \tag{A.29}$$

$$\mathbf{H}_t = \left(\frac{n_\perp^2}{n_z} \right) \cos\theta_t' \left(\hat{\mathbf{v}}^{(t)} \times \mathbf{E}_t \right), \tag{A.30}$$

respectively. Here $\hat{\mathbf{v}}$ is the complex ray vector, and θ_t' is the angle between the ray vector and the optical axis defined as the z-axis,

$$\tan\theta_t = \frac{n_\perp}{n_\parallel} \tag{A.31}$$

$$\Rightarrow \tan\theta_t' = \frac{\epsilon_\perp}{\epsilon_\parallel} \cdot \tan\theta_t = \frac{\epsilon_\perp}{\epsilon_\parallel} \frac{n_\perp}{n_\parallel}. \tag{A.32}$$

$\mathbf{E}^{(t)}$ is perpendicular to the ray vector, and lies in the principal plane defined by the z-axis and the x-axis. See Figure A.2. The boundary conditions require

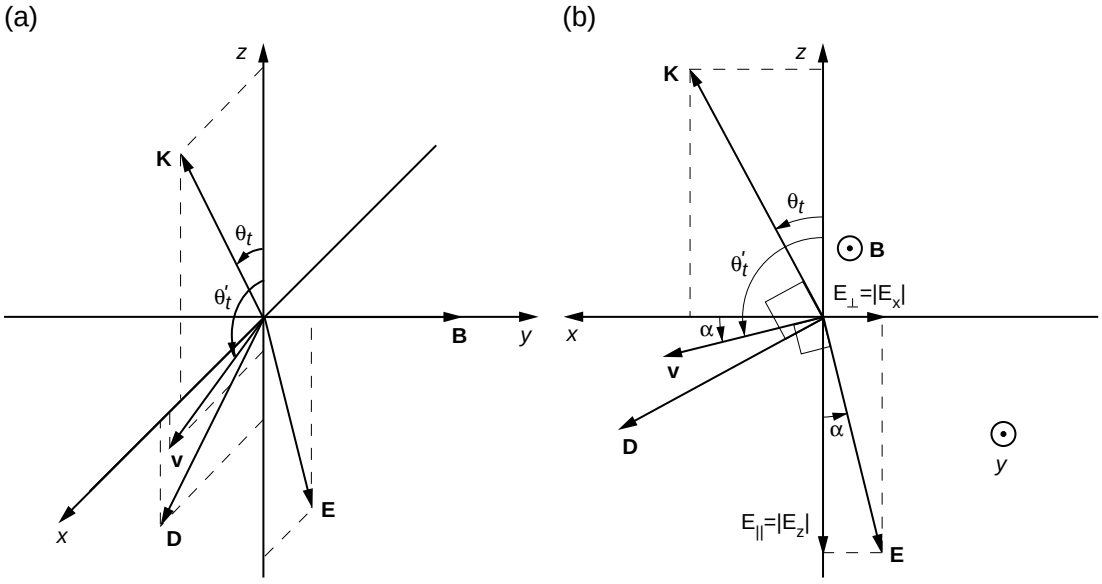

Figure A.2: (a and b) Illustration of the directions of the wave normal and the field vectors of an electromagnetic wave propagating in a uniaxial crystal.

the tangential components of $\mathbf{E}$ and $\mathbf{H}$ to be continuous at the interface plane.

Therefore,

$$E_{\parallel}^{(i)} \cos\theta_i - E_{\parallel}^{(r)} \cos\theta_i = E_{\parallel}^{(t)} \cos\theta_t', \tag{A.33}$$

$$n_1 E_{\parallel}^{(i)} + n_1 E_{\parallel}^{(r)} = \left(\frac{n_{\perp}^2}{n_z}\right) \cos\theta_t' E_{\parallel}^{(t)}. \tag{A.34}$$

Solving Equation (A.33) and (A.34) for $E_{\parallel}^{(t)}$ and $E_{\parallel}^{(r)}$ in terms of $E_{\parallel}^{(i)}$ yields

$$E_{\parallel}^{(t)} = \frac{n_{\perp}^2 \cos\theta_i - n_1 n_z}{(n_{\perp}^2 \cos\theta_i + n_1 n_z)\cos\theta_t'} E_{\parallel}^{(i)}, \tag{A.35}$$

$$E_{\parallel}^{(r)} = \frac{n_{\perp}^2 \cos\theta_i - n_1 n_z}{n_{\perp}^2 \cos\theta_i + n_1 n_z} E_{\parallel}^{(i)}. \tag{A.36}$$

n_z is found from Equation (A.16)

$$n_z = \frac{n_{\perp}}{n_{\parallel}} \left(n_{\parallel}^2 - n_1^2 \sin^2\theta_i\right)^{\frac{1}{2}}, \tag{A.37}$$

where $n_x = n_1 \sin\theta_i$, and $n_y = 0$. Thus, in going from an isotropic medium 1 to an anisotropic medium 2 the transmission coefficient is given by

$$T_{12} = \frac{2n_1 \cos\theta_1 \sqrt{\frac{n_1^2}{n_c^2}\sin^2\theta_1 \left(\frac{n_{ab}^2}{n_c^2} - 1\right) + 1}}{n_{ab}\cos\theta_1 + n_1 \sqrt{1 - \frac{n_1^2}{n_c^2}\sin^2\theta_1}}, \tag{A.38}$$

and the reflection coefficient is given by

$$R_{12} = \frac{n_{ab}\cos\theta_1 - n_1 \sqrt{1 - \frac{n_1^2}{n_c^2}\sin^2\theta_1}}{n_{ab}\cos\theta_1 + n_1 \sqrt{1 + \frac{n_1^2}{n_c^2}\sin^2\theta_1}}. \tag{A.39}$$

In going from an anisotropic medium 2 to an isotropic medium 3 the transmission coefficient is given by

$$T_{23} = \frac{2n_{ab}\sqrt{1 - \frac{n_1^2}{n_c^2}\sin^2\theta_1}}{\sqrt{1 + \frac{n_1^2}{n_c^2}\sin^2\theta_1 \left(\frac{n_{ab}^2}{n_c^2} - 1\right)} \left[n_{ab}\cos\theta_3 + n_3 \sqrt{1 - \frac{n_1^2}{n_c^2}\sin^2\theta_1}\right]}, \tag{A.40}$$

and the reflection coefficient is given by

$$R_{23} = \frac{n_3 \sqrt{1 + \frac{n_1^2}{n_c^2}\sin^2\theta_1} - n_{ab}\cos\theta_3}{n_3 \sqrt{1 + \frac{n_1^2}{n_c^2}\sin^2\theta_1} + n_{ab}\cos\theta_3}. \tag{A.41}$$

In case of an anisotropic crystal, $n_3 = n_1$ and $\theta_3 = \theta_1$, where medium 1 is air, medium 2 is the crystal, and medium 3 is air. In case of an anisotropic thin film on a thick substrate, medium 1 is air, medium 2 is the thin film, medium 3 is the thick substrate, and medium 4 is air. Then $n_4 = n_1$ and θ_3 is given by

$$\cos\theta_3 = \sqrt{1 - \frac{n_1^2}{n_3^2}\sin^2\theta_1}. \tag{A.42}$$

The propagation coefficient in the anisotropic medium 2 over a distance d is given by

$$P_2 = exp\left[i\frac{\omega d}{c}\tilde{n}_2\cos\theta_2\right]. \tag{A.43}$$

Here n_2 and θ_2 are the refractive index and angle of the extraordinary wave, respectively, $n_z = n_e\cos\theta_e = n_2\cos\theta_2$. Using Equation (A.37) for n_z

$$n_2\cos\theta_2 = n_{ab}\sqrt{1 - \frac{n_1^2}{n_c^2}\sin^2\theta_1}. \tag{A.44}$$

Thus,

$$P_2 = exp\left[i\frac{\omega d}{c}\tilde{n}_{ab}\sqrt{1 - \frac{\tilde{n}_1^2}{\tilde{n}_c^2}\sin^2\theta_1}\right]. \tag{A.45}$$

References

[1] Reprinted from Physica C, **282−287**, S. Berry, M. Konczykowski, P. H. Kes, and E. Zeldov, Local magnetic relaxation close to the second peak in BSCCO crystals, 2259−2260 (1997), © Copyright (1997), with permission from Elsevier Science

[2] Reprinted from Physical Review Letters, Y. Matsuda, M. B. Gaifullin, K. Kumagai, K. Kadowaki, and T. Mochiku, Collective Josephson Plasma Resonance in the Vortex State of $Bi_2Sr_2CaCu_2O_{8+\delta}$, **75**, 4512−4515 (1995), © Copyright (1995), with permission from The American Physical Society, and Yuji Matsuda from University of Tokyo in Japan

[3] Reprinted from Physical Review Letters, T. Shibauchi, T. Nakano, M. Sato, T. Kisu, N. Kameda, N. Okuda, S. Ooi, and T. Tamegai, Interlayer Phase Coherence in the Vortex Matter Phases of $Bi_2Sr_2CaCu_2O_{8+y}$, **83**, 1010−1013 (1999), © Copyright (1999), with permission from The American Physical Society, and Takasada Shibauchi from Kyoto University in Japan

[4] Reprinted from *Colossal Magnetoresistive Oxides*, Edited by Yoshinori Tokura, Advances in Condensed Matter Science, Volume **2**, © Copyright (2000), with kind permission from Gordon and Breach Publishing, a member of the Taylor and Francis Group, Amsterdam (2000)

[5] J. G. Bednorz and K. A. Mü, Z. Phys. B **64**, 189 (1986)

[6] M. K. Wu, J. R. Ashburn, C. J. Torng, P. H. Hor, R. L. Meng, L. Gao, J. Huang, Y, Q. Wang, and C. W. Chu, Phys. Rev. Lett. **58**, 109 (1987)

[7] Z. X. Zhao, L. Q. Chen, Y. H. Huang, G. H. Chen, R. M. Tang, G. R. Liu, C. G. Cui, L. Chen, L. H. Wang, S. Q. Guo, S. L. Li, and J. Q. Bi, Kexue Tongbao **32**, 661 (1987)

[8] H. Maeda, Y. Tanaka, M. Fukutomi, and T. Asano, Jpn. J. Appl. Phys. **27**, L209 (1988)

[9] Z. Z. Sheng and A. M. Hermann, Nature **232**, 55 (1988)

[10] L. Gao, Y. Y. Xue, F. Chen, Q. Xiong, R. L. Meng, D. Ramirez, C. W. Chu, J. H. Eggert, and H. K. Mao, Phys. Rev. B **50**, 4260 (1994)

[11] B. A. Baumert, J. Supercond. **8**, 175 (1995)

[12] A. Shengelaya, K. A. Müller, S. Reich, and Y. Tsabba, Eur. Phys. J. B **12**, 13 (1999)

[13] J. Akimitsu, Symposium on Transition Metal Oxides, Sendai, Jan 10 (2001); J. Nagamatsu, N. Nakagawa, T. Murakana, Y. Zenitani, and J. Akimutsu, Nature **410**, 63 (2001)

[14] C. H. Rosner, IEEE Trans. on Appl. Supercond. **11**, 39 (2001)

[15] T. Timusk and B. Statt, Rep. Prog. Phys. **62**, 61 (1999)

[16] L. F. Cohen and H. J. Jensen, Rep. Prog. Phys. **60**, 1581 (1997)

[17] Y. Yeshurun, A. P. Malozemoff, and A. Shaulov, Rev. Mod. Phys. **68**, 911 (1996)

[18] K. Kadowaki, Y. Songliu, and Koichi Kitazawa, Supercond. Sci. Technol. **7**, 519 (1994)

[19] A. A. Tsvetkov, D. van der Marel, D. Dulic, H. J. Molegraaf, N. N. Kolesnikov, B. Willemsen, and Z. F. Ren, Proc SPIE Int Soc Opt Eng, edited by I. Bozovic, D. Pavuna **3480**, p. 2−10 (Bellingham, WA, USA: SPIE 1998)

[20] V. K. Thorsmølle, R. D. Averitt, M. P. Maley, L. N. Bulaevskii, C. Helm, and A. J. Taylor, Opt. Lett. **26**, 1292 (2001)

[21] T. Xiang and J. M. Wheatley, Phys. Rev. Lett. **77**, 4632 (1996)

[22] M. B. Gaifullin, Y. Matsuda, N. Chikumoto, J. Shimoyama, and K. Kishio, Phys. Rev. Lett. **84**, 2945 (2000)

[23] L. Duvillaret, F. Garet, and J.-L. Coutaz, IEEE J. of Sel. Topics in Quantum Electr. **2**, 739 (1996)

[24] M. C. Nuss and J. Orenstein, Terahertz Spectroscopy in *Millimeter and Submillimeter Wave Spectroscopy of Solids*, G. Grüner, ed., Topics in Applied Physics **74**, 7−50 (1998)

[25] D. Grischkowsky and S. Keiding, Appl. Phys. Lett. **57**, 1055 (1990)

[26] M. van Exter and D. R. Grischkowsky, "Characterization of an opto-electronic terahertz beam system", IEEE Trans. MTT-**38**, 1684−1691 (1990)

[27] A. M. Johnson and D. H. Auston, IEEE J. Quantum Electron. **11**, 283 (1975)

[28] M. B. Ketchen, D. R. Grischkowsky, T. C. Chen, C.-C. Chi, I. N. Duling, N. J. Hallas, J.-M. Halbout, J. A. Kash, and G. P. Li, Appl. Phys. Lett. **48**, 751 (1986)

[29] Søren Rud Keiding, *THz-Pulses*, Dissertation, Department of Chemistry, Univ. of Aarhus, July 1998

[30] S. E. Ralph and D. R. Grischkowsky, Appl. Phys. Lett. **59**, 1972 (1991)

[31] Ch. Fattinger and D. R. Grischkowsky, Appl. Phys. Lett. **54**, 490 (1989)

[32] M. Born and E. Wolf, *Principles of Optics*, (Pergamon Press, Oxford, 1980), 6th ed.

[33] F. E. Doany, D. R. Grischkowsky, and C. C. Chi, Appl. Phys. Lett. **50**, 460 (1987)

[34] J. E. Pedersen, S. R. Keiding, C. B. Sørensen, P. E. Lindelof, W. W. Rühle, and X. Q. Zhou, J. Appl. Phys. **74**, 7022 (1993)

[35] P. U. Jepsen and S. R. Keiding, Opt. Lett. **20**, 807 (1995)

[36] X.-C. Zhang, Y. Yin, K. Yang, and L. J. Schowalter, Phys. Rev. Lett. **69**, 2303 (1992)

[37] B. B. Hu, X.-C. Zhang, D. H. Auston, and P. R. Smith, Appl. Phys. Lett. **56**, 506 (1990)

[38] A. Nahata, A. S. Weling, and T. F. Heinz, Appl. Phys. Lett. **69**, 2321 (1996)

[39] G. Gallot and D. Grischkowsky, J. Opt. Soc. Am. B **16**, 1204 (1999)

[40] L. Xu, X.-C. Zhang, and D. H. Auston, Appl. Phys. Lett. **61**, 1784 (1992)

[41] A. Leitenstorfer, S. Hunsch, J. Shah, and M. C. Nuss, Appl. Phys. Lett. **74**, 1516 (1990)

[42] Q. Wu and X.-C. Zhang, Appl. Phys. Lett. **70**, 1784 (1997)

[43] X.-C. Zhang, X. F. Ma, Y. Jin, T.-M. Lu, E. P. Boden, P. D. Phelps, K. R. Stewart, and C. P. Yakymyshyn, Appl. Phys. Lett. **61**, 3080 (1992)

[44] Q. Wu and X.-C. Zhang, Appl. Phys. Lett. **68**, 1604 (1996)

[45] G. Gallot, J. Zhang, R. W. McGowan, T.-I. Jeon, and D. Grischkowsky, Appl. Phys. Lett. **74**, 3450 (1999)

[46] Q. Wu and X.-C. Zhang, Appl. Phys. Lett. **71**, 1285 (1997)

[47] J. D. Jackson, *Classical Electrodynamics*, (Wiley & Sons, Inc., New York, 1975), 2nd ed.

[48] M. C. Nuss, D. H. Auston, and F. Capasso, Phys. Rev. Lett. **58**, 2355 (1987)

[49] R. D. Averitt, S. L. Westcott, and N. J. Halas, J. Opt. Soc. Am. B **16**, 1814 (1999)

[50] P. B. Corkum, F. Brunel, N. K. Sherman, and T. Shrinivasan-Rao, Phys. Rev. Lett. **61**, 2886 (1988)

[51] C.-K. Sun, F. Vallée, L. H. Acioli, E. P. Ippen, and J. G. Fujimoto, Phys. Rev. B **50**, 15337 (1994)

[52] S. G. Han, Z. V. Vardeny, K. S. Wong, O. G. Symko, and G. Koren, Phys. Rev. Lett. **65**, 2708 (1990)

[53] S. V. Chekalin, V. M. Farztdinov, and V. V. Golovlyov, Phys. Rev. Lett. **67**, 3860 (1991)

[54] C. J. Stevens, D. Smith, C. Chen, J. F. Ryan, B. Podobnik, D. Mihailovic, G. A. Wagner, and J. E. Evetts, Phys. Rev. Lett. **78**, 2212 (1997)

[55] V. V. Kabanov, J. Demsar, B. Podobnik, and D. Mihailovic, Phys. Rev. B **59**, 1497 (1999)

[56] J. Demsar, B. Podobnik, V. V. Kabanov, Th. Wolf, and D. Mihailovic, Phys. Rev. Lett. **82**, 4918 (1999)

[57] R. D. Averitt, G. Rodriguez, A. I. Lobad, J. L. W. Siders, S. A. Trugman, and A. J. Taylor, Phys. Rev. B **63**, 140502(R) (2001)

[58] R. D. Averitt, A. I. Lobad, C. Kwon, S. A. Trugman, V. K. Thorsmølle, and A. J. Taylor, Phys. Rev. Lett. **87**, 017401 (2001)

[59] J. Bardeen, L. N. Cooper, and J. R. Schrieffer, Phys. Rev. **106**, 162 (1957); Phys. Rev. B **108**, 1175 (1957)

[60] M. Tinkham, *Introduction to Superconductivity*, (McGraw-Hill, Inc., New York 1996), 2nd ed.

[61] E. M. Lifshitz and L. P. Pitaevskii, Landau and Lifshitz; Course of Theoretical Physics, Volume **9**, *Statistical Physics Part 2*, (Butterworth-Heinemann Ltd, Oxford, 1995)

[62] J. F. Annett, N. Goldenfeld, and A. J. Leggett, Experimental constraints on the pairing state of the cuprate superconductors: An emerging consensus in *Physical Properties of High Temperature Superconductors*, D. M. Ginsberg, ed., **V**, 375−461 (1996)

[63] D. A. Wollman, D. J. van Harlingen, J. Giapintzakis, and D. M. Ginsberg, Phys. Rev. Lett. **74**, 797 (1995)

[64] P. Monthoux and D. Pines, Phys. Rev. Lett. **69**, 961 (1992); Phys. Rev. B **47**, 6069 (1993); Phys. Rev. B **49**, 4269 (1994)

[65] G. Blatter, M. V. Feigel'man, V. B. Geshkenbein, A. I. Larkin, and V. M. Vinokur, Rev. Mod. Phys. **66**, 1125 (1994)

[66] L. Civale, A. D. Marvich, T. K. Worthington, M. A. Kirk, J. R. Thompson, L. Krusin-Elbaum, Y. Sun, and J. R. Clem, Phys. Rev. Lett. **67**, 648 (1991)

[67] P. W. Anderson and Y. B. Kim, Rev. Mod. Phys. **36**, 39 (1964)

[68] A. I. Larkin and Y. V. Ovchinikov, J. Low Temp. Phys. **34**, 409 (1979)

[69] D. R. Nelson, Phys. Rev. Lett. **60**, 1975 (1988)

[70] W. E. Lawrence and S. Doniach, Proc. 12th Int. Conf. Low Temp. Phys., p. 361 (Kyoto, 1970; Keigaku, Tokyo, 1971)

[71] M. J. W. Dodgson, V. B. Geshkenbein, H. Nordborg, and G. blatter, Phys. Rev. B **57**, 14498 (1998)

[72] M. Willemin, Phys. Rev. Lett. **81**, 4236 (1998)

[73] E. Zeldov, D. Majer, M. Konczykowski, V. B. Geshkenbein, V. M. Vinokur, and H. Strikman, Nature **375**, 373 (1995)

[74] L. N. Bulaevskii and J. R. Clem, Phys. Rev. B **44**, 10234 (1991)

[75] L. N. Bulaevskii, Tr. J. Phys. **20**, 594−626 (1996)

[76] A. E. Koshelev and V. M. Vinokur, Phys. Rev. B **57**, 8026 (1998)

[77] R. A. Doyle, B. Khaykovich, M. Konczykowski, E. Zeldov, N. Morozov, D. Majer, P. H. Kes, and V. Vinokur, Physica C **282−287**, 323 (1997)

[78] N. Chikumoto, M. Kosugi, Y. Matsuda, M. Konczykowski, and K. Kishio, Phys. Rev. B **57**, 14507 (1998)

[79] N. Morozov, M. P. Maley, L. N. Bulaevskii, V. K. Thorsmølle, A. E. Koshelev, A. Petrea, and W. K. Kwok, Phys. Rev. Lett. **82**, 1008 (1999)

[80] R. A. Doyle, S. F. W. R. Rycroft, C. D. Dewhurst, E. Zeldov, I. Tsabba, S. Reich, T. B. Doyle, and S. Ooi, Physica C **308**, 123 (1998)

[81] S. Berry, M. Konczykowski, P. H. Kes, and E. Zeldov, Physica C **282−287**, 2259 (1997)

[82] R. Cubbit and E. M. Forgan, Nature (London) **365**, 407 (1993)

[83] Y. Matsuda, M. B. Gaifullin, K. Kumagai, K. Kadowaki, T. Mochiku, and K. Hirata, Phys. Rev. B **55**, R8685 (1997)

[84] O. K. C. Tsui, N. P. Ong, and J. B. Peterson, Phys. Rev. Lett. **76**, 819 (1996)

[85] A. E. Koshelev, Phys. Rev. Lett. **77**, 3901 (1996)

[86] R. J. Drost, C. J. van der Beek, J. A. Heijn, M. Konczykowski, and P. H. Kes, Phys. Rev. B **58**, R615 (1998)

[87] M. Kosugi, Y. Matsuda, M. B. Gaifullin, L. N. Bulaevskii, N. Chikumoto, M. Konczykowski, J. Shimoyama, K. Kishio, K. Hirata, and K. Kumagai, Phys. Rev. Lett. **79**, 3763 (1997)

[88] M. Sato, T. Shibauchi, S. Ooi, T. Tamegai, and M. Konczykowski, Phys. Rev. Lett. **79**, 3759 (1997)

[89] N. Morozov, M. P. Maley, L. N. Bulaevskii, and J. Sarrao, Phys. Rev. B **57**, R8146 (1998)

[90] L. N. Bulaevskii, M. P. Maley, and V. M. Vinokur, Phys. Rev. B **57**, R5626 (1998)

[91] A. E. Koshelev, L. N. Bulaevskii, and M. P. Maley, Phys. Rev. Lett. **81**, 902 (1998)

[92] A. E. Koshelev, Phys. Rev. Lett. **76**, 1340 (1996)

[93] R. A. Doyle, W. S. Seow, Y. Yan, A. M. Campbell, T. Mochiku, K. Kadowaki, and G. Wirth, Phys. Rev. Lett. **77**, 1155 (1996); J. H. Cho, M. P. Maley, S. Flescher, A. Lacerda, and L. N. Bulaevskii, Phys. Rev. B **50**, 6493 (1994)

[94] A. Wahl, V. Hardy, J. Provost, C. Simon, and A. Buzdin, Physica (Amsterdam), **250C**, 163 (1995); C. Wengel and U. C. Täuber, Phys. Rev. Lett. **78**, 4845 (1997)

[95] A. A. Tsvetkov, D. van der Marel, J. F. Ren, J. R. Kirtley, J. L. de Boer, N. N. Kolesnikov, D. Dulic, A. Damascelli, M. Grüninger, J. Schützmann, J. W. van der Eb, H. S. Somal, and J. H. Wang, Nature **395**, 360 (1998)

[96] L. N. Bulaevskii, M. P. Maley, and M. Tachiki, Phys. Rev. Lett. **268**, 809 (1995)

[97] O. K. C. Tsui, N. P. Ong, Y. Matsuda, Y. F. Yan, and J. B. Peterson, Phys. Rev. Lett. **73**, 724 (1994)

[98] A. Barone and G. Paternó, *Physics and Applications of the Josephson Effect*, (John Wiley & Sons, Inc., New York, 1982)

[99] B. D. Josephson, in *Quantum Fluids*, edited by D. F. Brewer, (North-Holland Publishing Company, Amsterdam, 1966)

[100] A. I. Dahm, A. Denenstein, T. F. Finnegan, D. N. Langenberg, and D. J. Scalapino, Phys. Rev. Lett. **20**, 859 (1968)

[101] T. Koyama and M. Tachiki, Phys. Rev. B **54**, 16183 (1996)

[102] M. Sigrist and K. Ueda, Rev. Mod. Phys. **63**, 239 (1991)

[103] J. Annett, N. Goldenfeld, and S. R. T. Renn, Phys. Rev. B. **43**, 3448 (1991)

[104] M. Prohammer and J. P. Carbotte, Phys. Rev. B **43**, 5370 (1991)

[105] M. Wilson, *Superconducting Magnets* (Oxford, New York, 1983)

[106] C. J. Gorter and H. G. B. Casimir, Z. Phys. **35**, 963 (1934)

[107] D. A. Bonn, S. Kamal, A. Bonakdarpour, Liang Ruixing, W. N. Hardy, C. C. Homes, D. N. Basov, and T. Timusk, Czeh. J. Phys. **46**, 3195 (1996)

[108] C. Panagopoulos, J. R. Cooper, T. Xiang, G. P. Peacock, I. Gameson, and P. P. Edwards, Phys. Rev. Lett. **79**, 2320 (1997)

[109] T. Shibauchi, H. Kitano, K. Uchinokura, A. Maeda, T. Kimura, and K. Kishio, Phys. Rev. Lett. **72**, 2263 (1994)

[110] M. B. Gaifullin, Y. Matsuda, N. Chikumoto, J. Shimoyama, K. Kishio, and R. Yoshizaki, Phys. Rev. Lett. **83**, 3928 (1999)

[111] R. J. Radtke, V. N. Kostur, and K. Levin, Phys. Rev. B **53**, R522 (1966)

[112] Y. Ohashi and S. Takada, Phys. Rev. B **59**, 4404 (1999)

[113] S. E. Shafranjuk and M. Tachiki, Europhys. Lett. **59**, 11587 (1999)

[114] L. N. Bulaevskii, D. Domínguez, M. P. Maley, A. R. Bishop, O. K. C. Tsui, and N. P. Ong, Phys. Rev. B **54**, 7521 (1996)

[115] I. Kakeya, K. Kindo, K. Kadowaki, S. Takahashi, and T. Mochiku, Phys. Rev. B **57**, 3108 (1998)

[116] K. Kadowaki, I. Kakeya, M. B. Gaifullin, T. Mochiku, S. Takahashi, T. Koyama, and M. Tachiki, Phys. Rev. B **56**, 5617 (1997)

[117] A. E. Koshelev, L. N. Bulaevskii, and M. P. Maley, Phys. Rev. B. **62**, 14403 (2000)

[118] Y. Matsuda, M. B. Gaifullin, K. Kumagai, K. Kadowaki, and T. Mochiku, Phys. Rev. Lett. **74**, 4512 (1995)

[119] C. P. Poole, *Handbook of Superconductivity* (Academic Press, San Diego, 2000)

[120] S. N. Artemenko and A. G. Kobel'kov, Physica C **253**, 373 (1995)

[121] T. Jacobs, Phys. Rev. Lett. **75**, 4516 (1994)

[122] S.-F. Lee, D. C. Morgan, R. J. Ormeno, D. M. Broun, R. D. Doyle, J. R. Waldram, and K. Kadowaki, Phys. Rev. Lett. **77**, 735 (1996)

[123] Yu. I. Latyshev and T. Yamashita, Phys. Rev. Lett. **82**, 5345 (1999)

[124] A. Hosseini, S. Kamal, D. A. Bonn, R. Liang, and W. N. Hardy, Phys. Rev. Lett. **81**, 1298 (1998)

[125] P. J. M. van Bentum, A. Wittlin, M. E. J. Boonman, M. Gross, S. Uchida, and K. Tamasaku, Physica C **293**, 136−142 (1997)

[126] X-ray diffraction measurements performed by Superconductivity Technologies Inc., Santa Barbara, California who grows the Tl-2212 films

[127] A. Schilling, R. A. Fisher, N. E. Phillips, U. Welp, D. Dagupta, W. K. Kwok, and G. W. Crabtree, Nature (London) **382**, 791 (1996)

[128] X. Hu, S. Miyashita, and M. Tachiki, Phys. Rev. Lett. **79**, 3498 (1997); Phys. Rev. B **58**, 3438 (1998)

[129] B. Khaykovich, E. Zeldov, D. Majer, T. W. Li, P. H. Kes, and M. Konczykowski, Phys. Rev. Lett. **76**, 2555 (1996)

[130] H. Safar, P. L. Gammel, D. A. Huse, S. N. Majumdar, L. F. Schneemeyer, and D. J. Bishop, Phys. Rev. Lett. **72**, 1272 (1994)

[131] J. R. Clem, Phys. Rev. B **43**, 7837 (1991)

[132] T. Shibauchi, T. Nakano, M. Sato, T. Kisu, N. Kameda, N. Okuda, S. Ooi, and T. Tamegai, Phys. Rev. Lett. **83**, 1010 (1999)

[133] L. N. Bulaevskii , A. E. Koshelev, V. M. Vinokur, and M. P. Maley, Phys. Rev. B **61**, R3819 (2000)

[134] A. E. Koshelev and L. N. Bulaevskii, Physica C **341−348**, 1503 (2000)

[135] D. Dulić, S. J. Hak, D. van der Marel, W. N. Hardy, A. E. Koshelev, R. Liang, D. A. Bonn, and B. A. Willemsen, Phys. Rev. Lett. **86**, 4660 (2001)

[136] A. E. koshelev, L. I. Glazman, and A. I. Larkin, Phys. Rev. B **53**, 2786 (1996)

[137] T. Chen and S. Teitel, Phys. Rev. B **55**, 11766 (1997)

[138] P. Olsson and S. Teitel, Phys. Rev. Lett. **82**, 2183 (1999)

[139] A. E. Koshelev, Phys. Rev. B **56**, 11201 (1997)

[140] A. K. Nguyen and A. Sudbø, Phys. Rev. B **57**, 3123 (1998); Phys. Rev. B **58**, 2802 (1998)

[141] H. Nordborg and G. Blatter, Phys. Rev. Lett. **79**, 1925 (1997); Phys. Rev. B **58**, 14556 (1998)

[142] A. E. Koshelev and H. Nordborg, Phys. Rev. B **59**, 4358 (1999)

[143] M. J. W. Dodgson, A. E. koshelev, V. B. Geshkenbein, and G. Blatter, Phys. Rev. Lett. **84**, 2698 (2000)

[144] D. Dulić, D. van der Marel, A. A. Tsvetkov, W. N. Hardy, Z. F. Ren, J. H. Wang, and B. A. Willemsen, Phys. Rev. B **60**, R15051 (1999)

[145] V. Hardy, A. Maignan, C. Martin, F. varmont, and J. Provost, Phys. Rev. B **56**, 130 (1997)

[146] I. Arenson, A. E. Koshelev, and V. M. Vinokur, Phys Rev. B **56**, 5136 (1997)

[147] A. E. Koshelev and V. M. Vinokur, Phys. Rev. Lett. **73**, 3580 (1994)

[148] L. Balents and M. P. A. Fischer, Phys. Rev. Lett. **75**, 4270 (1995)

[149] T. Giamarchi and P. Le Doussal, Phys. Rev. Lett. **76**, 3408 (1996)

[150] K. Moon, R. T. Scaletter, and G. Zimányi, Phys. Rev. Lett. **77**, 2778 (1996)

[151] S. Ryu, M. Hellerquist, S. Doniach, A. Kapitulnik, and D. Stroud, Phys. Rev. Lett. **77**, 5114 (1996)

[152] S. Bhattacharya and M. J. Higgins, Phys. Rev. Lett. **70**, 2617 (1993)

[153] U. Yaron, P. L. Gammel, D. A. Huse, R. N. Kleiman, C. S. Oglesby, E. Bucher, B. Batlogg, D. J. Bishop, K. Mortensen, K. Clausen, C. A. Bolle, and F. De La Cruz, Phys. Rev. Lett. **73**, 2748 (1994)

[154] M. Marchevsky, L. A. Gurevich, P. H. Kes, and J. Aarts, Phys. Rev. Lett. **75**, 2400 (1995)

[155] E. Rodríguez, M. F. Goffman, A. Arribére, F. de la Cruz, and L. F. Schneemeyer, Phys. Rev. Lett. **71**, 3375 (1993)

[156] J. Corson, J. Orenstein, S. Oh, J. O'Donnell, and J. N. Eckstein, Phys. Rev. Lett. **85**, 2569 (2000)

[157] J. S. Dodge, C. P. Weber, J. Corson, J. Orenstein, Z. Schlesinger, J. W. Reiner, and M. R. Beasley, Phys. Rev. Lett. **85**, 4932 (2000)

[158] E. Knoesel, M. Bonn, J. Shan, and T. F. Heinz, Phys. Rev. Lett. **86**, 340 (2001)

[159] M. C. Beard, G. M. Turner, and C. A. Schmuttenmaer, Phys. Rev. B **62**, 15764 (2000)

[160] K. P. H. Lui and F. A. Hegmann, Appl. Phys. Lett. **78**, 3478 (2001)

[161] R. D. Averitt, G. Rodriguez, J. L. W. Siders, S. A. Trugman, and A. J. Taylor, J. Opt. Soc. Am. B **17**, 327 (2000)

[162] S. D. Brorson, R. Buhleier, I. E. Trofimov, J. O. White, Ch. Ludwig, F. F. Balakirev, H.-U. Habermeier, and J. Kuhl, J. Opt. Soc. Am. B **13**, 1979 (1996)

[163] J. Volger, Physica **20**, 49 (1954)

[164] S. Jin, T. H. Tiefel, M. McCormack, R. A. Fastnacht, R. Ramesh, and L. H. Chen, Science **264**, 413 (1994)

[165] A. J. Millis, Nature **392**, 147 (1998)

[166] *Colossal Magnetoresistive Oxides*, edited by Y. Tokura (Gordon and Breach, Amsterdam, 2000)

[167] G. L. Eesley, Phys. Rev. Lett. **51**, 2140 (1983)

[168] E. Beaurepaire, J.-C. Merle, A. Daunois, and J.-Y. Bigot, Phys. Rev. Lett. **76**, 4250 (1996)

[169] B. Koopmans, M. van Kampen, J. T. Kohlhepp, and W. J. M. de Jonge, Phys. Rev. Lett. **85**, 844 (2000)

[170] J. S. Dodge, A. B. Schumacher, J.-Y. Bigot, D. S. Chemla, N. Ingle, and M. R. Beasley, Phys. Rev. Lett. **83**, 4650 (1999)

[171] T. Kise, T. Ogasawara, M. Ashida, Y. Tomioka, Y. Tokura, and M. Kuwata-Gonokami, Phys. Rev. Lett. **85**, 1986 (2000)

[172] C. Kwon, Q. X. Jia, Y. Fan, M. F. Hundley, D. W. Reagor, J. Y. Coulter, and D. E. Peterson, Appl. Phys. Lett. **72**, 486 (1998)

[173] A. Biswas, M. Rajeswari, R. C. Srivastava, Y. H. Li, T. Venkatesan, R. L. Greene, and A. J. Milles, Phys. Rev. B **61**, 9665 (2000)

[174] M. F. Hundley, M. Hawley, R. H. Heffner, Q. X. Jia, J. J. Neumeier, J. Tesmer, J. D. Thompson, and X. D. Wu, Appl. Phys. Lett. **67**, 860 (1995)

[175] A. V. Boris, N. N. Kovaleva, A. V. Bazhenov, P. J. M. van Bentum, Th. Raising, S-W. Cheong, A. V. Samoilov, and N.-C. Yeh, Phys. Rev. B **59**, R697 (1999)

[176] G-M. Zhao, V. Smolyaninova, W. Prellier, and H. Keller, Phys. Rev. Lett. **84**, 6086 (2000)

[177] Y. Yafet, in *Solid State Physics **14***, edited by F. Seitz and D. Turnbull (Academic Press, New York, 1963)

[178] A. P. Ramirez, P. Schiffer, S-W. Cheong, C. H. Chen, W. Bao, T. T. M. Palstra, P. L. Gammel, D. J. Bishop, and B. Zegarski, Phys. Rev. Lett. **76**, 3188 (1996)

[179] M. N. Khlopkin, G. Kh. Panova, A. A. Shikov, V. F. Sinyavskii, and D. A. Shulyatev, Phys. Sol. State **42**, 114 (2000)